SPIN-PUMPING AND TWO-MAGNON SCATTERING IN MAGNETIC MULTILAYERS

by

Georg Woltersdorf
Diplom, Martin-Luther-Universität, Halle, 2001

Thesis submitted in partial fulfillment
of the requirements for the degree of
Doctor of Philosophy
in the department
of
Physics

SIMON FRASER UNIVERSITY
August 2004

APPROVAL

Name: Georg Woltersdorf

Degree: Doctor of Philosophy

Title of Thesis: Spin-Pumping and Two-Magnon Scattering in Magnetic Multilayers

Examining Committee: Howard D. Trottier Professor (Chair)

Bretislav Heinrich (Senior Supervisor)
Professor, Department of Physics

E. Daryl Crozier (Supervisor)
Professor, Department of Physics

Michael R. Scheinfein (Supervisor)
Adjunct Professor, Department of Physics

Michael E. Hayden (Internal Examiner)
Associate Professor, Department of Physics

Pavel Kaboš (External Examiner)
Staff Scientist, NIST, Boulder
Associate Professor, Slovak Technical University

Date Approved: 29 July 2004

Abstract

Epitaxial ultrathin Fe(001) film structures are grown by Molecular Beam Epitaxy (MBE) on GaAs(001) substrates. The magneto-dynamic properties are investigated using Ferromagnetic Resonance (FMR) and time-resolved magneto-optic Kerr microscopy (TRMOKE) over a wide range of microwave frequencies using Au/Fe/-GaAs(001) and Au/Fe/Au/Fe/GaAs(001) structures. A new long-range dynamic exchange interaction between ferromagnetic films separated by normal metal (NM) spacers is reported. This interaction is communicated by non-equilibrium spin currents. It is measured using FMR and explained by an adiabatic spin-pumping theory. At ferromagnetic resonance the spin-pump/spin-sink mechanism of two spatially separated magnetic layers leads to an appreciable increase in the resonant linewidth (damping) when the resonance fields of the two layers are well apart, and results in a linewidth narrowing when the resonant fields approach each other. The spin-pumping effect is also studied in magnetic single layers with thick NM cap layers. A significant spin-sink effect is observed only for NM=Pd.

In multilayer samples involving a sufficiently thick layer of Pd the formation of a self-assembled nanoscale network of misfit dislocations affects the spin dynamics and causes extrinsic magnetic damping. The misfit dislocations are detected during the film growth by fan-out diffraction features in reflection high electron energy diffraction (RHEED). Out-of-plane measurements of the FMR linewidth reveal that the extrinsic damping is caused by two-magnon scattering. The in-plane FMR linewidth is strongly anisotropic and follows the rectangular symmetry of the glide planes of the misfit dislocation network. The anisotropy is interpreted using the Fourier components of the magnetic defects. Following this model the frequency dependent variation of the in-plane angular dependence of the FMR linewidth is explained by an effective channelling of scattered spin waves parallel to the magnetic defects.

Dedication

To Sophia and my parents

Acknowledgement

First, I would like to sincerely thank my supervisor Prof. Bret Heinrich. I always enjoyed our discussions. His generosity and candidness created a very pleasant and productive environment. I benefited greatly from his knowledge and the opportunities he has given me. It was an honor to work with him.

I am very grateful to Ken Myrtle for his help and technical assistance during the course of this thesis. I benefited from his outstanding physical insight. His unconventional approach to solving technical problems taught me the art of 'Kengineering'.

To my co-workers in the magnetism and surface science group at Simon Fraser University I also owe gratitude, Prof. John Cochran, Prof. Mike Scheinfein, Dr. Axel Enders, Dr. Radek Urban, Bartek Kardasz, Oleksandr Mosendz, Dirk Riemann, and Jørn Foros. I wish to thank Prof. Bret Heinrich and Prof. John Cochran for a critical reading of my thesis and their valuable suggestions and comments.

There are several people that contributed with their specialized techniques to this thesis:

I would like to thank Prof. Hans Siegmann at the Stanford Linear Accelerator Center for inviting me to participate in their experiments on large angle spin dynamics.

I am grateful to Prof. Christian Back and wish to thank him for giving me the opportunity to carry out time-resolved Kerr effect studies in his laboratory at the University of Regensburg. I also wish to thank his students Matthias Buess and Ingo Neudecker for their assistance.

I gratefully acknowledge Prof. Mark Freeman and Dr. Xiaobin Zhu at the University of Alberta for our collaboration in time resolved Kerr effect studies as part of the Canadian Institute of Advanced Research (CIAR).

I would like to thank Dr. Rudolph Schäfer for giving me the opportunity to perform static Kerr microscopy measurements in his laboratory at the Institute for Materials Science in Dresden.

My thanks are also addressed to Ms. Sigrid Hopfe, Dr. Roland Scholz, and Prof. Jörg Woltersdorf at the Max-Planck-Institute for Microstructure Physics in Halle for the transmission electron microscopy (TEM) studies.

For a doctoral stipend, I graciously thank the German Academic Exchange Service (DAAD).

Finally, I would like to thank my parents for their early recognition and support of my inclination to technology and science. This thesis even gave me the opportunity to collaborate in the TEM studies with my father allowing us to be coauthors on a publication. I also thank Sophia for her support during our wonderful time in Vancouver.

Contents

List of Figures

List of Tables

Acronyms

AES	Auger Electron Spectroscopy
AFM	Atomic Force Microscope
BLS	Brillouin Light Scattering
FMR	Ferromagnetic Resonance
F	Ferromagnet
GMR	Giant Magneto-Resistance
LEED	Low Energy Electron Diffraction
LLG	Landau Lifshitz Gilbert
RHEED	Reflection High Energy Electron Diffraction
MBE	Molecular Beam Epitaxy
MOCVD	Metal Organic Chemical Vapor Deposition
MOKE	Magneto Optic Kerr Effect
TRMOKE	Time-Resolved Magneto-Optic Kerr Effect
MRAM	Magnetic Random Access Memory
MTJ	Magnetic Tunnel Junction
NM	Normal Metal
RPA	Random Phase Approximation
RT	Room Temperature
SEMPA	Scanning Electron Microscopy with Polarization Analysis
SLAC	Stanford Linear Accelerator Center
SPM	Scanning Probe Microscope
SQUID	Superconducting Quantum Interference Device
STM	Scanning Tunnelling Microscope
SV	Spin Valve
SWASER	Spin Wave Amplification by Stimulated Emission of Radiation

TEM	Transmission Electron Microscope
TMR	Tunnelling Magneto-Resistance
UHV	Ultra High Vacuum
UPS	Ultraviolet Photoemission Spectroscopy
XPS	X-ray Photoemission Spectroscopy
XRD	X-ray Diffraction
XTEM	Cross-sectional Transmission Electron Microscopy

Symbols and Constants

A	exchange stiffness $= 2.1 \times 10^{-6}$ erg/cm for Fe
A_r	interface scattering parameter
a	lattice constant
$\alpha_X, \alpha_Y, \alpha_Z$	directional cosines in the XYZ laboratory system
$\mathbf{B}$	magnetic induction vector
$\mathfrak{B}_{\text{eff}}$	effective magnetic induction
β	bulk spin asymmetry
c	velocity of light in free space $= 3 \times 10^{10}$ cm/s
χ_P	Pauli susceptibility
$\chi_\perp$	transversal susceptibility
D	diffusion coefficient
D	spin wave stiffness $= 2A/M_S$
e	elementary charge $= 1.602 \times 10^{-19}$ C
$\mathcal{E}$	energy or energy density
$\mathbf{E}$	electric intensity vector
f	frequency
φ_M	angle between magnetization and [100] direction
φ_H	angle between external field and [100] direction
φ_q	angle between spin wave and the [100] direction
g	electron g-factor $g = 2.0023$ (free electron)
G	Gilbert damping parameter
$g^{\uparrow\downarrow}$	dimensionless spin mixing conductance
h	magnetic rf field
$\hbar$	Planck constant divided by 2π
$\mathbf{H}$	magnetic field vector

$\mathfrak{H}_{\text{eff}}$	effective magnetic field
H_{FMR}	Ferromagnetic resonance field
$\mathbf{j}$	z-component of the spin current
$\mathbf{k}$	wave vector
k_F	Fermi wave vector
$K_1^{\|\|}$	four-fold in-plane anisotropy constant
$K_1^{\perp}$	four-fold perpendiular anisotropy constant
$K_U^{\|\|}$	uniaxial in-plane anisotropy constant
$K_U^{\perp,s}$	uniaxial surface perpendicular anisotropy constant
$\mathbf{M}$	magnetization vector
M_S	saturation magnetization = 1700 emu/cm^3 for Fe
M_{eff}	effective magnetization
$\hat{\mathbf{m}}$	unit vector of the magnetization
$m_{y,z}^{\text{rf}}$	rf components of the magnetization
n	density of electrons
$\psi_{\max}$	angle between spin wave vector and magnetization
ψ_q	angle between spin wave vector and magnetization
$\mathbf{q}$	small wave vector used for spin waves
θ_M	angle between magnetization and [001] direction
θ_H	angle between external field and [001] direction
$\hat{\mathbf{u}}$	unit vector of the in-plane uniaxial axis
v_F	Fermi velocity
α	dimensionless Gilbert damping parameter = $\frac{G}{\gamma M_S}$
γ	spectroscopic splitting factor = $\frac{g\|e\|}{2mc}$
δ	skin depth
δ_{ex}	exchange length =3.3 nm for Fe
δ_{ij}	Kronecker symbol
ΔH	half width at half maximum ferromagnetic (HWHM) resonance linewidth
ΔH^{PP}	peak to peak (PP) ferromagnetic resonance linewidth
$\Delta\omega$	adjusted frequency linewidth
ϵ	asymmetry parameter of resonance lines
ϵ	spin flip probability
ϵ_K	Kerr ellipticity angle
ε_0	permittivity of vacuum

ε_F	Fermi energy
θ_K	Kerr rotation
l_{sd}	spin diffusion length
λ_s	spin flip length
μ_B	Bohr magneton
m	electron mass
m^*	effective electron mass
$\mathbf{M}_{tot}$	total magnetic moment
$\psi_{\mathbf{q}}$	angle between magnetization and spin wave vector $\mathbf{q}$
Q_v	Voigt coefficient
R	two-magnon relaxation parameter
ϱ	electrical resistivity
σ	electrical conductivity
t_F	magnetic film thickness
t_{NM}	cap layer thickness
τ_{m}	electron orbital relaxation time
τ_{sf}	electron spin-flip relaxation time
ω	angular frequency $= 2\pi f$
$\hat{\mathbf{x}}, \hat{\mathbf{y}}, \hat{\mathbf{z}}$	unit vectors in the rotated (x, y, z) frame

Chapter 1

Introduction

Spintronics is a new variant of electronics in which the electron's spin rather than the electron's charge is used. This emerging field has the potential to revolutionize and to some extent replace conventional semiconductor electronics [1, 2, 3]. Spintronics has already led to the development of magnetic tunnelling junctions (MTJ) and giant magneto-resistive (GMR) spin valves (SV). These devices are based on ultrathin magnetic multilayers. MTJs have been used for prototypes of non-volatile magnetic random access memories (MRAM). GMR SV systems are already used in computer hard drive read heads and have revolutionized high density magnetic recording in recent years.

As the device operation approaches the GHz range of frequencies the magnetic relaxation starts to be an important aspect of the device performance. Magnetic relaxation, however, is the least developed and understood area in the study of magnetic ultrathin film properties. The understanding of magnetic damping in metallic multilayers remains a controversial topic largely due to the presence of unintended sample defects. Most spin dynamics experiments to date have been carried out using polycrystalline samples grown by sputtering where a poor crystalline quality and rough interfaces can obscure the intrinsic properties. It is therefore essential to study magneto-dynamics in nearly perfect single crystalline samples to understand the intrinsic relaxation mechanisms. Such understanding will allow to engineer the high speed performance of multilayer based spintronic devices.

This thesis examines the magnetic relaxation mechanisms in ultrathin epitaxial multilayer film structures. High quality single crystalline multilayer samples were prepared by molecular beam epitaxy (MBE) in ultra high vacuum (UHV). In spin-

tronics applications the multilayer films are grown on semiconductor and insulator substrates. One of the best semiconductor/ferromagnet systems is Fe(001) deposited on GaAs(001). GaAs(001) is fairly well lattice matched to Fe(001); its lattice constant is only 1.4% smaller than twice the lattice spacing of Fe, and the growth of Fe is not affected by alloying with the substrate. Fe is also advantageous compared to other 3d transition metallic films because of its low intrinsic damping and large magnetic moment.

Two complementary magneto-dynamic techniques were used: (i) Ferromagnetic resonance (FMR) where the rf precession of the magnetic moment is excited by a continuous microwave magnetic field. The resonance linewidth is related to the magnetic damping and was investigated as a function of microwave frequency and the angle between the static magnetization and the crystallographic axes. (ii) In time-resolved magneto-optic Kerr effect experiments (TRMOKE) the time evolution of the magnetic moment in response to an ultrashort magnetic field pulse was measured on a picosecond time scale. The rf magnetic field amplitude ranged from 0.5 Oe in FMR to 10-30 Oe in TRMOKE.

The Fe layers grown on GaAs(001) and covered by Au(001) exhibited only Gilbert damping. These samples provided an ideal starting point for the exploration of magnetic relaxation in multilayer structures.

In the first part of this thesis the spin dynamics are studied in magnetic double layers (two ferromagnetic layers separated by a non-magnetic spacer layer). It is shown that the exchange of angular momentum between the two ferromagnetic layers leads to non-local spin torques. This means that even in the absence of static interlayer exchange coupling the two magnetic layers are coupled through the normal metal spacer via non-equilibrium spin currents. This is an entirely new concept and essential to the understanding of magnetic dynamics of ultrathin magnetic multilayer structures.

The second part of the thesis deals with an extrinsic relaxation mechanism that is caused by a self assembled network of misfit dislocations in Pd/Fe/GaAs samples. This extrinsic relaxation is well described by a two-magnon scattering model. Two other systems affected by two-magnon scattering were studied: Cr/Fe/GaAs(001) and half metallic NiMnSb films grown on InP(001).

The thesis is organized as follows: chapter 2 covers theoretical aspects important to the interpretation of the results using FMR and TRMOKE measurements. chapter

3 describes the experimental systems used in this work. This chapter is split into three sections: (i) Sample preparation, (ii) FMR, and (iii) magneto-optical Kerr effect techniques. Chapter 4 consists of three parts. The first part discusses the intrinsic magnetic properties of Au/Fe single magnetic layers. The second part provides the experimental evidence for dynamic exchange coupling in Fe/Au/Fe magnetic double layers. This coupling is due to the spin-pump and spin-sink contributions. Finally, the third part presents and discusses the spin-pump and spin-sink effects due to the normal metal (NM) cap layers in contact with Fe films (NM=Au, Ag, Cu, and Pd). Chapter 5 covers the extrinsic damping observed in self-assembled networks of misfit dislocations in Pd/Fe structures. The results will be compared with the two-magnon scattering theory. Chapter 6 presents the time-resolved magneto-optic measurements on films having (i) intrinsic Gilbert damping, (ii) strong two-magnon scattering, and (iii) a spin-pumping contribution to the damping. In chapter 7 the important results and conclusions are summarized.

Additional work and information is presented in the appendices. In appendix A the results of large angle magnetization dynamics in Au/Fe/GaAs(001) films are presented. This work was carried out in the group of Prof. Hans Siegmann at the Stanford Linear Accelerator Center (SLAC). Appendix B discusses the magnetic properties of Fe/Pd superlattices grown on GaAs(001). In appendix C the adiabatic spin-pumping theory is derived using a time dependent scattering matrix and spin projection operators.

Chapter 2

Theoretical Considerations

The purpose of this chapter is to introduce the established concepts required to understand the experimental results presented later. Emphases are put on ferromagnetic resonance, magnetic relaxations, and magneto-optics. New theoretical concepts which are used for the interpretation of the experimental results will be described in chapters 4 and 5.

2.1 Energetics of Very Thin Ferromagnetic Films

In ferromagnets, the exchange energy favors parallel alignment of the magnetic moments (spins). The length scale across which the exchange interaction is dominant over the demagnetizing energy is often called the exchange length, and is given by $l_{\text{ex}} = \left(\frac{A}{2\pi M_S^2}\right)^{1/2}$ [4]. A is the exchange constant and M_S is the saturation magnetization. For Fe, $A = 2.1 \times 10^{-6}$ erg/cm and $M_S = 1700$ emu/cm^3. This results in $l_{\text{ex}}^{\text{Fe}} = 3.3$ nm which corresponds to a thickness of 23 monolayers (ML). Magnetic films whose thickness is comparable to or less than l_{ex} are referred to as ultrathin; their moments are locked together by the exchange interaction across the film thickness and can usually be treated as a macrospin.

2.1.1 Demagnetizing energy

In a thin uniform magnetic film the in-plane dimensions (l_X and l_Y) are much larger than the thickness t_F ($l_Z = t_F$). When the magnetization lies uniformly in the plane the magnetic charges are avoided altogether and this corresponds to the lowest

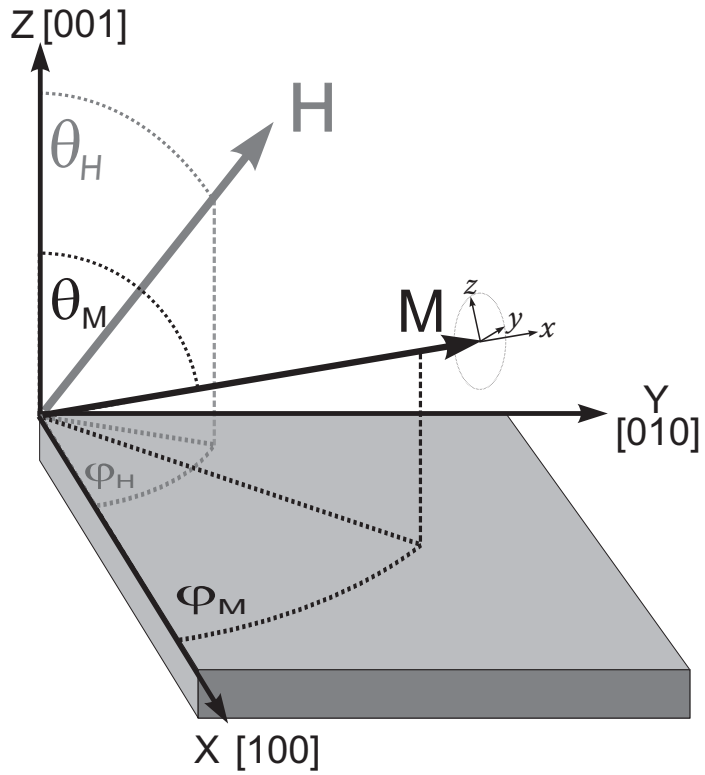

Figure 2.1: The laboratory coordinate system X, Y, Z is parallel to the principal crystallographic axes. **M** and **H** are magnetization and applied magnetic field, respectively. The (x, y, z) coordinates are rotated with respect the (X, Y, Z) system such that $\mathbf{x} \parallel \mathbf{M}$ and $\mathbf{y} \parallel XY$-plane.

magneto-static energy configuration. The magnetic charges on the outer edges in the l_X and l_Y directions can be neglected and the demagnetizing factors are $N_X = N_Y = 0$ and $N_Z = 1$. If the magnetization is tilted out of the plane by an external magnetic field, a magnetic surface charge density is created on the film surfaces resulting in a demagnetization (restoring) energy density

$$\mathcal{E}_{\mathrm{dem}} = 2\pi D \mathrm{M_S^2} \sin {\theta_\mathrm{M}}^2 = 2\pi \mathrm{M_\perp^2}, \tag{2.1}$$

where D is the effective demagnetizing factor obtained by averaging over the discrete sum of dipolar magnetic fields acting on the individual lattice planes [5]. D is very close to 1 for films thicker than a few monolayers (ML). $M_\perp$ is the magnetization component perpendicular to the film surface and θ_M is the angle of the magnetization with respect to the film normal, as illustrated in Fig. 2.1.

2.1.2 Crystalline anisotropy

The magnetization in ferromagnets has energetically preferred directions, dictated by the symmetry and the structure of the crystal. The dependence of magnetic energy on the orientation of the magnetization with respect to the crystallographic directions is called magneto-crystalline anisotropy. This anisotropy is caused by spin-orbit coupling; the electron orbital motion given by the lattice potential couples to the net spin moment. The Fe films discussed in this thesis are cubic and their bulk properties satisfy cubic symmetry. The GaAs(001) substrates upon which these films are grown, however, exhibit uniaxial symmetry, and therefore the magnetic films can also exhibit uniaxial in-plane anisotropy. It is convenient to split the anisotropy energy density functional into respective in-plane and perpendicular uniaxial and four-fold components:

$$\mathcal{E}_{\text{ani}} = -\frac{K_1^{\parallel}}{2}(\alpha_X^4 + \alpha_Y^4) - \frac{K_1^{\perp}}{2}\alpha_Z^4 - K_U^{\perp}\alpha_Z^2 - K_U^{\parallel}\frac{(\hat{\mathbf{n}} \cdot \mathbf{M})^2}{\mathrm{M_S^2}}, \tag{2.2}$$

where the $\alpha_{X,Y,Z}$ represent the direction cosines of the magnetization vector along the [100], [010], and [001] crystallographic directions, respectively. $K_1^{\parallel}$, $K_1^{\perp}$, $K_U^{\parallel}$, $K_U^{\perp}$ are constants describing the strength of the in-plane and perpendicular parts of four-fold and uniaxial anisotropies. $\hat{\mathbf{n}}$ is a unit vector along the in-plane uniaxial axis. The reduced symmetry at the interfaces can strongly enhance the role of spin-orbit interaction and hence contribute to the crystalline anisotropies. For ultrathin films the interface anisotropy is shared by all atomic layers due to the exchange interaction and can be separated from the bulk contribution by its inverse dependence on the film thickness. For a film with two interfaces A and B one can write

$$K = K^{\text{bulk}} + \frac{K^A}{t_F} + \frac{K^B}{t_F}, \tag{2.3}$$

where K stands symbolically for $K_1^{\parallel}$, $K_1^{\perp}$, $K_U^{\parallel}$, and $K_U^{\perp}$. K^{bulk} and $K^{A,B}$ are the bulk and interface contributions, respectively. Usually $K_U^{\perp,A,B}$ is by far the strongest interface anisotropy.

2.1.3 Zeeman energy

The presence of an external magnetic field vector $\mathbf{H}_0$ introduces the Zeeman energy density term

$$\mathcal{E}_{\text{zee}} = -\mathbf{H}_0 \cdot \mathbf{M}. \tag{2.4}$$

2.2 Motion of the Magnetization Vector

The time evolution of the magnetization in a magnetic medium in response to a non-equilibrium magnetic field was first addressed by Landau and Lifshitz in 1935 [6]. They introduced the Landau-Lifshitz equation (LL)

$$\frac{\mathrm{d}\mathbf{M}}{\mathrm{d}t} = -\gamma \mathbf{M} \times \mathbf{H}_{\text{eff}} + \lambda \left[\mathbf{H}_{\text{eff}} - \left(\mathbf{H}_{\text{eff}} \cdot \frac{\mathbf{M}}{M_S} \right) \frac{\mathbf{M}}{M_S} \right] \tag{2.5}$$

where γ is the absolute value of the gyromagnetic ratio defined as $\gamma = |\frac{ge}{2m_e c}|$. The first term on the right hand side represents the well known precessional torque. The energies discussed in the previous section enter the equation of motion via an effective field and are evaluated from the energy density functional [4, 7]:

$$\mathbf{H}_{\text{eff}} = -\frac{\partial \mathcal{E}_{\text{tot}}}{\partial \mathbf{M}}, \tag{2.6}$$

where $\mathcal{E}_{\text{tot}} = \mathcal{E}_{\text{dem}} + \mathcal{E}_{\text{ani}} + \mathcal{E}_{\text{zee}}$. The second term on the right hand side of Eq. 2.5 leads to relaxation of magnetization and can be rewritten in a more convenient form

$$\mathbf{T}^{LL} = \lambda \left[\mathbf{H}_{\text{eff}} - \left(\mathbf{H}_{\text{eff}} \cdot \frac{\mathbf{M}}{M_S} \right) \frac{\mathbf{M}}{M_S} \right] = -\frac{\lambda}{M_S^2} \mathbf{M} \times \left[\mathbf{M} \times \mathbf{H}_{\text{eff}} \right]. \tag{2.7}$$

This implies that the relaxation is driven by the effective field component that is perpendicular to $\mathbf{M}$. $\lambda = 1/\tau$ is a phenomenological damping constant and equal to the inverse relaxation time. In 1955 Gilbert introduced a slightly different damping torque [8], justified by the particle like lagrangian treatment of domain wall motion by Döring [9]. Döring found that a moving domain wall acquires an effective mass. Based on this result, he treated the time dependent motion of a domain wall in an oscillating field like a harmonic oscillator, and introduced a phenomenological damping term linear in $d\mathbf{m}/dt$, where $\mathbf{m} = \mathbf{M}/M_S$. Gilbert generalized this treatment to describe the motion of the magnetization vector itself and introduced the damping torque [8, 10]

$$\mathbf{T}^{G} = \frac{G}{M_S^2 \gamma} \mathbf{M} \times \frac{\mathrm{d}\mathbf{M}}{\mathrm{d}t} = \frac{\alpha}{M_S} \mathbf{M} \times \frac{\mathrm{d}\mathbf{M}}{\mathrm{d}t}. \tag{2.8}$$

$G = 1/\tau$ is the Gilbert damping constant. It is now more popular to use the dimensionless damping parameter $\alpha = \frac{G}{M_S \gamma}$. In the limit of small damping ($\alpha \ll 1$) Gilbert and Landau-Lifshitz damping torques are equivalent. Eq. 2.5 with the Gilbert damping torque 2.8 is usually referred to as the Landau-Lifshitz-Gilbert equation (LLG). The time evolution of the magnetization described by LL and LLG preserves the

length of **M**. Physically magnetic damping leads to a loss of angular momentum from the spin system. The rate of this loss is given by $\frac{1}{\tau}\frac{1}{\chi_\perp}$, where $\chi_\perp = M_S/H_{\text{eff}}$ is the transverse susceptibility.

Different microscopic damping mechanisms can be operative in metallic ferromagnets, and are discussed in section 2.4.

2.3 Ferromagnetic Resonance

In ferromagnetic resonance (FMR) experiments a small microwave field excites the magnetization at a fixed frequency f. At the same time a magnetic dc field is applied allowing one to change the precessional frequency. When the precessional frequency coincides with the microwave frequency, the sample undergoes FMR which is accompanied by increased microwave losses. The important parameters of an FMR spectrum are line position (related to the anisotropies) and linewidth (related to the damping).

2.3.1 The resonance conditions

In this section the FMR condition (resonance field) will be derived. The effective fields corresponding to the magneto-crystalline and demagnetizing energies are evaluated in a cartesian coordinate system where the magnetization is oriented along the x direction, as illustrated in Fig. 2.1. The direction cosines of the magnetization which enter Eq. 2.2 can be parameterized in terms of the in-plane angle φ_M between the magnetization and the [100] direction, and the out-of-plane angle θ_M between the magnetization and the [001] direction

$$\alpha_X = \frac{M_x}{M_S}\cos\varphi_M \sin\theta_M - \frac{M_y}{M_S}\sin\varphi_M - \frac{M_z}{M_S}\cos\varphi_M\cos\theta_M \tag{2.9}$$

$$\alpha_Y = \frac{M_x}{M_S}\sin\varphi_M \sin\theta_M + \frac{M_y}{M_S}\cos\varphi_M - \frac{M_z}{M_S}\sin\varphi_M\cos\theta_M \tag{2.10}$$

$$\alpha_Z = \frac{M_x}{M_S}\cos\theta_M + \frac{M_z}{M_S}\sin\theta_M. \tag{2.11}$$

In-plane configuration

In the parallel configuration, the magnetization and the applied magnetic dc field lie in the plane of the magnetic film $\theta_M = \theta_H = 90°$. With aid of Eqs. 2.2, 2.6, 2.9, 2.10, and 2.11 the effective field components due to anisotropies in the x, y, z cartesian

coordinates of the magnetization are

$$\begin{aligned} H_x^{\text{ani}} &= \frac{K_1^{\parallel}}{2M_S^4}\left[M_x^3(\cos 4\varphi_M + 3) - 3M_x^2 M_y \sin 4\varphi_M + M_x M_y^2(3 - 3\cos 4\varphi_M) + M_y^3 \sin 4\varphi_M\right] \\ &+ \frac{K_U^{\parallel}}{M_S^2}\left[M_x(1 + \cos 2(\varphi_M - \varphi_U)) - M_y \sin 2(\varphi_M - \varphi_U)\right] \qquad (2.12) \\ H_y^{\text{ani}} &= \frac{-K_1^{\parallel}}{2M_S^4}\left[M_x^3 \sin 4\varphi_M - M_x^2 M_y(3 - 3\cos 4\varphi_M) - M_x M_y^2(3 + 3\sin 4\varphi_M) - M_y^3(\cos 4\varphi_M + 3)\right] \\ &- \frac{K_U^{\parallel}}{M_S^2}\left[M_x \sin 2(\varphi_M - \varphi_U) - M_y(1 - \cos 2(\varphi_M - \varphi_U)\right] \qquad (2.13) \\ H_z^{\text{ani}} &= -4\pi D M_z + \frac{K_U^{\perp}}{M_S^2} M_z + \frac{2K_1^{\perp}}{M_S^4} M_z^3, \qquad (2.14) \end{aligned}$$

where φ_U is the angle between the in-plane uniaxial direction and the [100] axis. In addition to the anisotropy fields there is an externally applied magnetic dc field $\mathbf{H}_0$ and a rf driving field $\mathbf{h}$. The cartesian components of the external dc field are

$$\mathbf{H}_0 = H_0\left[\cos(\varphi_M - \varphi_H)\hat{\mathbf{x}} - \sin(\varphi_M - \varphi_H)\hat{\mathbf{y}}\right]. \qquad (2.15)$$

The effective magnetic field entering the torque equation 2.5 is given by the sum of all fields:

$$\mathbf{H}_{\text{eff}} = \mathbf{H}^{\text{ani}} + \mathbf{H}_0 + h\hat{\mathbf{y}}, \qquad (2.16)$$

where the rf h-field is applied in the y direction. In the small angle approximation ($M_x \gg M_y, M_z$) one can calculate the resonance condition with trial solutions of the form $m_y^{\text{rf}} \propto \mathrm{e}^{\mathrm{i}\omega t}$, where $\omega = 2\pi f$ is the microwave angular frequency. One can write

$$\mathbf{M} = M_S\hat{\mathbf{x}} + m_y^{\text{rf}}\hat{\mathbf{y}} + m_z^{\text{rf}}\hat{\mathbf{z}} \qquad (2.17)$$

and insert this and the effective fields into the LLG equation. The equation of motion becomes a system of two coupled equations for m_y^{rf} and m_z^{rf}. Because the rf components are very small compared to M_S, the equations are linearized by keeping only terms that are linear in m_y^{rf}, m_z^{rf} and h:

$$\begin{aligned} 0 &= i\frac{\omega}{\gamma} m_y^{\text{rf}} + \left(\mathfrak{B}_{\text{eff}} + i\alpha\frac{\omega}{\gamma}\right) m_z^{\text{rf}} \qquad (2.18) \\ hM_S &= -i\frac{\omega}{\gamma} m_z^{\text{rf}} + \left(\mathfrak{H}_{\text{eff}} + i\alpha\frac{\omega}{\gamma}\right) m_y^{\text{rf}}, \qquad (2.19) \end{aligned}$$

where

$$\begin{aligned} \mathfrak{B}_{\text{eff}} &= H_0\cos(\varphi_M - \varphi_H) + 4\pi D M_S - \frac{2K_U^{\perp}}{M_S} + \frac{K_1^{\parallel}}{2M_S}\left[3 + \cos 4\varphi_M\right] + \frac{K_U^{\parallel}}{M_S}\left[1 + \cos 2(\varphi_M - \varphi_U)\right] \\ \mathfrak{H}_{\text{eff}} &= H_0\cos(\varphi_M - \varphi_H) + \frac{2K_1^{\parallel}}{M_S}\cos 4\varphi_M + \frac{2K_U^{\parallel}}{M_S}\cos 2(\varphi_M - \varphi_U). \qquad (2.20) \end{aligned}$$

$\mathfrak{H}_{\text{eff}}$ and $\mathfrak{B}_{\text{eff}}$ can be viewed as effective magnetic field and effective magnetic induction. Since the demagnetizing ($4\pi DM_S$) and perpendicular uniaxial anisotropy ($\frac{2K_U^{\perp}}{M_S}$) contributions enter the equations of motion additively it is convenient to define an effective demagnetizing field

$$4\pi M_{\text{eff}} = 4\pi DM_S - \frac{2K_U^{\perp}}{M_S}. \tag{2.21}$$

For a given microwave angular frequency ω one can calculate the rf susceptibility as a function of the applied field H_0

$$\chi_y \equiv \chi_y' + i\chi_y'' = \frac{m_y^{\text{rf}}}{h} = \frac{M_S\left(\mathfrak{B}_{\text{eff}} - i\alpha\frac{\omega}{\gamma}\right)}{\left(\mathfrak{B}_{\text{eff}} - i\alpha\frac{\omega}{\gamma}\right)\left(\mathfrak{H}_{\text{eff}} - i\alpha\frac{\omega}{\gamma}\right) - \left(\frac{\omega}{\gamma}\right)^2}. \tag{2.22}$$

This expression assumes that h is uniform in the film, i.e. the film thickness is much smaller than the skin depth ($t_F \ll \delta$). The microwave absorption is maximum when the imaginary part of the susceptibility has a maximum. Ignoring the damping in Eq. 2.22, this occurs when the denominator is zero. The resonance condition in this case is

$$\left(\frac{\omega}{\gamma}\right)^2 = \mathfrak{B}_{\text{eff}}\mathfrak{H}_{\text{eff}}\Big|_{H_{\text{FMR}}}. \tag{2.23}$$

In general, the sample is not in a fully saturated state i.e. $\varphi_M \neq \varphi_H$ due to the anisotropies and if one wants to interpret e.g. H_{FMR} as a function of φ_H, one has to calculate φ_M for given φ_H and H_0 from the static equilibrium. The static equilibrium can be obtained from the condition that the static torque on the magnetization is zero after inserting effective fields (Eqs. 2.14 and 2.15) into 2.5 and setting $M_x = M_S$, $M_y = 0$, and $M_z = 0$. The z-component is the only nonzero torque component, and setting it to zero defines the static equilibrium:

$$H_0 M_S \sin(\varphi_H - \varphi_M) + K_U^{\parallel}\sin 2(\varphi_U - \varphi_M) - \frac{1}{2}K_1^{\parallel}\sin 4\varphi_M = 0. \tag{2.24}$$

One can show that in the saturated case ($\varphi_M = \varphi_H$) the imaginary part of the microwave susceptibility 2.22 as a function of the applied field is given by an almost perfect Lorentzian function [11]

$$\text{Im}[\chi_y] \equiv \chi_y'' = M_S\frac{\mathfrak{B}_{\text{eff}}}{\mathfrak{B}_{\text{eff}} + \mathfrak{H}_{\text{eff}}}\Bigg|_{H_{\text{FMR}}} \frac{\Delta H}{\Delta H^2 + (H_0 - H_{\text{FMR}})^2}, \tag{2.25}$$

where $\Delta H = \alpha\frac{\omega}{\gamma}$ is the half width at half maximum (HWHM) linewidth and H_{FMR} is the line position.

Perpendicular configuration

This is a special case of the out-of-plane configuration where the magnetization and applied magnetic field are oriented perpendicular to the sample ($\theta_M = \theta_H = 0°$). This simplifies the calculation of the resonance condition significantly because the four-fold in-plane anisotropy can be neglected. If one neglects the in-plane uniaxial anisotropy, both rf-magnetization components have identical amplitudes and can be converted into left and right handed circularly polarized components: $m_{\pm}^{\mathrm{rf}} = m_x^{\mathrm{rf}} \pm i m_y^{\mathrm{rf}}$. Since the LLG equation has a handedness FMR only occurs for the right handed component and the linearized equation of motion is given by [4]

$$h_{+}^{\mathrm{rf}} M_S = \left(H_0 - 4\pi M_{\mathrm{eff}} + \frac{2K_1^{\perp}}{M_S} - \frac{\omega}{\gamma} + i\alpha\frac{\omega}{\gamma} \right) m_{+}^{\mathrm{rf}}, \tag{2.26}$$

this leads to the resonance condition

$$\frac{\omega}{\gamma} = H_{\mathrm{FMR}} - 4\pi M_{\mathrm{eff}} + \frac{2K_1^{\perp}}{M_S}. \tag{2.27}$$

Out-of-plane configuration

In the general case of arbitrary out-of-plane angles θ_H for the applied field the magnetization is dragging behind the applied field and one has to calculate θ_M for given θ_H and H_0 from the equilibrium condition. The strongest contribution arises from the effective demagnetizing field; neglecting uniaxial in-plane and four-fold anisotropies one can write for the equilibrium condition [12]

$$\sin(\theta_H - \theta_M) = -\frac{4\pi M_{\mathrm{eff}}}{2H_0} \sin 2\theta_M. \tag{2.28}$$

The data analysis for the out-of-plane configuration is correctly treated (with all anisotropy contributions) by numeric solutions using a computer program.

2.4 Physical Origin of Intrinsic Spin Damping

There are three major mechanisms which can cause intrinsic damping in metallic ferromagnets. These are (i) eddy currents, (ii) magnon-phonon coupling, and (iii) itinerant electron relaxation. In the following subsections all three mechanisms will be examined with respect to their relevance to ultrathin metallic ferromagnets.

2.4.1 Eddy current mechanism

The precession of the magnetization induces eddy currents, and the dissipation of them is proportional to the conductivity of the sample. For samples that are thinner than the skin depth, the contribution of eddy currents to the equation of motion can be evaluated by integrating Maxwell's equations across the film thickness t_F. The resulting effective field has a Gilbert like form with an effective Gilbert damping constant [13]

$$\alpha_{\text{eddy}} = \frac{1}{6} M_S \gamma \left(\frac{4\pi}{c}\right)^2 \sigma t_F^2. \tag{2.29}$$

where σ is the electrical conductivity. This contribution becomes comparable to the intrinsic damping for samples thicker than 50 nm. The skin depth for Fe at a frequency of 24 GHz is $\delta \sim 100$ nm. The thickest sample considered in this thesis was only 5 nm thick, hence the eddy current damping can contribute only $\sim 1\%$ of the total damping.

2.4.2 Phonon drag mechanism

Direct magnon-phonon scattering is another possible relaxation mechanism. Suhl recently presented calculations for magnon relaxation by phonon drag [14]. His explicit results are applicable to small geometries where magnetization and lattice strain are homogeneous. Using the LLG and lattice strain equations of motion one can asymptotically describe the Gilbert phonon damping α_{phonon} by [14]

$$\alpha_{\text{phonon}} = \frac{2\eta\gamma}{M_S} \left(\frac{B_2(1+\nu)}{E}\right)^2 , \tag{2.30}$$

where η is the phonon viscosity, B_2 is the magneto-elastic shear constant, E the Young modulus, and ν is the Poisson ratio. All parameters can be readily obtained except for the phonon viscosity η. Fortunately, the phonon viscosity parameter η for Ni

in the microwave range of frequencies was experimentally determined in microwave transmission experiments by Heinrich et al. [15]. In these studies at 9.5 GHz, a fast transverse elastic shear wave was generated by magneto-elastic coupling inside the skin depth of a thick Ni(001) crystal slab. This transverse elastic shear wave propagated across the slab, and then reradiated microwave power at the other side of the Ni slab. The effect was called 'phonon assisted microwave transmission'. By fitting the experimental data to the LLG and elastic wave equations of motion including the magneto-elastic coupling, the elastic wave relaxation time was found to be $\tau_{ph} = 6.6 \times 10^{-10}$ s at 9.5 GHz. The phonon viscosity, as introduced in [14], is given by $\eta = c_{44}/(\tau_{ph}\omega^2)$, where c_{44} is the elastic modulus. For Ni $\eta = 3.4$ (in CGS units). Using Eq. 2.30 results in a phonon Gilbert damping of $\alpha_{\text{phonon}} \sim 1 \times 10^{-3}$ which is ~ 30 times smaller than the intrinsic Gilbert damping parameter of Ni. Since magnetostrictive effects are stronger in Ni than in Fe, Co, or Py, it is expected that the phonon drag mechanism will be even weaker in Fe, Co, and Py.

2.4.3 Itinerant electron mechanisms

The most important damping mechanism in ultrathin metallic ferromagnets is based on itinerant electrons. The original model proposed by Heinrich et al. [16, 17] was based on the interaction of s-p like electrons with localized d spins.

s-d interaction: spin-flip scattering

The s-d exchange interaction was calculated by integrating the s-d exchange energy density [18]. The particle representation of the s-d exchange interaction Hamiltonian for the rf-components of the magnetization is given by three particle collision terms

$$\mathcal{H}_{\text{sd}} = \sqrt{\frac{2S}{N}} \sum_{\mathbf{k}} J(\mathbf{q}) \mathsf{a}_{\mathbf{k},\uparrow} \mathsf{a}^{\dagger}_{\mathbf{k}+\mathbf{q},\downarrow} \mathsf{b}_{\mathbf{q}} + \ \mathsf{h.c.}, \tag{2.31}$$

where S is the spin, N is the number of atomic sites, $\mathsf{a}^{\dagger}$ and a respectively create and annihilate electrons, and $\mathsf{b}^{\dagger}$ and b create and annihilate magnons. The total angular momentum and wave vector are conserved in the 3 particle collisions. $\uparrow, \downarrow$ stand for majority and minority electrons, respectively. Itinerant electrons and magnons are coherently scattered by the s-d exchange interaction resulting in the creation and annihilation ($\mathsf{h.c.}$ term in Eq. 2.31) of electron-hole pairs as illustrated in Fig. 2.2. Due to conservation of the angular momentum, the itinerant electron has to flip its

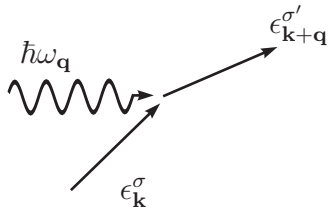

Figure 2.2: A spin wave with energy $\hbar\omega_{\mathbf{q}}$ and momentum $\mathbf{q}$ collides with an electron in state $\epsilon^{\sigma}_{\mathbf{k}}$ changing its spin and momentum state to $\epsilon^{\sigma'}_{\mathbf{k+q}}$.

spin when it is scattered by a magnon. This coherent scattering on its own leads only to a renormalized g-factor [16]. In order to cause relaxation, the electron-hole pair needs to be incoherently scattered by thermally excited phonons or magnons. Such incoherent scattering can be accounted for by introducing a finite life time τ_{eff} for the electron-hole pair excitation [16]

$$\delta\epsilon = \epsilon^{\downarrow}_{\mathbf{k+q}} - \epsilon^{\uparrow}_{\mathbf{k}} + i\frac{\hbar}{\tau_{\text{eff}}}. \tag{2.32}$$

τ_{eff} is given by the spin-flip time of the electron-hole pair τ_{sf}. τ_{sf} is longer than the momentum relaxation time τ_{m} which determines the conductivity. For simple metals Elliott [19] showed that this enhancement is related to the deviation of the g-factor from the free electron value due to spin-orbit interaction

$$\frac{\tau_{\text{sf}}}{\tau_{\text{m}}} = \frac{1}{(g-2)^2}. \tag{2.33}$$

More reliable estimates for τ_{sf} can be obtained from measurements of the spin diffusion length l_{sd}. Giant magneto-resistance (GMR) experiments with the current flowing perpendicular to the plane (CPP) allow one to estimate l_{sd} by measurement of GMR as a function of the magnetic layer thickness [20]. τ_{sf} and l_{sd} are directly related by [20, 21]:

$$\tau_{\text{sf}} = \frac{6l^2_{\text{sd}}}{v_F}\frac{\lambda_\uparrow + \lambda_\downarrow}{\lambda_\uparrow\lambda_\downarrow}, \tag{2.34}$$

where v_F is the Fermi velocity and $\lambda_\uparrow$ and $\lambda_\downarrow$ are the electron momentum mean free paths for spin up and spin down electrons. $\lambda_{\text{m}} = 2\frac{\lambda_\uparrow\lambda_\downarrow}{\lambda_\uparrow+\lambda_\downarrow} = v_F\tau_{\text{m}}$ is the average electron momentum mean free path of the ferromagnet. λ_{m} can be determined from the resistivity [20]

$$\varrho = \frac{mv_F}{ne^2}\frac{\lambda_{\text{m}}}{1-\beta^2}, \tag{2.35}$$

FM	g	$l_{\rm sd}$[nm]	β	$\varrho[\mu\Omega{\rm cm}]$	$\tau_{\rm sf}$[ps]	$G[10^7{\rm Hz}]$	$\alpha[10^{-3}]$	$M_S[\frac{\rm emu}{\rm cm^3}]$
Fe	2.09 [22]			9.7 [23]		5.8 [24]	2	1710 [25]
Co	2.18 [22]	59 [26]	0.36	6.2 [23]	3.8 [20]	30 [27]	11	1425 [25]
Ni	2.21 [28]			6.8 [23]		25 [28]	19	485 [25]
Py	2.14 [29]	4.3 [20]	0.73 [20]	12.3 [20]	0.03[20]	9	6	860 [25]
MnNiSb	2.03 [30]		1			3.1 [30]	2.8	580 [30]

Table 2.1: Table showing the spin relaxation times and other relevant quantities for several ferromagnetic materials (FM).

where β is the bulk spin asymmetry coefficient, m is the electron mass, and n is the total conduction electron density of the ferromagnet. In Permalloy ($Ni_{80}Fe_{20}$, Py) $\varrho_{\rm Py} = 12.3\ \mu\Omega$, $\beta_{\rm Py} = 0.73$, $v_{\rm F}$ =1.5×10^8 cm/s, and $n = 6.3\times10^{22}$ cm^{-3} corresponding to one conduction electron per atom [20]. The spin diffusion length in Py is $l_{\rm sd}^{\rm Py} = 4.3$ nm [20] which with the aid of Eqs. 2.34 and 2.35 leads to $\tau_{\rm sf}^{\rm Py} = 3\times10^{-14}$ s. A short spin diffusion length implies that the spin scattering enhancement factor $\tau_{\rm sf}/\tau_{\rm m}$ is only ~ 19 for Py. In Co similar GMR measurements [20] lead to $l_{\rm sd}^{\rm Co} = 59$ nm at 77 K and require $\tau_{\rm sf}^{\rm Co} = 3.8\times10^{-12}$ s. In this case the corresponding spin scattering enhancement factor is ~ 300. By simply applying Eq. 2.33, one obtains $\tau_{\rm sf}/\tau_{\rm m} \sim 21$ and ~ 35 for Py and Co respectively. This means that Elliott's formula predicts the spin scattering enhancement factor correctly for Py but is wrong by an order of magnitude for Co.

The rf susceptibility can be calculated using the Kubo Green's function formalism in the Random Phase Approximation (RPA) [31]. The imaginary part (damping) of the denominator of the circularly polarized rf susceptibility is usually expressed as an effective damping field [16]

$$\alpha_{\rm s-d}\frac{\omega}{\gamma} = \frac{2\langle S\rangle}{Ng\mu_B}\sum_{\mathbf{k}}|J(\mathbf{q})|^2\left(n^{\downarrow}_{\mathbf{k+q}} - n^{\uparrow}_{\mathbf{k}}\right)\delta(\hbar\omega_{\mathbf{q}} + \varepsilon_{\mathbf{k}\uparrow} - \varepsilon^{\downarrow}_{\mathbf{k+q}}), \tag{2.36}$$

where the summation is carried out over all available states on the Fermi surface and $\langle S\rangle$ is the reduced spin $\langle S\rangle = S(M_S(T)/M_S(0))$. The factor $g\mu_B = \gamma\hbar$ was used to convert the relaxation energy into an effective relaxation field and δ is Dirac's delta function. The incoherent scattering of electron-hole pair excitations broadens the delta function in Eq. 2.36 into a Lorentzian [16]

$$\delta(\hbar\omega_{\mathbf{q}} + \varepsilon^{\uparrow}_{\mathbf{k}} - \varepsilon^{\downarrow}_{\mathbf{k+q}}) \rightsquigarrow \frac{\hbar/\tau_{\rm sf}}{(\hbar\omega_{\mathbf{q}} + \varepsilon^{\uparrow}_{\mathbf{k}} - \varepsilon^{\downarrow}_{\mathbf{k+q}})^2 + (\hbar/\tau_{\rm sf})^2}. \tag{2.37}$$

The difference in occupation numbers is $\Delta n = n^{\uparrow}_{\mathbf{k+q}} - n^{\downarrow}_{\mathbf{k}} = \delta(\varepsilon_{\mathbf{k}} - \varepsilon_F)\hbar\omega_{\mathbf{q}}$, where ε_F is the Fermi energy. The delta function keeps the relaxation processes limited to electrons at the Fermi level. The energy $\hbar\omega_{\mathbf{q}} = \hbar\omega$ of a resonant magnon is the energy that is involved in the scattering process. One should view the Lorentzian function in Eq. 2.37 not as a smeared energy conservation, but rather as probability distribution to achieve a certain scattering event. FMR experiments are usually sensitive to the nearly homogeneous mode, $\mathbf{q} \sim 0$ and the change in the energy for the spin-flip electron-hole pair excitations is dominated by the exchange energy, $\varepsilon^{\downarrow}_{\mathbf{k+q}} - \varepsilon^{\uparrow}_{\mathbf{k}} = -2\langle S\rangle J(0)$. Using $N\langle S\rangle g\mu_B{=}M_s(T)$ one obtains a damping field proportional to the frequency ω and inversely proportional to the saturation magnetization M_S. These are exactly the features of Gilbert damping (see Eq. 2.8). After integration over the Fermi surface one can extract the Gilbert damping parameter

$$\alpha_{\mathrm{s-d}} = \frac{\chi_p}{M_S\gamma}\frac{1}{\tau_{\mathrm{sf}}}\ , \tag{2.38}$$

where χ_p is the Pauli susceptibility for itinerant electrons. χ_p can be calculated from the following expression

$$\chi_p = \left(\frac{\hbar\gamma}{2\pi}\right)^2 \int k^2 dk\delta(\varepsilon_{\mathbf{k}} - \varepsilon_F) = \mu_B^2 N(\varepsilon_F)\ , \tag{2.39}$$

where $N(\varepsilon_F)$ is the density of states at the Fermi level. χ_p for 3d transition metals is in the range of $3 - 9 \times 10^{-6}$ [32]. An uncertain point, however, is the relationship between τ_{sf} obtained from GMR measurements, see Eq. 2.34, and the τ_{sf} applicable to magnetic relaxation rate (see Eq. 2.38). In GMR one measures the longitudinal spin accumulation, while in FMR the transverse motion is relevant. The transverse and longitudinal spin relaxation times must be closely related, but could differ by a factor of 2. In ESR often the longitudinal relaxation is assumed to be 2 times slower than the transverse relaxation time [33]

$$\frac{1}{\tau_{\mathrm{sf}}} = \frac{1}{T_1} = \frac{1}{2T_2}. \tag{2.40}$$

In order to obtain the Gilbert damping constant from Eq. 2.38, in the experimentally observed range of $\alpha \sim 5 \times 10^{-3}$ one needs to have τ_{sf} in the range of $5{\times}10^{-14}$ s. This is satisfied for Py, see Tab. 2.1. Ignoring the presence of collisions with thermally excited magnons, the s-d relaxation is indirectly proportional to τ_{m}, and consequently scales with resistivity. In fact, recently Ingvarsson et al. [34] showed that the Gilbert

damping parameter in Py films can scale with the sample resistivity in agreement with Eq. 2.38. Py, however, is a special case in that respect; in pure materials like Co, Fe, and Ni the spin-flip relaxation time is too long and the s-d interaction hardly contributes to Gilbert damping.

The above calculations were carried out for circularly polarized magnons. It was shown that the ellipticity of magnons (in the parallel configuration) [35] does not change the intrinsic Gilbert damping which is based on scattering processes, as shown in Fig. 2.2. This result is not surprising considering that the FMR linewidth ΔH for circularly polarized magnons showed the explicit feature of Gilbert damping, $\Delta H \sim \frac{1}{M_S}\frac{\omega}{\gamma}$.

Spin orbit Hamiltonian: scattering without spin-flip

Kamberský [36] has shown that the intrinsic damping in metallic ferromagnets can be treated more generally by using a spin-orbit interaction Hamiltonian. The spin-orbit Hamiltonian for transverse spin and angular momentum components can be expressed in a three particle interaction Hamiltonian

$$\mathcal{H}^{\rm so} = \frac{1}{2}\sqrt{\frac{2S}{N}}\xi \sum_{\mathbf{k}} \sum_{\mu,\nu,\sigma} \langle \mu | L^{+} | \nu \rangle \mathsf{c}^{\dagger}_{\nu,\mathbf{k}+\mathbf{q},\sigma} \mathsf{c}_{\mu,\mathbf{k},\sigma} \mathsf{b}_{\mathbf{q}} + \mathsf{h.c.}, \tag{2.41}$$

where ξ is the coefficient of spin-orbit interaction, $L^{\pm} = L_{\rm x} \pm iL_{\rm y}$ are the right and left handed components of the atomic site transverse angular momentum $\mathbf{L}$. $\mathsf{c}_{\mu,\mathbf{k},\sigma}$ and $\mathsf{c}^{\dagger}_{\nu,\mathbf{k}+\mathbf{q},\sigma}$ annihilate and create electrons in the appropriate Bloch states with spin σ, and $\mathsf{b}_{\mathbf{q}}$ annihilates a spin wave with the wave-vector $\mathbf{q}$. The indices μ, ν represent the projected local orbitals of Bloch states, and are used to identify the individual electron bands. For simplicity the dependence of the matrix elements $\langle \nu | L^{+} | \mu \rangle$ on the wave-vectors is neglected. The rf susceptibility can again be calculated using the Kubo Green's function formalism in RPA. The imaginary part of the denominator of the circularly polarized rf susceptibility for a spin wave with the wave vector $\mathbf{q}$ and energy $\hbar\omega$ can be expressed in a manner similar to that for the s-d exchange interaction. The effective damping field is then given by

$$\begin{aligned} \alpha_{\rm so}\frac{\omega}{\gamma} &= \frac{\langle S \rangle^2}{2M_s}\xi^2 \left(\frac{1}{2\pi}\right)^3 \int d^3\mathbf{k} \sum_{\mu,\nu,\sigma} \left\langle \nu | L^{+} | \mu \right\rangle \left\langle \mu | L^{-} | \nu \right\rangle \\ &\times \delta(\varepsilon_{\mu,\mathbf{k},\sigma} - \varepsilon_F)\hbar\omega \frac{\hbar/\tau_{\rm m}}{(\hbar\omega + \varepsilon_{\mu,\mathbf{k},\sigma} - \varepsilon_{\nu,\mathbf{k}+\mathbf{q},\sigma})^2 + (\hbar/\tau_{\rm m})^2} \,. \end{aligned} \tag{2.42}$$

Since no spin-flip occurs during the scattering event, the relaxation time $\tau_{\rm sf}$ in Eq. 2.37 is replaced by the momentum relaxation time $\tau_{\rm m}$ which enters the conductivity of the ferromagnet.

Intraband transitions ($\mu = \nu$)

For small wave vector spin waves ($q \ll k_F$) the electron energy balance $\hbar\omega + \varepsilon_{\mu,\mathbf{k},\sigma} - \varepsilon_{\mu,\mathbf{k}+\mathbf{q},\sigma} = \hbar\omega - (\hbar^2/2m)(2\mathbf{kq} + q^2)$ in the denominator of Eq. 2.42 is significantly smaller than $\hbar/\tau_{\rm m}$. In good crystalline structures this limit is satisfied above cryogenic temperatures. After integration over the Fermi surface, the Gilbert damping can be approximated by

$$\alpha_{\rm so}^{\rm intra} \simeq \frac{\langle S \rangle^2}{M_S \gamma} \left(\frac{\xi}{\hbar}\right)^2 \left(\sum_\mu \chi_p^\mu \langle \mu | L^+ | \mu \rangle \langle \mu | L^- | \mu \rangle\right) \tau_{\rm m} \,, \tag{2.43}$$

where the χ_p^μ corresponds to the Pauli susceptibility of the given Fermi sheet. The Gilbert damping in this limit is proportional to the electron momentum relaxation time $\tau_{\rm m}$, and consequently scales with the conductivity.

Interband transitions ($\mu \neq \nu$)

The energy gaps $\Delta\varepsilon_{\nu,\mu}$ correspond to interband transitions and the electron-hole pair energy can be dominated by these gaps. For energy gaps larger than the momentum relaxation frequency $\hbar/\tau_{\rm m}$ the Gilbert damping constant can be approximated by

$$\alpha_{\rm so}^{\rm inter} \simeq \frac{\langle S \rangle^2}{M_S \gamma} \sum_\mu \chi_p^\mu (\Delta g_\alpha)^2 \frac{1}{\tau_{\rm m}} \,, \tag{2.44}$$

were $\Delta g_\alpha = 4\xi \sum_\beta \langle \mu | L_x | \nu \rangle \langle \nu | L_x | \mu \rangle / \Delta\varepsilon_{\nu,\mu}$ determines the contribution of the spin orbit interaction to the g-factor [37]. If the spin-flip relaxation time $\tau_{\rm sf}$ is obtained from Eq. 2.33 the spin-orbit interaction results in a Gilbert damping coefficient similar to that found for the s-d exchange interaction, as can be seen in Eq. 2.38. χ_p^μ only includes those electron states for which the change in energy during the interband transition is much bigger than $\hbar/\tau_{\rm m}$, i.e. $\Delta\varepsilon \gg \hbar/\tau_{\rm m}$. In this approximation the Gilbert damping constant is proportional to $1/\tau_{\rm m}$, and consequently scales with the resistivity. In reality, the distribution of energy gaps determines the overall temperature dependence of the Gilbert damping constant. Interband damping is expected to scale with the resistivity only at low temperatures. With increasing temperature the relaxation rate

$\hbar/\tau_{\rm m}$ becomes comparable to the energy gaps, $\Delta\varepsilon_{\mu,\nu}$, resulting in a gradual saturation of $\alpha_{\rm so}^{\rm inter}$ [36].

Classical picture

Kamberský's model was motivated by the observation that the Fermi surface changes slightly when the magnetization is rotated [38]. This corresponds to intraband transitions and can be described by a classical picture. As the precession of the magnetization evolves in time and space, the Fermi surface distorts periodically in time and space. This is often referred to as a *breathing Fermi surface*. The effort of the electrons to appropriately repopulate the changing Fermi surface is delayed by their momentum relaxation time $\tau_{\rm m}$ and results in a phase lag between the Fermi surface distortions and the precessing magnetization. On the other hand, the interband transitions lead to a dynamic orbital polarization, i.e. changes of the orbital electron wave functions in addition to changes of the itinerant electron energies.

The s-d exchange interaction can be viewed as two precessing magnetic moments corresponding to the localized d and itinerant s electrons, which are mutually coupled by the s-d exchange field. In the absence of damping the low energy excitation (acoustic mode) corresponds to a parallel alignment of the magnetic moments precessing together and in phase. Due to the finite spin mean free path of the itinerant electrons, their equation of motion has to include the spin relaxation towards the direction of the instantaneous effective field,

$$-\frac{1}{\tau_{\rm sf}\gamma}\left(\mathbf{m}-\chi_P\mathbf{h}_{\rm eff}\right)\ , \tag{2.45}$$

where $\mathbf{h}_{\rm eff}$ also includes the exchange field between the localized and itinerant electrons. This leads to a phase lag between the two precessing magnetic moments (s and d) [39], and consequently to magnetic damping. The magnetic damping obtained by means of this classical approach is equivalent to that obtained using the Kubo formalism, as described above.

The phase lag for the *breathing Fermi surface* and the s-d exchange interaction is proportional to the microwave angular frequency ω. Clearly, in both cases one has 'friction' like damping, which is described by Gilbert relaxation terms.

Experimental evidence

In Ni the Gilbert damping increases significantly as the temperature is lowered from room temperature (RT) and saturates for temperatures less than 50° K [40]. The Gilbert damping parameter α was found to be 2.8×10^{-2} at RT, and 16×10^{-2} at 4° K [40]. Korenman and Prange [41] explained the saturation of α using an equation similar to Eq. 2.42. For intraband electron-hole pair excitations one has: $\varepsilon_{\mathbf{k}} - \varepsilon_{\mathbf{k+q}} = (\mathbf{k}_F\mathbf{q}/m + q^2/2m)\hbar^2$. With increasing τ_{m} the energy balance in the denominator of Eq. 2.42 eventually becomes comparable to $\hbar/\tau_{\mathrm{m}}$. Both, momentum *and* energy conservation now play an important role in the sum over the Fermi surface in Eq. 2.42, and one finds

$$\alpha \sim \frac{\tan^{-1}(q v_{\mathrm{F}} \tau_m)}{q v_{\mathrm{F}}} , \tag{2.46}$$

where q is the wave number of a resonant magnon. For $v_{\mathrm{F}}\tau_m \gg 1/q$ this expression saturates and depends inversely on q. This behavior has also been observed in connection with the anomalous skin depth, where only electrons moving within the skin depth contribute to the effective conductivity, and is usually referred to as the concept of ineffective electrons [42]. The importance of ineffective electrons to the Gilbert damping measured at low temperatures shows explicitly that the magnetic damping in metallic ferromagnets is caused by itinerant electrons. This is further supported by the results of Ferromagnetic Antiresonance (FMAR) experiments. By using microwave transmission at FMAR ($q \to 0$) one can avoid problems related to the ineffective electrons [43] and obtain precise values of the intrinsic damping. Heinrich et al. found that in high purity single crystal slabs of Ni the Gilbert damping below RT was well described by two terms, one of which was proportional to the conductivity, the other proportional to the resistivity [43]. At RT these two terms were approximately equal in strength and compensated each other resulting in a nearly temperature independent Gilbert damping parameter [28]. This is in agreement with the above predictions. The saturation of the damping parameter above RT is quite well accounted for in quantitative calculations by Kamberský [44] and is explained by the interband contributions which saturate above RT.

Summary

FMR measurements in high quality crystalline Ni samples convincingly showed that the intrinsic damping in metals is mostly caused by the itinerant nature of the elec-

trons and the spin-orbit interaction. Quantitative calculations [16, 36, 44, 45, 46] identified the spin-orbit interaction as the leading intrinsic damping mechanism in ferromagnetic metals.

2.5 Extrinsic Damping: Two-Magnon Scattering

It was shown in section 2.4.3 that intrinsic damping results in a resonance linewidth which is linearly proportional to the microwave frequency. Experimentally, however, the linewidth is often found to have a linear frequency dependence with an extrapolated non-zero linewidth for zero frequency ($\Delta H(0)$) [47]. Consequently, the measured linewidth versus frequency is often interpreted using the simple relationship

$$\Delta H(\omega) = \Delta H(0) + \alpha\frac{\omega}{\gamma}, \tag{2.47}$$

where the linear term is assumed to be a measure of the intrinsic damping and the magnitude of $\Delta H(0)$ depends on the film quality and approaches zero for the best samples. This implies that $\Delta H(0)$ is extrinsic and is caused by defects. In the model of extrinsic damping by two-magnon scattering a uniform precession magnon, $\mathbf{q} \sim 0$ (FMR mode), scatters into $\mathbf{q} \neq 0$ magnons. Energy conservation requires that the resonant mode ($\mathbf{q} \sim 0$) can only scatter into spin waves oscillating at the same frequency i.e. $\omega(0) = \omega(\mathbf{q})$. $\mathbf{q}$ is determined by the magnon dispersion relation. Momentum conservation is not required due to the loss of translational invariance. This mechanism was envisioned four decades ago to explain the extrinsic FMR line broadening in YIG spheres [48]. Since then magnon scattering has been extensively used to describe extrinsic damping in ferrites [49, 50, 51, 52, 53]. Patton and coworkers pioneered this concept in metallic films [54].

The two-magnon scattering matrix is proportional to components of the Fourier transform of the magnetic inhomogeneities $A(\mathbf{q}) = \int d\mathbf{r}\Delta U(\mathbf{r})e^{-i\mathbf{qr}}$, where $U(\mathbf{r})$ stands symbolically for a local anisotropy energy. In ultrathin films the magnon $\mathbf{q}$ vectors are confined to the film plane (i.e. $\mathbf{q} = \mathbf{q}_\parallel$).

Recently, Arias and Mills [12] introduced a theory of two-magnon scattering that applies to ultrathin films. For arbitrary azimuthal angles and neglecting magnetocrystalline anisotropies the spin wave dispersion relation has the form [12]

$$\begin{aligned}\frac{\omega^2}{\gamma^2} = \frac{\omega_{\text{hom}}^2}{\gamma^2} &- 2\pi M_S q_\parallel t_F\{[\sin^2\theta_M - \cos^2\theta_M\cos^2\psi_q][H_0\cos(\theta_H-\theta_M)\\ &- 4\pi M_{\text{eff}}\sin^2\theta_M] - \sin^2\psi_q[H_0\cos(\theta_H-\theta_M) - 4\pi M_{\text{eff}}\cos 2\theta_M]\}\\ &+ Dq_\parallel^2[2H_0\cos(\theta_H-\theta_M) + 4\pi M_{\text{eff}}(1-3\cos^2\theta_M)],\end{aligned} \tag{2.48}$$

where $D = 2A/M_S$ is the spin wave stiffness constant and ψ_q is the angle between the in-plane projection of the static magnetization and the propagation direction of the

spin wave with wave vector $\mathbf{q}_\parallel$ in the sample plane. $\omega_{\rm hom}$ is the resonance frequency of the homogeneous precession of the magnetization and is given by

$$\frac{\omega_{\rm hom}^2}{\gamma^2} = [H_0\cos(\theta_H-\theta_M) - 4\pi M_{\rm eff}\sin^2\theta_M][H_0\cos(\theta_H-\theta_M) + 4\pi M_{\rm eff}\cos 2\theta_M]. \quad (2.49)$$

In the parallel FMR configuration the second term on the right hand side of Eq. 2.48 is negative and proportional to $q_\parallel$, and therefore it lowers the resonance frequency for magnons with $\mathrm{q}_\parallel > 0$ (see Fig. 2.3a). For bigger $\mathbf{q}_\parallel$ vectors, the third term in Eq. 2.48 increases the magnon energy again due to the exchange field, and the magnon dispersion curve crosses the the energy of the homogeneous precession of the magnetization at a magnon wave vector $\mathbf{q}_\parallel^0(\psi_q)$. This means that the homogenous FMR mode is degenerate with the $q_\parallel^0(\psi_q)$ mode (see Fig. 2.3a) and can be involved in two-magnon scattering. By inspection of Eq. 2.48 one can also see that when the magnetization is tipped out of the plane at angles smaller than $\theta_M = \pi/4$, no degenerate magnons are available (in this case the second term in Eq. 2.48 becomes positive and the spin wave energy can never be lower than or equal to the energy of the homogeneous mode).

The value of $\mathrm{q}_\parallel^0(\psi_\mathrm{q})$ decreases with increasing angle ψ_q between $\mathbf{q}_\parallel$ and $\mathbf{M}$, as shown in Fig. 2.3b. No degenerate modes are available for an angle ψ_q larger than [12]

$$\psi_{\rm max} = \arcsin\left(\frac{H_{\rm FMR}}{H+4\pi M_{\rm eff}}\right)^{\frac{1}{2}}, \quad (2.50)$$

where $H_{\rm FMR}$ is the field at FMR.

Arias and Mills developed a detailed theory for the case that the magnetization and applied field are parallel to each other and confined to the film plane [12]. Their quantum mechanical theory was based on a response (Green's) function formalism and a continuum approach [55]. The response functions were defined as

$$S_{\alpha\beta} = i\frac{\theta(t)}{\hbar}\langle[m_\alpha(\mathbf{q}_\parallel,t), m_\beta^\dagger(\mathbf{q}'_\parallel,0)]\rangle, \quad (2.51)$$

where the $m_{\alpha,\beta}(\mathrm{q}_\parallel,t)$ are operators for the transverse magnetization components. A magnon-magnon scattering potential was introduced in the most general way

$$V = \sum_{\mathbf{q}'_\parallel,\mathbf{q}_\parallel} \frac{1}{2}m_x^\dagger(\mathbf{q}'_\parallel)V_{xx}(\mathbf{q}'_\parallel,\mathbf{q}_\parallel)m_x(\mathbf{q}'_\parallel) + m_x^\dagger(\mathbf{q}'_\parallel)V_{xy}(\mathbf{q}'_\parallel,\mathbf{q}_\parallel)m_y(\mathbf{q}'_\parallel) + \frac{1}{2}m_y^\dagger(\mathbf{q}'_\parallel)V_{yy}(\mathbf{q}'_\parallel,\mathbf{q}_\parallel)m_y(\mathbf{q}'_\parallel). \quad (2.52)$$

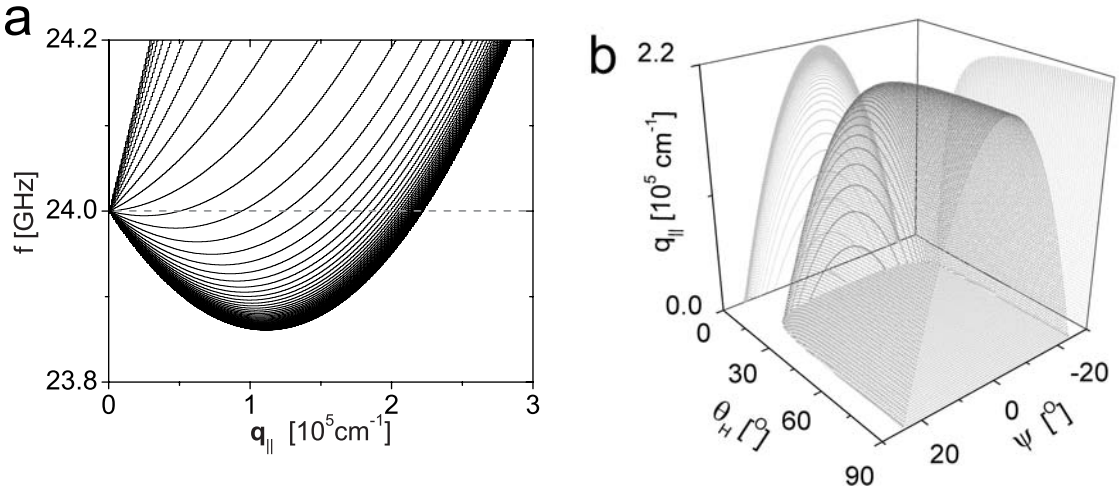

Figure 2.3: **(a)** Calculated spin wave dispersion spectra for a 30 ML thick Fe film at a frequency of 24 GHz. Here $\psi_q = 0$, where ψ_q is the in-plane angle between the magnetization and wave vector $\mathbf{q}_\parallel$. The various curves correspond to a magnetic field inclined by 1° steps from the in-plane configuration (lowest spectrum, $\theta_H = \theta_M = 90°$) to the perpendicular configuration (highest spectrum, $\theta_H = \theta_M = 0°$). The $q_\parallel^0$ wave vectors for degenerate magnons are given by the intersection with the dashed line. **(b)** Shows the dependence of $q_\parallel^0(\psi_q)$ on θ_H. Note that the degenerate magnons are lost for $\theta_H \leq 15°$ which corresponds to $\theta_M \leq \pi/4$.

For the case relevant to the FMR mode ($\mathbf{q}_\parallel = 0$) one can show that the susceptibility is given by [12]

$$S_{xx} = \frac{(H_0 + 4\pi M_{\text{eff}})M_S}{\left(\frac{\omega_{\text{hom}}}{\gamma}\right)^2 - \left(\frac{\omega}{\gamma}\right)^2 - i\alpha\frac{\omega}{\gamma}[M_{\text{eff}} + 2H_0] - R_{2\text{m}}}, \tag{2.53}$$

were $R_{2\text{m}}$ is the additional relaxation parameter due to two-magnon scattering and defined as

$$\begin{aligned} R_{2\text{m}} \;\equiv\; & \frac{\pi\gamma^4 M_S^2}{2\omega_{\text{hom}}} \sum_{\mathbf{q}} \Big| (4\pi M_{\text{eff}} + H_0) V_{xx}(0, \mathbf{q}_\parallel) + H_0 V_{yy}(0, \mathbf{q}_\parallel) \\ + \;\; & i[H_0(4\pi M_{\text{eff}} + H_0)]^{\frac{1}{2}} [Vxy(0, \mathbf{q}_\parallel) - Vxy(0, \mathbf{q}_\parallel)] \Big|^2 \delta[\omega(\mathbf{q}_\parallel) - \omega_{\text{hom}}]. \end{aligned} \tag{2.54}$$

The imaginary part of $R_{2\text{m}}$ is responsible for the two-magnon relaxation and provides additional damping of the FMR mode, while the real part of $R_{2\text{m}}$ shifts the resonance field slightly. In order to calculate the strength and frequency dependence of two-magnon scattering, Arias and Mills [12] evaluated the matrix elements $V_{\alpha\beta}$ by using

3 different sources of perturbation: (i) spatially inhomogeneous Zeeman energy, (ii) spatially inhomogeneous dipolar energy, and (iii) spatial variation of the perpendicular uniaxial anisotropy axis [12]. Only (iii) was found to produce a sizable two-magnon effect. The inhomogeneities were assumed to have a rectangular shape with lateral dimensions a and c and a random size distribution between 1 and N_a, N_c. After a series of complicated algebraical steps it was shown that the two-magnon contribution to the FMR linewidth can be written as [12, 56]

$$\Delta H^{2\mathrm{m}} = \frac{32(K_U^{\perp})^2 b^2 p}{\pi M_S^2 \sqrt{3} D} \sin^{-1}\left(\frac{H_0}{2H_0 + 4\pi M_{\mathrm{eff}}}\right)\left[\langle\frac{a}{c}\rangle - 1\right], \tag{2.55}$$

where p is the fraction of the surface area covered by defects, and b is the average defect height. This calculation allows one to refine the empirical formula Eq. 2.47 by the replacement of $\Delta H(0)$ by $\Delta H^{2\mathrm{m}}$ from Eq. 2.55.

2.6 Magneto-Optic Kerr Effect

Magneto-optic effects change the polarization of light by interaction with magnetized matter. This effect was dicovered by John Kerr in 1877 [57, 58] and is called the Kerr effect. The plane of polarization of incoming linearly polarized light rotates slightly by an angle θ_k and becomes elliptically polarized upon reflection from a magnetic sample. The origin of the Kerr effect is briefly discussed below in terms of the Lorentz model.

In the macroscopic theory the magneto-optic properties of a material can be described by the dielectric permittivity tensor $\overleftrightarrow{\varepsilon}$. For magnetic media this tensor has off-diagonal elements, the magnitude of which is proportional to the magnetization. The permittivity tensor for an isotropic magnetic medium can be written as

$$\overleftrightarrow{\varepsilon} = \varepsilon_0 \begin{pmatrix} 1 & -iQ_v\alpha_Z & iQ_v\alpha_Y \\ iQ_v\alpha_Z & 1 & -iQ_v\alpha_X \\ -iQ_v\alpha_Y & iQ_v\alpha_X & 1 \end{pmatrix}, \tag{2.56}$$

where ε_0 is the dielectric constant, Q_v is the Voigt coefficient (proportional to M_S), and α_{XYZ} are direction cosines of the magnetization. The Maxwell equation relating the vectors of the electric displacement density $\mathbf{D}$ and the electric field strength $\mathbf{E}$ can be written as

$$\mathbf{D} = \overleftrightarrow{\varepsilon}\mathbf{E} = \epsilon_0(\mathbf{E} + iQ_v\hat{\mathbf{m}} \times \mathbf{E}). \tag{2.57}$$

where $\hat{\mathbf{m}}$ is a unit vector aligned with the magnetization. The polarization vector of the light therefore rotates around the magnetization.

There are three principal configurations for Kerr effect measurements, as shown in Fig. 2.4. These configurations differ in their relative orientation of the light polarization, magnetization, and film plane. They are: (i) Polar configuration, the magnetization points normal to the sample plane and the light polarization lies in the sample plane; (ii) Longitudinal configuration, the magnetization is in-plane and parallel to the plane of incidence; and (iii) Transverse configuration, the magnetization is in the sample plane and oriented perpendicular to the plane of incidence. To understand the origin of the Kerr effect classically one can consider the equation of motion for electrons in an harmonic (crystal) potential driven by the electric field of the incident light

$$m\ddot{\mathbf{x}} + m\omega_0^2\mathbf{x} = e\mathbf{E}_0e^{i\omega t} + e(\dot{\mathbf{x}} \times \mathbf{B}), \tag{2.58}$$

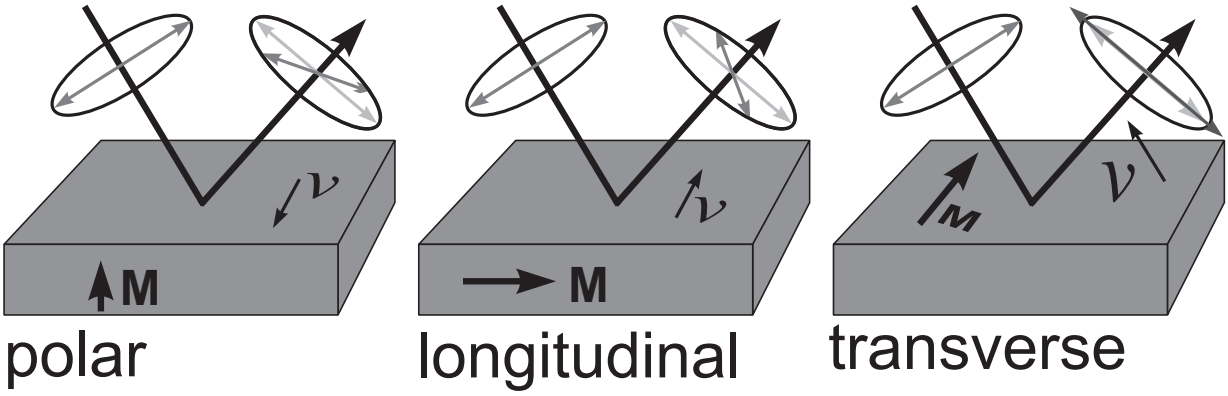

Figure 2.4: Polar, longitudinal, and transverse configurations for Kerr effect measurements. The arrows inside the circles represent the direction of the electric vector **E** of linearly polarized light. The rotation of the polarization and the intensity change due to the Kerr effect is illustrated by the darker arrow on the reflected light side. ν indicates the direction of the Lorentz force exerted on the moving electrons inside the magnetic medium ($\nu \parallel \mathbf{M} \times \mathbf{E}$).

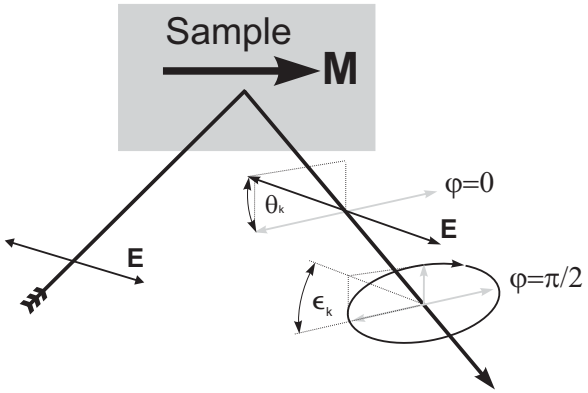

Figure 2.5: Longitudinal configuration illustrating the meaning of the Kerr angles θ_k and ϵ_k. The reflected light can be split into a linearly polarized in-phase component ($\varphi = 0$) with rotation angle θ_k and an elliptically polarized out-of-phase component ($\varphi = \pi/2$) with ellipticity angle ϵ_k.

where **x** is the electron displacement and ω_0 is the angular frequency of the incoming light. It is assumed that the light polarization $\mathbf{E}_0$ is in the film plane and $\mathbf{E}_0 \parallel \mathbf{x}$. The Lorentz force on the right hand side of Eq. 2.58 is in the plane of the surface if **B** is perpendicular to the surface ($\mathbf{B} \parallel \mathbf{z}$). This corresponds to the polar configuration, see Fig. 2.4a. Therefore the polarization of the reradiated (reflected) light will be rotated. Similar arguments apply to the other Kerr configurations.

The true microscopic origin of the magneto-optic effect lies in exchange and spin-

orbit coupling which gives rise to a large effective field in the direction of **M**. This field leads to a Lorentz force and rotates the polarization. The light reflected from the metallic sample only interacts with a thin surface layer whose thickness is given by the skin depth. For metals the skin depth is of the order of 100 Å in the visible light spectrum. Hence the Kerr rotation of the polarization is very small and usually only of the order of 10^{-3} degrees.

Since the permittivity tensor is complex the Kerr signal is measured by two quantities: rotation angle θ_k and ellipticity angle ϵ_k. Their definition is shown in Fig. 2.5. In the polar Kerr configuration θ_k and ϵ_k are roughly 10 times bigger than in the longitudinal configuration. This is due to the large refractive index (sum of real and imaginary parts) of metals which causes the effective angle of incidence to be small (typically 5-8°). In this case the light propagates mostly perpendicular to the magnetization and the component of the Lorentz force which is perpendicular to the electric field is small.

Chapter 3

Experimental Methods

In this chapter the ultra-high vacuum (UHV) system that was used for sample preparation and the techniques that were employed in the magneto-dynamic studies are discussed. The chapter starts with a detailed description of the UHV system and associated techniques used for film growth and characterization. The second part of this chapter will address the Ferromagnetic resonance (FMR) and magneto optic Kerr effect (MOKE) technique which were employed in static and dynamic magnetic measurements.

3.1 The Ultra-High Vacuum System

Epitaxial metallic films were prepared in UHV by means of molecular beam epitaxy (MBE). The UHV system is composed of 4 interconnected chambers, as illustrated in Fig. 3.1. (a) The intro chamber was used for outgassing and hydrogen cleaning after the samples were introduced into UHV from the load lock. (b) The analysis chamber houses an apparatus for Auger electron spectroscopy (AES), X-ray photo emission spectroscopy (XPS), and ultraviolet photoemission spectroscopy (UPS). These tools permit atomic and chemical characterization of the sample surface. In addition an Ar^+ ion gun in the analysis chamber allows one to remove surface contaminants and to conduct depth profile analysis. (c) The growth chamber has 8 thermal evaporation furnaces embedded in a cryo-shroud. The atomic surface topography and growth rate were monitored using reflection high energy electron diffraction (RHEED) and a quartz crystal micro balance. (d) The SPM chamber accommodates an Omicron large area scanning probe microscope (SPM) which includes a scanning tunnelling

microscope (STM) and an atomic force microscope (AFM). The sample holder is mounted on a linear transfer arm, and includes goniometers for adjustment of the azimuthal and polar angles of the sample. The transfer arm has 130 cm of travel, allowing one to move the sample between the various chambers. The sample can therefore be oriented at arbitrary azimuthal and polar angles in all chambers. The temperature of the sample substrate can be varied between -200 °C and $+700$ °C.

3.1.1 Substrate preparation

All samples were grown on single crystalline GaAs(001) wafers. Commercial epi-ready GaAs substrates (manufactured by American Xtal Technology) are always covered by a several nm of natural oxide. This oxide layer was removed under UHV conditions using two techniques: (i) Ar^+ ion bombardment and (ii) atomic hydrogen etching. Both techniques have advantages and shortcomings, and are described below.

Ar^+ sputtering

Samples are introduced into the intro UHV chamber via the small independently pumped load lock chamber. This allows the pressure in the intro chamber to be held at less then 1×10^{-8} torr during loading of a GaAs sample holder onto the UHV goniometer. Subsequently, the GaAs substrates are outgassed at 400 °C for several hours until the base pressure in the intro chamber fell below 5×10^{-10} torr. The wafer is then cooled down to RT and bombarded by 600 eV Ar^+ ions at a grazing angle (65° with respect to the surface normal) to remove surface contaminants. During sputtering the sample is rotated around its normal and the ion beam was rastered over the sample. The ion beam bombardment is imaged as a function of the beam x-y deflection voltages. An image of the sample is acquired by measuring the ion current flowing into one of the tungsten clips which are used to hold the wafer. During ion bombardment the surface of an otherwise semi-insulating GaAs wafer becomes conducting (probably due to the atomic disorder and site exchange doping As$\leftrightarrows$Ga) allowing one to follow the position of the ion beam by monitoring the absorbed ion current, as shown in Fig. 3.2. In this way it is possible to maximize the ion flux over the sample by optimizing the ion-gun optics, sample position, and raster size. In our differential ion gun, the Ar gas was bled directly into the ionization chamber allowing one to maintain an Ar back-pressure of 3×10^{-7} torr during sputtering. While

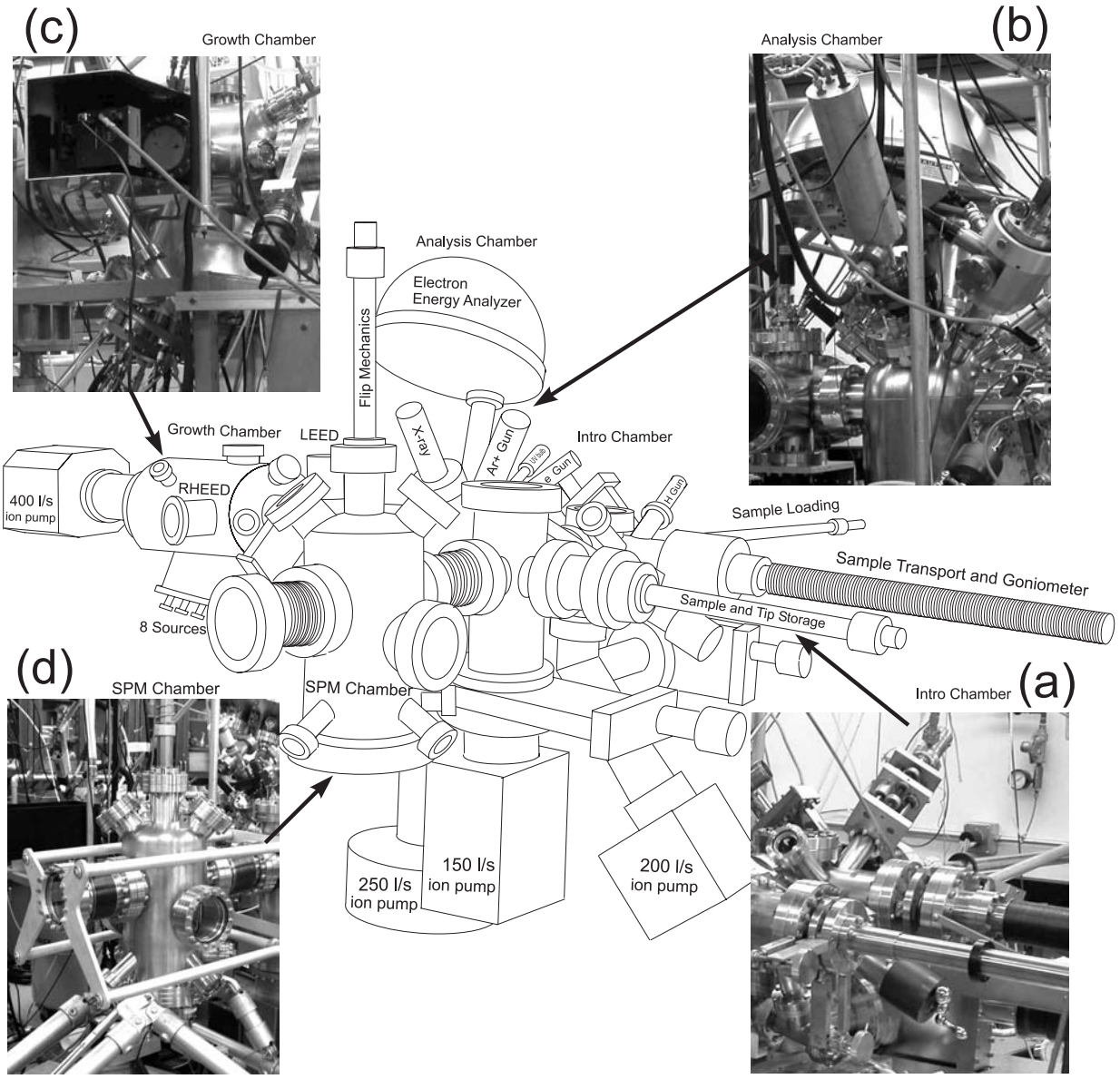

Figure 3.1: Sketch of the UHV MBE system. The MBE system consists of four chambers: (a) intro chamber (bottom right), (b) analysis chamber (top right), (c) growth chamber (top left), (d) and SPM chamber (bottom left).

sputtering, the chamber was pumped by two 500 l/s turbo pumps. A clean surface was obtained after $5-7$ hours of sputtering depending on the thickness of the oxide layer.

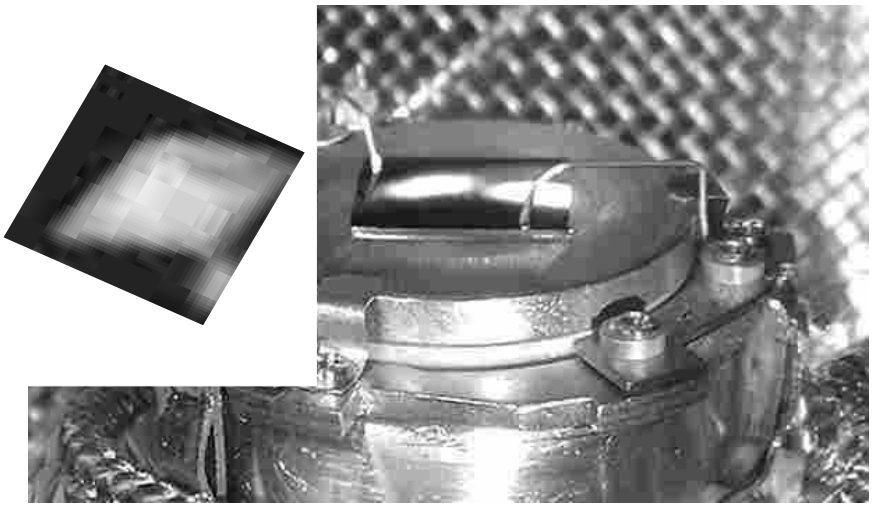

Figure 3.2: UHV sample holder with a 10×10 mm GaAs wafer held by two tungsten clips. The inset on the left side shows an image of the GaAs wafer acquired by monitoring the absorbed ion current during Ar^+ sputtering, as discussed in the text.

H· cleaning

Atomic hydrogen provides a faster and easier way to remove surface contaminants. During the cleaning procedure the sample temperature was held at 400 °C. A hydrogen doser (Oxford Scientific) thermally cracks hydrogen molecules into neutral atoms by passing H_2 gas through a narrow 2000 °C hot tungsten tube; the tungsten tube is heated by electron bombardment. H_2 molecules are dissociated into atomic hydrogen (H·) during collisions with the hot wall of the tube. This provides an atomic hydrogen beam with about 15 degrees divergence and a cracking ratio H/H_2 of up to $\sim 95\%$ [59]. Without atomic hydrogen the thermal desorption temperatures for Arsenic and Gallium oxides on GaAs are 450 °C and 580 °C, respectively [60]. Atomic hydrogen removes both oxides at 400 °C.

The chemistry of the hydrogen surface cleaning process may be summarized as follows [61, 62]: Arsenic oxides can be removed from the surface (↑) by H· cleaning in the following reaction:

$$As_2O_x + 2xH\cdot \rightarrow xH_2O \uparrow + As_2 \uparrow, \tag{3.1}$$

were x= 1, 3, or 5 stands for the various oxides of arsenic. Ga_2O_3 is decomposed as

$$Ga_2O_3 + 4H\cdot \rightarrow Ga_2O \uparrow + 2H_2O \uparrow . \tag{3.2}$$

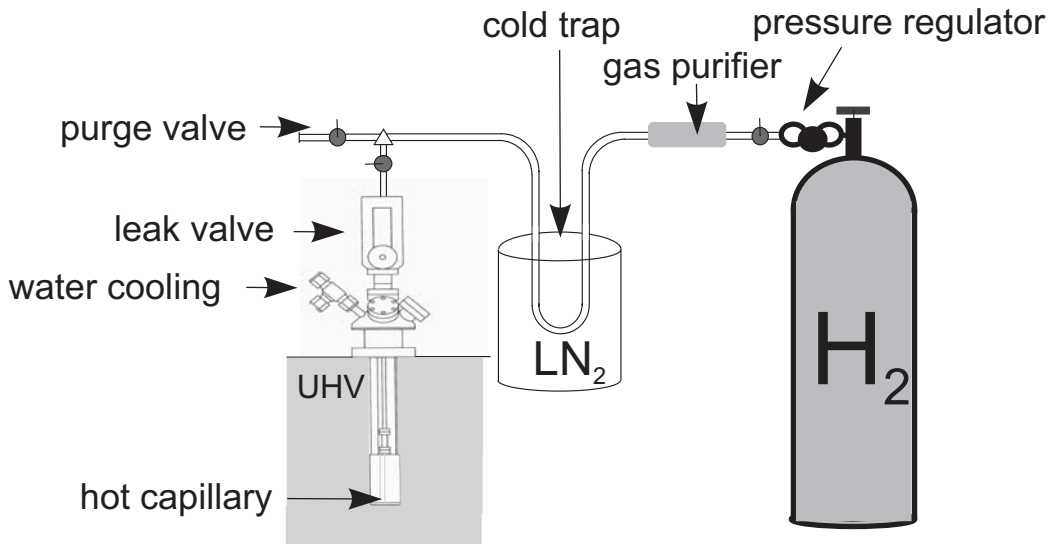

Figure 3.3: Schematic view of the hydrogen doser.

Ga_2O becomes volatile at temperatures greater than 200 °C. If permitted to remain on the surface Ga_2O would act as an etch stop, or lead to a Ga-rich surface as a result of the subsequent reaction

$$Ga_2O + 2H\cdot \rightarrow 2Ga + H_2O \uparrow, \tag{3.3}$$

which is undesirable. Therefore, the temperature should not be chosen to be less than 350 °C; greater than 400 °C is preferable, allowing for rapid Ga_2O desorption. It has been shown that hydrocarbons and CO contaminants can also be removed using atomic hydrogen [62]. Thus one can prepare a clean and stoichiometric GaAs surface [61].

During cleaning the hydrogen back pressure is 5×10^{-7} torr. The ion pump in the intro chamber was not used during cleaning because the hydrogen exposure leads to the release of water from the ion pump electrodes. A liquid nitrogen cooled titanium sublimator pump (TSP), however, inside the ion pump allows very efficient pumping of hydrogen. The TSP housing in the intro chamber has an inner diameter of 10 cm and is about 16 cm tall giving an internal area of about 500 cm^2. At 77 °K TSP has a pumping speed for hydrogen of about 10 $l s^{-1} cm^{-2}$ [63]. The effective pumping speed depends on the length and diameter of the pipe connecting the intro chamber to the TSP. The conductance of this pipe in ($l s^{-1}$) is given by [63]:

$$C_{\text{pipe}} = 3.81 \times \sqrt{\frac{\mathrm{T}}{\mathrm{M}}} \left(\frac{\mathrm{D}^3}{\mathrm{L} + 1.33\mathrm{D}} \right) \frac{l}{\mathrm{s}}, \tag{3.4}$$

were T is the temperature (300 °K), M is the molecular mass (for hydrogen), and D(16 cm) and L(40 cm) are the pipe diameter and length, respectively. This yields a pipe conductance of 2400 l/s. Therefore the effective TSP hydrogen pumping speed is approximately 1600 l/s.

Using this pumping speed one can estimate the hydrogen pressure in the tungsten tube and find the molecular hydrogen dissociation rate [59]. The tungsten capillary has a diameter of D = 0.5 mm and a length of $L = 5$ cm, resulting in $C_{\rm tube} = 0.04$ l/s; the hydrogen dissociation takes place in the last 5 mm of tube [59]. During cleaning the hydrogen pressure is $p_{\rm intro} = 5 \times 10^{-7}$ torr in the intro chamber and combined with 1600 l/s pumping speed requires a pressure of $p_{\rm tube} \simeq 2 \times 10^{-2}$ torr in the hot tube (steady state solution: $p_{\rm tube} C_{\rm tube} = p_{\rm intro} 1600$ l/s). At this pressure the dissociation rate of H_2 is expected to be 90 %, assuming a tube temperature of 2000 °K [59]. The gas throughput Q is given by

$$Q = C(p_{\rm tube} - p_{\rm chamber}) = 0.04 \ \frac{l}{\rm s} \ (2 \times 10^{-2}) \ {\rm torr} = 1.1 \times 10^{-4} \frac{{\rm m^3 Pa}}{\rm s}. \qquad (3.5)$$

Using the ideal gas equation one can write

$$Q = p\frac{dV}{dt} = k_B T \frac{dN}{dt} \quad \rightsquigarrow \quad \frac{dN}{dt} \quad = \quad \frac{1.1 \times 10^{-4}}{k_B T} \frac{{\rm m^3 Pa}}{\rm s} = 3.8 \times 10^{15} \frac{\rm atoms}{\rm s}. \ (3.6)$$

From the molar volume at RT and atmospheric pressure the corresponding amount of hydrogen in cc is:

$$\frac{dV}{dt}\Big|_{\rm 1atm}^{\rm 300K} = 0.5 \ \frac{\rm cc}{\rm hour}. \qquad (3.7)$$

A time interval of 30 min was required for cleaning. This means that a volume of 0.25 cc of hydrogen (at atmospheric pressure) was used during cleaning. One can estimate the number density of impinging hydrogen atoms on the sample surface and their reaction probability. The nozzle of the tungsten capillary was at a distance of 4 cm from the sample during cleaning and hence the hydrogen beam covered an area of ~ 4 cm^2. Therefore only a quarter of the H· flux impinged on the 10×10 mm sample. Using Eq. 3.7 the number of hydrogen atoms hitting the GaAs wafer in 30 min was $N_H^{\rm 30min} = 1.7 \times 10^{18}$ atoms. This number can be used to estimate the reaction probability. Assuming 50 monolayers of oxide one gets $\sim 50 \times 10^{15}$ oxide sites resulting in a reaction probability of ~ 3 %. This is only a crude estimate, but the number seems very reasonable. In a more accurate calculation the ineffectiveness of cleaning for a sub monolayer oxide coverage should be considered.

3.1.2 Electron spectroscopy

Auger electron spectroscopy (AES) and x-ray photoemission spectroscopy (XPS) allow one to measure the elemental and chemical composition at the surface of a sample. In these techniques an incident electron beam (AES) or an incident x-ray beam (XPS) results in the emission of electrons from the sample surface. The kinetic energy spectrum of the emitted electrons exhibits peaks that are element specific since the energy of these electrons depends on the binding energy of the excited electron (XPS) or on the energy difference between the specific atomic energy levels (AES) [64, 65]. Both techniques are surface sensitive because the electron mean free path is less than 2 nm in the relevant energy range (100 eV-2 keV) [66]. Hence only a 2 nm thick surface layer of the sample can contribute to the signal. Using the UHV goniometer, the angle of the analyzer with respect to the sample surface can be changed, which further allows one to separate the bulk and surface contributions to the signal. XPS is based on the analysis of the kinetic energy of electrons emitted from a surface in response to a monochromatic x-ray beam (in our case Al-K_α, $h\nu = 1486.6$ eV or Mg-K_α, $h\nu = 1253.6$ eV). The energy spectrum of emitted electrons was measured by means of a hemispherical capacitive analyzer (SCA). The analysis chamber is equipped with a Physical Electronics digital analyzer system (PHI 5400). The electron energy spectrum is analyzed by sweeping the potential V_A (see Fig. 3.4), thus shifting the analyzer Fermi level relative to the sample Fermi level. Electrons are not used as a primary beam in XPS because electron-electron scattering processes in solids would result in a broad primary energy unsuitable for the analysis of the narrow XPS peaks. In x-ray spectroscopy the primary energy is transferred to the photo electron, and electron-electron scattering only plays a role when the photo electron leaves the crystal. Energy conservation determines the kinetic energy (KE) of the photo emitted electron,

$$\mathrm{KE_{XPS}} = \mathrm{h}\nu - \mathrm{BE} - \phi_\mathrm{A}, \tag{3.8}$$

where BE is the core hole binding energy measured relative to the Fermi energy, as illustrated in Fig. 3.4. In addition, the resulting core hole is eventually filled with an electron originating from an outer shell. At the same time an Auger electron from another shell is emitted, carrying away the excess energy. The AES kinetic energy ($\mathrm{KE_{AES}}$) is given by

$$\mathrm{KE_{AES}^{KLL}} = \mathrm{EB_K} - \mathrm{EB_{L2}} - \mathrm{EB_{L3}} - \phi_\mathrm{A}, \tag{3.9}$$

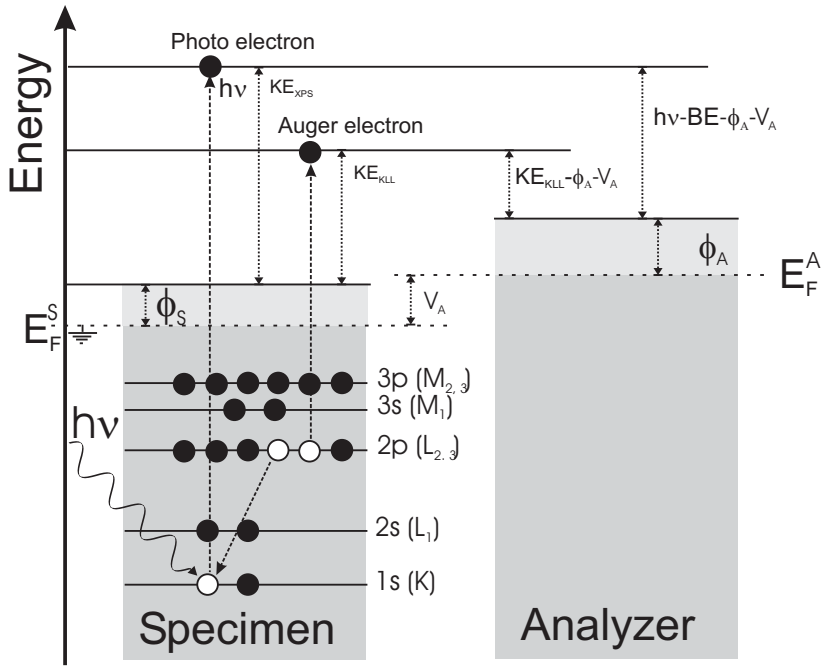

Figure 3.4: Energy level diagram for XPS and AES. KE and BE are the electron kinetic energy and binding energy, respectively. $\phi_{S,A}$ are the sample and spectrometer work functions. E_F^S, E_F^A are the sample and analyzer Fermi levels, respectively. hν is the incident photon energy. The energy levels of the sample are indicated in the left part. On the right, the potential of the electron analyzer is shown relative to the sample potential on the left. In electron spectroscopies the binding energy is measured with respect to the Fermi level. Note that for the retarding potential $V_A = 0$, the Fermi levels of the sample and the analyzer are equal.

where the EB's correspond to the appropriate electron level binding energies (see Fig. 3.4). AES utilizes the element specificity of the binding energies. In AES the initial core hole is usually generated by high energy electrons originating from a primary electron beam with a fixed energy (3keV in our system). Auger electrons, however, are also present in XPS (see Fig. 3.4). The sensitivity of electron spectrometers allows one to detect a surface coverage of ~ 0.01 monolayer (ML).

During relaxation of the core hole the generation of Auger electrons and x-ray fluorescence are competing processes for carrying away the excess energy. For light elements the probability of generating Auger electrons is almost unity but with increasing atomic number this probability drops dramatically. For atomic numbers larger than 30, the x-ray fluorescence signal becomes larger than the Auger electron

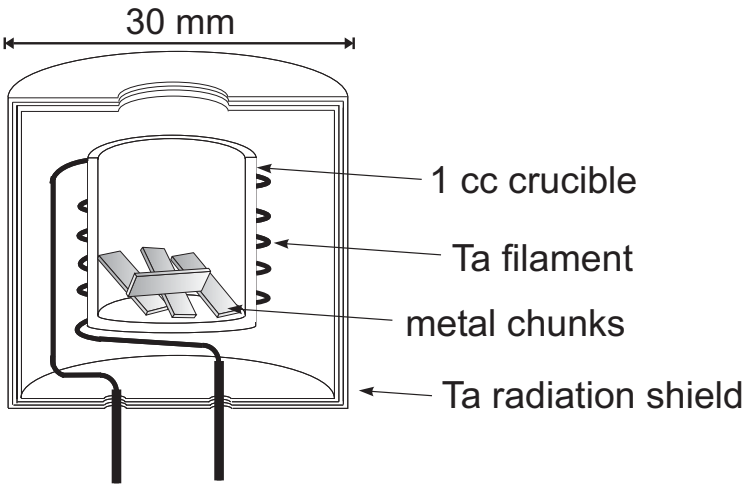

Figure 3.5: Cross section of a MBE source.

signal. Therefore AES is a less sensitive technique for elements with large atomic numbers when compared to XPS.

3.1.3 Metallic film growth

Metallic films were grown by means of molecular beam epitaxy (MBE) directly on GaAs(001) templates. The molecular beam sources were based on thermal evaporation in UHV and the growth rate was usually ~ 2 ML/min. In all samples the first metallic layer grown on GaAs(001) was Iron. Fe grows well on GaAs(001) [67] and has a lattice spacing that is closely matched to the size of half a unit cell of GaAs(001). The lattice mismatch of Fe to GaAs is only -1.4%. A crystalline epitaxial seed layer of Fe(001) served as a template for the epitaxial growth of other metallic layers: Au(001), Ag(001), Cu(001), Pd(001), and Cr(001).

Metal Sources

Fig. 3.5 shows the basic design of the evaporation sources used for the samples in this thesis. A crucible filled with the desired metal was placed inside a multilayer tantalum radiation shield and resistively heated by means of a tantalum filament having an impedance of $\sim 0.5\ \Omega$ at a current of $\sim 40 - 60$ A. All metal sources Ag(830 °C), Cu(1030 °C), Fe(1180 °C), Cr(1160 °C), and Pd(1190 °C) had an Alumina (Al_2O_3) crucible except for Au(1130 °C), which had a pyrolytic boron nitride (PBN) crucible. PBN cannot be used for transition metals because they tend to react with PBN to

form N_2 and nitrides when hot. The numbers in brackets listed with each of the elements represent the temperature required to achieve a vapor pressure which is sufficient for evaporation ($\sim 10^{-3}$ torr). A Ta liner inside the alumina crucible was used for the Ag and Cu furnaces in order to prevent stress induced cracking of the crucible. All furnaces were surrounded by a liquid nitrogen cooled cyro shroud and the copper power feed-throughs (2.5") were water cooled. The cryo-shroud served to absorb unwanted gas species originating from the hot furnaces during film growth.

Reflection high energy electron diffraction

Reflection High Energy Electron Diffraction (RHEED) is a powerful analytical technique which was used during the sample growth. It is a non-invasive tool that can provide real-time information about surface morphology and symmetry. At the same time it allows one to measure the thickness of the growing film with sub monolayer accuracy. In this technique a 10 keV electron beam impinges on the sample surface at a grazing angle of $\sim 1^\circ$ (see Fig. 3.6). Due to the shallow angle of incidence, very little momentum perpendicular to the surface is available and hence the electron beam interacts with only one or two atomic layers at the surface. On an ideal surface this would result in diffraction from a two dimensional periodic mesh. The three dimensional reciprocal lattice is replaced by rods due to the lack of scatterers perpendicular to the surface. The diffracted beams are given by the intersection of the Ewald sphere with the reciprocal rods [68] (see Fig 3.6). The electron energy is chosen such that the Ewald sphere is large enough to intercept several reciprocal rods having a spacing of $2\pi/a$, where a is the in-plane atomic spacing. Hence RHEED is sensitive to the periodicity of the surface lattice. The first order diffraction spots, specularly reflected electrons, and the through beam lie on one circle, as illustrated in Fig. 3.6. The diffracted and reflected electrons illuminate the phosphorescent screen, and a digital charge coupled device (CCD) camera is used to monitor the diffraction pattern and its time evolution during the sample growth.

Surface reconstruction of GaAs(001)

GaAs is an ionic crystal having zinc blende structure and a lattice constant of $a = 5.654$ Å. The zinc blende structure corresponds to two interpenetrating fcc lattices of Ga and As atoms shifted mutually along the [111] direction by 1/4 of the body diagonal [69]. The bonding between atoms is ionic and covalent in character. An ideal

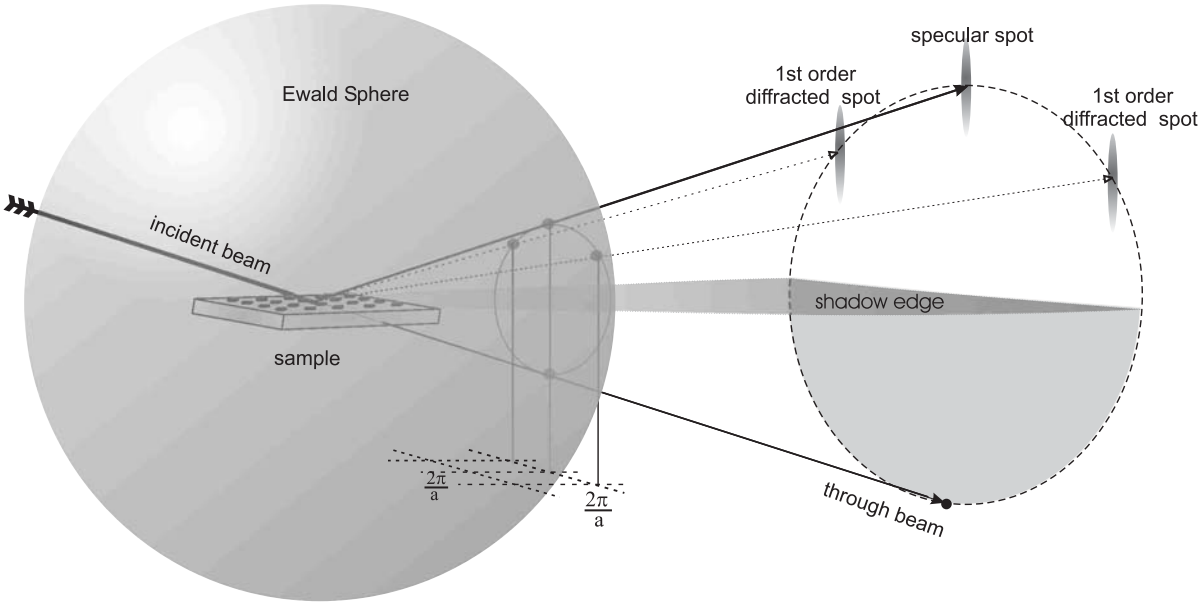

Figure 3.6: The geometry of RHEED. The Ewald sphere represents the k-space of electrons having the same energy as the incident beam. The intersection of the reciprocal rods with the Ewald sphere determines the diffraction beams. Low index diffraction beams intersect the phosphorescent screen and provide information about the film surface symmetry and roughness.

GaAs(001) surface would be either As or Ga terminated. The surface atoms, however, do not have neighbors in the [001] direction and thus the GaAs{001} plane would be charged. In order to avoid a surface charge density, the equilibrium positions of the surface atoms have to differ from the bulk. Which reconstruction occurs depends upon temperature and surface stoichiometry. On the GaAs(001) surface the [110] and [1$\bar{1}$0] directions are not equivalent and the convention adopted is that in-plane components of the Ga bonds are parallel to the [110] direction, and the in-plane components of the As bonds are parallel to the [1$\bar{1}$0] direction [70]. This uniaxial property results in a magnetic uniaxial interface anisotropy for Fe films grown on GaAs(001). Energy level calculations for GaAs(001) [71] predict that the As dangling bond energy lies in the valence band (i.e. filled) and the dangling bond energy of Ga lies above the conduction band (i.e. empty). This means that in order to minimize the total energy, the surface electrons have to go from Ga to As [72]. This is achieved by the formation of dimers at the surface and results in surface reconstructions which can be identified by 2 numbers A×B, where A is the size of the unit cell (in units of

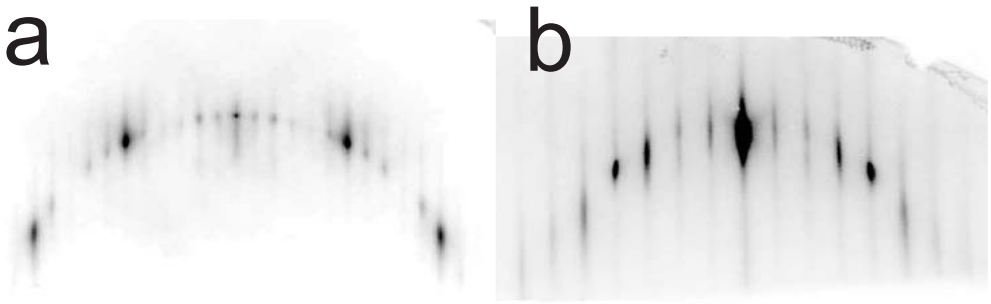

Figure 3.7: RHEED patterns of a hydrogen cleaned GaAs sample after annealing at 600 °C. Image **(a)** was recorded with the primary electron beam oriented along the $[1\bar{1}0]$ direction and shows 5 satellite spots between the main diffraction spots characteristic of the 1×6 reconstruction. In **(b)** the primary electron beam was oriented along the [110] direction. The 3 satellites between the primary spots correspond to the 2×4 reconstruction.

atomic spacings) in the [110] direction, and B is the size of the unit cell in the $[1\bar{1}0]$ direction. With increasing temperature As is preferentially lost from the surface due to its higher vapor pressure compared to Ga and the surface becomes Ga rich. The following reconstructions sequenced from As-rich to Ga-rich are commonly found on GaAs(001): (4×4), (2×4), (1×6), (2×4), and (8×2).

After the GaAs wafers were cleaned the surface was annealed while monitoring the RHEED pattern. The wafer temperature was gradually raised to 600 °C within 30 minutes. Under these conditions the atoms at the surface become mobile and form domains of 4×2 and 6×1 surface reconstructions [67, 73, 74]. These reconstructions represent additional periodicities of the surface and can be observed in RHEED. Fig. 3.7 shows the diffraction patterns of a GaAs(001) wafer after annealing. The surface consists of (1×6), and (2×4) reconstructed domains [73].

RHEED oscillations

When the angle of the incident electron beam θ_i is set up to correspond to the anti Bragg condition, the measured intensity of the specular spot can oscillate during film growth. Simple layer by layer growth can be described in a kinematic approximation as proposed by van Hove et al. [75]. This model assumes that the electrons are

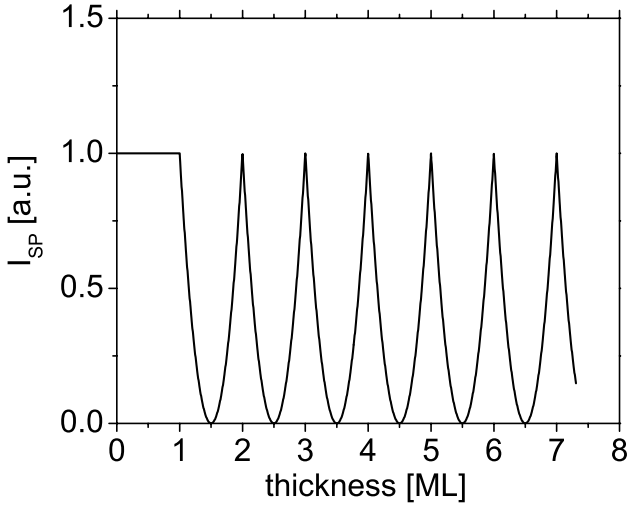

Figure 3.8: RHEED oscillations calculated from Eq. 3.11 with θ_i corresponding to the anti Bragg condition.

scattered only from the topmost surface atomic layers 1 and 2. In perfect layer by layer growth, the lower layer is always completely filled while the top layer coverage Θ increases periodically from 0 to 1 during the film deposition. The diffracted electrons scattered from atoms at level 1 and 2 have a relative phase shift $\Delta\phi$. Using Bragg's law

$$\Delta\phi = 2|\mathbf{k}_i|a_\perp \sin\theta_i, \tag{3.10}$$

where $\mathbf{k}_i$ is the incident electron $\mathbf{k}$-vector and $a_\perp$ is the lattice spacing perpendicular to the surface. The intensity of the specular spot is determined by the interference of the scattered electron wave functions. The electron wave scattered from the top layer will be proportional to the coverage $\psi_1 \sim \Theta$ and the wave from the bottom layer will be proportional to $\psi_2 \sim (1-\Theta)e^{i\Delta\phi}$. This implies that the intensity of the specular spot is proportional to

$$I_{SP} \sim |\psi_1 + \psi_2|^2 \sim \Theta^2 + (1-\Theta)^2 + 2\Theta(1-\Theta)\cos(\Delta\phi). \tag{3.11}$$

As the polar angle of incidence θ_i is changed, the electron waves from layers 1 and 2 can interfere constructively or destructively depending on their phase difference $\Delta\phi$. The extrema occur when the phase shift is $\Delta\phi = n\pi$. θ_i for even n are called Bragg angles and the interference is constructive. In this case I_{SP} does not depend on Θ and no RHEED oscillations are present. θ_i for odd n are called anti-Bragg angles and the Θ-dependence of $I_{SP}(\Theta)$ reaches a maximum because electrons scattered from

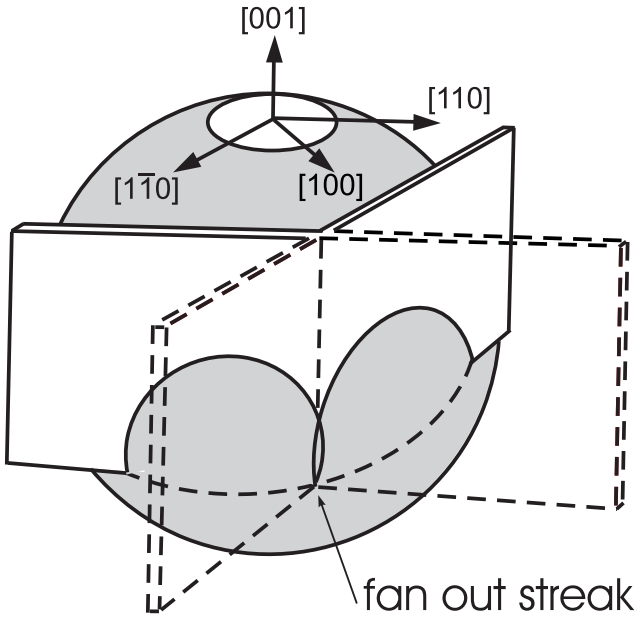

Figure 3.9: The k-space sheets represent the reciprocal space of a network of atomic surface steps oriented along the ⟨110⟩ directions. The intersection of k-space sheets with the Ewald sphere illustrates the origin of fan-out streaks when the electron beam is directed in the [100] direction [76].

layers 1 and 2 interfere destructively (i.e. for $\Theta = \frac{1}{2} \rightarrow I_{SP} = 0$). Fig. 3.8 shows an example of the RHEED oscillations predicted by Eq. 3.11. In practice, the cusps are rarely observed because a new layer usually begins to grow before the bottom layer is finished. When the total number of unfinished layers increases with increasing film thickness, the surface becomes rougher leading to an exponentially decreasing amplitude of the RHEED oscillations. Good oscillations are visible as long as the number of unfinished layers is limited to the top 3 atomic layers across the coherence length of the electron beam (typically 1000 Å). This type of growth is referred to as 'quasi layer by layer' growth.

Surface corrugations

RHEED can also detect surface imperfections such as corrugations or island formation arising from a surface reconstruction or a network of misfit dislocations. The gliding of misfit dislocation half loops from the surface can cause a rectangular network of surface steps during the growth. In this case the reciprocal rods broaden into two interpenetrated sheets due to partial loss of well defined translational invariance, as

illustrated in Fig. 3.9. It was shown by Pukite [76, 77] that when the rectangular network of surface steps is oriented along the $\langle 110 \rangle$ directions while the electron beam is parallel to the [100] direction the RHEED streaks are split showing a typical fan-out diffraction pattern. This effect is caused by the intersection of the Ewald sphere with k-space sheets (generated by the defect lines) [76, 77], as illustrated in Fig. 3.9. The fan-out effect is entirely absent when the electron beam is oriented along the [110] direction, and only simple straight streaks are produced.

This phenomenon can also be understood in terms of kinematic scattering. The intensity of diffracted beams is determined by components of the Fourier transform, $S(k_x, k_y)$, of the distribution of surface atoms [78], where k_x and k_y are the in-plane k-vectors. Pukite's analysis was based on evaluating the surface reciprocal lattice structure in the presence of randomly distributed rectangular surface mesas. The mesa cells were generated by a geometric distribution of lines along the x and y in-plane coordinates parallel to the atomic steps of the mesas. The scattering intensities in this case are given by the product of two Lorentzian functions [76]

$$I(k_x, k_y) = S^* S \sim \frac{\beta}{k_x^2 + \beta^2} \cdot \frac{\beta}{k_y^2 + \beta^2} \,, \tag{3.12}$$

where β is given by the average size of atomic terraces; $\beta = 2/\langle L \rangle$. The reciprocal surface scattering rods are replaced by reciprocal space sheets oriented along the surface atomic steps [76]. Their intensities are described by Eq. 3.12, and the electron diffraction in RHEED is given by the intersection of the Ewald sphere with the reciprocal sheets. This leads to simple diffraction streaks when the electron beam is oriented along the atomic edges (line defects), and results in fan-out streaks for the electron beam oriented 45° with respect to the atomic steps (see details in [76]). Atomic mesas are one possible surface arrangement leading to reciprocal sheets. Other systems with rectangular defect distribution can lead to a similar reciprocal space. Parallel dislocation bundles in Fe on W(001) also resulted in well defined reciprocal sheets oriented along $\langle 100 \rangle_{\mathrm{Fe}}$, as shown by Wulfhekel et al. [79].

3.1.4 In-situ STM, AFM

The reciprocal space images obtained using RHEED and LEED are helpful, but it can be very difficult to interpret their meaning in real space. Scanning probe microscopy (SPM) provides real space information. The Omicron in-situ SPM system allows

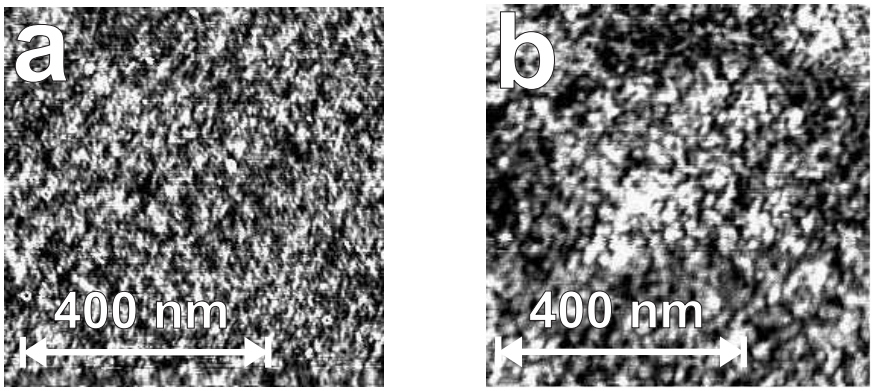

Figure 3.10: In-situ AFM image of a GaAs(001) wafer **(a)** after hydrogen cleaning and **(b)** after hydogen cleaning and annealing at 600°C. The hight scale is 6 Åin both images. By annealing, the terrace size is increased from 5 nm in **(a)** to 20 nm in **(b)**, while the rms-roughness decreased from 2.5 Å to 2.0 Å.

one to carry out scanning tunnelling microscopy (STM) and atomic force microscopy (AFM).

In Fig. 3.10 in-situ AFM images of a hydrogen cleaned GaAs(001) wafer are shown before and after annealing. The hydrogen treatment produces a surface that is very flat (2.5 Å rms-roughness), but causes nanoscale roughness with an average terrace width of only 5 nm. Annealing at 600 °C increases the terrace width and decreases rms-roughness (see Fig. 3.10). The atomic terraces of hydrogen cleaned surfaces are only half as wide compared to those prepared by a sputtering/annealing cycle. The rms-roughness, however, is equal for both preparation techniques.

3.2 Ferromagnetic Resonance

Ferromagnetic resonance (FMR) occurs in the microwave range of frequencies in magnetic samples and has been extensively employed to study magnetic properties in this thesis. The FMR absorption signal was measured by monitoring the microwave losses in a magnetic film as a function of an external dc magnetic field.

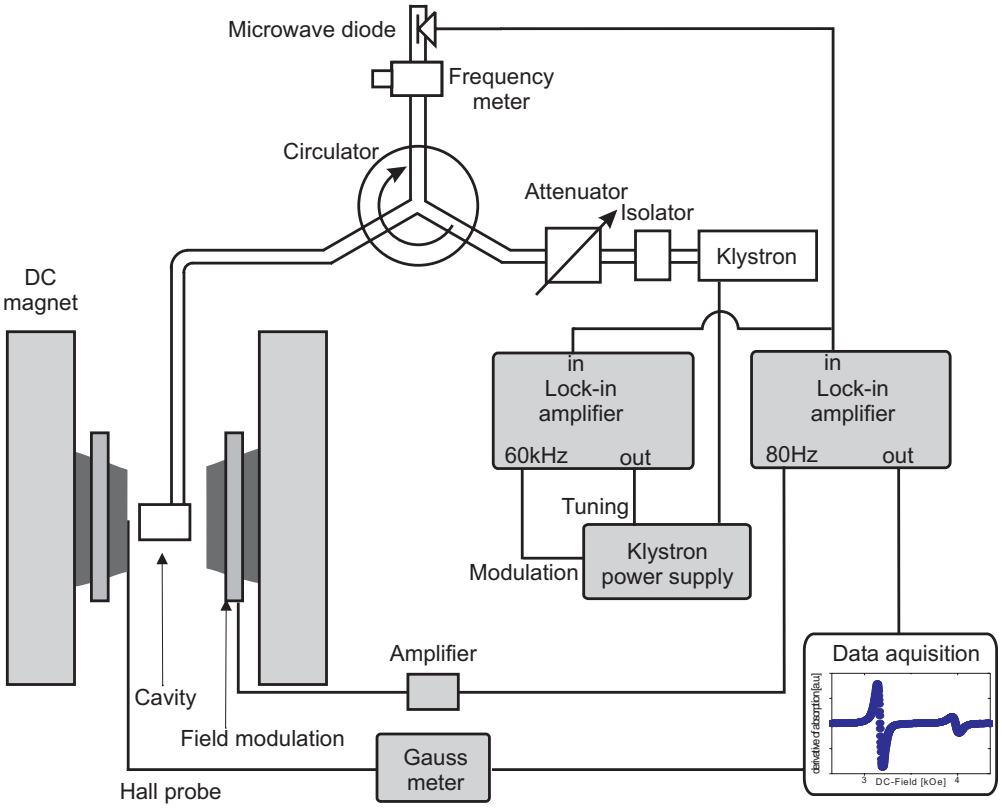

Figure 3.11: Block diagram of the microwave spectrometer used for FMR measurements. The microwave radiation is generated by a klystron and reflected from the sample cavity located between the pole pieces of an electro magnet. The amplitude of the reflected radiation as a function of the external field is monitored by means of a microwave diode detector.

3.2.1 Microwave spectrometer

Fig. 3.11 shows a typical setup of an FMR spectrometer. The microwave radiation is generated by a reflex klystron operating at a fixed frequency. The operation of a reflex klystron tube is based on high frequency electron bunching. This concept was invented by the Varian brothers in 1939 [80]. Interestingly, the klystrons used in our FMR spectrometers ($9 - 73$ GHz) were all manufactured by the Varian company which was founded by these inventors. Unfortunately Varian has since discontinued the production of low power klystrons. Reflex klystrons contain a reflector plate, called a repeller. An electron beam is modulated (bunched) by passing it through the grids of an oscillating resonant cavity. The unique feature of a reflex klystron is that the feedback required to maintain oscillation within the cavity is obtained by reversing the electron beam and sending it back through the grids of the cavity. The electrons

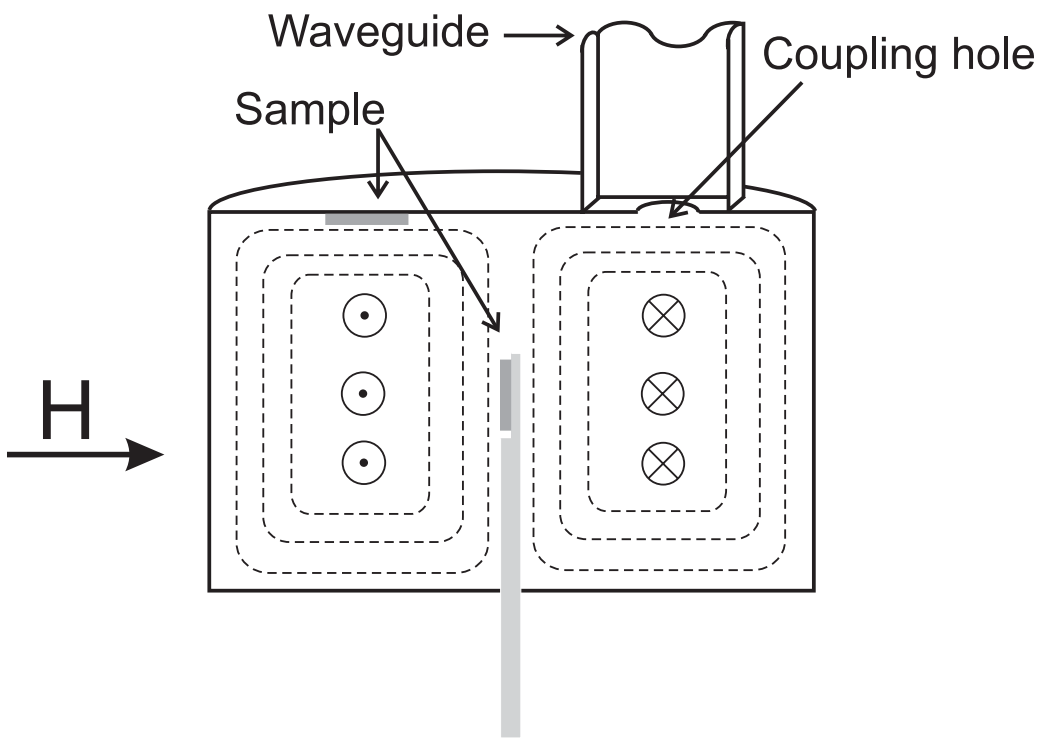

Figure 3.12: Cross-section of a cylindrical microwave cavity operating in the TE_{011} (doughnut) mode. The distribution of the rf **h**-field for this mode is indicated by the dashed lines (in the drawing plane) and the distribution of the rf **e**-field is indicated by dots/crosses pointing out of the drawing plane. The sample is mounted in positions where the **h**-field has a maximum. The position on the top of the cavity is used for measurements with the applied H field parallel to the sample plane, and the other position in which the sample is mounted on a quartz rod is used for the out-of-plane measurements in which the applied field H is directed out of the sample plane.

in the beam therefore undergo velocity-modulation. The phase of this modulation can be chosen in such a way that, when the beam passes through the cavity the second time, it gives up the energy required to maintain the rf oscillation. The electron beam is turned around by the negative repeller (negative with respect to the cathode). The anode is at the same potential as the cavity, and the repeller plate is located behind the cavity grids. The output frequency is primarily determined by the geometry of the cavity inside the vacuum tube and to a lesser extent ($\sim$ 100 MHz) by the repeller voltage.

The magnetic sample of interest was mounted inside a microwave cavity which was tuned to resonance with the microwave frequency of the source (klystron), as illustrated in Fig. 3.12. The microwave absorption was measured by monitoring the

power reflected from the microwave cavity using a diode detector (see Fig. 3.11). When the magnetic sample undergoes ferromagnetic resonance the microwave losses are increased, the effective Q-factor of the cavity decreases, and the reflected power changes slightly.

The microwave cavity was placed between the pole pieces of a large electromagnet (Varian 3800). This magnet is capable of producing magnetic fields up to 29 kG in a 2.5 cm gap. Most cavities were cylindrical and operated in the TE_{011} mode as shown in Fig. 3.12. The subscripts of the mode identify the standing wave pattern and represent the number of nodes in the angular, radial, and longitudinal directions, respectively [81, 82]. The **h**-field distribution of the TE_{011} mode, shown in Fig 3.12, is torus shaped (doughnut mode). The cavity quality factor is defined as

$$Q = 2\pi \frac{\text{stored energy}}{\text{energy dissipated per cycle}} = \frac{f}{\Delta f}, \tag{3.13}$$

where f and Δf are the frequency and the half power frequency linewidth of the cavity absorption. Usually the quality factor of the cavity was $Q \sim 4000$, its value is given by internal and external losses:

$$\frac{1}{Q} = \frac{1}{Q_{\text{int}}} + \frac{1}{Q_{\text{ext}}}. \tag{3.14}$$

Q_{int} is limited by mode perturbation caused by the inserted sample, cavity imperfections, and microwave losses due the finite conductivity of the cavity walls which were made out of brass. Q_{ext} is determined by the size of the cavity coupling hole (see Fig. 3.12). The sample absorption contributes to the internal losses, and one can write

$$\frac{1}{Q_{\text{int}}} = \frac{1}{Q_{\text{wall}}} + \frac{1}{Q_{\text{S}}}. \tag{3.15}$$

The coupling coefficient for microwaves incident on the cavity is given by

$$\frac{1}{\beta} = \frac{P_L^{\text{int}}}{P_L^{\text{ext}}} = \frac{Q_{\text{ext}}}{Q_{\text{int}}} = \frac{Q_{\text{ext}}}{Q_{\text{wall}}} + \frac{Q_{\text{ext}}}{Q_{\text{S}}}, \tag{3.16}$$

where P_L^{ext} and P_L^{int} are the microwave power losses due to leakage through the coupling hole and eddy currents in the walls of the cavity and sample absorption, respectively. The ratio of the amplitudes of the reflected wave to the incident wave is given by

$$\frac{\mathbf{e}_R}{\mathbf{e}_0} = \frac{\beta - 1}{\beta + 1}, \tag{3.17}$$

where $\mathbf{e}_R$ and $\mathbf{e}_0$ are reflected and incident amplitudes of the electric field. According to Eqs. 3.15 and 3.16 the coupling can be spit into a field independent part $\frac{1}{\beta_0} = \frac{Q_{\rm ext}}{Q_{\rm wall}}$ and a part that depends on the losses in the sample $\frac{1}{\beta_S} = \frac{Q_{\rm ext}}{Q_{\rm S}}$. The absorption due to FMR of the magnetic sample decreases $Q_{\rm S}$

$$\frac{1}{Q_{\rm S}} = \kappa\chi''(H), \tag{3.18}$$

where $\chi''(H)$ is the imaginary part of the rf susceptibility and κ is the cavity filling factor of the sample, defined as ratio of the microwave energy stored in the sample to that in the cavity. Assuming that the film is much thinner than the skin depth ($t_F \ll \delta$) one can write

$$\kappa = \frac{\Delta S t_F \langle h^2_{\rm max}\rangle}{\frac{1}{8\pi}\int_{cav}\langle h(\mathbf{r})^2\rangle d^3r}, \tag{3.19}$$

where ΔS and t_F are sample area and thickness. $\langle h(\mathbf{r})^2\rangle$ is the time average of the $\mathbf{h}$-field intensity inside the cavity and $h_{\rm max}$ is the maximum field. The integral is carried out over the volume of the cavity. Typically κ is very small ($\sim 10^{-8}$) because the sample volume is very small compared to the cavity volume. This allows one to rewrite the coupling coefficient in Eq. 3.16 as

$$\beta = \frac{\beta_0}{1 + \beta_0 Q_{\rm ext}\kappa\chi''}. \tag{3.20}$$

The ratio $\frac{\mathbf{e}_R}{\mathbf{e}_0}$ for $\beta_0 Q\kappa\chi'' \ll 1$ can be approximated using a Taylor expansion

$$\frac{\mathbf{e}_R}{\mathbf{e}_0} \simeq f(x)\Big|_{x=0} + x\frac{df(x)}{dx}\Big|_{x=0} = \frac{\beta_0 - 1}{\beta_0 + 1} - \frac{2\beta_0^2 Q_{\rm ext}\kappa\chi''}{(\beta_0+1)^2}. \tag{3.21}$$

The first term of the reflected signal amplitude is a constant. The second term is proportional to the imaginary part of the susceptibility of the sample. Note that in the under-coupled case ($\beta_0 < 1$) FMR leads to an increase in the reflected power while for over-coupling ($\beta_0 > 1$) it leads to a decrease. The highest sensitivity is realized when β is close to 1, while at the same time maintaining a sufficient amplitude in the off-resonance reflected microwave field ($\frac{\mathbf{e}_r}{\mathbf{e}_0} \to 0$ for $\beta_0 \to 1$) to keep the detector response in the linear regime. Linearity of the microwave diode detector is well satisfied for detector output voltages $V_R \sim 150$ mV corresponding to ~ 5 mW incident microwave power. V_R is directly proportional to $\mathbf{e}_R$.

It is worthwhile to compare the sensitivity obtained by using a cavity to the sensitivity achieved if the sample is simply placed at the end of a shorted waveguide.

The power absorbed by the sample is given by $P_S = \frac{1}{2}\omega\chi''_\perp|\mathbf{h}|^2\Delta S t_F$, where ω is the microwave angular frequency [83]. For the change in the reflected amplitude due to FMR one has

$$\frac{\Delta \mathbf{e}_R}{\mathbf{e}_0} = \frac{4\pi}{c}\omega\chi'' t_F \frac{\Delta S}{S}, \tag{3.22}$$

where S is the area of the waveguide. Using $\beta_0 = 0.9$, sample area $\Delta S = 1$ mm^2, $Q_{\text{ext}} = 4000$, $\omega = 2\pi \times 24 \times 10^9$ s^{-1}, and the cavity and waveguide dimensions for 24 GHz radiation one arrives at the conclusion that the sensitivity using a cavity should be roughly 40 times larger than the sensitivity using the shorted waveguide configuration.

The klystron frequency was locked to the sample cavity frequency $\text{f}_{\text{klysron}}$=$\text{f}_{\text{cavity}}$. In this case the reflected amplitude is linearly proportional to the imaginary part of the transverse susceptibility χ''. This condition is achieved using a high gain and phase sensitive feedback loop operating at 60 kHz: The klystron output frequency was externally modulated by means of a 60 kHz oscillator. The microwave power that is reflected from the cavity has a minimum at $\text{f}_{\text{klysron}}$=$\text{f}_{\text{cavity}}$, and the signal at the diode detector contains only the second harmonic (120 kHz) of the 60 kHz frequency modulation for this condition. If $\text{f}_{\text{klysron}} \neq \text{f}_{\text{cavity}}$, however, the voltage at the microwave diode contains a 60 kHz correction signal, which is monitored by a phase sensitive detector (PAR lock-in) whose output is fed back to increase or to decrease (depending on its phase) the klystron's reflector voltage (see Fig. 3.11). This closes the loop driving the klystron back into the condition $\text{f}_{\text{klysron}} = \text{f}_{\text{cavity}}$. In addition, magnetic field modulation (at $\sim$ 80 Hz) and lock-in detection was used in order to improve the signal to noise ratio of the signal due to specimen absorption.

Using 3.21 the signal measured by the lock-in amplifier is

$$\text{Signal} = \frac{2\delta H V_R \beta_0^2 Q_{\text{ext}} \kappa}{(\beta_0+1)^2}\frac{\partial \chi''}{\partial H}, \tag{3.23}$$

where δH is the amplitude of the ac field modulation and V_R is the voltage measured at the microwave diode. This signal is proportional to the field derivative of the imaginary part of the sample rf susceptibility. A Hall probe was used to record the magnetic dc field as the field was swept through the resonance condition.

3.2.2 Spectrometer calibration

The Hall probe reading was calibrated using the nuclear magnetic resonance (NMR) of protons in H_2O, and the microwave frequency of the klystron was measured using

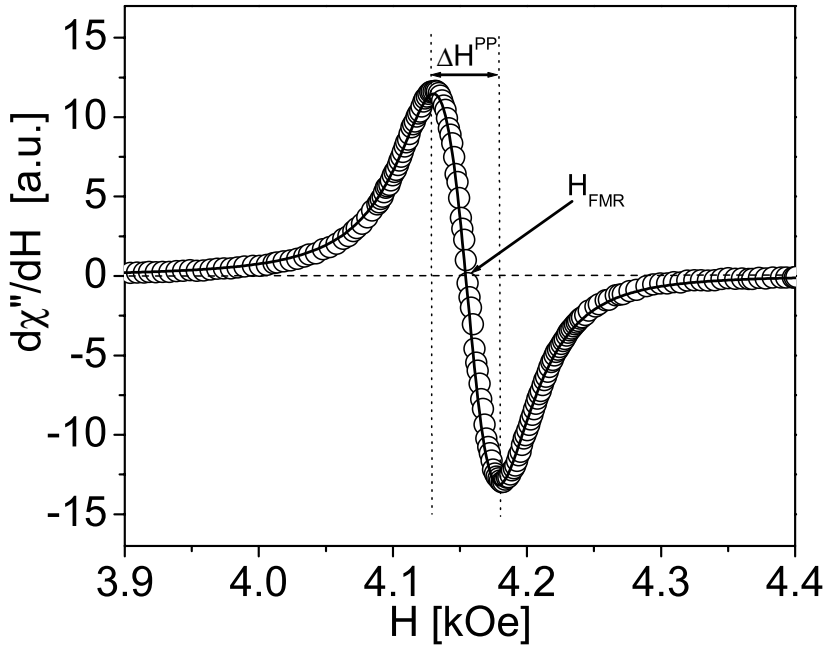

Figure 3.13: Typical FMR spectrum measured at 24 GHz using a 120Au/16Fe/GaAs sample. The open circles show the data and the solid line is a fit to Eq. 3.25. The peak-to-peak linewidth $\Delta H^{\rm PP} = 50$ Oe and the resonance field $H_{\rm FMR} = 4.15$ kOe are indicated on the diagram.

a calibrated cavity frequency meter. The frequency calibration was independently checked by means of the electron spin resonance (ESR) of the electron free radical species in diphenylpicrylhydrazyl (DPPH) characterized by $g = 2.0037$ [84].

3.2.3 Typical spectra

An FMR spectrum contains two important pieces of information: line position and linewidth. The line position is given by the internal fields, and their angular and frequency dependence allows one to determine magnetic anisotropies, effective magnetization, and g-factor. The linewidth is related to the magnetic damping (see Eq. 2.25) and the angular and frequency dependence of the linewidth provides information about the magnetic damping mechanism.

The line position and linewidth were usually extracted by fitting the FMR data to the derivative of an asymmetric Lorentzian. Asymmetry has to be considered because the coupling between the magnetic sample and microwave cavity can partly mix real

and imaginary parts of the susceptibility. The asymmetric absorption function is given by

$$\cos\epsilon\chi'' + \sin\epsilon\chi' \sim \frac{\Delta H\cos\epsilon + (H - H_{\rm FMR})\sin\epsilon}{\Delta H^2 + (H - H_{\rm FMR})^2}, \tag{3.24}$$

and the function used to fit the FMR data is its derivative with respect to H

$$\frac{d[\cos\epsilon\chi'' + \sin\epsilon\chi']}{dH} \sim -\frac{2(H - H_{\rm FMR})\Delta H\cos\epsilon}{[\Delta H^2 + (H - H_{\rm FMR})^2]^2} - \frac{\left[\Delta H^2 - (H - H_{\rm FMR})^2\right]\sin\epsilon}{[\Delta H^2 + (H - H_{\rm FMR})^2]^2}, \tag{3.25}$$

where ϵ denotes the mixing angle between dispersive and absorptive components and ΔH is the half width at half maximum (HWHM) of the absorption line. It is possible that the cavity absorption peak is a superposition of several modes operating at the same frequency due to perturbations introduced by the sample. When the sample undergoes FMR only the modes with large **h** field at the sample position are detuned while the feedback mechanism is sensitive to the overall absorption of the cavity and may lock to the spurious modes. This situation would lead to an admixture of dispersion into the absorption and cause asymmetric line shapes. Another possible reason for asymmetric lines is the skin effect, but the magnetic films studied in this thesis are very thin compared to the skin depth. The asymmetry was usually found to be weak ($\epsilon = 0 - 10^\circ$), as shown in Fig. 3.13.

For fairly symmetric lines the resonance field and linewidth are easy to determine. The resonance field is given by the zero crossing, and the peak-to-peak line width ΔH^{PP} is equal to the separation between the inflection points, see Fig. 3.13. The peak-to-peak linewidth is related to the HWHM ΔH by

$$\Delta H = \frac{\sqrt{3}}{2}\Delta H^{PP}. \tag{3.26}$$

3.3 Magneto-Optic Kerr Effect

The magneto-optic Kerr effect (MOKE) allows one to use light to determine the direction of the magnetization. The polarization vector of the incoming light rotates slightly upon reflection from a magnetic sample [57, 58], as described in section 2.6.

3.3.1 Static MOKE system

A high sensitivity MOKE system for longitudinal and transverse Kerr measurements was built at SFU as part of this thesis. A schematic diagram of this setup is shown in Fig. 3.14. The light source is an intensity stabilized laser diode (535 nm) with an anamorphic prism pair that is used to transform the elliptical beam profile (from the laser diode) into a nearly circular Gaussian beam. The magnetic sample is placed between two Glan-Thompson polarizers (P1 and P2) and the light beam is p-polarized (in the plane of incidence) and focussed onto the sample. The diameter of the focussed beam spot on the sample is $\sim 100\ \mu$m. The optical direction of the analyzer is oriented almost perpendicular to the plane of incidence. Behind the analyzer, P2, the light is focussed onto a high-gain low-noise Si hybrid detector. An interference filter (IF) with its center wavelength matched to the laser diode (535 nm) is placed in front of the detector to suppress ambient light. The sample is mounted on a X-Y-θ-ϕ stage which is installed on a motorized rotational drive. The translation allowed one to adjust the sample position while the tilt is used to adjust the plane of the sample to be perpendicular to the rotational axis. The sample is placed between the pole pieces of a four quadrant electromagnet which permitted fields up to 2 kOe to be oriented in an arbitrary direction in the film plane. It is therefore possible to measure both in-plane components of the magnetization (in longitudinal and transverse Kerr configurations) by switching the magnetic dc field from parallel to the optical plane of incidence to perpendicular to the optical plane. This is achieved by rotating the sample and field by 90°, but leaving the optical setup unchanged. The magnetic contrast (due to rotation of the polarization) is optimal in this setup because no optical components other than the sample are placed between polarizer and analyzer.

3.3.2 Time resolved MOKE microscopy

High resolution Kerr microscopes are less sensitive than the above system because they require an objective lens to be placed between polarizer and analyzer. In order

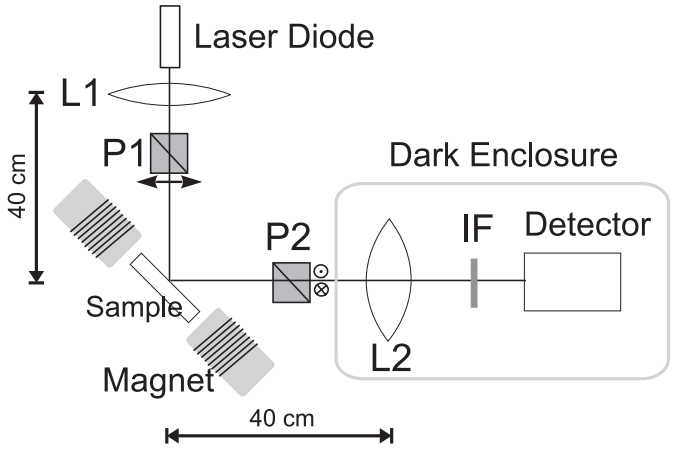

Figure 3.14: Experimental setup used for longitudinal and transverse MOKE measurements.

to achieve time resolution in Kerr effect imaging, two additional ingredients (compared to static microscopy) are necessary: (i) a pulsed light source and (ii) a synchronous means of magnetic excitation of the sample. A good review of time-resolved Kerr microscopy (TRMOKE) can be found in [85].

Spatial resolution requires scanning of either sample or laser beam. The magnetization of the sample is excited by a magnetic field pulse with a rise time of a few ps generated by an optical pulse (the pump beam). Time resolution is achieved by a stroboscopic technique using a pump and a probe beam. After the sample is excited (pumped) the sample is interrogated (probed) at a delay time τ using an ultrashort light pulse to measure the time evolution of the perpendicular component of the magnetization (polar MOKE). The source of the ultrashort light pulses is a commercial Titanium Sapphire (Ti:Sa) Laser system with ~ 100 fs pulse width, a repetition rate of ~ 80 MHz, and a wavelength of 800 nm. A beam splitter (BS) is used to split the light into pump (field pulse generation) and probe (Kerr effect measurement) beams, as illustrated in Fig. 3.15. The optical path length of the pump beam is variable, so that the probe pulses can be delayed with respect to the pump pulses (see Fig. 3.15). Most of the 1/f noise and non-magnetic signals are suppressed by using a lock-in technique. The 80 MHz pulse train used to generate the magnetic field pulses (the pump pulses) is modulated using an optical chopper operating at 1.5 kHz and the signal coming from the photodiodes is fed into a lock-in amplifier sensitive to this frequency; see Fig. 3.16 for an illustration of the pump probe pulse sequence. In this way it is possible to use low-bandwidth and low-noise photodiodes and amplifiers. The time

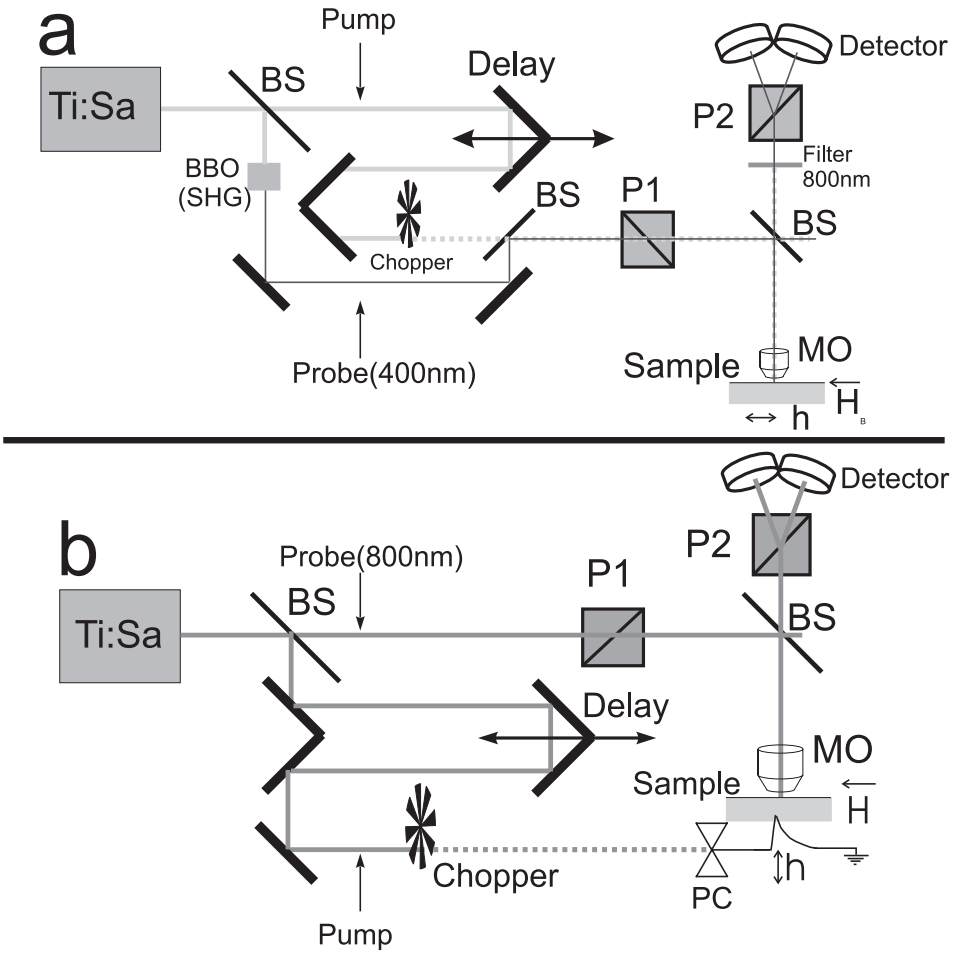

Figure 3.15: **(a)** Optical layout of the TRMOKE setup used at the University of Regensburg. A Coherent Ti:Sa laser system provides light pulses having 100 fs duration at a repetition rate of 76 MHz. The pump beam has a wavelength of 800 nm and the probe beam is frequency doubled (400 nm). Exciting field and external bias field are oriented in the sample plane. **(b)** Optical layout of the TRMOKE setup used at the University of Alberta. A Spectra Physics Ti:Sa laser system provides pulses having 100 fs duration at a repetition rate of 82 MHz. The pump and probe beams have a wavelength of 800 nm. The bias field is in the sample plane and the magnetic field pulses are generated in a photo conductive switch (PC) and are perpendicular to the plane of the sample. In both setups the delay line and the chopper are part of the pump beam circuit. Kerr effect measurements are performed using a Wollaston polarizer (P2) and two detectors operated in differential mode. Spatial resolution is achieved by scanning the sample under the microscope objective lens (MO).

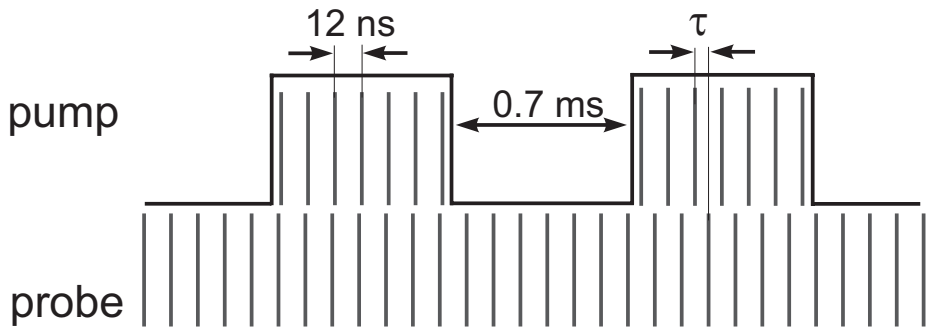

Figure 3.16: Pulse sequence for pump and probe beams. The 12 ns interval between individual pulses corresponds to the 80 MHz repetition rate of the laser. Pump and probe are delayed with respect to each other by a delay time τ and the pump pulses are chopped at 1.5 kHz.

interval between subsequent laser pulses is 12 ns (1/80 MHz) and sufficiently long for the magnetization to reach equilibrium after having been perturbed by a pump pulse.

Two different systems are used in this thesis for time resolved Kerr studies and the different methods of exciting the magnetization will be discussed in the following.

Schottky barrier as field source (Regensburg)

In the TRMOKE setup at the University of Regensburg the Schottky barrier of the Fe/GaAs interface is used to generate magnetic field pulses. When a biased Schottky barrier between the n-doped GaAs substrate and ferromagnetic film is illuminated by a light pulse, the resulting photo current gives rise to a circular magnetic field pulse in the plane of the sample [86], as illustrated in Fig. 3.17a. The photons from the pump beam (800 nm $\rightsquigarrow$ 1.54 eV) create electron-hole pairs in the semiconducting substrate beneath the magnetic film. A photo current is generated when electrons and holes are spatially separated by an electric field. In the absence of an externally applied bias voltage the band curvature (built-in voltage) at the Fe/GaAs^{n} interface separates electrons and holes, thereby generating a photo current directed perpendicular to the interface. This photocurrent can be enhanced by a factor of 4 by applying a voltage to reverse bias the Schottky diode, and hence sweep out the carriers from the depletion region faster [87]. The macroscopically measured pump current is about 20 mA [86]. Assuming a Gaussian spatial distribution for the current (corresponding to the pump beam intensity profile) and using the rise and fall times of the current

pulse (determined from the time dependent reflectivity of the Schottky barrier) the amplitude of the field pulse was estimated to be ~ 25 Oe [87]. The current pulse rises to its full amplitude within a few ps and the fall time was estimated to be ~ 120 ps without bias and less than 50 ps when applying a reverse bias voltage larger than 1 V [87].

A n^+-doped GaAs$(001)^{n^+}$ wafer (5×10^{19} cm^{-3} carriers) was covered with a n-doped GaAs buffer layer (5×10^{17} cm^{-3} carriers) deposited using metal organic vapor deposition (MOCVD). The lower doping level in the buffer layer ensured a high Schottky barrier at the Fe/GaAs interface. At the same time the n^+-doping of the substrate allowed easy formation of an ohmic contact to a gold wire on the other side of the wafer using an InGa eutectic solder [88], as shown in Fig. 3.17a. The best Schottky diodes are obtained when the GaAs wafers are not annealed after hydrogen cleaning. Even then the Fe/GaAs Schottky barriers were found to be leaky with ideality factors around $\sim$ 1.1 and barrier heights of ~ 0.6 eV. Similarly poor characteristics of Fe/GaAs Schottky diodes have been reported by other groups (using different preparation techniques) [89, 90, 91]. Therefore, it appears likely that Fe/GaAs^n Schottky barriers are intrinsically leaky.

In order to allow straightforward optical separation of the reflected pump and probe beams, the probe beam is frequency doubled in a Barium Beta-Borate (BBO) crystal and recombined with the pump beam using a dielectric mirror. Both, the pump beam (800 nm) and the probe beam (400 nm) are then fed into a polarization maintaining microscope (Zeiss Axiomat) and focussed by the same objective lens, as illustrated in Fig. 3.17a. The polarization changes of the reflected probe beam are detected using a Wollaston polarizer and diode detectors operated in a differential mode.

Strip line as a field Source (Edmonton)

In the measurements carried out at the University of Alberta in the group of Professor Mark Freeman a microwave transmission line is used to generate the magnetic pump field pulses. The wave guide (slot line) is connected to a reverse biased GaAs photoconductive switch (PC). The pump beam illuminates the PC switch, and generates a current pulse which travels down the waveguide discharging the capacitance of the biased slot line. The conductors of the waveguide are deposited on a thin glass substrate and the gap between the conductors is tapered down to 10 μm in width in

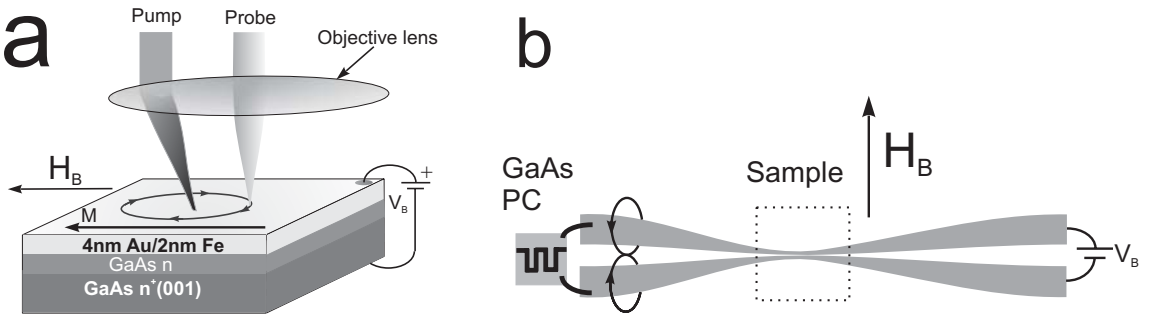

Figure 3.17: (**a**) Exciting field generated by the Fe/GaAs Schottky diode. The pulsed magnetic field is circular and lies in the plane of the sample. (**b**) Waveguide used to generate the magnetic pump field at the University of Alberta. A GaAs based photo conductive switch (PC) is attached to the Au waveguide by short Indium wires and the gap of the waveguide provides optical access to the sample. The orientation of the magnetic bias field, H_B, is indicated in both configurations.

order to maximize the pump field intensity. The magnetic film side of the Fe/GaAs sample is pressed directly onto the waveguide, and the time evolution of the magnetization is monitored through the (waveguide supporting) glass plate in the region of the 10 μm wide gap of the slot line (see Fig. 3.17b). In this configuration the pump field is mainly oriented perpendicular to the film plane. Due to the presence of the waveguide supporting glass plate (0.5 mm thickness) between the microscope objective lens and the magnetic film, the spatial resolution is limited to ~ 2 μm. This setup delivers magnetic field pulses oriented perpendicular to the film plane with an amplitude of ~ 20 Oe, and rise and fall times of 10 ps and 100 ps, respectively.

Chapter 4

Damping in Au/Fe/GaAs Multilayers

In this chapter the static and dynamic properties of Au/Fe/GaAs magnetic single layers and Au/Fe/Au/Fe/GaAs magnetic double layers will be presented. It will be shown that the magnetic double layers are affected by an additional relaxation mechanism that can be described by a spin-pump and spin-sink model.

4.1 Sample Growth

The preparation of the Au/Fe/GaAs(001) film structures was carried out by means of Molecular Beam Epitaxy (MBE). Semi-insulating epi-ready GaAs(001) wafers were used as templates for the growth of Fe. The GaAs substrates were mostly cleaned by hydrogen cleaning (see section 3.1.1 for details) and subsequently annealed at 600 °C. The annealing process was monitored by means of Reflection High Energy Electron Diffraction (RHEED) until a well defined (4×6) reconstruction appeared [67].

All metallic films were deposited at RT from thermal sources at base pressures less than 2×10^{-10} torr and deposition rates of ~ 2 ML/min. The film thicknesses were monitored by means of a quartz crystal microbalance and RHEED intensity oscillations.

Fe(001) has a lattice constant that is only 1.4% smaller than the size of the half unit cell of GaAs(001) and therefore the in-plane epitaxial relation is $[100]_{\mathrm{Fe}} \parallel [100]_{\mathrm{GaAs}}$. From the size of this mismatch one can anticipate that the critical thickness for the formation of misfit dislocations is about 10 nm [92, 93]. RHEED oscillations

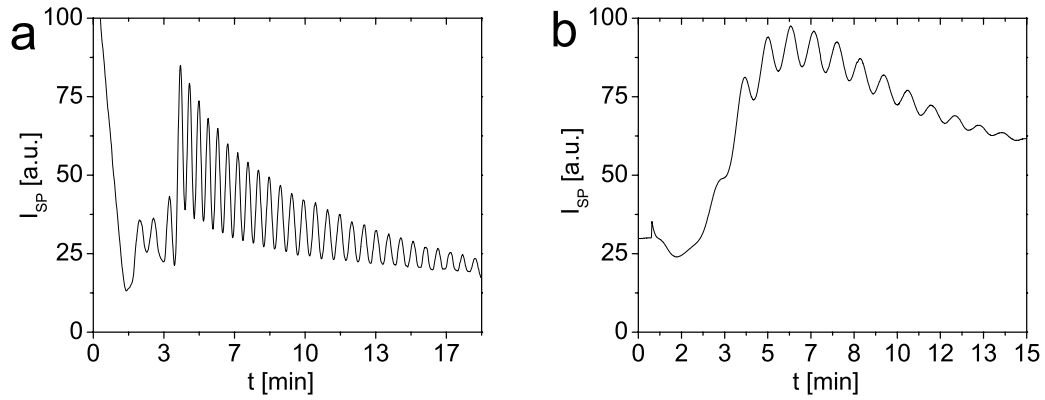

Figure 4.1: RHEED intensity oscillations of **(a)** 30 ML Fe on GaAs(001) and **(b)** 20 ML Au on 15Fe/GaAs(001).

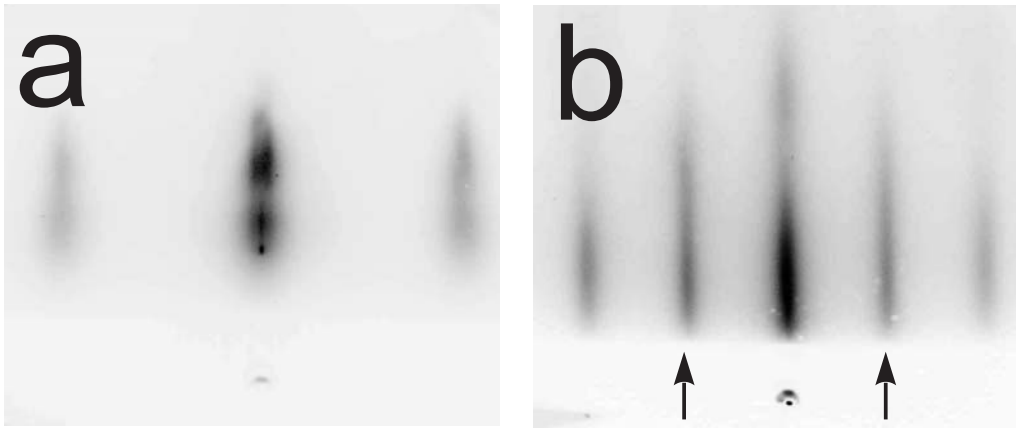

Figure 4.2: RHEED pattern of **(a)** a 15Fe/GaAs(001) surface with the electron beam oriented along the $\langle 110 \rangle_{\mathrm{Fe}}$ direction and **(b)** a 20Au/15Fe/GaAs(001) surface with the primary beam oriented along the $\langle 100 \rangle_{\mathrm{Au}}$ direction. Note that additional streaks appear (indicated by arrows) between the zeroth and first order diffraction streaks due to the 2×2 reconstruction of As that behaves like a surfactant.

during the growth of Fe on GaAs(001) were visible for up to 50 ML indicating an excellent quasi layer-by-layer growth (see Fig. 4.1a). During the initial stages of growth the RHEED oscillations are weak, but after deposition of roughly 3 atomic layers, a continuous film is formed [94] and the intensity of the specular spot as well as the amplitude of the RHEED oscillations increase dramatically, as shown in Fig. 4.1a. All of the Fe samples that were studied were thicker than 7 ML. This avoided complexities that might be related to the initial phase of the growth. X-ray Photoemission Spectroscopy (XPS) measurements indicated that during the Fe

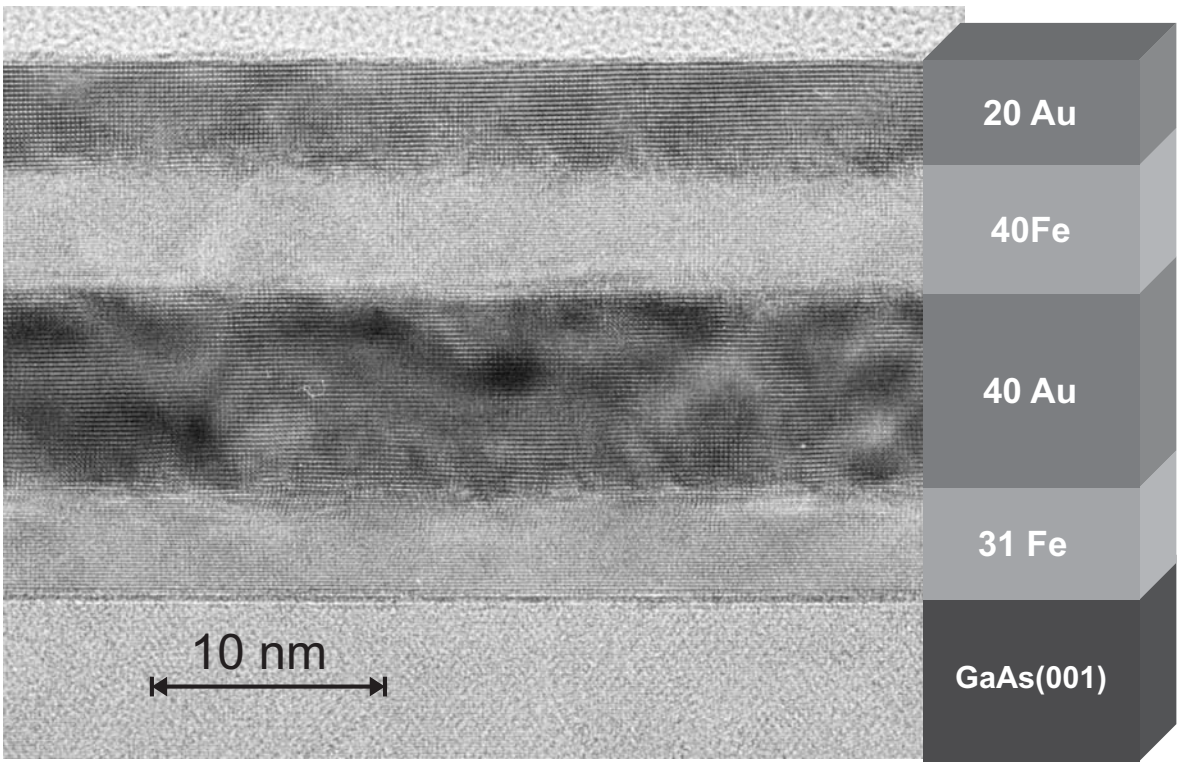

Figure 4.3: High resolution cross-sectional TEM image of a 20Au/40Fe/40Au/31Fe/GaAs multilayer. The sample was tilted by 1° to enhance the contrast between the Au and Fe layers.

deposition on GaAs, approximately 0.6 ML of As segregated on top of the Fe film [67]. After deposition of additional metallic layers the same amount of As was found on the surface. This implies that the As atoms are floating and act as a surfactant; i.e. no As stays inside the metallic layers or interfaces. The RHEED intensity oscillations for Au on Fe/GaAs were visible for up to 20 atomic layers, as shown in Fig. 4.1b. Due to the presence of As atoms at the surface the RHEED diffraction patterns of Au(001) always showed a 2×2 reconstruction instead of the usual 5×1 reconstruction, as illustrated in Fig. 4.2b. The lattice mismatch between Fe(001) and Au(001) is only 0.5% with $\langle 110 \rangle_{\mathrm{Au}} \parallel \langle 100 \rangle_{\mathrm{Fe}}$. The presence of RHEED intensity oscillations for all layers suggests that the roughness is confined to 3 atomic layers across distances of the order of 100 nm. This was confirmed using high resolution cross-sectional transmission electron microscopy (XTEM). Fig. 4.3 shows an atomic resolution XTEM image of a Au/Fe multilayer grown on GaAs(001). The thicknesses obtained by counting the individual atomic layers from the TEM image agrees perfectly with the thicknesses

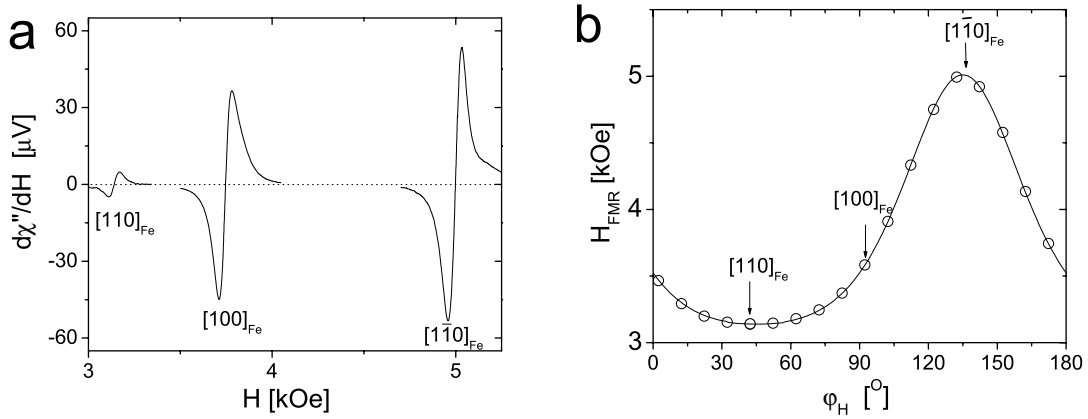

Figure 4.4: **(a)** Typical FMR spectra measured at 23.9 GHz with the applied field oriented along the $[110]_{\mathrm{Fe}}$, $[100]_{\mathrm{Fe}}$, and $[1\bar{1}0]_{\mathrm{Fe}}$ directions on a 20Au/10Fe/GaAs(001) sample. The low peak intensity along the $[110]_{\mathrm{Fe}}$ direction is due to the fact that the rf driving field inside the microwave cavity was almost parallel to the $[110]_{\mathrm{Fe}}$ direction and was therefore very ineffective at exciting the magnetization since for this case **M** and **h** were almost parallel. **(b)** ($\circ$) symbols represent the measured in-plane angular dependence of the resonance field H_{FMR}, where φ_H is the angle of the applied field measured with respect to the $[100]_{\mathrm{Fe}}$ direction. The solid line is the theoretical dependence which was calculated using the following magnetic parameters as fitting coefficients: $K_1 = 1.8$ erg/cm^3, $K_U = -8.4$ erg/cm^3, and $4\pi M_{\mathrm{eff}} = 16.5$ kOe (the g factor was fixed at $g = 2.09$ for this fit).

determined from the RHEED intensity oscillations observed during the film growth. As expected from the small lattice mismatch, very few dislocations are observed in XTEM, with an average separation of approximately 80 nm.

4.2 Magnetic Properties of Au/Fe Single Layers

FMR and MOKE were used to determine the magnetic properties of the Fe layers directly grown on the GaAs. A series of 4 magnetic single layer samples was prepared: 20Au/nFe/GaAs(001), where the integers represent the number of atomic layers and n was 8, 11, 16, and 31 ML. The FMR absorption peaks were narrow and symmetric Loretzian lines, as illustrated in Fig. 4.4a.

Film	$K_1^{\|,\mathrm{B}}[10^5 \frac{\mathrm{erg}}{\mathrm{cm}^3}]$	$K_1^{\|,\mathrm{S}}[10^{-2} \frac{\mathrm{erg}}{\mathrm{cm}^2}]$	$K_U^{\|,S}[10^{-2} \frac{\mathrm{erg}}{\mathrm{cm}^2}]$	$4\pi M_S$[kG]	$K_U^{\perp,S}[10^{-2} \frac{\mathrm{erg}}{\mathrm{cm}^2}]$
AuFeGaAs	4.3 ± 0.1	-3.5 ± 0.3	-14 ± 1	20.8 ± 0.2	88 ± 4
AuFeAu	4.6 ± 0.3	-4.5 ± 0.3		20.5 ± 0.3	90 ± 10

Table 4.1: Values of the interface (S) and bulk (B) contributions to the magnetic anisotropies determined from the data shown in Fig. 4.5. The interface anisotropies correspond to the sum of the contributions from both interfaces.

Magnetic Anisotropies

The angular dependence of the FMR field was used to determine the magnetic anisotropies, effective demagnetizing field $4\pi M_{\mathrm{eff}}$, and g-factor, as shown in Fig. 4.4b. It was possible to determine $4\pi M_{\mathrm{eff}}$ and g by fitting self-consistently data obtained on the same sample at different microwave frequencies. The g-factor was found to be $g = 2.09 \pm 0.01$, while the anisotropy values for all samples having different Fe thicknesses t_{Fe} are shown in Fig. 4.5a. In ultrathin films the interface contribution to the anisotropies is shared by all layers and consequently the effective anisotropies scale inversely with the film thickness t_{Fe} (see Eq. 2.3). This behavior is clearly observed in Fig. 4.5a where the effective anisotropies are plotted as a function of $1/t_{\mathrm{Fe}}$. The intercept with the y-axis corresponds to infinite thickness, and therefore represents the bulk anisotropy. The slope is related to the interface contribution of the anisotropy (see Fig. 4.5a and Tab. 4.1). The saturation magnetization can be obtained from the effective demagnetizing field for infinite thickness (bulk), i.e. $4\pi M_{\mathrm{eff}} = 4\pi M_S = 20.6 \pm 0.3$ kOe. This leads to $M_S = 1640 \pm 25$ emu/cm^3, which is very close to the bulk value expected for Fe (see Tab. 2.1).

The values for the in-plane anisotropies reported in Tab. 4.1 are in good agreement with results obtained by other groups [70, 95]. Brockmann et al. used a slightly different substrate preparation technique (sputtering at elevated temperatures); their value for $K_U^{\|,\mathrm{Fe/GaAs}}$ was 15% smaller, while their value for $K_1^{\|,\mathrm{Fe/GaAs}}$ was 20% larger than the the value shown in Tab. 4.1 [95]. The perceived value of $4\pi M_S$ can be affected by the tetragonal distortion of the film. Gordon et al. carried out X-ray absorption fine structure (XSAFS) measurements on Fe/GaAs(001), and showed that a 10 ML Fe film has a c/a ratio of 1.03 ± 0.02 [96]. Due to the magneto-elastic coupling this tetragonal strain results in an additional bulk-like anisotropy field perpendicular to the film surface. This strain anisotropy contributes to the effective demagnetizing

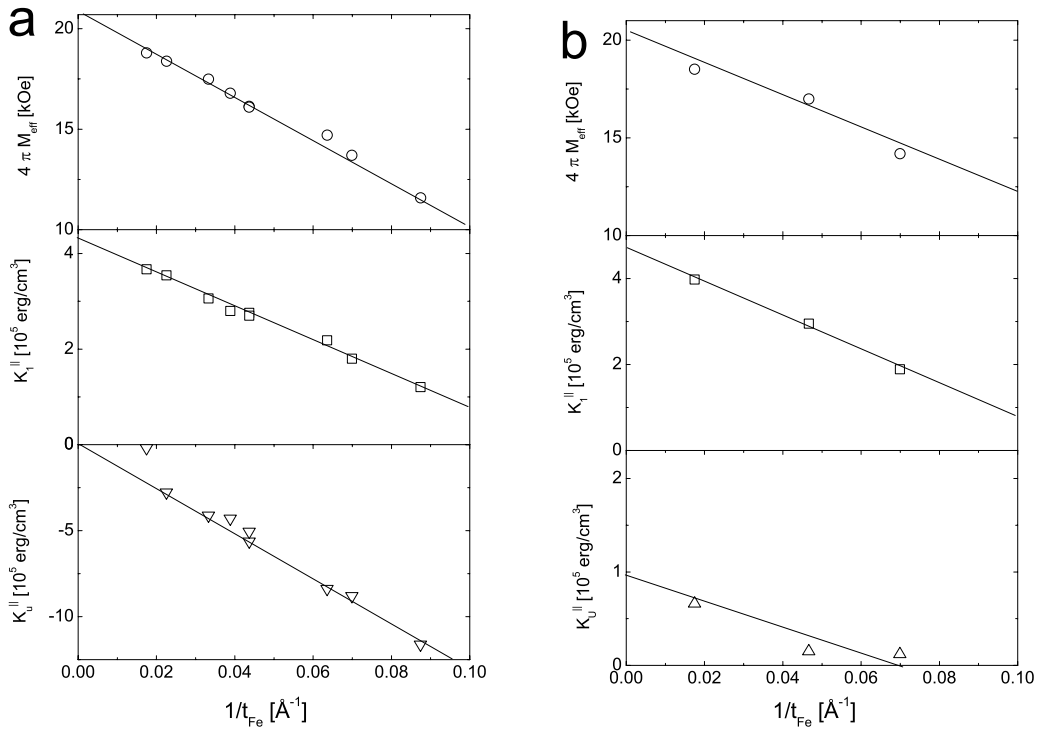

Figure 4.5: These plots show **(a)** the inverse thickness dependence of the in-plane anisotropies and effective demagnetizing field for Au/**Fe**/GaAs layers and **(b)** for the top Fe layer in Au /**Fe**/Au/Fe/GaAs structures. In **(b)** the presence of a bulk-like uniaxial anisotropy is very likely strain induced [70] with an easy axis parallel to the $[1\bar{1}0]_{\mathrm{Fe}}$ direction.

field [97]

$$4\pi M_{\mathrm{eff}} = 4\pi M_S - \frac{2K_U^{\perp,s}}{M_S t_{\mathrm{Fe}}} - \frac{2B_1(e_\perp - e_\parallel)}{M_S}, \tag{4.1}$$

where $e_\parallel$ and $e_\perp$ are the in-plane and perpendicular strain fields and B_1 is the first magneto-elastic coupling coefficient. For Fe $B_1 = -2.95 \times 10^7$ erg/cm^3 [97]. Recently, Thomas et al. [70] used high resolution x-ray diffraction to show that the strain in Fe films on GaAs remains constant for Fe thicknesses of up to 8 nm. The values for $e_\parallel$ and $e_\perp$ from [96] result in $2B_1(e_\perp - e_\parallel)/M_S = 1.1 \pm 0.5$ kOe and would lower the value for $4\pi M_S$ in Tab. 4.1 slightly. Considering the fact, however, that the value for $4\pi M_S$ in Tab. 4.1 is already close to the value expected for bulk iron, and given the size of the error bar on the c/a ratio from EXAFS measurements, it is likely that the strain anisotropy contribution is small.

Magneto-optic Kerr effect (MOKE) measurements showed that for samples with

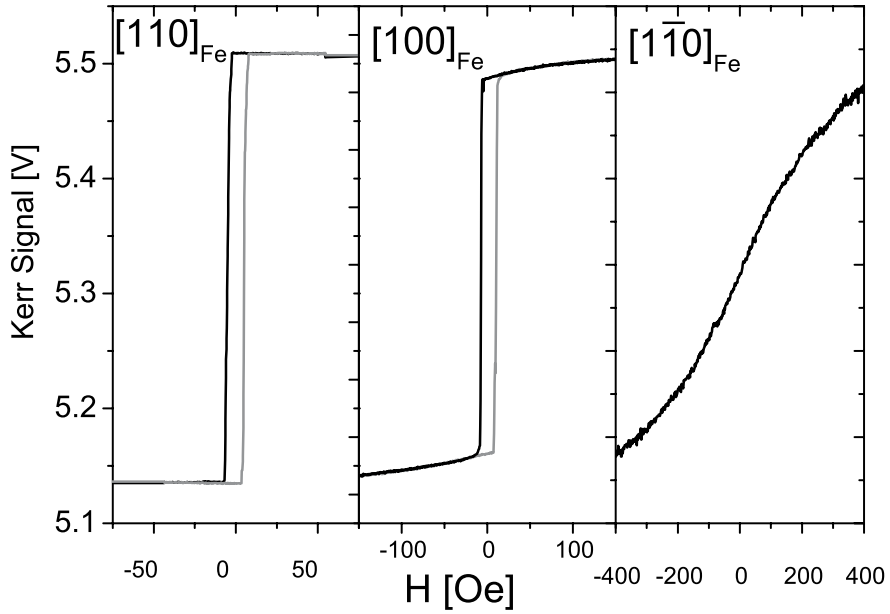

Figure 4.6: Static MOKE loops measured on a 20Au/15Fe/GaAs(001) sample with the magnetic field applied along the $[110]_{\mathrm{Fe}}$, $[100]_{\mathrm{Fe}}$, and $[1\bar{1}0]_{\mathrm{Fe}}$ directions. Note that the hard axis loop ($H \parallel [1\bar{1}0]_{\mathrm{Fe}}$) is not linear due to presence of $K_1^{\parallel}$ in addition to $K_U^{\parallel}$.

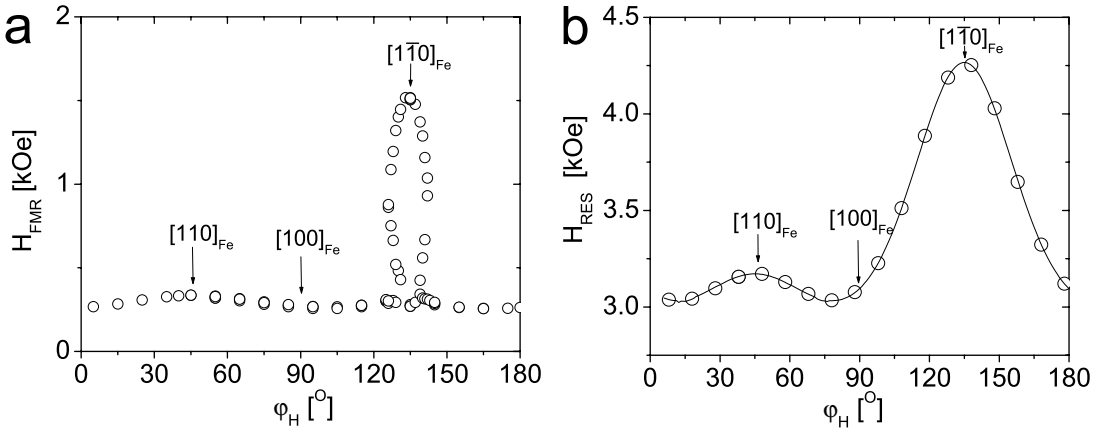

Figure 4.7: H_{FMR} as a function of the in-plane angle of the magnetic field, φ_H, for 20Au/15Fe/GaAs(001) measured at **(a)** 10.0 GHz and **(b)** 23.9 GHz.

Fe films thinner than 35 ML the $[110]_{\mathrm{Fe}}$ direction is the easy magnetic axis and the $[1\bar{1}0]_{\mathrm{Fe}}$ direction is the hard magnetic axis (see Fig. 4.6). This behavior can be easily understood from the in-plane angular dependence of the magnetic energy without an

applied field

$$\mathcal{E}(\varphi_M) = K_1^{\parallel} \sin^2 \varphi_M \cos^2 \varphi_M - K_U^{\parallel} \cos^2(\varphi_M - \varphi_U), \tag{4.2}$$

where $\varphi_U = -45°$. The minimum energy corresponds to $\varphi_M = 45°$, i.e. $\mathbf{M} \parallel [110]_{\mathrm{Fe}}$, and the maximum energy corresponds to $\varphi_M = -45°$ (i.e. $\mathbf{M} \parallel [1\overline{1}0]_{\mathrm{Fe}}$), provided that $K_U \geq K_1$. It is interesting to note that the smallest FMR field is measured with $\mathbf{H}$ applied along the $\langle 100 \rangle_{\mathrm{Fe}}$ direction (see Fig. 4.7) and does not coincide with the easy magnetic direction. The easy magnetic axis is determined by the global energy minimum, while the angular dependence of the FMR field corresponds to a constant stiffness (frequency) contour as a function of the applied field and field angle (see Fig. 4.8). If only one in-plane anisotropy is present (uniaxial or four-fold), then the FMR field minimum always coincides with the easy magnetic axis. The presence of K_1 and K_U with $\varphi_U = -45°$ also gives rise to 3 FMR peaks at low frequencies, as shown in Figs. 4.7 and 4.8.

Magnetic Relaxation

The linewidths of the FMR peaks were found to be very narrow and to scale linearly with the microwave frequency in parallel and perpendicular configurations with no appreciable zero frequency offset, as shown in Fig. 4.9a. These features are characteristic of Gilbert damping. α was determined from the slope of the linewidth as a function of the microwave frequency. The damping parameter was found to be $\alpha = 4.4 \pm 0.3 \times 10^{-3}$ and nearly independent of the film thickness and the orientation of the magnetization. This value is about double the intrinsic Fe bulk value (see Tab. 2.1). The enhanced damping is probably due to the modified electronic structure of the ultrathin film compared to the bulk in combination with impurity and interface scattering. Recently, Safonov and Bertram have shown that electron-magnon scattering caused by local perturbations in the spin-orbit interaction due to defects can result in an additional Gilbert damping [98].

Temperature dependence of anisotropies and relaxation

In the temperature range between RT and -200 °C the Gilbert damping was observed to be constant, and below -200 °C the linewidth increased rapidly, as shown in Fig. 4.9b. A similar behavior was observed in Ni bulk samples (see section 2.4.3) and can be explained by increased electron mean free path at low temperatures.

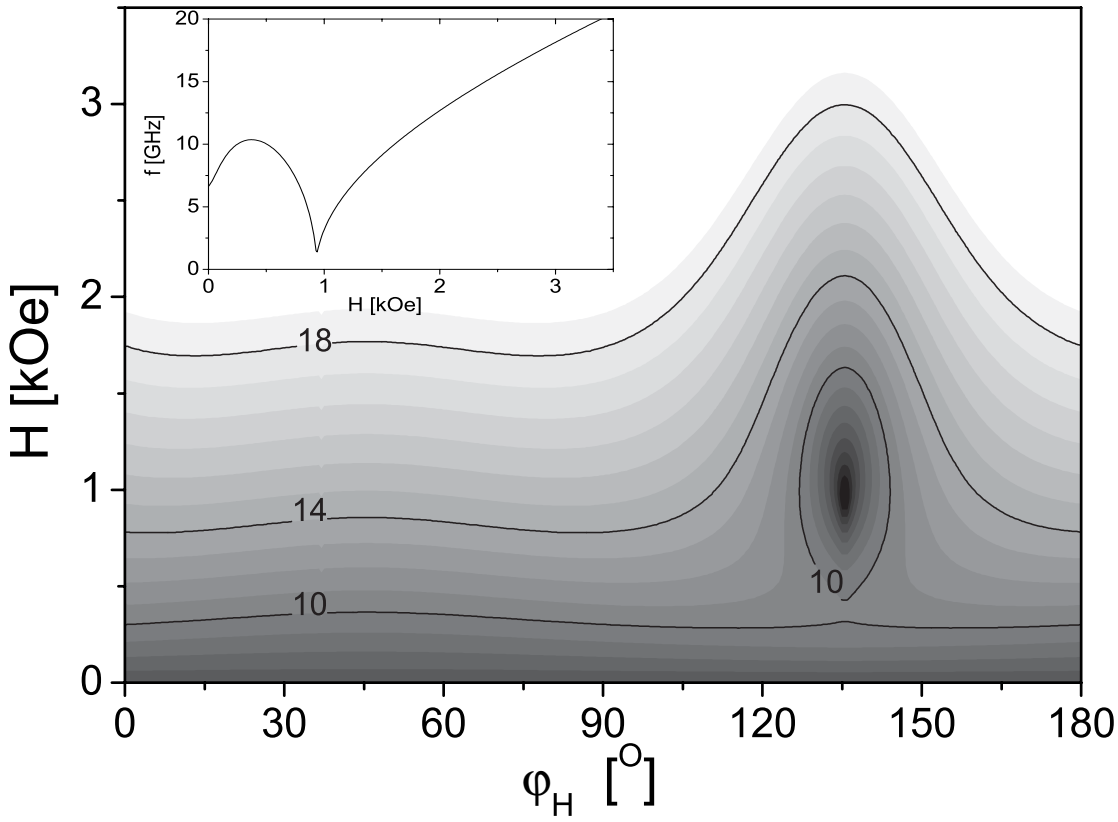

Figure 4.8: Calculated contour plot of resonance frequencies versus the in-plane applied field angle and field strength for the 20Au/16Fe/GaAs sample. White corresponds to $f \geq 18$ GHz and black is equivalent to $f = 0$ GHz. The black lines highlight the 18, 14, and 10 GHz contours. Note that the 10 GHz contour is not continuous and splits into an ellipse and a line around the hard axis giving rise to 3 separate FMR fields between 8 and 10 GHz, as observed in Fig. 4.7. This is further illustrated in the inset, where calculated resonance frequency as a function of bias field along the hard direction ($[1\bar{1}0]_{\mathrm{Fe}}$) with a misalignment of 0.2° (to break the symmetry) is shown.

Uniaxial and four-fold in-plane anisotropies exhibit a strictly linear temperature dependence in the range between RT and -200 °C and increase with decreasing temperature, as shown in Fig. 4.10.

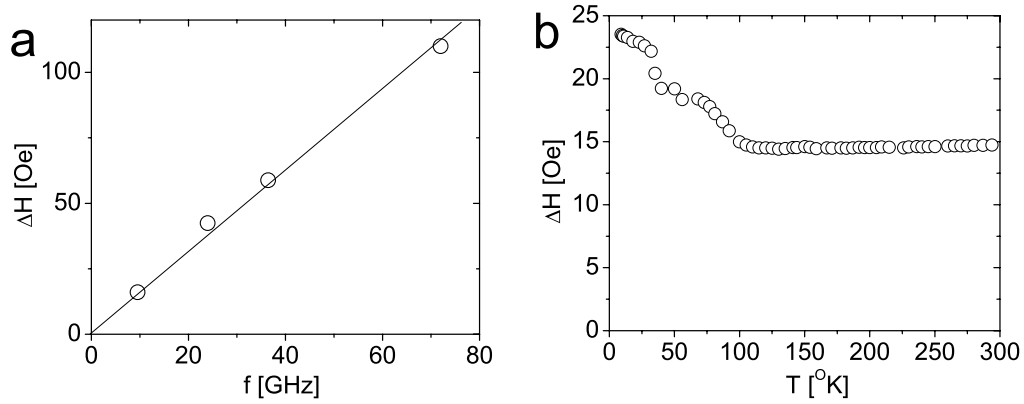

Figure 4.9: **(a)** Frequency dependence of the FMR linewidth for the 20Au/16Fe/GaAs sample. The magnetic field was applied along the $[100]_{\mathrm{Fe}}$ direction. **(b)** Temperature dependence of the FMR linewidth measured with the same sample at 10 GHz as a function of temperature. The magnetic field was applied along the $[110]_{\mathrm{Fe}}$ direction.

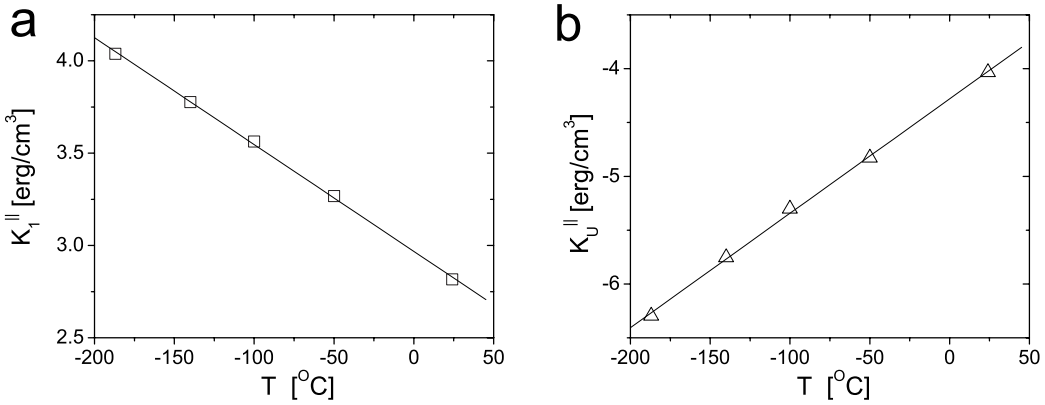

Figure 4.10: Temperature dependence of the in-plane anisotropies measured with a 20Au/18Fe/GaAs sample at 24 GHz **(a)** $K_1^{\parallel}$ and **(b)** $K_U^{\parallel}$.

4.3 Magnetic Double Layers

The intrinsic relaxation properties obtained for Au/Fe/GaAs single layer films enable one to test the influence of a second ferromagnetic layer on magnetic relaxation. Magnetic multilayers are a special case where the interaction between itinerant electrons and magnetic moments can lead to unprecedented and exciting effects in spin dynamics. The electric resistance of a magnetic double layer depends on the relative orientation of the magnetic moment of the two layers; this effect is called Giant

Magneto-Resistance (GMR). Berger [99, 100, 101] and Slonczewki [102, 103] pointed out that the inverse process can also take place. That is, the direction of the current flowing perpendicular to the interfaces can change the relative orientation of magnetic moments in magnetic double layers (parallel or antiparallel). Recently, this switching effect has been experimentally realized in point contacts [104, 105] and nano-pillars [106, 107]. Slonczewski [102] has shown that the flow of spin momentum that is carried by a current flowing perpendicular to the interfaces of a magnetic double layer system NM/F1/NM/F2/NM results in Landau Lifschitz like torques (see Eq. 2.5) acting on layers F1 and F2 and the sense of this torque depends on the direction of the current. Here NM stands for normal metal and F1,2 stand for a ferromagnetic metal. The magnetization in F2 is usually assumed to be fixed, while the magnetization in F1 is allowed to precess (free magnetic layer). Very high current densities lead to spin torques that can overcome the intrinsic damping torques and lead to spin instabilities and switching phenomena [103]. Spin instabilities in turn can lead to phase coherent emission of microwaves in the presence of a magnetic field. This phenomenon was recently observed by the Cornell and NIST groups [108, 109].

4.3.1 Berger's model

Berger's treatment of a current flowing perpendicular to the NM/F1/NM/F2/NM layer system differs from Slonczewski's approach: the magnetization in layer (F2) is assumed to be static and precession of the magnetization of the free layer F1 is explicitly included using a magnon occupation number. The itinerant electrons entering F1 cannot immediately assume the instantaneous direction of the precessing magnetization. This leads to an exchange torque directed towards the equilibrium axis and corresponds to an additional relaxation torque acting on the F1/NM interface. This torque is shared by the whole magnetic film due to exchange coupling. Conservation of the total angular momentum requires that spins in the normal metal layer be flipped. An electron spin in the NM layer has to flip from up to down as a magnon in FM is annihilated and vice versa. The rate equations for spin up and spin down electrons can be derived from Fermi's golden rule which includes the interaction with magnons [99]. This leads to a shift of the Fermi levels for spin up and spin down electrons $\Delta\mu = \Delta\mu^{\uparrow} - \Delta\mu^{\downarrow}$, and causes an additional relaxation torque which may be written as [99, 110]

$$\mathbf{H}^{\mathrm{Berger}} \sim (\Delta\mu + \hbar\omega)\hat{\mathbf{m}}_1 \times \hat{\mathbf{m}}_2, \tag{4.3}$$

where $\hat{\mathbf{m}}_{1,2}$ are the unit vectors of the magnetizations in layers F1 and F2. The absolute value and sign of $\Delta\mu$ are determined by the density and direction of the current flowing perpendicular to the interfaces. Note that the second term in Eq. 4.3 is proportional to the microwave frequency and is always positive. This term is not present in Slonczewski's model because it does not include the dynamic s-d interaction. This term is present even in the absence of a current flowing though the interfaces and represents an additional Bloch-Blombergen like interface damping [83].

4.3.2 Experimental test

Berger's predictions regarding additional interface damping can be tested by comparing the magnetic damping in the Au/Fe/GaAs single layer structures discussed in the previous section with the magnetic damping observed in magnetic double layer Au/Fe/Au/Fe/GaAs structures. The absence of extrinsic damping in the magnetic single layer samples allows one to isolate the effect of the second magnetic layer (F2) on the damping in the first magnetic layer F1. A series of double layer samples complementary to the single layer samples was grown: 20Au/40Fe/40Au/nFe/GaAs, where n was 8, 11, 16, 21, and 31. The Au spacer thickness was chosen such that the interlayer exchange coupling was very small but electron transport across the spacer remained ballistic. The electron mean free path in Au grown on an Fe/GaAs(001) template was found to be 38 nm, i.e. $\sim$ 190 ML Au [111]. The spin diffusion length in Au is much bigger than the electron mean free path and was estimated by Johnson to be $l_{\mathrm{sd}}^{\mathrm{Au}} \approx 1$ μm [112]. Therefore spin transport between the ferromagnetic layers F1 and F2 through the 8 nm thick Au spacer is unimpeded by electron scattering. Fig. 4.12a shows a typical FMR spectrum acquired from a double layer sample at 36.6 GHz. The two absorption peaks corresponding to the two layers (F1 and F2) are well separated (by $\sim$ 1 kOe) because the bottom and the top layer have different interface anisotropies and thicknesses. This allows one to measure a FMR spectrum of layer F1 while layer F2 is detuned from resonance and has a negligible precessional angle, and vice versa. The FMR linewidth in single and double layers was also observed to be only weakly dependent on the angle of the static magnetization (see Fig. 4.11b). The good agreement between the FMR fields of the magnetic single layer and the bottom layer in the corresponding double layer (see Fig. 4.11a) shows that the interlayer exchange coupling is negligible ($j_1 \leq 0.03$ erg/cm^3) and that the magnetic properties of the Au/Fe/GaAs film system are very reproducible.

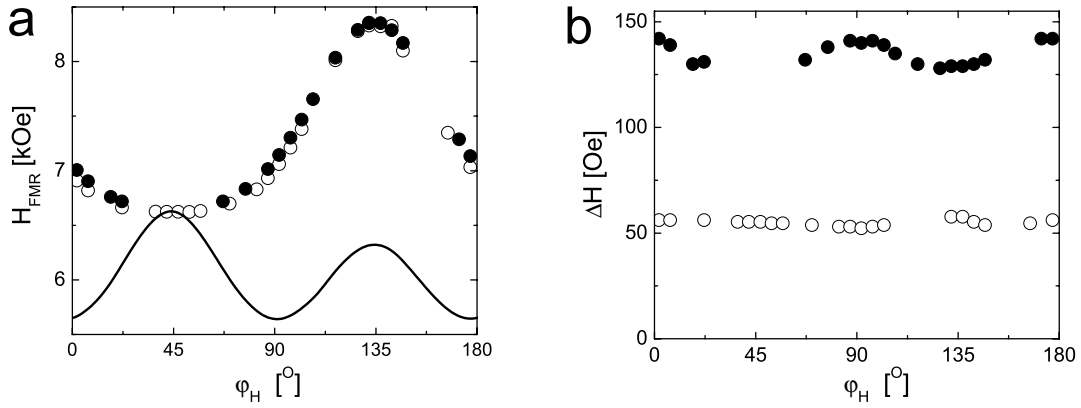

Figure 4.11: Angular dependence of **(a)** FMR field and **(b)** FMR linewidth in the 20Au/40Fe/40Au/**10Fe**/GaAs double layer and 20Au/**10Fe**/GaAs single layer structure measured at 36.6 GHz. (○) symbols represent the data for the **10Fe** single layer and (●) symbols represent the **10Fe** bottom layer in the double layer sample. The solid line in **(a)** corresponds to the resonance field of the 40Fe top layer in the double layer structure.

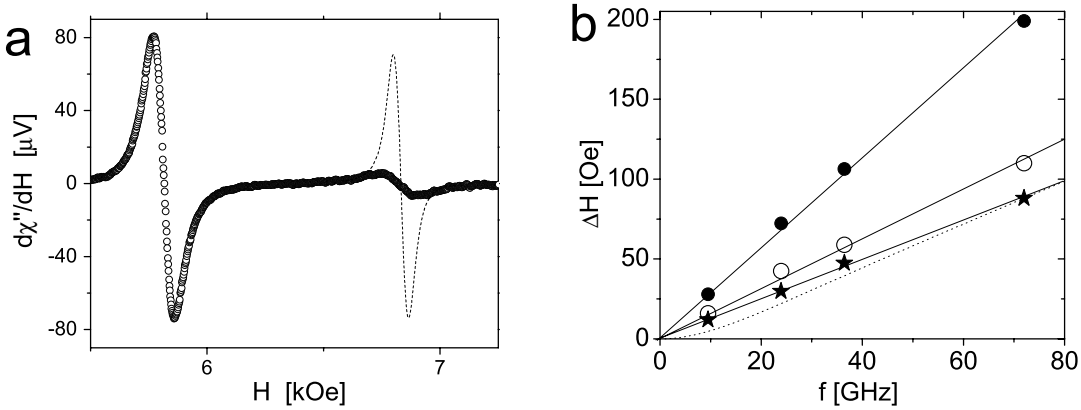

Figure 4.12: **(a)** FMR spectrum of the magnetic double layer 20Au/40Fe/40Au/11Fe/GaAs at 36.6 GHz with $\mathbf{M} \parallel [100]_{\mathrm{Fe}}$. The dashed line shows the FMR signal measured on the corresponding single layer sample 20/11Fe/GaAs(001). Note that the amplitude of the dashed line is $\sim 30\%$ bigger than expected from the ratio of the linewidths; this was caused by the different size of the samples. **(b)** Frequency dependence of ΔH for 16Fe in the 20Au/**16Fe**/GaAs (○) single layer and 20Au/40Fe/40Au/**16Fe**/GaAs (●) double layer with $\mathbf{M} \parallel [100]_{\mathrm{Fe}}$. The (★) symbols correspond to the difference of single and double layer linewidths and the dotted line shows the frequency dependence of the additional linewidth as predicted by Berger's theory scaled to fit the experimental data.

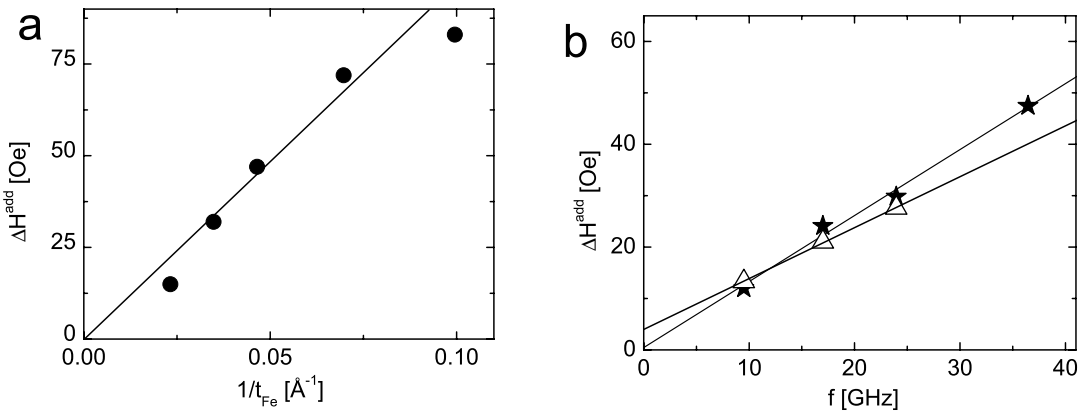

Figure 4.13: **(a)** ΔH^{add} as a function of $1/t_{\text{Fe}}$ measured at 36.6 GHz. **(b)** The in-plane (★) and out-of-plane (△) frequency dependence of ΔH^{add} in the 20Au/40Fe/40Au/16Fe/GaAs sample.

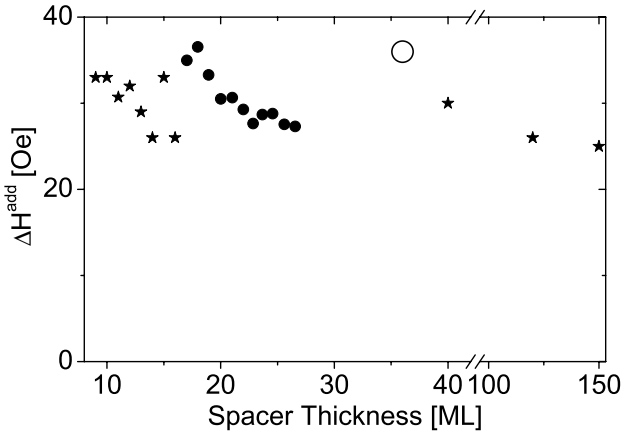

Figure 4.14: The additional FMR linewidth, ΔH^{add}, at 23.9 GHz as a function of the Au spacer thickness in 20Au/40Fe/8-150Au/16Fe/GaAs(001). (•) represent samples that were grown on a wedge (17-27ML), while (★) represent individually grown samples. The (○) symbol stands for a sample with a 40 ML Cu spacer.

All measurements showed that the FMR linewidth of F1 increased due to the presence of a second layer F2 (see Fig. 4.12). This increase ΔH^{add} scales inversely with the thickness of F1, as shown in Fig. 4.13a. The linear dependence of ΔH^{add} on $1/t_{\text{Fe}}$ indicates that the additional relaxation is an interface effect [110]. The additional FMR linewidth ΔH^{add} in both the parallel (H in-plane) and perpendicular (H perpendicular to the plane of the specimen) FMR configurations is approximately equal

in magnitude, linearly dependent on the microwave frequency, and has no appreciable zero frequency offset [13] (see Fig. 4.13b). For all double layers the additional Gilbert damping is found to be only very weakly dependent on the crystallographic direction. For the 10ML Fe film the average value is $\alpha_{10\mathrm{Fe}}^{\mathrm{add}} = 11.0 \pm 0.5 \times 10^{-3}$. This is almost triple the intrinsic Gilbert damping in the single Fe films, $\alpha^{\mathrm{int}} = 4.4 \pm 0.3 \times 10^{-3}$ (see Fig. 4.11b).

Berger's theory predicts that the strength of the additional damping depends on the average spin-flip relaxation time, conduction electron densities, and volume fractions of F1, F2, and NM (see Eq. (19) in [99] and Eq. (10) in [101]). As a consequence, the additional damping becomes a function of the respective volume fractions of F1, F2, and NM. For very thin Au spacers (20-30 ML) his predicted value for the additional damping strength is roughly double the experimentally observed value. Moreover, experimentally the additional damping is independent of the spacer thickness for Au spacers having thicknesses ranging from 12 to 150 ML (while keeping the thicknesses of F1 and F2 fixed), as can be seen in Fig. 4.14. In Berger's theory the magnitude of the additional damping depends on the ellipticity of the precession of the magnetization. This corresponds to a strange type of 'Bloch-Blombergen' damping with a frequency dependent relaxation parameter, as shown by the dotted line in Fig. 4.12b. This aspect of Berger's model is in disagreement with the experimental results, only simple Gilbert damping was observed.

4.4 Spin-Pump/Spin-Sink Theory

Brataas et al. [113] have generalized the theory of peristaltic charge pumping [114] by including a spin dependent scattering potential. Peristaltic charge pumping is based on the quantum mechanical scattering matrix approach introduced by Landauer and Büttiker [115]. Tserkovnyak et al. [116] showed that an interface Gilbert damping can be created by spin current flowing away from a ferromagnet (F) into adjacent normal metal reservoirs (NM). A complete derivation of the spin-pumping theory is given in appendix C. The emission of spin current is a consequence of the precessing magnetization. Scattering at the time dependent spin potential at the F/NM interface leads to a 'peristaltic' spin-pumping. The flow of the spin current is perpendicular to the F/NM interface, and oriented from F into NM. The direction of the spin

momentum carried away by this current is given by [116]

$$\mathbf{j}_{\text{spin}} = \frac{\hbar}{4\pi} A_r \hat{\mathbf{m}} \times \frac{d\hat{\mathbf{m}}}{dt} \ , \tag{4.4}$$

where $\hat{\mathbf{m}}$ is the unit vector of the magnetization in F and A_r is an interface scattering parameter. Note that the spin current is a tensorial quantity where each component is a vector. A_r is given by

$$A_r = \frac{1}{2} \sum_{m,n} \left\{ |r^{\uparrow}_{mn} - r^{\downarrow}_{mn}|^2 + |t^{\uparrow}_{mn} - t^{\downarrow}_{mn}|^2 \right\} \ , \tag{4.5}$$

where $r^{\uparrow\downarrow}_{mn}$ and $t^{\uparrow\downarrow}_{mn}$ are the electron reflection and transmission matrix elements at the NM/F interface for the spin up and spin down electrons of the transverse modes n, m at the Fermi level. Spin-pumping theory is an adiabatic concept, i.e. the electrons inside the NM spacer are always in equilibrium with the precessing magnetization at the NM/F interface. To illustrate this one can compare the time an electron spends in the NM spacer before it scatters at the NM/F interface with the time of a precessional period of the ferromagnet. At 10 GHz and for a 10 nm thick NM spacer the precessional period is 10^{-10} s while the spacer transit time is only $\tau = t_{\text{NM}}/v_F \sim 10^{-14}$ s. Therefore the adiabatic approximation is clearly valid.

Brataas et al. [113, 117] further showed that A_r can be evaluated from the interface spin mixing conductance $G^{\uparrow\downarrow}$ [118]. $A_r = \frac{h}{e^2} G^{\uparrow\downarrow} = S g^{\uparrow\downarrow}$, where $g^{\uparrow\downarrow}$ represents the dimensionless interface spin mixing conductivity. For interfaces with some degree of diffuse scattering, $g^{\uparrow\downarrow}$ is very close to the number of the transverse channels in the NM and is given by [117]

$$g^{\uparrow\downarrow} = \frac{k_F^2}{4\pi} = \frac{3^{2/3}}{4} \pi^{1/3} n^{2/3} \ , \tag{4.6}$$

where S is the area of the interface, k_F is the Fermi vector in NM, and n is the density of electrons per spin in the NM.

Once the spin current is generated, it traverses through the normal metal spacer, and is deposited at the NM/F2 interface. Zangwill et al. [119] recently showed that the transverse component of the spin current is entirely absorbed at the NM/F2 interface. For small precessional angles and assuming that $\mathbf{M_1} \parallel \mathbf{M_2}$ the spin current is almost entirely transverse with respect to the direction of the static magnetization. This means that the NM/F2 interface acts as an ideal spin-sink, and therefore provides a spin brake for the precessing magnetic moment in F1 [13, 120, 121]. The spin current

$\mathbf{j}_{\text{spin}}$ which takes spin momentum away from F1 has the form of Gilbert damping (compare Eqs. 4.4 and 2.8). The strength of the Gilbert damping can be evaluated from conservation of the total angular momentum

$$\mathbf{j}_{\text{spin}} - \frac{1}{\gamma}\frac{\partial \mathbf{M}_{\text{tot}}}{\partial t} = 0 \,, \tag{4.7}$$

where $\mathbf{M}_{\text{tot}}$ is the total magnetic moment in F1. After simple algebraical steps (see section C.10 for details), one obtains an expression for the dimensionless spin-pump contribution to the Gilbert damping constant in ultrathin films,

$$\alpha^{\text{sp}} = g\mu_B \frac{g^{\uparrow\downarrow}}{4\pi M_s}\frac{1}{t_1} \,, \tag{4.8}$$

where t_1 is the thickness of F1 and μ_B is the Bohr magneton. The inverse dependence of α^{sp} on the film thickness clearly testifies to its interfacial origin. Self-consistent calculations using the full LLG equations of motion including the exchange interaction torque have shown that the $1/t_1$ scaling of the damping due to spin-pumping is almost perfectly satisfied even if the magnetic film thickness significantly exceeds the exchange length [122]. Both layers, F1 and F2, act as mutual spin-pumps and spin-sinks. For small precessional angles the equation of motion for F1 can be written as [121]

$$\begin{aligned}\frac{\partial \mathbf{m}_1}{\partial t} = & - \gamma\left[\mathbf{m}_1 \times \mathbf{H}^1_{\text{eff}}\right] + \alpha_1\left[\mathbf{m}_1 \times \frac{\partial \mathbf{m}_1}{\partial t}\right] \\ & + \frac{g\mu_B g^{\uparrow\downarrow}}{4\pi M s t_1}\mathbf{m}_1 \times \frac{\partial \mathbf{m}_1}{\partial t} - \frac{g\mu_B g^{\uparrow\downarrow}}{4\pi M_S t_1}\mathbf{m}_2 \times \frac{\partial \mathbf{m}_2}{\partial t} \,,\end{aligned} \tag{4.9}$$

where $\mathbf{m}_{1,2}$ are the unit vectors along the magnetization directions in F1 and F2, and t_1 is the thickness of F1. The exchange of spin currents is a symmetric concept and the equation of motion for layer F2 can be obtained by the interchange of the indices $1 \rightleftarrows 2$ in Eq. 4.9. The third and fourth terms on the right hand side of Eq. 4.9 represent the spin-pump and spin-sink effects on the magnetization in F1. The fourth term is generated by the precession (spin-pump) of the magnetization in F2. For clarity, it is worthwhile to point out that the signs (+) and (−) in the third and fourth terms in Eq. 4.9 represent the spin current directions (F1 → F2) and (F2 → F1), respectively.

4.5 Other Models for Non-Local Gilbert Damping

4.5.1 Dynamic Exchange Coupling

Since the spin-pump model is a rather exotic concept for those working in magnetism, one would expect that there is a direct relation to a more common concept applicable to magnetic multilayers. The obvious choice is to describe these effects as a consequence of interlayer exchange coupling which has been studied extensively by a large group of people. Historically the interlayer exchange interaction has been treated only in the static limit [123]. Recently, this coupling has been studied for a time dependent magnetization. It has been found that the out-of-phase part of the exchange coupling results in magnetic damping [120, 121, 124, 125, 126]. It also has been shown that the spin-pumping theory is equivalent to a dynamic interlayer exchange coupling [124]. Šimánek and Heinrich have shown that the additional Gilbert damping is enhanced by the square of the Stoner factor [124] when compared to the spin-pumping theory. This calculation was based on the electron-electron interaction in an unpolarized electron gas. In a subsequent paper Šimánek considered the more realistic situation were the electron gas is polarized by the static component of the magnetization and concluded that the Stoner enhancement of the damping is only a small effect [125].

4.5.2 Breathing Fermi surface

The damping of magnetic double layers can be affected by the finite momentum life time of electrons in the NM spacer. Interlayer exchange coupling is based on the itinerant nature of the electrons. In a ferromagnet the energy of the electrons depends on the instantaneous orientation of the magnetic moments, and consequently the occupation number $n_{\mathbf{k},\sigma}$ of electronic states having energy $\varepsilon_{\mathbf{k},\sigma}$ changes during the precession of the magnetization, resulting in a 'breathing Fermi surface'. This concept was used in ferromagnetic bulk materials, as outlined in section 2.4.3; here it is applied to the NM spacer. The redistribution of electrons cannot be achieved instantaneously and the time lag between the instantaneous exchange field and the induced moment in the spacer layer can be described by the transverse spin relaxation time, τ_{sf}, which is proportional to the momentum relaxation time entering the conductivity [19]. In the limit of slow precessional motion the effective damping field on the magnetization

due to spin relaxation in the NM spacer can be evaluated as [120, 121],

$$\mathbf{H}_{\text{damp}} = \tau_{\text{sf}} \sum_{\text{k},\sigma} \delta(\varepsilon_{\text{k},\sigma}[\mathbf{M_1}] - \varepsilon_F) \left(\frac{\partial \varepsilon_{\text{k},\sigma}[\mathbf{M}_1]}{\partial \mathbf{M}_1} \right)^2 \frac{1}{t_F} \frac{\partial \mathbf{M}_1}{\partial t} , \tag{4.10}$$

where the sum is carried out per unit area. In this case, the damping field is proportional to the spin relaxation time τ_{sf}. This mechanism is therefore dependent on the conductivity and represents an additional contribution to the non-local damping. Note that the spin-pumping mechanism described in section 4.4 is independent of τ_{sf}.

4.6 Applicability of the Models

The spin-pumping and breathing Fermi surface theories predict strictly Gilbert damping. This feature was observed experimentally over a wide range of microwave frequencies [121, 127], as illustrated in Figs. 4.12b and 4.13b.

The validity of the spin-pumping theory can be tested by comparing calculations using Eqs. 4.9 with the experimental results. Fig. 4.15 shows two extreme situations. In the left panel of Fig. 4.15 the FMR fields of F1 and F2 are separated by a big margin, while in the right panel of Fig. 4.15 the FMR fields are the same. In the left situation one expects the full spin-pump contribution to the damping, and ΔH^{add} for layers F1 and F2 should scale inversely with their respective thicknesses. In the right panel the situation is symmetric; the net spin momentum current through both interfaces is zero, and the additional damping should disappear. This behavior was experimentally verified by measuring FMR spectra near the crossover of the FMR fields at 24 GHz, as shown in Fig. 4.16. Asymmetry of the resonance peaks (due to an admixture of χ' in χ'') was avoided by placing the sample at the end of a shorted waveguide instead of a resonant cavity for the FMR measurements. This way it was possible to analyze the superimposed FMR spectra corresponding to F1 and F2 without the asymmetry parameter ϵ described in section 3.2.3 (χ' corrections), thereby reducing the number of fitting parameters. Fig. 4.17 shows an example of such FMR data. The behavior from the spin-pump spin-sink theory was obtained by calculating FMR peaks using Eq. 4.9 and the magnetic parameters determined from FMR measurements. The excellent agreement between the experimental results and the spin-pumping theory is obvious in Fig. 4.17. In Fig. 4.16 the experimental and calculated spectra where analyzed using Loretzian line shapes. The experimentally observed disappearance of the additional damping around the crossing of the FMR fields of F1 and F2 is

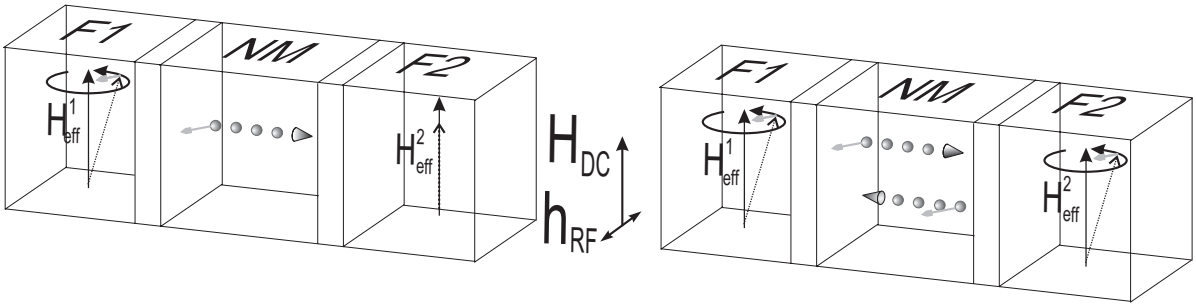

Figure 4.15: A cartoon of the dynamic coupling phenomenon. In the left drawing, layer F1 is at resonance and its precessing magnetic moment pumps spin current into the spacer, while F2 is detuned from resonance. In the right drawing, both films resonate at the same effective field, inducing spin currents of equal amplitude in opposing directions. The short arrows in NM indicate the instantaneous direction of the spin angular momentum $\propto \mathbf{m}_i \times \frac{d\mathbf{m}_i}{dt}$ carried away by the spin currents. The thin layers at the Fi/NM interfaces represent the regions where the spin current is absorbed.

extremely well described by the theory, as illustrated in Figs. 4.16b and 4.17. The excellent agreement between theory and experiment demonstrates the validity of the spin-pump and spin-sink concept which is described by Eq. 4.9. It follows that even in absence of static interlayer exchange coupling, the magnetic layers are coupled by the dynamic part of the interlayer exchange. The spin-sink effect at the NM/F interface starts to be inefficient only when the thickness of the NM spacer becomes comparable to the spin diffusion length [128]. In this case spin accumulation inside the NM layer acts as a resistance for the spin current in series with $1/g^{\uparrow\downarrow}$ and drives a back-flow of spins into F [129]. In the spin-pump spin-sink model it is expected that the additional damping is nearly independent of the Au spacer thickness considering the fact that the spin diffusion length in Au is of the order of 1 μm [112]. This was experimentally confirmed for thicknesses ranging from 2 to 30 nm (see Fig. 4.14). The static interlayer exchange coupling vanishes for Au thicknesses exceeding a mere 10 ML (2 nm). This rapid decay is caused by the Au/Fe interface roughness. One should point out that when the NM spacer thickness becomes comparable to the spin diffusion length, then the NM spacer can absorb a part of the spin current on its own [122, 130].

The quantitative comparison of the measured magnitude of the additional damping with the prediction from the spin-pumping theory is very favorable. First principles electron band calculations resulted in $g^{\uparrow\downarrow} \approx 1.42 \times 10^{15}$ cm^{-2} for a Cu/Co(111)

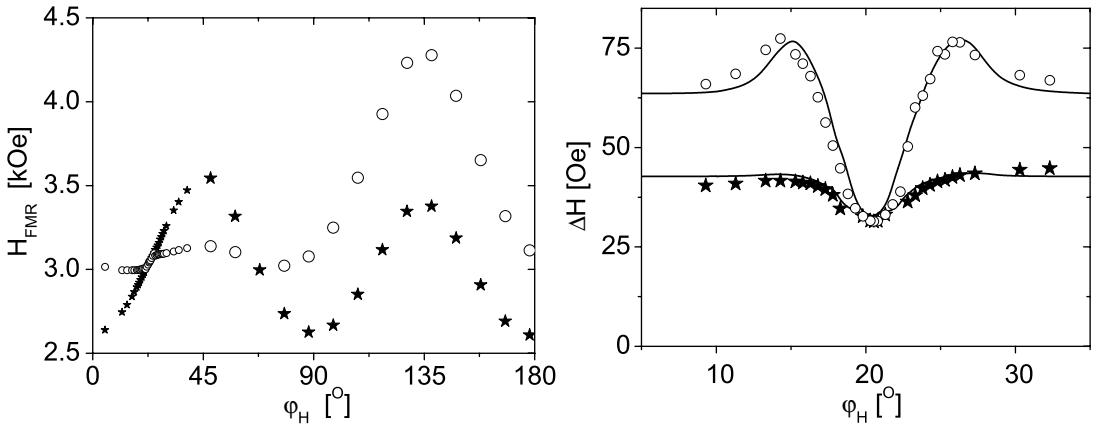

Figure 4.16: **(a)** The FMR fields for the layer F1(16Fe, shown by (○)) and the layer F2(40Fe, (★)) in the 20Au/40Fe/16Au/16Fe/GaAs(001) structure at 23.9 GHz as a function of the angle φ_H. The in-plane uniaxial anisotropy field in F1 leads to an accidental crossover at φ_H =20° and 55°. Notice that the FMR fields of F1 and F2 get locked together by the spin-pumping effect at the accidental crossover. **(b)** FMR linewidths of F1(○)) and F2(★)) around the crossover at $\varphi_H = 20°$. The black line was obtained from calculations using the spin-pumping theory with the appropriate anisotropies from Fig. 4.5, the intrinsic relaxation parameters $\alpha_{\rm int}^{\rm 40Fe} = 3.68 \times 10^{-3}$, $\alpha_{\rm int}^{\rm 16Fe} = 4.0 \times 10^{-3}$, and the spin-pumping coefficient $\frac{g\mu_B g^{\uparrow\downarrow}}{4\pi M_S} = 8.52 \times 10^{-10}$ cm^{-1}. Measured and calculated FMR spectra were analyzed using two Lorenzian lineshapes.

interface with 2 ML of alloying [118]. By scaling this value to Au by changing n in Eq. 4.6 and using $(k_F^{\rm Cu}/k_F^{\rm Au})^2 = 1.26$ [69] one obtains $\alpha_{\rm 16Fe}^{\rm sp} = 4.4 \times 10^{-3}$ for a 16 ML thick Fe film. This calculated additional contribution to the damping parameter agrees with the observed additional contribution to within 20% ($\alpha_{\rm 16Fe}^{\rm add} = 3.7 \pm 0.2 \times 10^{-3}$ measured at RT). Moreover, the additional damping observed for a sample with a Cu spacer is 20% bigger than the values obtained for Au spacers, as shown in Fig. 4.14. This is exactly what is expected considering that Cu has a higher density of conduction electrons than Au; i.e. based on the electron densities this enhancement, see Eq. 4.6, is expected to be 26%.

This qualitative and quantitative agreement between theory and experiment is striking. Calculations of the intrinsic damping in bulk metals have been carried out over the last three decades; none have produced a comparable agreement with experiments [131]. The reason is that the spin-pumping effect is calculated based on the free electron behavior in the NM; in contrast to this the intrinsic damping

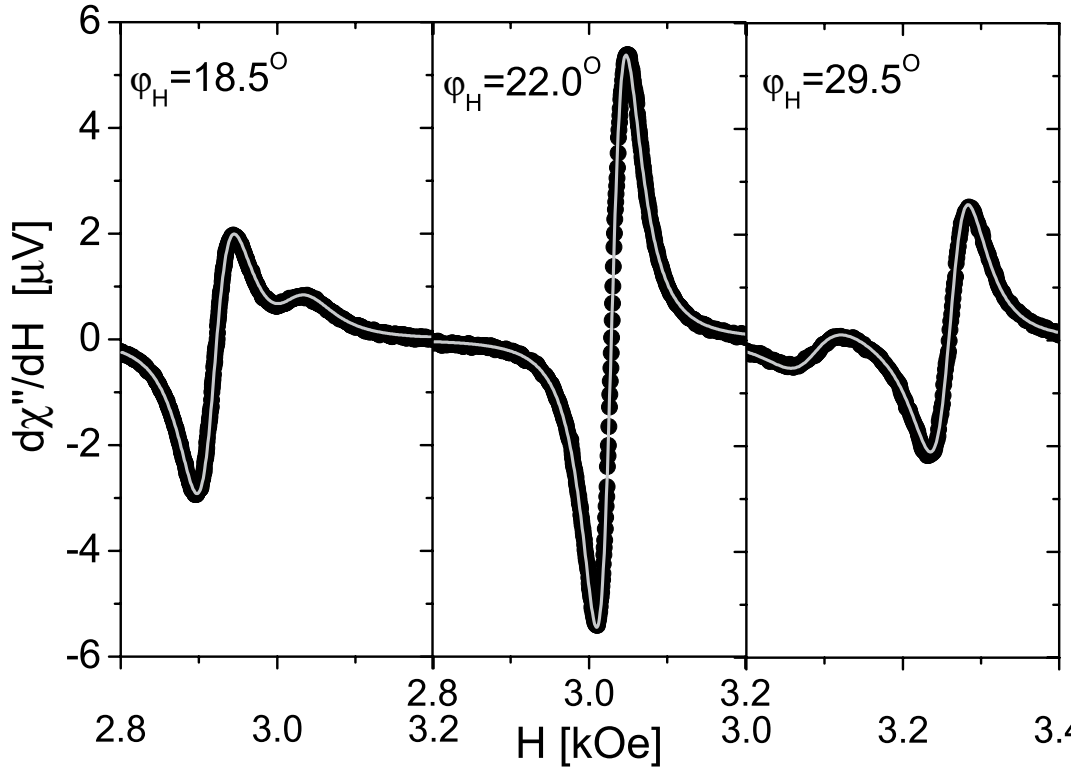

Figure 4.17: FMR spectra measured at 23.9 GHz around the crossover of FMR fields in the 20Au/40Fe/16Au/16Fe/GaAs(001) structure. The spectra where measured with $\varphi_H = 18.5°$, $\varphi_H = 22.0°$ (crossover), and $\varphi_H = 29.5°$ (from left to right). The (•) symbols represent the measured data and the grey solid line was calculated using Eq. 4.9 with the anisotropies from Fig. 4.5, the intrinsic relaxation parameters $\alpha_{\rm int}^{\rm 40Fe} = 3.68 \times 10^{-3}$, $\alpha_{\rm int}^{\rm 16Fe} = 4.0 \times 10^{-3}$, and the spin-pumping coefficient $\frac{g\mu_B g^{\uparrow\downarrow}}{4\pi M_S} = 8.52 \times 10^{-10}$ cm^{-1}. In all three graphs the same scaling factor between theory and calculation was used, and individual fine tuning of the uniaxial anisotropy field (up to 20 Oe) and angle φ_H (up to 0.5°) was allowed to obtain a perfect agreement between theory and experiment.

in metallic ferromagnets depends on difficult relativistic and spin dependent electron band properties, as outlined in section 2.4.3.

The breathing Fermi surface contribution to the non-local Gilbert damping is proportional to the electron relaxation time $\tau_{\rm sf}$ of the NM spacer (see Eq. 4.10). Since this contribution is based on the concept of interlayer exchange coupling one would expect some oscillatory behavior to result form changing the spacer thickness. The data shown in Fig. 4.14 indicate that this type of behavior is only marginally present if

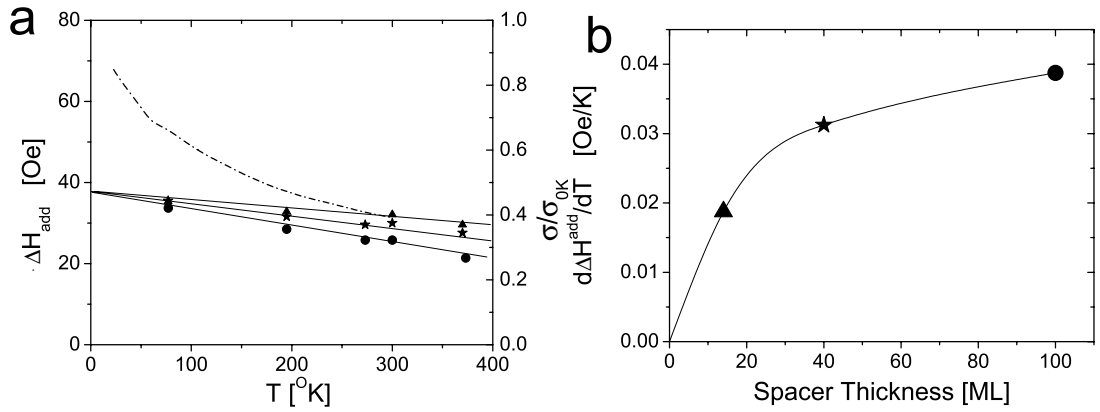

Figure 4.18: **(a)** shows the temperature dependence of $\Delta H^{\rm add}$ at 24 GHz, for 3 different samples: (▲) 20Au/40Fe/14Au/16Fe/GaAs(001), (★) 20Au/40Fe/40Au/16Fe/GaAs(001), and (•) 20Au/40Fe/100Au/16Fe/GaAs(001). The temperature dependence of the sheet conductivity, σ, for the sample (•) is shown by the dashed line. Note that the temperature dependence of $\Delta H^{\rm add}$ is linear and weak for all samples. The temperature dependence of $\Delta H^{\rm add}(T)$ was fit using Eq. 4.11. **(b)** Shows the slope, $(\partial \Delta H^{\rm add}/\partial T)$, as a function of the spacer thickness.

at all. The breathing Fermi surface contribution can be better tested by measuring the temperature dependence of the non-local damping. One would expect the non-local damping to scale with the sheet conductance of the NM spacer ($\tau_{\rm sf} \sim \tau_{\rm m} \sim \sigma$). The temperature dependence of the sheet conductance and $\Delta H^{\rm add}$ is shown in Fig. 4.18. $\Delta H^{\rm add}$(T) is linear in temperature and obviously does not scale with the conductivity. This indicates that the breathing Fermi surface contribution is not significant.

Note that the slope of $\Delta H^{\rm add}$ as a function of temperature increases with increasing Au spacer thickness. One can fit the temperature dependence using a linear function

$$\Delta H^{\rm add}(T) = C{\rm T} + \Delta H^{\rm add}\big|_{\rm T=0K} \ . \tag{4.11}$$

The extrapolated $\Delta H^{\rm add}\big|_{\rm T=0K}$ was equal for all Au spacers that were studied and the temperature dependent contribution C saturates for higher spacer thicknesses, as shown in Fig. 4.18b. This implies that the Au spacer decreases the effectiveness of the spin-pump mechanism at finite temperatures and acts as an additional resistance for the spin current that is in series with the interface mixing resistance $1/g^{\uparrow\downarrow}$. This resistance would decrease the spin current reaching the NM/F2 interface. Since the spin diffusion length in Au is much bigger than the Au spacer thickness, no additional

Sample	α [10^{-3}]	G [10^8Hz]	ΔH [Oe] 24 GHz
$16Fe_{RT}^{single}$	4.4 ± 0.2	1.4	37
$16Fe_{RT}^{double}$	8.3 ± 0.3	2.6	67
$16Fe_{RT}^{double}$-$16Fe_{RT}^{single}$	3.7 ± 0.2	1.15	30
$16Fe_{T=0\ K}^{double}$-$16Fe_{T=0\ K}^{single}$	4.5 ± 0.3	1.41	37
$16Fe_{sp}$	4.47	1.37	36.6

Table 4.2: Table summarizing the damping parameters and linewidth at 24 GHz for the 16 ML Fe film in magnetic single layers and double layers. The values in row $16Fe_{sp}$ show the prediction from the spin-pump model. Note that the T=0° K values are extrapolated from Fig. 4.18a.

resistance in Au is expected [132]. The origin of this temperature dependence has not been resolved yet.

It is worthwhile to point out that the extrapolated value of $\alpha_{16Fe}^{add}\big|_{0K} = 4.5 \pm 0.2 \times 10^{-3}$ is in excellent agreement with the value estimated from the spin-pumping theory, $\alpha_{16Fe}^{sp} = 4.4 \times 10^{-3}$. This behavior could also be related to the fact that the spin-pumping theory is strictly valid only at $T = 0°$ K, as outlined in appendix C (see Eq. C.93).

4.7 NM Cap Layer as Spin-Sink

4.7.1 Spin accumulation and back-flow

In the previous section the manner in which the injected spin current gets absorbed by a second ferromagnetic layer was discussed. In this section the relaxation of non-equilibrium spins inside the NM layer is addressed. In the NM the pumped spin momentum is relaxed into the lattice by electron momentum scattering in the presence of spin-orbit interaction. This process requires some degree of spin accumulation in the NM. For example, in the absence of spin-lattice scattering the accumulated magnetic moment in the NM creates a back-flow of spin momentum into the ferromagnetic layer. In equilibrium the back-flow is equal to the pumped spin current [116]. Therefore the net flow of spin momentum across the F/NM interface is

$$\mathbf{j}_{\mathrm{net}} = \mathbf{j}_{\mathrm{pump}} - \mathbf{j}_{\mathrm{back}}. \tag{4.12}$$

The pumped spin current $\mathbf{j}_{\mathrm{pump}}$ is given by Eq. 4.4 and an expression for the back-flow was derived by Tserkovnyak et al. [129] and Urban et al. [122]. The net spin current crossing the F/NM interface is given by

$$\mathbf{j}_{\mathrm{net}} = \left[1 + \frac{\tau_{\mathrm{sf}} g^{\uparrow\downarrow}}{hNSl_{\mathrm{sd}} \tanh(t_{\mathrm{NM}}/l_{\mathrm{sd}})}\right]^{-1} \mathbf{j}_{\mathrm{pump}}, \tag{4.13}$$

where l_{sd} is the spin diffusion length in the NM, N is the density of states per spin in the NM, t_{NM} is the thickness of the NM layer, and S is the area of the F/NM interface. The spin diffusion length is defined as $l_{\mathrm{sd}} = \sqrt{D\tau_{\mathrm{sf}}}$ [129], where τ_{m} and τ_{sf} are the electron momentum scattering and spin-flip times, respectively. $D = v_F^2\tau_{\mathrm{m}}/3$ is the electron diffusion constant. In the derivation of Eq. 4.13 the boundary condition for the F/NM interface was assumed to be given by Eq. 4.12 and the boundary condition at the outer NM/vacuum interface was $\mathbf{j}_{\mathrm{net}}(t_{\mathrm{NM}}) = 0$.

For $\tau_{\mathrm{sf}} = 0$ there is no back-flow, and the normal metal acts as a perfect spin-sink. As demonstrated in the previous section, a net spin current flowing out of the ferromagnet creates additional damping for the precessing magnetization due to the conservation of angular momentum.

4.7.2 Induced Gilbert damping

From Eqs. 4.4, 4.8, and 4.13 the additional Gilbert damping constant (taking spin accumulation into account) is

$$\alpha_{\mathrm{cap}}^{\mathrm{sp}} = \frac{\gamma\hbar g^{\uparrow\downarrow}}{4\pi M_S t_{\mathrm{NM}} S}\left[1 + \frac{\tau_{\mathrm{sf}} g^{\uparrow\downarrow}}{hNSl_{\mathrm{sd}}\tanh(t_{\mathrm{NM}}/l_{\mathrm{sd}})}\right]^{-1}. \tag{4.14}$$

This enhanced Gilbert damping is always smaller than that discussed in section 4.4 (provided that $g^{\uparrow\downarrow}$ is the same or smaller) since a NM layer on its own is not a perfect spin-sink. For a free electron gas $N = mk_F/(2\pi^2\hbar^2)$ and Eq. 4.14 can be rewritten as

$$\alpha_{\mathrm{cap}}^{\mathrm{sp}} = \frac{\gamma\hbar g^{\uparrow\downarrow}}{4\pi M_S t_{\mathrm{NM}} S}\left[1 + \frac{\sqrt{3}}{2\sqrt{\epsilon}}(\tanh(t_{\mathrm{NM}}/l_{\mathrm{sd}})^{-1}\right]^{-1}, \tag{4.15}$$

where $\epsilon = \tau_{\mathrm{m}}/\tau_{\mathrm{sf}}$ is the spin-flip probability per scattering event.

For very small NM thicknesses ($t_{\mathrm{NM}} \ll l_{\mathrm{sd}}$) Eq. 4.15 leads to $\alpha_{\mathrm{cap}}^{\mathrm{sp}} = 0$. The back-flow of spin momentum from NM compensates the spin-pumping current from the ferromagnet. This is the reason why the magnetic single layers covered by gold that were discussed at the beginning of this chapter did not exhibit a spin-pumping contribution to the damping. When the thickness of the NM is larger than the spin diffusion length, an additional resistance is created for the spin current. This resistance acts in series with the mixing resistance $\frac{1}{g^{\uparrow\downarrow}}$ and the effective mixing resistance may be written as [129]

$$\frac{1}{g_{\mathrm{eff}}^{\uparrow\downarrow}} = \frac{1}{g^{\uparrow\downarrow}} + R_{\mathrm{sd}} = \frac{1}{g^{\uparrow\downarrow}} + \frac{l_{\mathrm{sd}}}{S\sigma_{\mathrm{NM}}}\frac{e^2}{h}, \tag{4.16}$$

where R_{sd} is the resistance per spin (in units of h/e^2) for a NM layer with a thickness equal to the spin diffusion length ($t_{\mathrm{NM}} = l_{\mathrm{sd}}$). For infinite thickness the NM cap layer acts like a partial spin-sink and the saturation value depends on the size of R_{sd}.

4.7.3 NM cap layer experiments

The role of a NM layer on the non-local damping was studied in magnetic single layer samples with NM cap layers of various thicknesses. The magnetic Fe layer always had a fixed thickness of 16 ML. The NM layer was one of Au, Ag, Cu, and Pd, and its thickness was varied between 0 and 80 nm.

The Au, Ag, and Cu cap layers did not introduce a measurable additional damping in this range of thicknesses, as illustrated in Fig. 4.19. For Cu, Ag, and Au cap

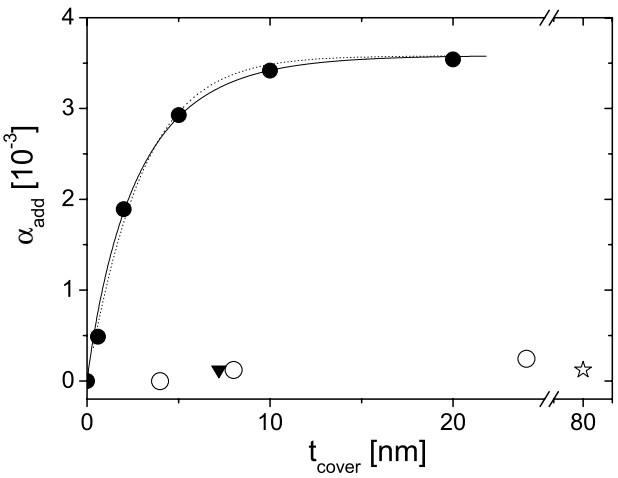

Figure 4.19: Dependence of the additional damping, α^{add}, on the cap layer thickness in NM/16Fe/GaAs(001) samples measured at 23.9 GHz. The NM was one of Au (○), Cu (▼), Ag (☆), and Pd (●). The dotted line is a fit to the Pd data using Eq. 4.15 and the solid line is a fit using Eq. 4.21.

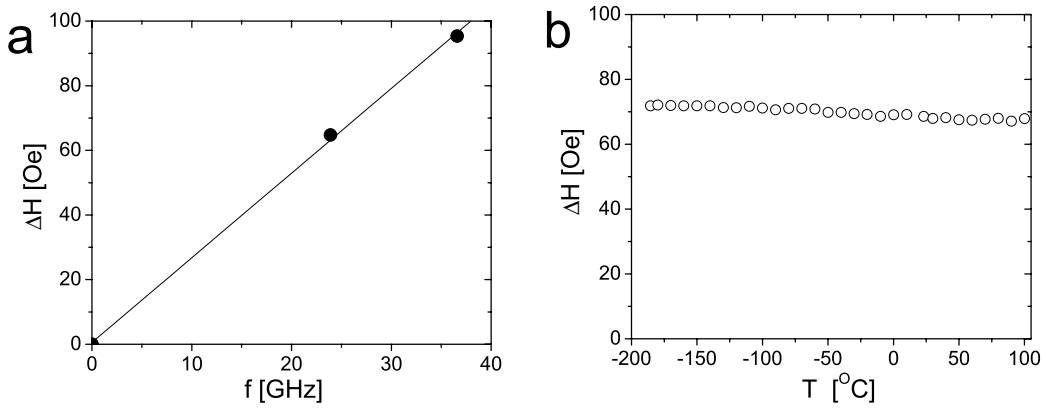

Figure 4.20: **(a)** Frequency dependence of ΔH and **(b)** temperature dependence of ΔH at 23.9 GHz for the 50Pd/16Fe/GaAs sample.

layers the linewidth changed by less than 2 Oe which corresponds to the experimental uncertainty of the linewidth measured at 24 GHz.

The situation was found to be very different for Pd cap layers, in this case the linewidth rapidly increased with the Pd thickness and saturated at $t_{\mathrm{Pd}} \approx 10$ nm. The magnitude of this increase was comparable to that produced by the intrinsic damping, and the corresponding frequency dependence (see Fig. 4.20a) clearly showed that the

additional linewidth scaled with the microwave frequency with no appreciable zero frequency offset (2 Oe). The linear frequency dependence justifies the interpretation of the increase in linewidth as an additional Gilbert damping parameter (see Fig. 4.19).

Equation 4.15 provides an analytic expression for the enhanced damping parameter as a function of the NM thickness assuming diffusive electron transport. Since the additional damping occurred for very small NM thicknesses, the use of spin diffusion theory is questionable.

A simple estimate for $g^{\uparrow\downarrow}/S$ can be obtained from the density of electrons using Eq. 4.6. Andersen [133] estimated the number of conduction electrons per Pd atom to be 0.37. This implies a carrier density of $n = 2.5 \times 10^{22}$ cm^{-3} and leads to $g^{\uparrow\downarrow}/S = 0.65 \times 10^{15}$. This number is reasonable when compared to the values for $g^{\uparrow\downarrow}/S$ calculated from first principles for Cu/Co interfaces, in which case Xia et al. [118] found $g^{\uparrow\downarrow}/S = 1.1 \times 10^{15}$. One expects $g^{\uparrow\downarrow}/S$ to be smaller for Pd than for Cu since Pd has a smaller number of conduction electrons per atom than Cu.

$g^{\uparrow\downarrow}/S = 0.65 \times 10^{15}$ cannot explain the data in Fig. 4.19 since the resulting saturation value is too low. A reasonable fit requires $g^{\uparrow\downarrow}/S = 1.2 \times 10^{15}$, $\epsilon = 4$, and $l_{\mathrm{sd}} = 5.1$ nm (dotted line). $\epsilon = 4$ means that it is four times more likely for an electron in Pd to flip its spin than to change its momentum upon scattering and renders Eq. 4.13 invalid. The saturation value of the enhanced Gilbert damping was $\alpha^{\mathrm{add}} = 3.5 \times 10^{-3}$ which is close to the additional damping found in magnetic double layers (see section 4.3).

Validity of the spin diffusion theory for Pd

To explain the experimental results with NM=Pd it was necessary to use values for ϵ bigger than 1. This is not compatible with the spin-diffusion equation, and the spin transport in the Pd layer cannot really be described as diffusive.

To gain further insight, the electron mean free path in the Pd layer was determined from the resistivity. To accomplish this, the sheet resistances of two samples 20Au/50Pd/16Fe/GaAs and 20Au/16Fe/GaAs were measured by means of the van der Pauw technique [134]. The resistances were found to be 9.6 $\frac{\Omega}{\square}$ and 19.9 $\frac{\Omega}{\square}$, respectively. Since the individual layers contribute in parallel, one can infer that the sheet resistance of the isolated 50 ML Pd film was 18.7 $\frac{\Omega}{\square}$. Using a Pd thickness of 9.7 nm (50 ML), the resistivity of the Pd layer would be $\varrho = 18.2$ $\mu\Omega$cm which is almost double the resistivity of bulk Pd ($\varrho_{\mathrm{Pd}} = 10.8$ $\mu\Omega$cm [23]). The measured resistance

allows one to estimate an effective electron momentum scattering time τ_{m} in the Pd layer from the relation

$$\frac{1}{\varrho} = \frac{e^2 n \tau_{\mathrm{m}}}{m^*}, \tag{4.17}$$

where e is the elementary charge, m^* the effective mass, and n the density for conduction electrons. The electron mean free path is given by $\lambda_{\mathrm{m}} = v_F \tau_{\mathrm{m}}$, the effective mass of the conduction electrons in Pd is $m^* \approx 2m$, and the Fermi velocity is $v_F = 5.6 \times 10^7$ cm/s [135]. It follows that $\lambda_{\mathrm{m}} \approx 8.6$ nm. Since this number is bigger than the spin diffusion length (obtained from fitting Eq. 4.14 to the data) and the film thickness the diffusive theory is clearly not applicable.

4.7.4 Alternate model of spin transport in Pd

Bulk Pd is a strongly enhanced paramagnet with a large Stoner enhancement factor and known to be on the verge of ferromagnetism with locally fluctuating magnetic moments (paramagnons) [136, 137, 138, 139]. One could imagine that these fluctuating moments act as very effective spin scatterers. The spin current which is injected into the NM by the precession of the magnetization interacts with these paramagnons and the spin-spin scattering leads to a local randomization of the direction of the spin momentum of the spin current [140]. This randomization represents a loss of (lateral) coherence of the spin current and is reminiscent of 'mode-mode coupling'. On average the spins travel the spin-flip length λ_s, before their initial spin momentum is flipped. This length is not equivalent to the spin diffusion length since it is not assumed that electrons experience a number of momentum scattering events before their spin is flipped.

Thus the spin current injected into the Pd layer ($\mathbf{j}_{\mathrm{pump}}$) will gradually loose its coherence as a function of the Pd thickness and the angular momentum is effectively absorbed. This means that different locations of the F/NM interface accept the back-flow of spin momentum with a randomized phase. The exchange interaction in Fe averages these local contributions and consequently the net back-flow approaches zero with increasing Pd thickness. The magnitude of the coherent spin current returning to the Fe layer, $\mathbf{j}_{\mathrm{back}}$, is given by the amount of spin current that is not lost as the electrons make a round trip through the Pd layer. Since the electrons can move in arbitrary directions from the F/NM interface an effective layer thickness L_{eff} is introduced. L_{eff} is an effective NM layer thickness which is averaged over all available

in-plane electron momenta $k_\parallel$ up to the Fermi wave vector k_F with an appropriate weighing. One can write [141]

$$\frac{\pi k_F^2}{(2\pi)^2} e^{-\frac{L_{\rm eff}}{\lambda_s}} = \int_0^{k_F} \frac{2\pi k_\parallel dk_\parallel}{(2\pi)^2} e^{-\frac{t_{\rm NM}}{\cos\theta}\frac{1}{\lambda_s}}, \tag{4.18}$$

with $\cos\theta = \sqrt{1-(\frac{k_\parallel}{k_F})^2}$, where θ is the direction of the electron momentum measured with respect to the surface normal. Therefore the back-flow is

$$\mathbf{j}_{\rm back} = \mathbf{j}_{\rm pump} e^{-\frac{2L_{\rm eff}}{\lambda_s}}. \tag{4.19}$$

An additional factor of 2 appears in the exponent, because the average distance travelled by spins that make it back into the ferromagnet after a round trip through the Pd layer is $2L_{\rm eff}$. The net spin current through the NM/F interface is then given by

$$\mathbf{j}_{\rm net} = \mathbf{j}_{\rm pump}\left(1 - e^{-\frac{2L_{\rm eff}}{\lambda_s}}\right). \tag{4.20}$$

Using this in Eq. 4.14 one arrives at a new expression for the enhanced Gilbert damping

$$\alpha_{\rm cap}^{\rm sp} = \frac{\gamma\hbar g^{\uparrow\downarrow}}{4\pi M_S t_{\rm Fe} S}\left(1 - e^{-\frac{2L_{\rm eff}}{\lambda_s}}\right). \tag{4.21}$$

Now the Pd data in Fig. 4.19 can be fit again using Eq. 4.21. This fit determines only two truly independent parameters. As seen in Fig. 4.19, the fit describes the Pd data very well, resulting in $g^{\uparrow\downarrow}/S = 0.9 \times 10^{15}$ cm^{-2}. This value is significantly smaller than that determined by fitting the data to the diffusion theory, and is approximately equal to the value estimated from the conduction electron density in Pd. This model does not allow for spin accumulation so that Pd acts as a perfect spin-sink when thick enough. From the fit, the spin mean free path λ_s was determined to be $\lambda_s =$ 9.0 nm. This implies that the spin mean free path is only slightly bigger than the electron mean free path calculated from the conductivity, $\lambda_{\rm m} = 8.6$ nm. This is an unusual situation and may be a consequence of electron-electron correlation effects occurring in Pd. Recently, Kurt et al. also observed a very short spin-flip length in Pd at low temperatures [142]. Using current perpendicular to the plane (CPP) GMR measurements, they found $\lambda_s^{Pd} = 25 \pm 7$ nm at 4 °K. The discrepancy between this value and the λ_s estimated from FMR very likely has two origins: (i) λ_s at low temperature is usually longer than at RT; in simple metals the spin-flip length decreases by a factor of 2 between 4 °K and 300 °K [143, 144]; (ii) CPP GMR measures

the longitudinal spin-flip length while FMR is sensitive to the transverse spin-flip length.

The lack of a pronounced temperature dependence for ΔH^{add} with NM=Pd (see Fig. 4.20b) supports the conjecture that the scattering of the spin current in Pd is due to temperature independent electron-electron correlation effects.

4.8 Spin-Pumping in Other Experiments

4.8.1 Single layers

Heinrich et al. [24] reported FMR line broadening for very thin Fe films grown on Ag(001) substrates. In this case the damping parameter increased from $\alpha = 2.1 \times 10^{-3}$ for a film having a thickness of 24 ML to $\alpha = 18.2 \times 10^{-3}$ for a 4 ML thick film. In light of the fact that the thicker film exhibited a damping parameter very close to the intrinsic value for bulk Fe [145], it is likely that only a very small fraction of the increased damping in the thinner film was due to spin-pumping. One can therefore conclude that Ag is a very poor spin-sink. More recently, Platow et al. [146] measured the thickness dependence of the FMR linewidth for Ni grown on Cu(001). In this experiment Cu also provided a very poor spin-sink.

Mizukami et al. [147, 130] conducted a systematic FMR study of the NM/Py/NM system prepared by sputtering on glass substrates, where the NM was Cu, Ta, Pd, and Pt. The thickness of the NM cladding layers was held fixed at 50 Å while the thickness of the Permalloy layer was varied between 20 and 100 Å. For Cu and Ta cladding layers the damping parameter for Py was equal to its intrinsic value and independent of the Py thickness. Pd and Pt cladding layers however caused a strong increase in damping such that the additional damping increased with the inverse Py thickness. For NM=Pd the effect was 40% stronger than in the studies presented in this thesis (taking into account two interfaces and the lower magnetization of Py relative to Fe). In a subsequent paper Mikazumi et al. investigated the FMR line broadening of a 30 Å Py layer due to the proximity of a Pt layer [148, 149]. In this case a 50 Å Pt layer was spatially separated from the Py layer by a Cu spacer of variable thickness. For Cu spacer thicknesses less than 100 nm, the Pt layer resulted in a measurable line broadening. With the thinnest Cu spacer (3 nm) the strength of the enhanced damping agrees in magnitude with the enhanced damping observed in

the 50Pd/16Fe/GaAs(001) system, and is presumably due to spin-pumping effects.

4.8.2 Double layers

The spin-pumping effect also has profound consequences for the dynamics of exchange coupled magnetic bilayers. Coupled bilayers have acoustic and optic precessional modes [4]. Using Eq. 4.9 and including exchange coupling terms one can calculate the effect of spin-pumping and exchange coupling. For example for a 5Fe/12Cu/10Fe bilayer with no interlayer exchange coupling, the calculated spin-pumping contribution to the FMR linewidth at 36 GHz is 150 Oe for the 5Fe film and 75 Oe for the 10Fe film. By turning on a moderate antiferromagnetic exchange coupling $J = -0.2$ erg/cm^2 the optical peak is broadened by 200 Oe while the acoustic peak is broadened by only 36 Oe. For moderate antiferromagnetic exchange coupling the optical peak mainly arises from the 5Fe layer (with $J = -0.2$ erg/cm^2 one has $m^{\rm rf}_{\rm 5Fe}/m^{\rm rf}_{\rm 10Fe} = 3.6$ at 36 GHz). It is not surprising that the 5Fe peak broadens further in the presence of exchange coupling, considering that the optical mode corresponds to an out-of-phase precession of the magnetic moments of the 5Fe and 10Fe layers. In this case the spin momentum is more efficiently pumped between the two layers and results in more damping. By the same argument, the in-phase precession of the moments for the acoustic peak (10Fe) narrows the FMR line of the acoustic mode.

Experimentally, optical FMR peaks were always observed to be wider than the acoustic peaks. In a 5Fe/12Cu/10Fe sample grown on a Ag(001) substrate the linewidth of the optical peak was found to be enhanced by as much as 500 Oe compared to the single layer [150]. This indicates that approximately 50% of this broadening was due to spin-pumping and the reminder was caused by an inhomogeneous exchange coupling [121].

Recently, Lubitz et al. [151] also found an increase of the FMR linewidth in thin polycrystalline Fe films grown on Silicon which was induced by Cu/Fe cap layers. These measurements are in qualitative agreement with the Fe/Au/Fe/GaAs double layer results presented in section 4.3, but the thickness dependent FMR linewidth observed for their polycrystalline Fe single layers [151] makes a quantitative comparison difficult.

Chapter 5

Two-Magnon Scattering

5.1 Au/Pd/Fe/GaAs Multilayers

The resonance linewidth in Au/Pd/Fe/GaAs(001) multilayers was observed to exhibit a strong extrinsic contribution. This effect will be discussed in terms of the two-magnon scattering model in this chapter.

5.1.1 Growth, RHEED, STM, TEM studies

The Pd(001) in-plane lattice constant has a large mismatch of 4.4% with respect to the Fe(001) template, even when $[110]_{\mathrm{Pd}} \parallel [100]_{\mathrm{Fe}}$. Au grows over Pd with the in-plane cubic axes parallel to each other ($[100]_{\mathrm{Au}} \parallel [100]_{\mathrm{Pd}}$). The Pd and Au lattice spacings are mismatched by 4.5 percent. The presence of Pd in crystalline Au/Pd/Fe(001) multilayers provides a large lattice strain which, above a critical Pd thickness, is relieved by the formation of misfit dislocations. Results in this section are mainly presented for the magnetic single layer nPd/**30Fe**/GaAs(001) and Au/nPd/**16Fe**/GaAs(001) films, where n was varied between 0 and 300 ML.

The RHEED pattern for the Au(001) cap layer in 20Au/nPd/16Fe/GaAs(001) depends on the number of atomic layers of Pd, n. For $n < 4$ the RHEED patterns of the Au(001) surface layers were similar to those observed for case of Au/Fe/GaAs(001), as shown in Fig. 4.2. For $n \geq 4$ the RHEED patterns for Au(001) developed fan-out streaks when the primary electron beam was oriented along the $\langle 100 \rangle_{\mathrm{Au}}$ directions (see Fig. 5.1a). The intensity of this effect saturated for $n \geq 9$. Fan-out RHEED streaks are a well known feature in MBE epitaxy. It has been shown by Pukite [76, 77]

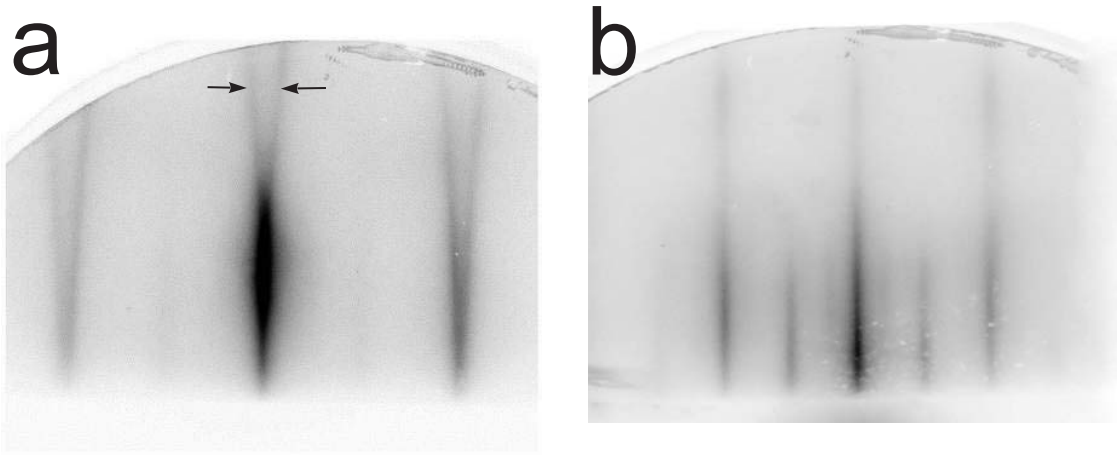

Figure 5.1: **(a)** Shows a RHEED pattern with strong fan-out features (indicated by arrows) on the surface of Au(001) due to a network of misfit dislocations in 20Au/9Pd/16Fe/GaAs(001). The electron beam was oriented along the $[100]_{\mathrm{Au}}$ direction. Note that in this orientation the RHEED streak intensities which are caused by the As 2×2 surface reconstruction are significantly diminished in the presence of misfit dislocations (cf. Fig. 4.2b), indicating that the long range order of the surfactant As in the [100] directions deteriorated. **(b)** The primary electron beam was oriented along the $[110]_{\mathrm{Au}}$ direction. No fan-out streaks are visible.

that their presence is related to surface clustering involving rectangular symmetry, as outlined in section 3.1.3. Pukite's result allows one to make the following practical conclusion: *The presence of RHEED fan-out streaks with* 90° *symmetry is due to the formation of a rectangular network of surface line defects.* For the RHEED electron beam oriented at 45° with respect to the direction of line defects the fan-out streak pattern is symmetric and reaches its maximum intensity; while for an electron beam oriented along the line defects (for angles 0 and 90°) only simple straight streaks are present. This is exactly what is observed, as shown in Fig. 5.1.

The rectangular network of line defects on the surface is caused by nucleation and glide of misfit dislocation half-loops entering the crystal surface during the film growth to compensate for the lattice mismatch. This gliding of dislocations along the $\{111\}_{\mathrm{Pd,Au}}$ planes is illustrated in Fig. 5.3.

From the RHEED patterns shown in Fig. 5.1a it can be concluded that the surfaces of the Au/nPd/Fe/GaAs(001) structures with $n \geq 9$ consist of a network of line defects, which are oriented along the $\langle 110 \rangle_{\mathrm{Au}}$ crystallographic directions of Au(001).

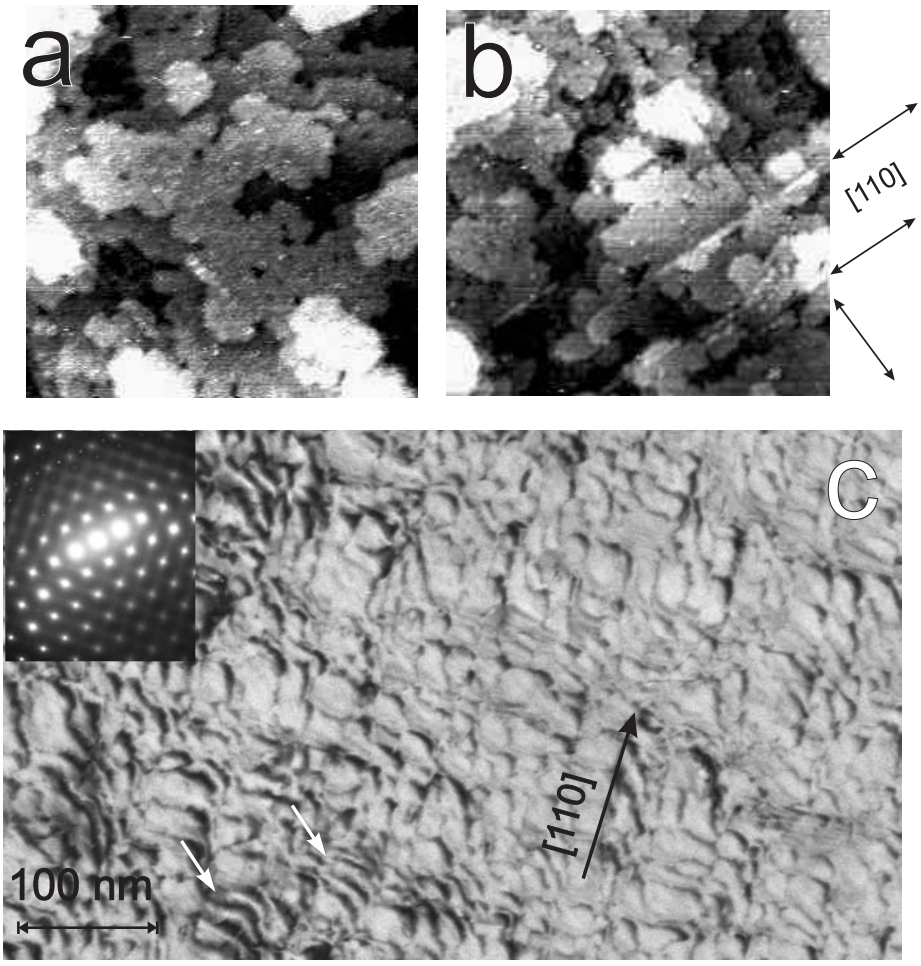

Figure 5.2: Ex-situ 1500 Å × 1500 Å STM images of **(a)** 90Au/16Fe/GaAs(001) and **(b)** 90Au/9Pd/**16Fe**/GaAs(001). The arrows along the $\langle 110 \rangle_{\mathrm{Au}}$ directions highlight surface steps which are caused by the dislocation glide. The z-scale (from white to black) in both images is 8 Å, and the RMS roughness was $\sim$ 1 Å. **(c)** Plan view TEM image of the 90Au/9Pd/**16Fe**/GaAs(001) sample. The black arrow indicates the $[110]_{\mathrm{Au}}$ crystallographic direction and the contrast that exhibits a clear four-fold symmetry (parallel and perpendicular to the arrow) is due to the misfit dislocation network. The features oriented at 45° with respect to the $[110]_{\mathrm{Pd}}$ direction indicated by the white arrows are caused by moire fringes [152]. The inset shows the corresponding electron diffraction pattern. The intensity connecting diffraction spots parallel to the $\langle 110 \rangle_{\mathrm{Au}}$ directions give a hint to the defects.

These line defects correspond to atomic steps caused by the intersection of the $\{111\}_{\mathrm{Au}}$ glide planes with the surface [153, 154]. This conjecture is further confirmed by STM

studies of the Au(001) layer of the 90Au/9Pd/**16Fe**/GaAs(001) sample. Fig. 5.2b shows surface steps arising from the network of misfit dislocations, indicating that the atomic displacements along the $\{111\}_{\mathrm{Au}}$ glide planes propagate through the top Au layer.

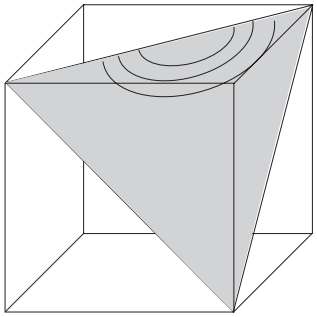

Figure 5.3: Dislocation half loops on a {111} glide plane.

The presence of a self-assembled network of misfit dislocations was observed using transmission electron microscopy (TEM) by plan view orientation of the layer system 90Au/9Pd/**16Fe**/GaAs(001), (see Fig. 5.2c). The observed orientation and density of the dislocation arrangement resembles the misfit dislocation network observed by Jörg Woltersdorf in epitaxially grown Au/Pd bicrystals [155, 152] of the corresponding thicknesses. During the growth of the first Pd monolayers on the Au(001) substrate, complete misfit dislocations are generated and form a rectangular network located at the Pd/Au interface. After reaching the critical thickness of 4 ML, the process of gliding of substrate dislocations can no longer produce a sufficiently high density of dislocations to compensate the misfit; thus additional dislocation half loops are generated [156, 157] starting at the top Pd layer and extending to the interface, as illustrated in Fig. 5.3. The corresponding interference of moire patterns and dislocation contrast phenomena treated in [152] is also recognizable in Fig. 5.2c, as indicated by the white arrows. The mechanisms for generation of interface dislocations and their efficiency for misfit compensation was outlined in [158].

5.1.2 FMR studies

The magnetic anisotropies of the **Fe**(001) layer in nPd/**30Fe**/GaAs(001) and in Au/nPd/**16Fe**/GaAs(001) were similar to those observed for dislocation free Au/**Fe**/-GaAs(001) systems of the corresponding thicknesses [110]. The easy axes of the **30Fe** layer were oriented along the $\langle 110\rangle_{\mathrm{Fe}}$ directions due to the in-plane uniaxial anisotropy originating at the GaAs interface [110]. The striking difference between the samples having a thick Pd layer in nPd/Fe/GaAs(001), $n \geq 130$, and those with $n \leq 110$ was in the level of magnetic damping. The Fe layers in nPd/**Fe**/GaAs(001) structures with $n \leq 110$ exhibited only Gilbert damping enhanced by spin-pumping of the Fe layer and having a spin-sink inside the Pd layer, as described in section 4.7.3 and

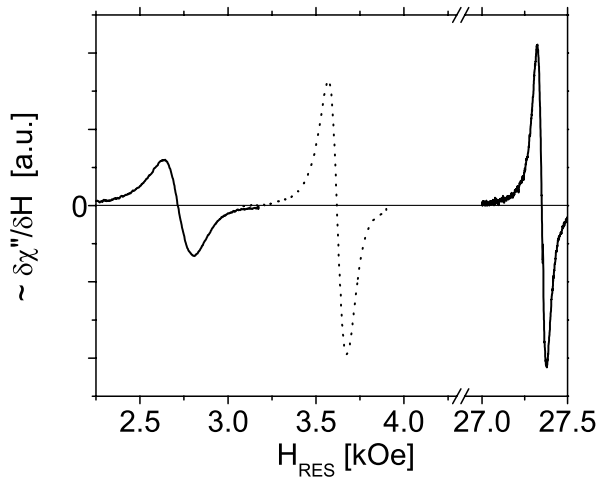

Figure 5.4: Typical FMR spectra measured at 23.9 GHz on the 200Pd/**30Fe**/GaAs(001) sample. The left spectra were taken with the magnetization **M** in the plane: **M** $\parallel [100]_{\mathrm{Fe}}$ (solid line) and **M** $\parallel [110]_{\mathrm{Fe}}$ (dotted line). The right spectrum corresponds to the perpendicular configuration (**M** $\parallel [001]_{\mathrm{Fe}}$). Note that the FMR linewidths for the in-plane configuration are anisotropic, and the narrowest line is measured in the perpendicular configuration.

[159, 140]. The FMR linewidth in nPd/Fe/GaAs(001) samples with $n \geq 130$, was different. In these samples the FMR linewidth was strongly dependent on the angle φ_M between the magnetization and the crystallographic $\langle 100 \rangle_{\mathrm{Fe}}$ axes, showing a distinct four-fold symmetry, as can be seen in Fig. 5.5. The minima and maxima in ΔH are along the $\langle 110 \rangle_{\mathrm{Fe}}$ and $\langle 100 \rangle_{\mathrm{Fe}}$ crystallographic directions, respectively. It is interesting to note that $\Delta H(\varphi_M)$ does not show a two-fold symmetry. This implies that the chemical bonding between Fe and the uniaxial dangling bonds of GaAs at the Fe/GaAs(001) interface is not important for the formation of magnetic defects by the network of misfit dislocations. The FMR linewidth also changed in a very pronounced way as a function of microwave frequency. The frequency dependence of the FMR linewidth, $\Delta H(f)$, along the $\langle 100 \rangle_{\mathrm{Fe}}$ and $\langle 110 \rangle_{\mathrm{Fe}}$ directions is shown in Fig. 5.6. Along the $\langle 110 \rangle_{\mathrm{Fe}}$ (easy magnetic axes) and $\langle 1\bar{1}0 \rangle_{\mathrm{Fe}}$ (hard magnetic axes), the FMR linewidth is nearly linearly dependent on the microwave frequency between 10 and 73 GHz, but is accompanied by a zero frequency offset $\Delta H(0) = 50$ Oe. The slope of $\Delta H(f)$, however, is nearly that corresponding to the intrinsic Gilbert damping (including spin-pumping into a 100Pd(001) cap layer [140]) obtained in the

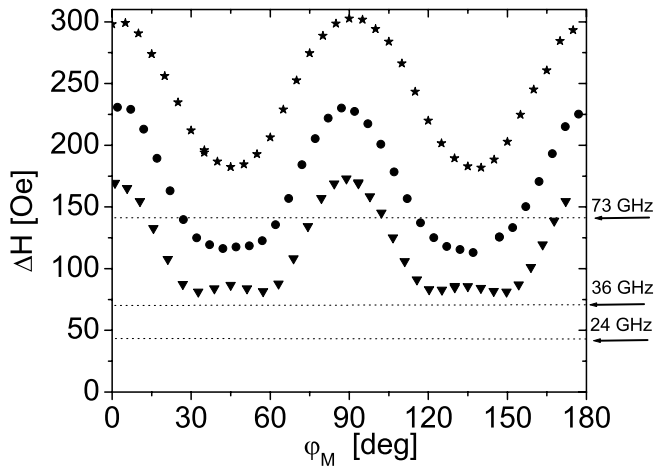

Figure 5.5: The ferromagnetic resonance linewidth for the 200Pd/**30Fe**/GaAs(001) film at 73(★), 36(•), and 24(▼) GHz as a function of the in-plane angle φ_M between the magnetization and the $[100]_{\mathrm{Fe}}$ axis. The angles φ_M were calculated from φ_H using the magnetic anisotropies and the applied field; the dotted lines indicate the ΔH due to the intrinsic damping (including spin-pumping) at 73.0, 36.4, and 23.9 GHz.

samples without extrinsic damping. ΔH was quite different when measured with the saturation magnetization along the $\langle 100 \rangle_{\mathrm{Fe}}$ directions. Note that for the 30 ML thick Fe film the $\langle 100 \rangle_{\mathrm{Fe}}$ directions are neither easy nor hard magnetic axes, and therefore it is not possible to avoid dragging of the magnetization behind the applied external field at FMR. ΔH was determined by finding the in-plane external field angle, φ_H, which corresponds to $\mathbf{M} \parallel \langle 100 \rangle_{\mathrm{Fe}}$ at resonance. The open circles in Fig. 5.6 show this measured linewidth. Dragging the magnetization behind the external field, however, results in additional FMR line broadening. This effect is usually present at low frequencies, because the FMR fields become comparable to the in-plane anisotropy fields. Dragging was nearly absent at and above 24 GHz. In order to remove the dragging contribution at 10 and 14 GHz, the FMR linewidth was evaluated in the following manner: FMR peaks were calculated including dragging of the magnetization, and the effective Gilbert damping (α_{eff}) was adjusted in such a way that the total ΔH was equal to that observed experimentally (open circles). Then the FMR linewidths without the dragging contribution were obtained using the effective Gilbert damping ($\Delta H = \frac{2\pi f}{\gamma}\alpha_{\mathrm{eff}}$). These are shown as the filled points in Fig. 5.6. The following features can are noteworthy: (i) The dependence on the microwave frequency,

Sample	$\Delta H_{\langle 100\rangle}$ [Oe]	$\Delta H_{\langle 110\rangle}$ [Oe]
200Pd**30Fe**GaAs	180	75
90Au10Pd**16Fe**GaAs	210	60
20Au**40Fe**40Au9Pd16FeGaAs	175	50
20Au40Fe40Au9Pd**16Fe**GaAs	160	50
20Au**40Fe**40Au4Pd[FePd]$_5$14FeGaAs	123	55
20Au40Fe40Au4Pd[**FePd**]$_5$**14Fe**GaAs	123	55
20Au**40Fe**[**PdFe**]$_5$4Pd40Au4Pd[FePd]$_5$14FeGaAs	200	50
20Au 40Fe[PdFe]$_5$4Pd40Au4Pd[**FePd**]$_5$**14Fe**GaAs	120	45
20Au**40Fe**40Pd16FeGaAs	210	75
20Au40Fe40Pd**16Fe**GaAs	75	75
20Au**20Fe**40Pd16FeGaAs	210	75
20Au20Fe20Pd**16Fe**GaAs	75	75

Table 5.1: Summary of the anisotropic FMR linewidths for samples with a network of misfit dislocations measured at 23.9 GHz. The data correspond to the magnetic layer that is highlighted in bold.

ΔH, is not described by a simple linear dependence on the frequency as would be expected for Gilbert damping. (ii) The slope of the FMR linewidth vs. frequency is nearly that expected for the intrinsic damping for frequencies between 36 and 73 GHz, but $\Delta H(0) = 160$ Oe is significantly increased compared to the $\langle 110\rangle_{\rm Fe}$ orientations. (iii) For frequencies less than 36 GHz the frequency dependence of ΔH shows a clear downturn (see Fig. 5.6).

A similar frequency dependence for ΔH was found recently by Twisselmann et al. [160] for Permalloy (Py) films grown on NiO and Lindner et al. [161] for Fe/V superlattices. In fact, the frequency dependence observed along the $\langle 100\rangle_{\rm Fe}$ orientations resembles recent calculations by Arias and Mills [162] of extrinsic damping due to two-magnon scattering, as shown by the thin solid line in Fig. 5.6. The Arias-Mills model result was calculated using Eq. 2.55. It does not exhibit sufficient downturn at low frequencies, likely because it is not applicable to the present case since a very different defect model was assumed (spatial variation of the direction of the uniaxial perpendicular anisotropy [12]).

The increase of the FMR linewidth noted above has been observed in several different sample structures involving a lattice mismatched layer of Pd. In Tab. 5.1 the linewidths measured along the $\langle 100\rangle_{\rm Fe}$ and $\langle 110\rangle_{\rm Fe}$ directions are summarized for sev-

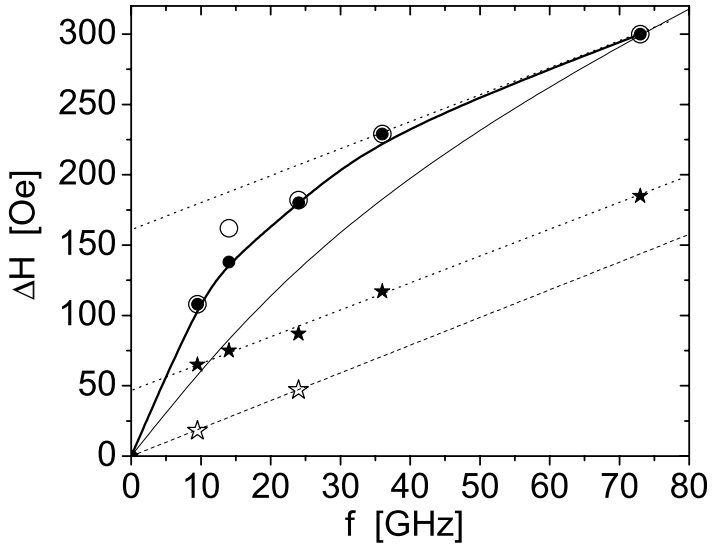

Figure 5.6: The frequency dependence of the FMR linewidth for the 200Pd/**30Fe**/GaAs(001) structure along the $\langle 110 \rangle_{\mathrm{Fe}}$ (★) and $\langle 100 \rangle_{\mathrm{Fe}}$ (•) directions, respectively. (○) points show ΔH along $\langle 100 \rangle_{\mathrm{Fe}}$ before the dragging contribution to the linewidth was removed (see further details in the text). The purpose of the thick solid line spline fit is to guide the eye. The thin solid line corresponds to the calculated frequency dependence of ΔH, using Eqs. 2.55 and 2.47 (Arias and Mills model [12]). The dashed line shows the frequency dependence of the intrinsic FMR linewidth (Gilbert damping) obtained by using the 100Pd/**30Fe**/GaAs(001) sample with no magnetic defects in the Fe film. The spin-pumping contribution in 100Pd/**30Fe**/GaAs(001) to ΔH is saturated (see Fig. 4.19). The ☆-symbols on the dashed line show the FMR linewidth in the perpendicular configuration at 9.7 and 23.9 GHz for the 200Pd/**30Fe**/GaAs(001) sample. Note that the ☆-symbols are right on the dashed line, indicating that in the perpendicular configuration the FMR linewidth ΔH is given by the Gilbert damping ($\alpha = 0.006$) with no zero frequency offset ($\Delta H(0)_{\perp} = 0$). The dotted lines indicate the range of microwave frequencies where the slope of $\Delta H(f)$ nearly corresponds to Gilbert damping. Note that the dotted lines have zero frequency offsets.

eral samples. All samples had one thing in common: extrinsic damping was triggered by lattice defects which are caused by the misfit dislocation network. The onset of two-magnon scattering required a critical thickness of Pd and this critical value depends on where the Fe layer is located. For an Fe layer deposited on the Pd spacer, the critical thickness for the onset of two-magnon scattering is equivalent to the critical thickness

for the formation of misfit dislocations in Pd with $n \geq 4$ [155]. The area density of misfit dislocations [155] and the magnitude of two-magnon scattering saturate for $n \geq 9$. For Fe layers grown directly on GaAs(001), the formation of magnetic defects required either a thick Pd layer ($n > 130$) or a combination of a thin Pd ($n \geq 9$) and a thick Au layer (> 70); e.g. 90Au/9Pd/**16Fe**/GaAs(001) or 200Pd/**30Fe**/GaAs(001). In all samples the strength of the two-magnon scattering was found to be nearly independent of the thickness of the Fe. This implies that the two-magnon scattering is a bulk effect for the range Fe thicknesses studied (10 to 40 ML). This behavior can be expected in good crystalline films; once dislocation half loops are generated, they propagate along the $\{111\}_{\mathrm{Pd}}$ glide planes and are terminated at the outer interfaces. The extrinsic damping in all the samples listed in Tab. 5.1 exhibited a similar qualitative and quantitative behavior as a function of microwave frequency and magnetization angle. Since spin-pumping in magnetic bilayers affects the angular dependence of the FMR linewidth due to accidental crossovers of the resonance fields [159], the discussion will be now limited to the simple 200Pd/**30Fe**/GaAs(001) magnetic single layer sample.

5.1.3 Two-magnon scattering model

Two-magnon scattering, if applicable, can provide a simple model for the description of extrinsic damping in FMR. Inhomogeneous magnetic properties generate scattering of the resonant mode (uniform mode with q $\sim$ 0) into non-uniform modes ($\mathbf{q} \neq 0$ magnons), as discussed in section 2.5. From Eq. 2.48 it follows that magnon scattering is confined to degenerate magnons following the path of lobes, $\mathbf{q}_0(\psi_q)$, around the direction of the magnetic moment (see Fig. 5.7).

Two-magnon scattering formally enters the in-plane rf susceptibility [12] as an additional term R in the denominator (cf. Eq. 2.53)

$$\chi_{||} = \frac{M_s B}{B_{\mathrm{eff}} H - (\frac{\omega}{\gamma})^2 + i(H+B)\alpha\frac{\omega}{\gamma} + [\Re(R) + i\Im(R)]} \,, \tag{5.1}$$

where $B_{\mathrm{eff}} = H + 4\pi M_{\mathrm{eff}}$ is the effective magnetic induction, and the in-plane anisotropies are neglected for simplicity. The real part, $\Re(R)$, leads to a shift in the FMR field and the imaginary part $\Im(R)$ provides additional damping. $\Re(R)$ and $\Im(R)$ have to satisfy the symmetry of the magnetic inhomogeneities. In a rectangular network of misfit dislocations one expects to get additional four-fold anisotropies,

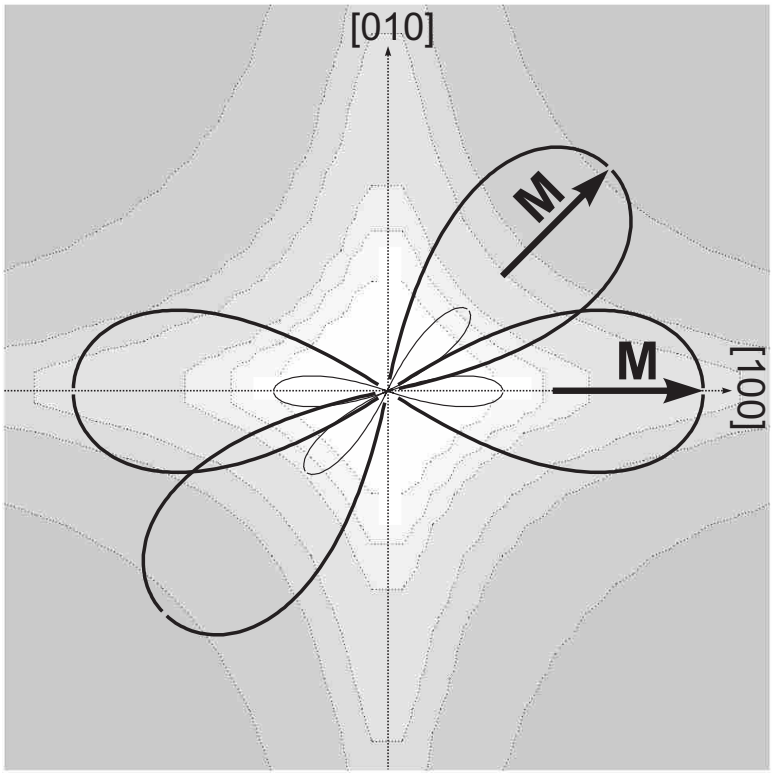

Figure 5.7: The black lines show the lobes of degenerate magnons calculated for 73 GHz (big lobes) and 24 GHz (small lobes). The background is a contour plot of the in-plane Fourier components from Eq. 3.12. Note that Pukite's type of $I(\mathbf{q})$, even if it were scaled to produce an anisotropic behavior for small q-vectors (large $\langle L \rangle$), would result only in a weak anisotropy for ΔH.

affecting both the FMR field and magnetic damping. In addition both, $\Re(R)$ and $\Im(R)$ are dynamic effects and depend on the microwave frequency. This leads to an important conclusion: *Magnetic anisotropies measured using FMR can have a frequency dependent contribution which is absent in dc measurements.*

The strength of two-magnon scattering as a function of the angle φ_M of the magnetization with respect to the in-plane crystallographic axis can be tested by inspecting the expression $\Im(R)$. The imaginary part of the two-magnon contribution to the susceptibility is proportional to the Fourier components of the scattering potential. Using this one can write

$$\Im\left[R(\varphi_M)\right] \sim \int I(\mathbf{q}_\parallel)\delta(\omega - \omega_{\mathbf{q}_\parallel}) d\mathbf{q}_\parallel^2 = 2 \int_{-\psi_{\max}}^{\psi_{\max}} I(q_0, \varphi_q, \varphi_M) \frac{q_0 d\psi_q}{\frac{\partial \omega}{\partial q}(q_0, \psi_q)} \ , \qquad (5.2)$$

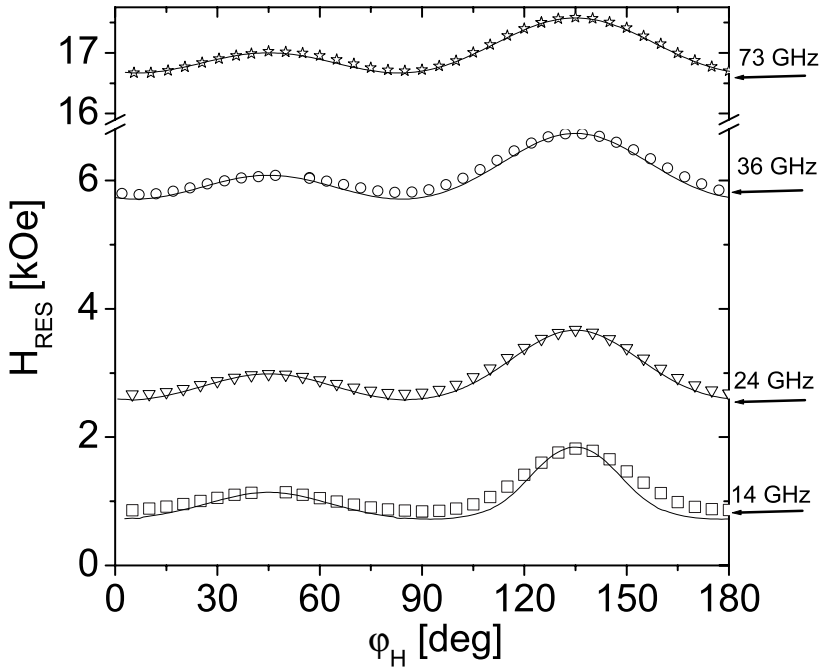

Figure 5.8: The FMR fields for the **30Fe** layer in 200Pd/**30Fe**/GaAs(001) as a function of the in-plane angle φ_H. Where $\varphi_H = 0$ corresponds to the $[100]_{\rm Fe}$ direction. Measurements were carried out at 73.0(☆), 36.4(○), 24.9(▽), and 14.1(□) GHz. The solid lines were calculated using the following parameters: The effective demagnetizing field $4\pi M_{\rm eff} = 18.7$ kG, in-plane uniaxial field $2K_U^{||}/M_S = -360$ Oe, four-fold in-plane anisotropy field $2K_1^{\parallel}/M_S = 330$ Oe, and g-factor, $g = 2.11$. The uniaxial in-plane anisotropy has the hard axis along the $[1\bar{1}0]_{\rm Fe}$ direction. With these parameters the agreement between the measured and calculated FMR fields along the $\langle 110\rangle_{\rm Fe}$ direction is within 10 Oe for all frequencies. This is not true when the field applied along the $\langle 100\rangle_{\rm Fe}$ directions where the discrepancy is of the order of 100 Oe. It is not possible to get a perfect fit for all microwave frequencies by using a single set of parameters, indicating that the magnetic anisotropies are partly frequency dependent.

where $I(\mathbf{q}_\parallel)$ represents the intensity of two-magnon scattering, and $\varphi_q = \varphi_M + \psi_q$ is the angle of the $\mathbf{q}_\parallel$ vector with respect to the $[100]_{\rm Fe}$ (defect) axis. The magnon group velocity $\frac{\partial\omega}{\partial q}(q_0, \psi_q)$ in Eq. 5.2 is proportional to the strength of the dipolar and exchange fields and represents the dipole-exchange narrowing of local inhomogeneities [49]. The term $\frac{\rm q_0}{\frac{\partial\omega}{\partial \rm q}(\rm q_0,\psi_q)}$ describes a weighting parameter along the path of the two-magnon scattering lobes $\mathbf{q}_\parallel(\psi_q)$. It turns out that for a given microwave frequency this factor is nearly independent of ψ_q. This means that the whole two-magnon scat-

tering lobe contributes to $\Im(R)$ with an equal weight, independent of the angle ψ_q. The exception is the q-space close to the origin of the reciprocal space. It is important to realize that long wavelength (small q) variations in magnetic properties lead to a simple superposition of local FMR peaks. The extrinsic FMR linewidth in this case merely reflects large length scale sample inhomogeneities and should not be treated by two-magnon scattering. McMichael et al. [160] concluded that the FMR linewidth is given by a superposition of local resonances when *the characteristic inhomogeneity field is larger than the interaction field* [163]. In the range of long wavelength defects the important part of the interaction field between grains having different magnetic properties is the magneto-static contribution $2\pi M_s \mathrm{q} t_F$ to the magnon energy dispersion, where t_F is the film thickness. The FMR spectrum is given by a simple superposition of local FMR peaks when

$$H_p L \geq 3\pi M_s t_F, \tag{5.3}$$

where H_p is the root mean square value of random variations of a local anisotropy field satisfying a Gaussian distribution, and L is the average grain size (see Fig. 4 in [164]). The summation of local FMR signals can result in a genuine zero frequency offset $\Delta H(0)$, (see reference [164]).

The critical angle $\psi_{\max}$ appearing in Eq. 5.2 decreases with a decreasing angle θ_M of the magnetization with respect to the sample plane. For $\theta_M \leq \pi/4$ no degenerate magnons are available [56]. The angle θ_H satisfying $\theta_M \leq \pi/4$ has to be calculated by minimizing the total magnetic energy. For the 200Pd/**30Fe**/GaAs sample this angle was $\theta_H = 12^\circ$ at 24 GHz, as can be seen in Fig. 5.10. This is an important criterion that allows one to test the applicability of two-magnon scattering to the interpretation of extrinsic damping. *ΔH from the extrinsic damping has to disappear when the direction of the magnetization is in the vicinity of the film normal.* It is interesting to note that the weighing parameter $\frac{\mathrm{q}_0}{\frac{\partial \omega}{\partial \mathrm{q}}(\mathrm{q}_0, \psi_q)}$ is nearly independent of θ_M. It increases somewhat very close to the critical angle $\theta_M = \pi/4$, where the two-magnon scattering is switched off.

5.1.4 Discussion of the FMR linewidth

The dependence of the FMR field and linewidth on the angle θ_H between the dc magnetic field and the sample normal is shown in Fig. 5.9. The data in Fig. 5.9b show that the damping decreases significantly in the vicinity of the perpendicular

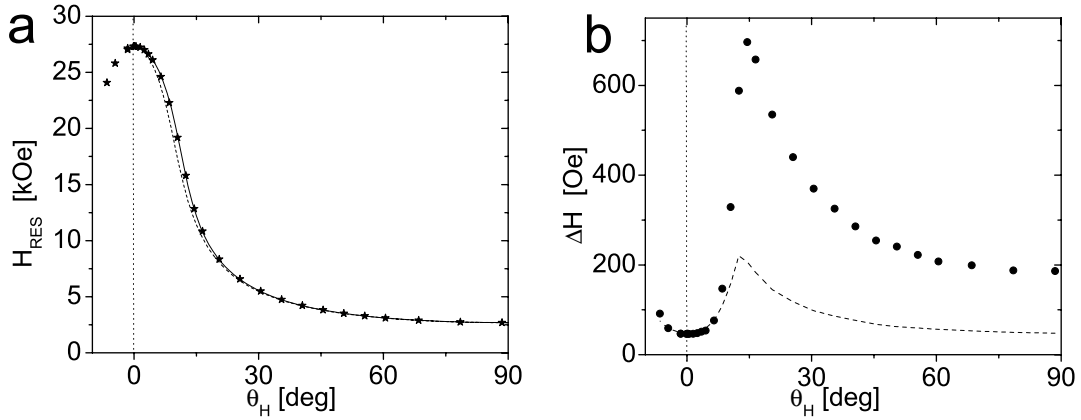

Figure 5.9: **(a)** The ferromagnetic resonance field in the **30Fe** layer in 200Pd/-**30Fe**/GaAs(001) as a function of the angle θ_H between the sample normal and the applied field H measured at 24 GHz. The the magnetic field was rotated in the (001) plane. The parameters used for to fit the data are as follows: $4\pi M_{\rm eff} = 20.6$ kG, $2K_1^{||}/M_S = 330$ Oe, $2K_U^{||}/M_S = -360$ Oe, $2K_1^{\perp}/M_S = -350$ Oe, and g =2.02. The in-plane anisotropy fields were determined from FMR measurements in the parallel configuration (see Fig. 5.8). The dashed line shows the fit obtained by fixing $4\pi M_{\rm eff}$, $2K_1^{||}/M_S$, $2K_U^{||}/M_s$, and g factor to the values from the in-plane FMR measurements (see a list of these parameters in the caption of Fig. 5.8). The only adjustable parameter is $2K_1^{\perp}/M_s = -700$ Oe. **(b)** Ferromagnetic resonance linewidth, ΔH, as a function of θ_H at 23.9 GHz. The dots represent the measured data and the dashed line represents the FMR linewidth $\Delta H_G(\theta)$ that was calculated using the Gilbert damping from the perpendicular configuration. The peak in the FMR linewidth for $\theta_H = 12^\circ$ is caused by the dragging of the magnetization behind the applied field.

configuration. In fact, the measured ΔH in the perpendicular configuration at 10 and 24 GHz was given exactly by the intrinsic damping, as previously illustrated in Figs. 5.4, 5.6, and 5.9b.

The strength of two-magnon scattering as a function of θ_H is usually expressed in terms of the adjusted frequency linewidth [53]

$$\frac{\Delta\omega}{\gamma} = \left(\frac{d\omega}{dH}\right)\Delta H_{\rm ext}(\theta_H)\ , \tag{5.4}$$

where $d\omega/dH = [\omega(H+\Delta H, \theta_H + \Delta\theta_H) - \omega(H,\theta_H)]/\Delta H$ using the FMR condition for the resonance frequency which includes the in-plane and out-of-plane magnetic anisotropies. It is more convenient to calculate $d\omega/dH$ by picking $\Delta\omega$ and evaluating the corresponding change in ΔH and $\Delta\theta_H$ satisfying the resonance condition.

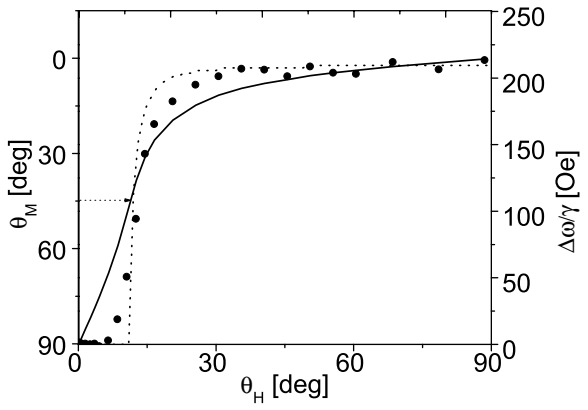

Figure 5.10: (•) represents the adjusted frequency FMR linewidth $\Delta\omega/\gamma$ from the extrinsic contribution as a function of θ_H at 23.9 GHz. The solid line shows the angle of magnetization θ_M as a function of θ_H. The dashed line shows the critical angle $\psi_{\max}$ as a function of θ_H. Notice that $\psi_{\max}$ describes the angular dependence of $\Delta\omega/\gamma$ quite well. $\psi_{\max}$ was scaled in order to compare it with $\Delta\omega/\gamma$.

The difference between the measured linewidth $\Delta H(\theta_H)$ and the linewidth predicted $\Delta H_G(\theta_H)$, using intrinsic Gilbert damping, determines the contribution arising from the extrinsic damping, $\Delta H_{\text{ext}}(\theta_H) = \Delta H(\theta_H) - \Delta H_G(\theta_H)$.

The dots in Fig. 5.10 show that the angle θ_M at which the two-magnon contribution rapidly disappears is in excellent agreement with the theoretical prediction of $\pi/4$. This behavior was found in all samples affected by the network of misfit dislocations. The extrinsic damping contribution remains nearly constant as a function of θ_H until the direction of the magnetic moment is in the vicinity of $\pi/4$ where it abruptly collapses to zero, as shown in Fig. 5.10. Fig. 5.9b shows that the FMR linewidth in the vicinity of the perpendicular configuration is given entirely by Gilbert damping. It follows that the extrinsic damping generated by a self-assembled network of misfit dislocations can be described by the two-magnon scattering mechanism. Since the angular dependence of $\Delta\omega(\theta_H)/\gamma$ is virtually traced by $\psi_{\max}(\theta_H)$ one can conclude that the two-magnon scattering intensity $I(\mathrm{q}, \theta_H)$ is independent of θ_H (see Fig. 5.10 and Eq. 5.2).

The presence of a marked difference in the magnetic parameters that were required for fitting the angular dependence of the FMR field in the parallel and perpendicular configuration (as illustrated in Figs. 5.8 and 5.9a) requires a brief discussion. The

origin of this discrepancy can be found in Fig. 5.9b. Two-magnon scattering affects the FMR linewidth most strongly when the resonance field increases rapidly with increasing θ_H. One can anticipate that in this range of θ_H the corresponding $\Re(R)$ term is present as well. This leads to a noticeable shift in the resonance field compared to that expected using the intrinsic (dc) magnetic anisotropies. The curvature of the FMR field as a function of θ_H in Fig. 5.9 is very sensitive to the g-factor. The change in this curvature due to the contribution of $\Re(R)$ requires that the data be fit with a different value of the g-factor compared to that corresponding to intrinsic magnetic properties. The artificially low value $g = 2.02$ that was required to fit the curvature in Fig. 5.9a consequently affected the value of $4\pi M_{\text{eff}}$ needed to fit the FMR field in the parallel configuration ($\theta_H = 90°$). Two-magnon scattering also affected the FMR field in the parallel configuration. In this case, the contribution of two-magnon scattering to the FMR field is not as strong, and therefore the deviations from a simple fitting (ignoring frequency dependent $\Re(R)$) are not as obvious. Even in the parallel configuration, however, it is not possible to fit the data at all microwave frequencies with the same set of parameters, as illustrated in Fig. 5.8. In fact the FMR data in the parallel configuration were fit quite well by assuming a partly frequency dependent in-plane four-fold anisotropy $K_1^{||}$. $2K_1^{||}/M_s$ changed from 305 Oe at 14 GHz to 390 Oe at 73 GHz. This is exactly what is expected, since two-magnon scattering in a rectangular network of misfit dislocations has to satisfy the in-plane four-fold symmetry which leads to a frequency dependent four-fold anisotropy given by the anisotropic contribution of $\Re(R)$.

The two-magnon scattering in samples with a self-assembled network of misfit dislocations showed a very pronounced four-fold in-plane dependence on the angle φ_M between the saturation magnetization and the crystallographic axes, as can be seen in Fig. 5.5. At the same time, the functional form of the four-fold anisotropy is dependent on the microwave frequency. These features require further discussion.

In ultrathin films the Fourier components of two-magnon scattering are restricted to the in-plane **q**-vectors; this is also the case for Pukite's model of RHEED at surface defects. Consequently, one could consider Pukite's in-plane Fourier components for the interpretation of the FMR results. There are, however, crucial differences. q_0 in two-magnon scattering is small, $\sim 6\times10^5$ cm^{-1} at 73 GHz and $\sim 1\times10^5$ cm^{-1} at 14 GHz for a 30ML thick Fe film. This means that two-magnon scattering is mainly sensitive to the reciprocal space of low q vectors. In RHEED large **k**-vectors, which

are comparable to the reciprocal space of the lattice, are important. There is an even more profound difference: In magnetism, defects result in a angular magnetic anisotropy. This means that the two-magnon scattering intensity can have an explicit dependence on the direction of the magnetization with respect to the symmetry axis of the magnetic defects. This case was recently addressed by Lindner et al. [161]. They observed an anisotropic extrinsic damping (measured along the $\langle 100 \rangle$ and $\langle 110 \rangle$ axes) for FeV superlattices. No detailed dependence of the FMR linewidth as a function of φ_M was shown. It was assumed that the defects were caused by surface steps. By using a simple argument based on the angular dependence of the uniaxial anisotropy Lindner et al. concluded that a rectangular distribution of interface steps results in two-magnon scattering with an anisotropic ΔH having a $\cos^2(2\varphi_M)$ dependence. This argument also applies to a rectangular network of misfit dislocations. However, this is not the only factor that depends on the angle with respect to the crystallographic axes. The Fourier components of the scattering intensity are the product of two parts. One is explicitly dependent on the angle φ_M and the other depends on the magnon wave vector $\mathbf{q}$,

$$I(\mathbf{q}, \varphi_M) = Q(\mathbf{q}) \cos^2(2\varphi_M). \tag{5.5}$$

In addition, lower order symmetry terms need to be considered. This is an isotropic contribution depending only on the magnitude of $\mathbf{q}$. One can write

$$I(\mathrm{q}, \varphi_M) = Q(\mathbf{q}) \cos^2(2\varphi_M) + Y(\mathrm{q}). \tag{5.6}$$

The $Y(\mathrm{q})$ term corresponds to a random distribution of defects and $Q(\mathbf{q})$ has to satisfy the symmetry of the defects. The lattice defects in crystalline samples are correlated with crystallographic axes and consequently $Q(\mathbf{q}) = Q(q, \varphi_q)$, where φ_q is the angle between $\mathbf{q}$ and the $[100]_{\mathrm{Fe}}$ defect axis. It turns out that $Q(\mathbf{q})$ is essential to explain the experimentally observed angular dependence of $\Delta H(\varphi_M)$ at various microwave frequencies.

$Q(q, \varphi)$ should be related to the average separation of misfit dislocations. The average separation of misfit dislocations is 10-20 nm corresponding to a Fourier component $\mathrm{q} \sim 2\pi \times 10^6$ cm^{-1}. In magnetic scattering one has to consider the exchange coupling within the ferromagnetic film. Lateral inhomogeneities on the scale of 10-20 nm create exchange fields that significantly average out the lateral variations of the magnetic anisotropy. This means that the defect length scale of 10-20 nm does not have to be directly applicable to the discussion of two-magnon scattering.

In order to explain the angular dependence of the two-magnon scattering the FMR results need to be addressed directly. The filled stars in Fig. 5.6a show $\Delta H(f)$ with the magnetization along $\langle 110 \rangle_{\mathrm{Fe}}$. $\Delta H(f)$ has a linear dependence on microwave frequency f with a slope corresponding to Gilbert damping and a modest zero frequency offset $\Delta H(0)_{\parallel}$. $\Delta H(0)_{\parallel}$ can be caused by long range inhomogeneities (superposition of local FMR lines) or an isotropic term $Y(q)$ in the scattering matrix $I(\mathbf{q})$ (see Eq. 5.6). If one assumes a genuine $\Delta H(0)_{\parallel}$, one has to ask why those long wave length inhomogeneities were not observed in the perpendicular FMR configuration. Long wave length inhomogeneities of the in-plane uniaxial anisotropy would result in a zero frequency offset for H applied perpendicular to the plane $\Delta H(0)_{\perp}$. This perpendicular offset would be $\sim \frac{1}{2}\Delta H(0)_{\parallel}$, and detectable. The absence of $\Delta H(0)_{\perp}$ can be explained by assuming an inhomogeneous in-plane four-fold anisotropy. Such an inhomogeneous anisotropy would cause $\Delta H(0)_{\parallel}$ but not $\Delta H(0)_{\perp}$. In the perpendicular FMR configuration $K_1^{\parallel}$ contributes to the free energy with the 4th power in the rf magnetization components and therefore produces an effective field proportional to the cube of the rf magnetization component and drops out from the resonance condition. One should point out that the perpendicular four-fold anisotropy $K_1^{\perp}$ is stronger than $K_1^{\parallel}$, see caption of Fig. 5.9, and if inhomogeneous would result in $\Delta H(0)_{\perp}$. The absence of $\Delta H(0)_{\perp}$ suggests that $K_1^{\perp}$ is homogeneous, and it is reasonable to assume that the same is true for $K_1^{\parallel}$.

Inhomogeneities in $K_1^{\parallel}$ should also result in an angular dependence of $\Delta H(0)_{\parallel}$ which would exhibit not a for fold, but an 8-fold symmetry. This contribution should disappear when the magnetization is oriented half way between $\langle 100 \rangle_{\mathrm{Fe}}$ and $\langle 110 \rangle_{\mathrm{Fe}}$ where the four-fold anisotropy field is zero. There is some evidence for this behavior in Fig. 5.5 at 23.9 GHz in the form of two additional shallow minima around the $\langle 110 \rangle_{\mathrm{Fe}}$ directions, but this effect is very weak. This leads to the second possible cause of $\Delta H(0)_{\parallel}$ which is based on the presence of $Y(\mathrm{q})$. The linear slope of $\Delta H(f)$ was given by the Gilbert damping and therefore the two-magnon contribution to the FMR linewidth was constant between 10 and 73 GHz. This implies that the two-magnon scattering approaches zero only below 10 GHz. A gradual approach to zero in two-magnon scattering below 10 GHz was observed by Twisselmann and McMichael in Py/NiO samples [160] and the constant two-magnon scattering above 10 GHz in this sample can be accounted for by the q-dependence of $Y(\mathrm{q})$.

Further analysis will be carried out for the angular dependent part of the two-

magnon scattering. The objective is to explain the in-plane angular dependence of the FMR linewidth and its frequency dependence. The pronounced four-fold angular dependence is due to the explicit $\cos^2(2\varphi_M)$-dependence of the scattering matrix on the angle φ_M (see Eq. 5.5). One needs to find a function $Q(\mathbf{q})$ that accounts for the measured angular dependence $\Delta H(\varphi_M)$ at various microwave frequencies. The $Q(\mathbf{q})$ has to satisfy the symmetry of the lattice defects. The following ansatz may be used

$$Q(q,\varphi) = \cos^4(2\varphi_q). \tag{5.7}$$

No dependence on q has been assumed at this point. The angular dependence of $\Delta H^{2\mathrm{m}}$ was evaluated by using the following simple expression

$$\Delta H^{2\mathrm{m}} = \frac{\Im(R(\varphi_M))}{2H + 4\pi M_{\mathrm{eff}}}. \tag{5.8}$$

This equation accounts only partly for the elliptical polarization at FMR in the parallel configuration. No explicit dependence of $\Im(R)$ on the elliptical polarization was considered.

A simple evaluation of $\Delta H^{2\mathrm{m}}$ using Eqs. 5.2 and 5.8 explains the experimental results quite well (cf. Figs. 5.5 and 5.12). The calculations result in a big anisotropy in $\Delta H^{2\mathrm{m}}$. It is interesting to note that one does not have to rescale the $I(\mathbf{q},\varphi_M)$ ansatz for each microwave frequency in order to get a reasonable quantitative agreement between the calculated and measured $\Delta H(\varphi_M)$. The measured angular dependence of $\Delta H(\varphi_M)$ is sinusoidal at 73 GHz. At lower frequencies the curvature around the maxima is bigger than around the minima. This feature is quite pronounced at 24 GHz. All of these characteristics are well reproduced in the calculations, compare Figs. 5.5 and 5.12. The good agreement between the experimental results and calculated values for $\Delta H(\varphi_M)$ allows one to draw the following conclusion: integration along the lobes of degenerate magnons, see Fig. 5.11, indicates that the scattered magnons are propagating preferentially along the $\langle 100\rangle_{\mathrm{Fe}}$ crystallographic directions [154]. This means that the two-magnon scattering by defects from the network of misfit dislocations leads to channelling of magnons. A more detailed and quantitative comparison between the two-magnon scattering model and experiment would require to evaluate the relaxation term R, using the Kubo formalism in order to properly account for the ellipticity of the rf polarization in the in-plane configuration. This procedure would allow further refinement of $Q(\mathrm{q},\varphi)$.

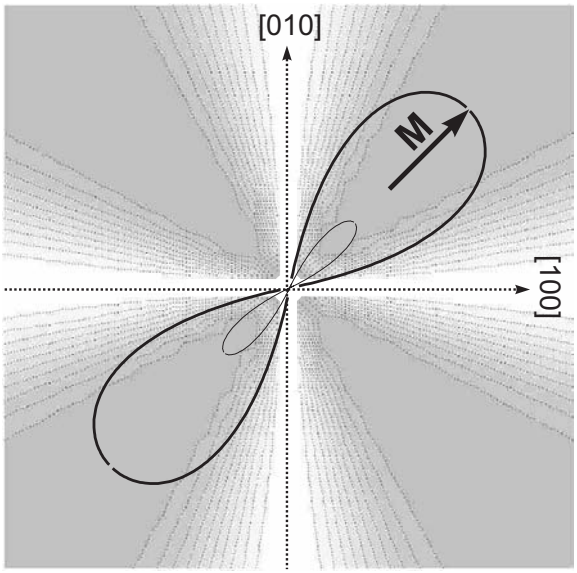

Figure 5.11: Two magnon scattering lobes at 24 and 73 GHz in the q-space of the magnetic scattering intensity $Q(q, \varphi)$ given by Eq. 5.7. The dashed lines are a contour map of the function in Eq. 5.7. Note that the orientation of lobes (magnetization) affects the angular dependence of FMR linewidth caused by the misfit dislocation network. When the lobes are oriented parallel the $\langle 110 \rangle_{\mathrm{Fe}}$ directions they have a weaker contribution than when they are oriented along the $\langle 100 \rangle_{\mathrm{Fe}}$ directions.

5.1.5 Summary

FMR studies were carried out on lattice strained Au/Pd/**Fe**/GaAs(001) and Pd/**Fe**/-GaAs(001) structures. It has been shown that the lattice strain in Pd is relieved by a self-organized rectangular network of misfit dislocations. The dislocations have an average separation of 10-20 nm. This network of misfit dislocations is revealed during the growth by fan-out of RHEED streak patterns in the cap Au(001) layers. The lattice defects driven by the dislocation network resulted in strong two-magnon scattering having a four-fold anisotropy due to the rectangular symmetry of the magnetic defects given by the glide planes of the misfit dislocations. The two-magnon scattering was found to be nearly independent of the Fe film thickness. This implies that the defects, due to the misfit dislocation network, propagate through the whole multilayer structure and therefore the associated magnetic defects represent bulk properties. The angular dependence of two-magnon scattering has been discussed by using the Fourier transform of the magnetic defects. It has been shown that measurement of the FMR linewidth as a function of the angle of the magnetization with respect to the

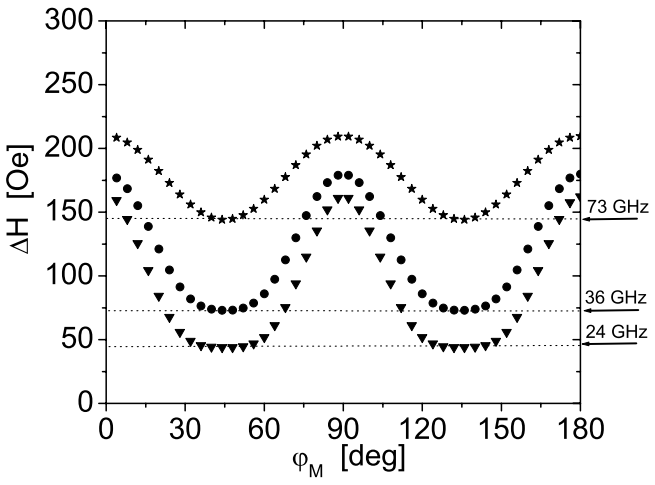

Figure 5.12: Calculated ferromagnetic resonance linewidth at 73(★), 24(•), and 14(▼) GHz as a function of the in-plane angle φ_M. Where $\varphi_M = 0°$ corresponds to the $[100]_{\mathrm{Fe}}$ direction of Fe. The calculations were carried out using $I(\mathbf{q}, \varphi_M) = Q(\mathbf{q}) \cos^2(2\varphi_M)$, where $Q(\mathbf{q})$ is given by Eq. 5.7. Dotted lines indicate the linewidth due to intrinsic damping at 73, 36, and 24 GHz.

crystallographic axes and as a function of microwave frequency allow one to determine the main features of the magnetic scattering intensities in the range of small $\mathbf{q}$ vectors. The angular dependence of the required scattering intensity, $Q(\mathbf{q})$, suggests the presence of channelling of scattered spin waves along the defect lines (the $\langle 100 \rangle_{\mathrm{Fe}}$ directions). Two-magnon scattering also leads to additional magnetic anisotropies which are dependent on the microwave frequency. An analysis of the out-of-plane FMR measurements based on frequency independent magnetic anisotropies, results in an unrealistic g-factor and and an unrealistic effective demagnetizing field $4\pi M_{\mathrm{eff}}$.

5.2 Other Systems with Two-Magnon Scattering

5.2.1 NiMnSb/InP(001)

Half metallic NiMnSb films were grown on InP(001) wafers by the Molenkamp group [165]. High resolution x-ray diffraction confirmed the very good crystalline quality of the NiMnSb(001) films with the lattice constant $a = 5.91 \pm 0.005$ Å. This lattice spacing implies a lattice mismatch between NiMnSb and InP(001) of only 0.6 percent. Details can be found in [165]. The NiMnSb films investigated had thicknesses $t_F = 5$, 10, 15, 20, 30, 42, and 85 nm. FMR was measured at 23.9 and 36.4 GHz.

The g-factor was found to be 2.03 and 2.02 for the 42 and 15 nm thick films, respectively. This g-factor is very close to the free electron value, indicating a weak spin-orbit interaction. The magnetic moment was determined to be $M_S = 590 \pm 10$ emu/cm^3 at RT [30].

The angular dependence of ΔH for the samples with $t_F = 5$, 42, and 85 nm is shown in Fig. 5.13. One can identify an angular independent ΔH_0, a four-fold $\Delta H_4 \cos^2(2\varphi_M)$, and a two-fold $\Delta H_2 \cos^2(\varphi_M)$ contribution. ΔH also rapidly increased with the film thickness, as shown in Fig. 5.13. For the thinnest sample ($t = 5$ nm), the lowest value of the FMR linewidth was 20 Oe at 23.9 GHz for the magnetization directed along the $\langle 100 \rangle$ crystallographic directions. This FMR linewidth scaled linearly with the microwave frequency with no zero frequency offset. The Gilbert damping parameter was remarkably small, $\alpha = 5 \times 10^{-3}$. The small deviation of the g-factor from 2 and the small Gilbert damping are consistent and indicate that the intrinsic spin-orbit interaction in cubic NiMnSb is weak.

The FMR linewidth with the direction of the magnetic field close to the film normal decreased rapidly to the value that corresponds to the intrinsic Gilbert damping, as illustrated in Fig. 5.13b. This behavior is a hallmark of two-magnon scattering. In the NiMnSb films the dragging effect is small at 24 GHz since the demagnetizing field is significantly smaller than the applied field and therefore the features of two-magnon scattering are reflected directly in the FMR linewidth ΔH, as shown in Fig. 5.13b.

Plan view TEM studies on the NiMnSb films carried out by Kavanagh's group at SFU have shown that thicker films have two rectangular networks of lattice defects with defect lines parallel to the $\langle 100 \rangle$ and $\langle 110 \rangle$ in-plane crystallographic axes [166]. The measured angular dependence of the FMR linewidth, shown in Fig. 5.13, allows one to draw the following conclusions [30]:

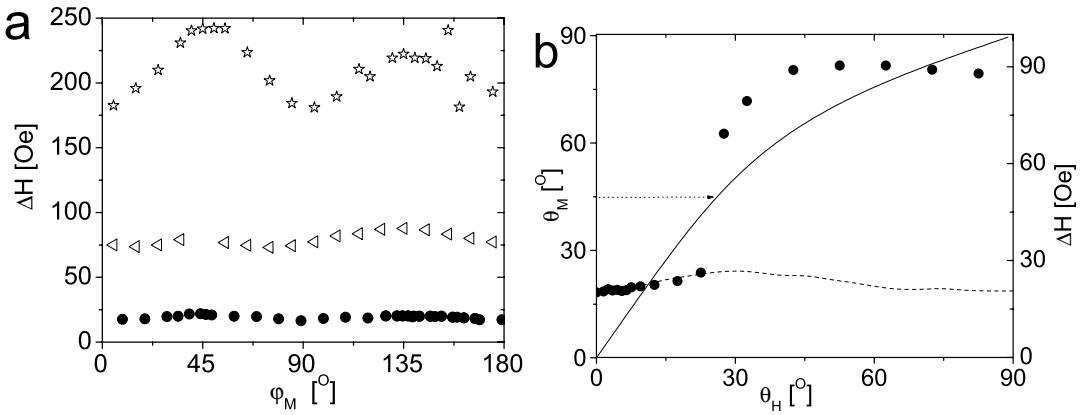

Figure 5.13: **(a)** ΔH for NiMnSb films as a function of the in-plane orientation of the magnetization , φ_M, measured at 23.9 GHz. The symbols (•), (◁), and (☆) correspond to film thicknesses 5, 42, and 85 nm, respectively. **(b)** The out-of-plane dependence of the FMR linewidth. θ_H is the polar angle that describes the orientation of the applied field H: $\theta_H = 0$ corresponds to H applied along the film normal. The dashed line represents the calculated angular dependence of the intrinsic damping, $\alpha = 6 \times 10^{-3}$. The difference between the data and the solid line shows the effectiveness of two-magnon scattering as a function of the angle of the applied field θ_H. The angle of the magnetization with respect to the sample normal, θ_M, is shown by the solid line. Note that the two-magnon scattering is switched off at $\theta_M \leq \pi/4$ in excellent agreement with the two-magnon scattering model.

(i) The effectiveness of the two-magnon scattering mechanism is independent of the angle of the magnetic moment with respect to the sample surface until the magnetization is close to the film normal where it rapidly collapses to zero (see Fig. 5.13b). This appears to be a general feature of two-magnon scattering, as shown in the previous section.

(ii) The large angular independent contribution ΔH_0 indicates that thick NiMnSb films were affected by a sizeable isotropic in-plane lattice disorder which can be described by $Y(\mathrm{q})$, (see Eq. 5.6).

(iii) An increasing density of crystallographic defects also affects the width of the hysteresis loops. The coercive field increased from 3 Oe to 60 Oe with increasing thickness.

5.2.2 Cr/Fe/GaAs(001)

Ultrathin Fe layers covered by Cr are another system which showed strong two-magnon scattering [167]. In this system, roughness driven frustration in the antiferromagnetic Cr cap layer is very likely responsible for the loss of translational invariance [168, 169] and allows two-magnon scattering to be operative. The out-of-plane angular dependence of the FMR linewidth and the complete absence of extrinsic linewidth in the perpendicular FMR configuration allows one to identify two-magnon scattering as the source of the extrinsic line broadening in the parallel configuration [167]. Similar line broadening effects where observed for ultrathin magnetic films grown on antiferrogametic NiO substrates by other groups [170, 171, 56, 172, 173, 174]. The antiferrogmagnetic nature of Cr [175, 176] and the nanoscale roughness of the Fe template most likely lead to magnetic frustration effects and cause a spatially inhomogeneous exchange bias [177]. Recently, step induced frustration of the antiferromagnetic order in ultrathin Mn on Fe(001) was directly observed recently by Schlickum et al. [178] using spin polarized STM.

5.3 General Remarks

Angular dependent extrinsic damping created by a rectangular network of defects appears to be a common phenomenon. It was observed in previous studies by Heinrich's group, using metastable bcc Ni/Fe(001) bilayers grown on Ag(001) substrates [179], and Fe(001) films grown on bcc Cu(001) [47]. After depositing 3 ML of Ni the Ni/Fe bilayers exhibited a major structural change from a body centered tetragonal structure to a face centered structure which better approximated the stable fcc phase of Ni(001). The resulting network of rectangular lattice defects was perhaps similar to those observed by Wulfhekel et al. [79]. For these Ni/Fe bilayers not only the magnetic damping had a large anisotropy, but also the in-plane four-fold anisotropy field was enhanced to several kOe which is significantly above the corresponding Fe bulk value $\sim \frac{1}{2}$ kOe. Coercive fields of several hundred Oe were observed due to the presence of enhanced anisotropy and lattice defects and dependent on the Ni film thickness [180]. The angular dependence of the FMR linewidth indicated that the defect lines were oriented along the $\langle 100 \rangle$ directions of Fe(001). Another example of such behavior are bcc Fe/Cu(001) layers grown on Ag(001) substrates. In this case, the bcc Cu(001) layer went through a lattice transformation after the thickness of the Cu layer exceeded 10 ML. Again, a strong anisotropy in ΔH was observed for the Fe(001) films grown on these lattice transformed Cu(001) substrates. The angular dependence indicated that the defect lines in the Cu(001) layers and the symmetry axes of magnetic defects in Fe(001) are directed along the $\langle 100 \rangle$ crystallographic directions. In these samples, however, no significant enhancement of the in-plane four-fold anisotropy was found.

All these FMR studies have shown that the presence of angular dependent damping and frequency dependent anisotropies is in general a 'smoking gun', indicating lattice defects. In no instance has an in-plane angular dependent intrinsic damping been observed.

In Fig. 5.14, the effective FMR linewidth due to two-magnon scattering $\Delta H^{2\mathrm{m}}$ measured at 24 GHz has been plotted against the coercive fields for all the samples discussed in this section (Pd/Fe/GaAs, NiMnSb/InP, and Cr/Fe/GaAs). It is remarkable that the strength of the two-magnon scattering in all samples can be described by the *same* linear relationship between $\Delta H^{2\mathrm{m}}$ and H_c, as shown in Fig. 5.14. This clearly indicates that the defects that lead to an increase of the coercive fields are at the same time responsible for two-magnon scattering.

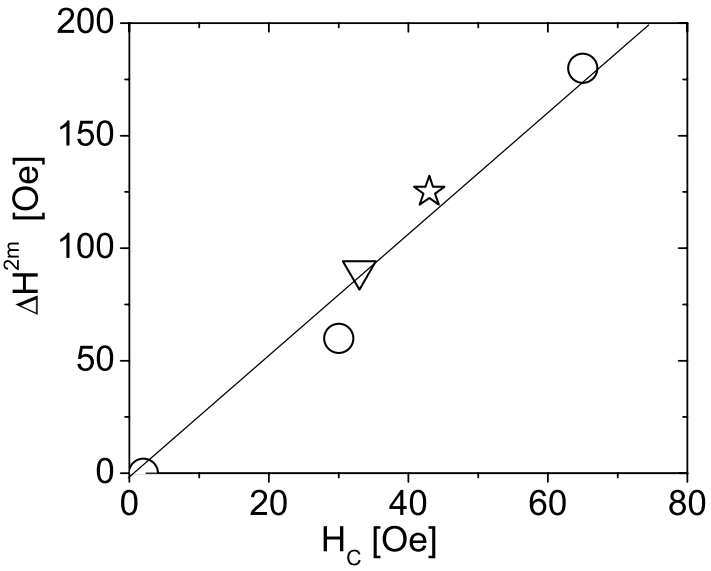

Figure 5.14: ΔH due to two-magnon scattering measured at 23.9 GHz versus the coercive fields for the 3 thicknesses of NiMnSb/InP(001) shown in Fig. 5.13a (○), a 20Cr/16Fe/GaAs(001) sample (▽), and a 200Pd/30Fe/GaAs(001) sample (☆).

Chapter 6

Time-Resolved MOKE Measurements

Time-resolved magneto-optic Kerr effect microscopy (TRMOKE) is a stroboscopic technique with which magneto-dynamics can be investigated with pico second time resolution and sub micron spatial resolution. The TRMOKE studies were carried out in Regensburg with Professor Back's group and in Edmonton with Professor Freeman's group. For details of the experimental setup see section 3.3.2.

6.1 Gilbert damping: (Au, Pd)/Fe/GaAs(001)

Fig. 6.1 shows the time evolution of the measured perpendicular (polar) component of the magnetization in a 20Au/16Fe/GaAs^{n}/GaAs$^{n^+}$ sample, obtained with the TRMOKE setup in Regensburg. The magnetization was excited by the magnetic in-plane field associated with a photo current generated by illumination of the Fe/GaAs Schottky barrier [86, 181]. In addition to the magnetic pump field pulse the specimen were subjected to a uniform dc bias field, H_B, applied in the plane of the magnetic film. In response to the magnetic field pulse the magnetization was triggered to a free FMR-like precession resulting in an oscillatory TRMOKE signal. In Fig. 6.1 raw data are shown (open circles) for $H_B = 1$ kOe applied parallel to the easy axis ($[110]_{Fe}$). The electro-optic effects (due to the pump beam) and the quasi magneto-static component of magnetization (related the the field pulse shape) cause a mostly linear signal background (see Fig. 6.1). This background was removed by subtracting a running average value from the data, as shown in Fig. 6.1. The size of the averaging window

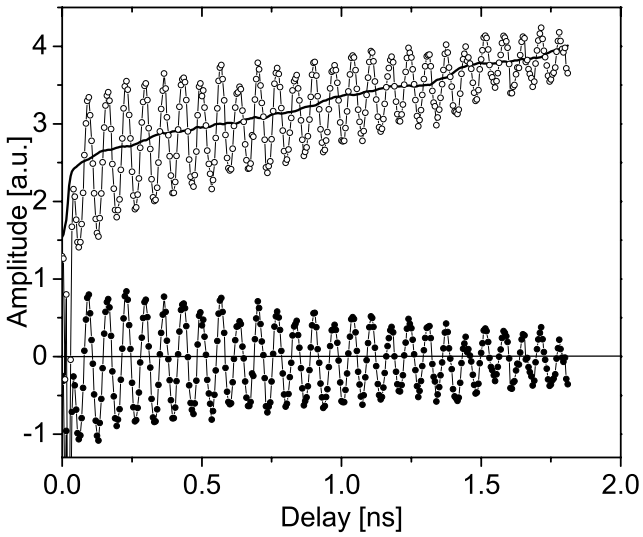

Figure 6.1: This figure illustrates how the background was removed from the raw data (∘). The solid line corresponds to the average background value of (∘) with an averaging window of one oscillation period (90 ps). (•) symbols represent the data without the background. The sample was 20Au/16Fe/GaAs^{n}(001) with a bias field $H_B = 1$ kOe $\parallel [110]_{Fe}$ leading to oscillations of the magnetization at $f = 14.8$ GHz.

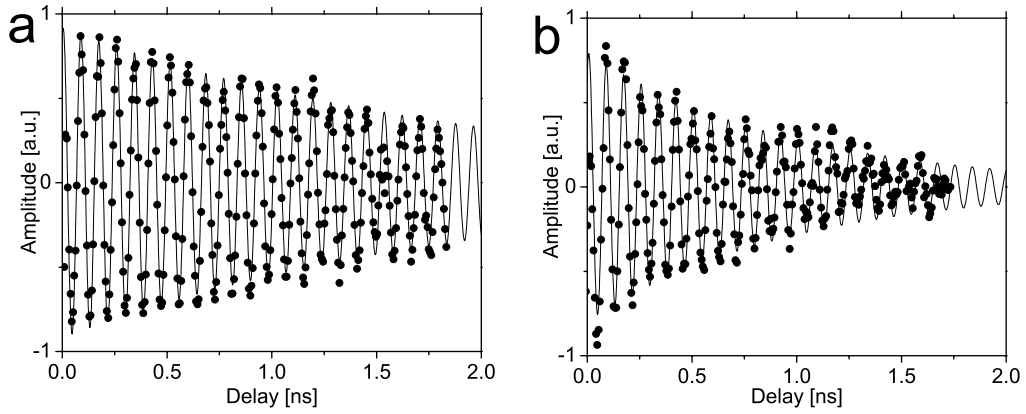

Figure 6.2: Time resolved magnetization data for **(a)** 20Au/16Fe/GaAs^{n} with the bias field $H_B = 500$ Oe $\parallel [110]_{Fe}$ ($f = 11.8$ GHz) and **(b)** 20Au/25Pd/16Fe/GaAs^{n} with $H_B = 500$ Oe $\parallel [110]_{Fe}$ ($f = 12.0$ GHz). The solid lines are fits obtained using Eq. 6.3.

was synchronized to one oscillation period of the magnetization to avoid oscillations in the running average. The time evolution of the magnetization was measured for several magnetic bias fields between 0 and 1 kOe, applied parallel to the easy axis

($[110]_{\mathrm{Fe}}$). In Fig. 6.2 two examples (20Au/16Fe/GaAs and 20Au/25Pd/16Fe/GaAs) with $H_B = 500$ Oe are shown.

6.1.1 Data analysis

For homogeneous precession of the magnetization (single spin approximation) the spin dynamics can be analyzed in two ways: (i) Numeric integration of the LLG (e.g. by the Runge Kutta method). (ii) Analytic solution of the LLG that is valid for small angle motion. The amplitude, damping constant, and magnetic anisotropy fields are adjusted to achieve the best fit. Since the pump fields were only of the order of 20 Oe and the samples had in-plane anisotropy fields of the order of ~ 500 Oe the precessional angle in all TRMOKE measurements was less than 0.5°. Therefore $m_{\mathrm{rf}} \ll M_S$ and small angle solutions are fully justified.

For small angle motion in a coordinate system in which the static magnetization is parallel with the X-axis the LLG is given by a set of two coupled differential equations in m_Y^{rf} and m_Z^{rf} which can be easily transformed into a single second order differential equation for a damped harmonic oscillator in m_Z^{rf},

$$(1+\alpha^2)\ddot{m}_Z = -\gamma\alpha(\mathfrak{B}_{\mathrm{eff}} + \mathfrak{H}_{\mathrm{eff}})\dot{m}_Z - \gamma^2 \mathfrak{H}_{\mathrm{eff}}\mathfrak{B}_{\mathrm{eff}} m_z, \tag{6.1}$$

where m_Z is the rf component of the magnetization normal to the specimen plane. Using the oscillator ansatz of the form $m_Z = m_Z^0 e^{iAt}$ in Eq. 6.1, one gets

$$A = \frac{i\gamma\alpha(\mathfrak{B}_{\mathrm{eff}} + \mathfrak{H}_{\mathrm{eff}})}{2(1+\alpha^2)} + \sqrt{-\frac{\gamma^2\alpha^2(\mathfrak{B}_{\mathrm{eff}} + \mathfrak{H}_{\mathrm{eff}})^2}{4(1+\alpha^2)^2} + \frac{\gamma^2 \mathfrak{B}_{\mathrm{eff}}\mathfrak{H}_{\mathrm{eff}}}{1+\alpha^2}}. \tag{6.2}$$

In the small damping limit $\alpha \ll 1$ one can write for free FMR precession

$$m_Z(t) = m_Z(0) e^{-\frac{t}{\tau}} \cos\omega t, \tag{6.3}$$

where τ is the decay time $\tau = \frac{2}{\alpha\gamma(\mathfrak{B}_{\mathrm{eff}} + \mathfrak{H}_{\mathrm{eff}})}$ and ω is the angular frequency of the precession $\omega = \gamma\sqrt{\mathfrak{B}_{\mathrm{eff}}\mathfrak{H}_{\mathrm{eff}}}$. The effective magnetic induction $\mathfrak{B}_{\mathrm{eff}}$ and effective field $\mathfrak{H}_{\mathrm{eff}}$ include magnetic anisotropies and external bias field and were defined in section 2.3.1. In the special case of H_B and M_S parallel to the easy direction ($[110]_{\mathrm{Fe}}$) one has $\mathfrak{B}_{\mathrm{eff}}^{[110]} = H_B + 4\pi M_{\mathrm{eff}} + \frac{K_1^{\parallel}}{M_S}$ and $\mathfrak{H}_{\mathrm{eff}}^{[110]} = H_B - \frac{2K_1^{\parallel}}{M_S} - \frac{2K_U^{\parallel}}{M_S}$.

6.1.2 Discussion

Fits to the data using Eq. 6.3 and numeric solutions of the LLG are indistinguishable and describe the data well. The results of both kinds of analysis (analytic

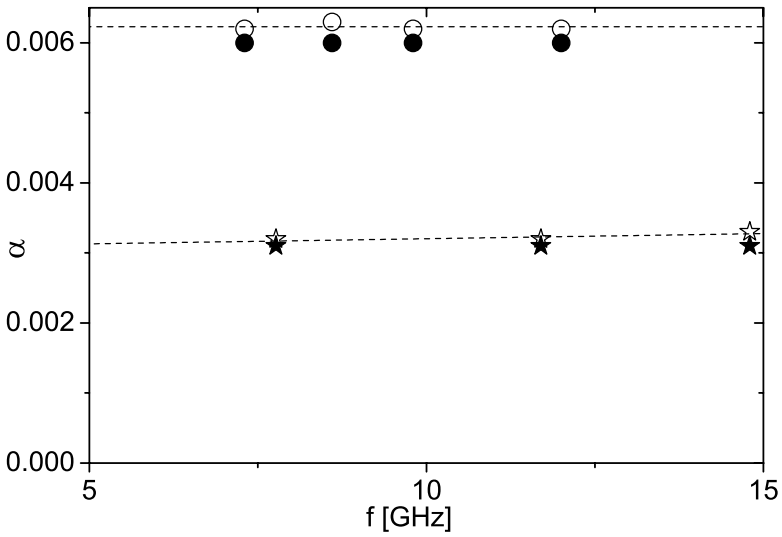

Figure 6.3: The damping parameter α determined for different bias fields (frequencies) for the 20Au/16Fe/GaAs (★☆) sample and the 20Au/25Pd/16Fe/GaAs (●○) sample. The filled symbols were obtained from fits using numeric solutions of the LLG equations and the open symbols were obtained from fits using the analytic function described by Eq. 6.3.

and numeric) are identical and the corresponding damping parameters are shown in Fig. 6.3. The frequency independence of the damping parameter α in Au/Fe/GaAs and Au/Pd/Fe/GaAs samples clearly shows that the damping is intrinsic. The magnitude of the damping in the 20Au/16Fe/GaAs sample determined by TRMOKE was found to be 10% smaller than that found by a standard FMR technique in the same sample[1]: $\alpha_{\mathrm{TRMOKE}} = 3.2 \pm 0.2 \times 10^{-3}$, $\alpha_{\mathrm{FMR}} = 3.8 \pm 0.2 \times 10^{-3}$. The additional damping due to spin-pumping in the 20Au/25Pd/16Fe/GaAs sample was found to be $\alpha_{\mathrm{TRMOKE}}^{\mathrm{add\ 25Pd}} = 3.0 \pm 0.2 \times 10^{-3}$ in excellent agreement with that found using standard FMR; $\alpha_{\mathrm{FMR}}^{\mathrm{add\ 25Pd}} = 2.9 \pm 0.2 \times 10^{-3}$ (cf. Fig. 4.19).

Fig. 6.4 is a Fourier transformation of the time domain data set shown in Fig. 6.2a. Due to the finite length of the time scan (2 ns) the frequency resolution of the Fourier transformation is limited to 500 MHz. The Fourier transform in Fig. 6.4 appears to have a better resolution because the time scan was artificially extended to 20 ns by filling it with zeros (zero padding) prior to the Fourier transformation. In the same

[1]In the samples with Schottky barrier the annealing of the $GaAs^{n}/GaAs^{n^{+}}(001)$ substrate after hydrogen cleaning was avoided and led to a 15 % smaller damping constant (linewidth) when compared to samples grown on annealed GaAs, cf. Tab. 4.2.

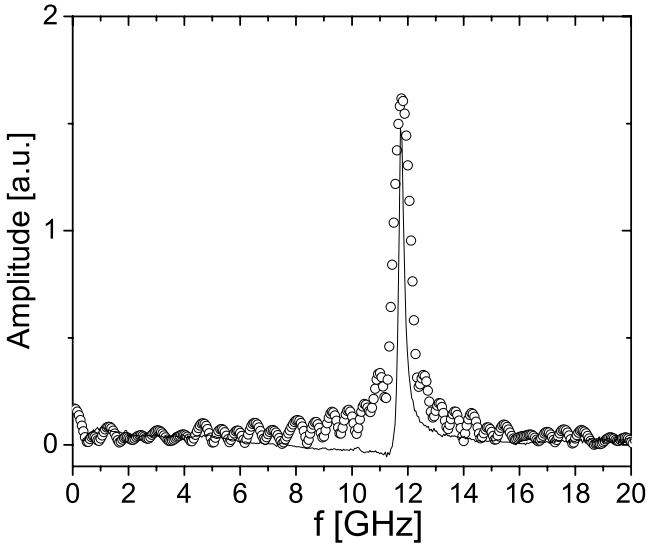

Figure 6.4: (∘) symbols are a Fourier transform of the TRMOKE data shown in Fig. 6.2a. The solid line corresponds to the microwave absorption spectrum of the same sample with the same bias filed measured using a network analyzer. The broadening of the peak in the TRMOKE data is caused by the finite length of the optical delay (2 ns).

figure, a FMR spectrum measured on the same sample with the same bias Field, using a network analyzer, was superimposed to illustrate the true frequency linewidth of the sample. The frequency linewidth is narrower than that obtained from the Fourier transformed TRMOKE data and given by $\Delta f_{\mathrm{FMR}} = 90$ MHz. Using $\Delta f/f = 2\alpha$ this results in $\alpha = 3.7 \pm 0.1 \times 10^{-3}$ and is in perfect agreement with conventional FMR measurements performed at higher frequencies.

The bias field dependence of the precessional frequency with ($H_B \parallel [110]_{\mathrm{Fe}}$) can be used to determine the g-factor and $4\pi M_{\mathrm{eff}}$. This was done for the 20Au/16Fe/GaAs sample by combining TRMOKE and network analyzer data measured on the same sample and resulted in $g = 2.10 \pm 0.01$ and $4\pi M_{\mathrm{eff}} = 17.0 \pm 0.2$ kOe (see Fig. 6.5).

There are two reasons why the FMR measurements were more suitable (when compared with TRMOKE) to determine magnetic parameters such as g-factor, $4\pi M_{\mathrm{eff}}$, and anisotropies. In TRMOKE the range of accessible frequencies was small (only from 7 to 14 GHz), in addition the precessional frequency cannot be determined very accurately due to the finite length of the time scan (uncertainty $\sim$ 100 MHz). These disadvantages resulted in a bigger error.

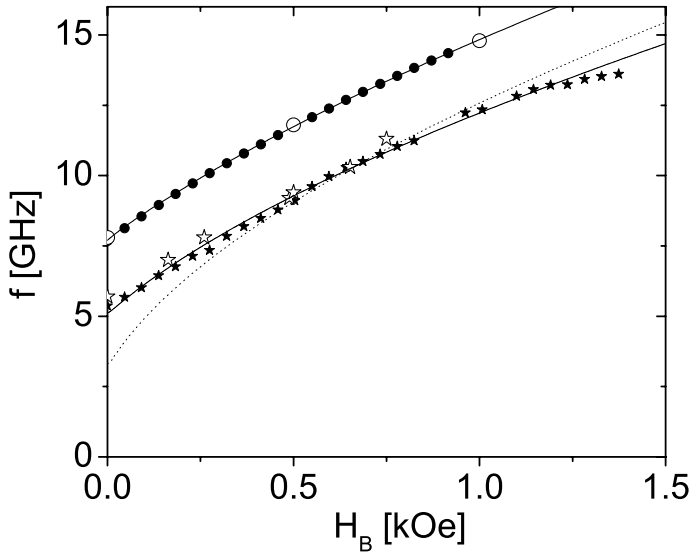

Figure 6.5: Resonance frequency as a function of applied bias field with $H_B \parallel [110]_{\mathrm{Fe}}$ in the 20Au/16Fe/GaAs$^{\mathrm{n}}$ (●○) and 20Au/20Cr/16Fe/GaAs$^{\mathrm{n}}$ (★☆) films. The filled points were obtained using FMR data acquired by means of a network analyzer, while the open points were obtained using TRMOKE. The solid lines are fits allowing one to determine the g-factor and $4\pi M_{\mathrm{eff}}$. The results of this fitting procedure yielded $g = 2.10$, $4\pi M_{\mathrm{eff}} = 17.0$ kOe for 20Au/16Fe/GaAs and $g = 1.79$, $4\pi M_{\mathrm{eff}} = 18.4$ kOe for 20Au/20Cr/16Fe/GaAs. The dotted line was calculated for the 20Au/20Cr/16Fe/GaAs sample using $g = 2.09$ and $4\pi M_{\mathrm{eff}} = 18.4$ kOe.

6.2 Two-Magnon Scattering: Cr/Fe/GaAs

6.2.1 Measurements on Cr/Fe/GaAs

Based on a good understanding of the TRMOKE data for the samples with Gilbert damping it is now interesting to compare these results with those obtained using samples which exhibited strong two-magnon relaxation in FMR. The 20Au/20Cr/16Fe/-GaAs$^{\mathrm{n}}$/GaAs$^{\mathrm{n}^+}$(001) sample provides such a case. In Fig. 6.6 the data for this sample were measured for four different bias fields directed along the $[110]_{\mathrm{Fe}}$ direction. Clearly, the relaxation appears to be much faster compared to the samples with intrinsic damping. In Fig. 6.8 the relaxation corresponding to this series of measurements was put into context with the FMR measurements on the same sample (relaxations are represented by the effective damping parameter, $\alpha_{\mathrm{eff}}\frac{\gamma}{\omega}\Delta H$. The apparent damping

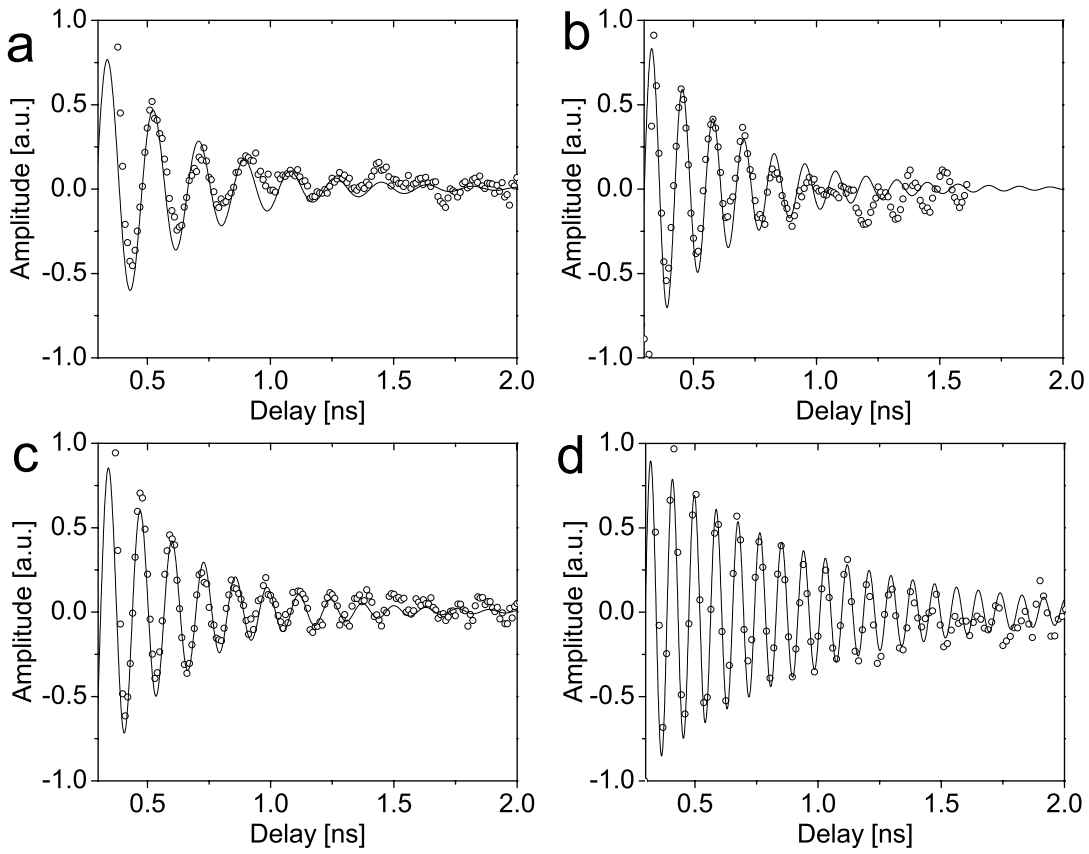

Figure 6.6: Four data sets showing the time evolution of the magnetization in the 20Au/20Cr/16Fe/GaAs sample with $H_B \parallel [110]_{\mathrm{Fe}}$ at four different bias fields **(a)** $H_B = 0$ Oe ($f = 6.1$ GHz), **(b)** $H_B = 250$ Oe ($f = 8.6$ GHz), **(c)** $H_B = 500$ Oe ($f = 9.4$ GHz), and **(d)** $H_B = 750$ Oe ($f = 11.3$ GHz). Note that the apparent damping in **(d)** is significantly reduced. The effective damping parameters determined from all fits are shown in Fig. 6.8.

in the TRMOKE measurements is always smaller than is obtained from the FMR results. Under certain experimental conditions (bias field, focussing of the pump beam) the two-magnon contribution to the damping was reduced by approximately 80%, as shown in Figs. 6.6d and 6.8 (open star at 11.3 GHz), and as shown in Fig. 6.6b the measured oscillations suddenly changed their phase. To understand these two unexpected features one has to consider the spatial and time dependence of the magnetic pulse field created by the Schottky diode switch.

6.2.2 Pump field inhomogeneity

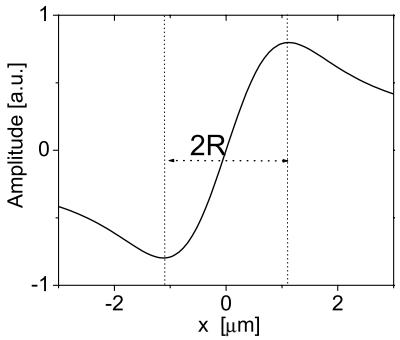

Figure 6.7: Cross-section of the excitation profile generated by the Schottky diode, where x is parallel to $\mathbf{M}$.

Since the photo current flows perpendicular to the Fe/GaAs^{n} interface, its corresponding magnetic field is oriented in the film plane with circular field lines centered around the spot of the pump beam, as illustrated in Fig. 3.17a. On the circle all angles from 0 to 2π between pump field direction and the direction of $\mathbf{M}$ are realized. The direction of $\mathbf{M}$ was fixed by the bias field to be parallel with $[110]_{\mathrm{Fe}}$. This excitation field configuration is similar to that used in experiments at SLAC [182, 183] (see also appendix A). As illustrated in Fig. 3.17a at points, where the pump field direction is perpendicular to the magnetization the exciting torque reaches a maximum, and in places where $\mathbf{M}$ is parallel or antiparallel to the pump field no excitation takes place. Since the pump beam and the corresponding photo current have a Gaussian profile, the field amplitude as a function of distance r from the pump spot center is given by [87]

$$h \sim \frac{1}{r}\left(1 - e^{-r^2/R^2}\right), \tag{6.4}$$

where R is the radius of the pump spot. The magnetic excitation is sickle shaped on both sides of the pump spot and is antisymmetric. The spatially most inhomogeneous Fourier component of the excitation is parallel to $\mathbf{M}$ and can be reasonably well described by a k-vector corresponding to $\mathrm{k}^* = 2\pi/(4R)$ with $\mathbf{k}^* \parallel \mathbf{M}$, as shown in Fig. 6.7. This result can be used for the discussion of magnon scattering.

6.2.3 Scattering of inhomogeneous modes

In Fig. 6.9 the spin wave dispersion spectra for in-plane $\mathbf{k}$-vectors were calculated for $f = 6.1$ and 11.3 GHz with magnetic parameters corresponding to the 16 ML Fe film. Based on this figure one can understand why the strength of the two magnon scattering critically depends on the bias field and the diameter of the laser pump beam focal spot. At $f = 11.3$ GHz the excited mode has a k-vector close to the minimum (bottom) of the spin wave band. In this case there are obviously fewer degenerate magnons available compared to the lower bias fields where the initial excitation can find many degenerate spin waves, as illustrated by the intersection of the horizontal

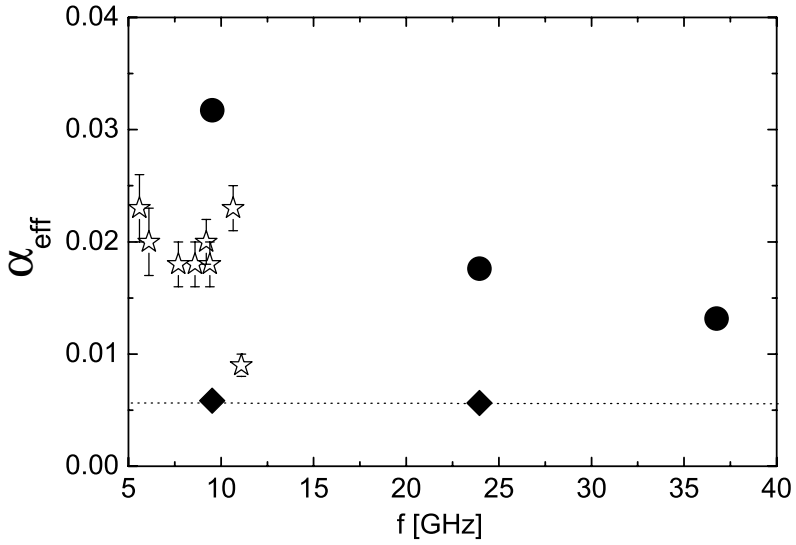

Figure 6.8: Effective damping parameter as a function of the frequency for the 20Au/20Cr/16Fe/GaAs sample. (●) data points were obtained using FMR [167] and (☆) are the results from the TRMOKE fits. In these experiments the applied field was $\parallel [110]_{\mathrm{Fe}}$. The (⧫) symbols correspond to FMR measurements in the perpendicular configuration and represent the Gilbert damping.

dotted line with the spin wave manifold in Fig. 6.9. In addition the magnon group velocity ($\partial\omega/\partial k$) is zero at the bottom of the spin wave band. These two effects explain the decreased relaxation which was observed in Figs. 6.6d and 6.8 [184].

The presence of out-of-phase oscillations in Fig. 6.6b might be a consequence of a mode-mode coupling phenomenon where a significant amount of the initial excitation scatters into a spin wave mode which is out-of-phase with the initial excitation at the probed position.

In Fig. 6.8 the relaxation corresponding to this series of measurements was put into context with the FMR measurements on the same sample [167] (the FMR linewidth was expressed by an effective damping parameter: $\alpha_{\mathrm{eff}} = \Delta H \frac{\gamma}{\omega}$). The effective damping in the TRMOKE measurements is significantly smaller than that obtained from FMR at the same frequency (10 GHz). This is probably a consequence of the reduced number of available spin wave states for scattering in the TRMOKE experiment compared to the FMR experiment, as shown in Fig. 6.9.

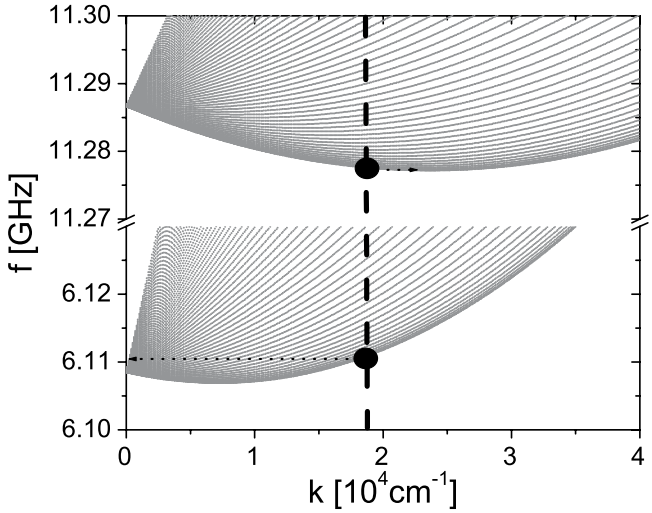

Figure 6.9: Spin wave dispersion band (spin wave manifold) for a 16 ML Fe film calculated for $H_B = 0$ ($f = 6.1$ GHz) and $H_B = 750$ Oe ($f = 11.3$ GHz) corresponding to the measurements shown in Figs. 6.6a and 6.6d. The family of curves in the spin wave manifold is obtained using different angles ψ_q between the magnetization the spin wave ($\mathbf{M}$ and $\mathbf{q}$). The bottom of the spin wave band corresponds to $\mathbf{q} \parallel \mathbf{M}$. The dashed vertical line represents the k-vector of the initial excitation of the magnetization $\sim \pi/2R$ in the TRMOKE experiment and the (•) symbols highlight the position of this excitation within the spin wave band. Note that at $f = 6.1$ GHz many degenerate spin waves are available for scattering (horizontal dotted line) while at $f = 11.3$ GHz their number is substantially reduced.

6.2.4 Magnetic frustration and coercive fields

The Cr cap layer not only causes increased relaxation due to two-magnon scattering, but it also increases the coercive field from 4 Oe (for 20Au/16Fe/GaAs) to 30 Oe (20Au/21Cr/16Fe/GaAs), and strongly changes the magnetic anisotropies. These phenomena are very likely a consequence of antiferromagetic step induced (roughness driven) frustration effects at the Fe/Cr interface [168, 169, 178].

The increase of the coercive field as a function of the Cr thickness was measured using static Kerr microscopy on a sample with a wedged Cr cap layer. One side of the wedge corresponded to 20Au/16Fe/GaAs(001), and the other side of the wedge corresponded to 20Au/20Cr/16Fe/GaAs(001), as illustrated in Fig. 6.10. The wedge from 0 to 20 ML Cr was as wide as the Kerr microscope's field of view of ~ 350 μm. This wedge was produced by a shadow mask inside the MBE chamber during

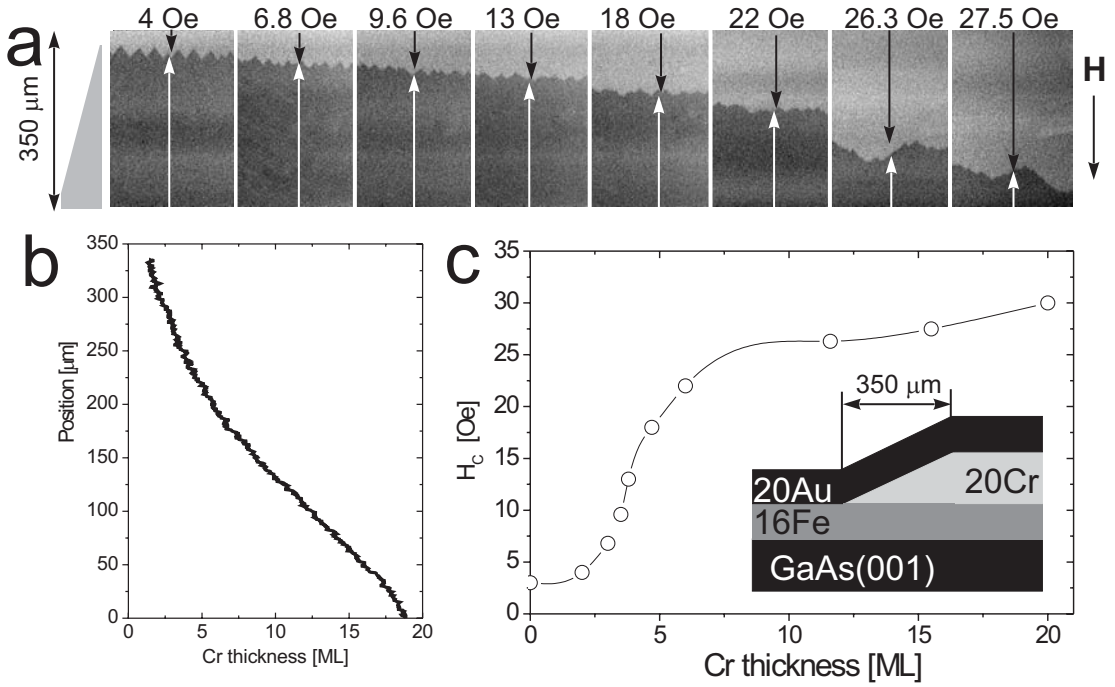

Figure 6.10: **(a)** Shows a series of domain images (200 μm×350 μm) for a wedged 20Au/0-20Cr/16Fe/GaAs(001) sample. The black and white arrows indicate the magnetic domains and the arrow on the right shows the direction of the applied field. **(b)** Sample reflectivity and the corresponding thickness of the Cr wedge across the vertical direction of the images. **(c)** The coercive fields as a function of the Cr thickness deduced from the series of domain images in **(a)** along with a cartoon of the wedged sample.

the growth of the Cr layer. The Cr thickness as a function of the position was obtained from the changing sample reflectivity (assuming a linear relation between the reflectivity and the Cr thickness), as can be seen in Fig. 6.10b. A domain wall was injected from the 20Au/16Fe/GaAs(001) side into the wedge. 20Au/16Fe/GaAs(001) samples have small coercive fields and the domain walls can be easily controlled in the field of view of the Kerr microscope by means of an external magnetic field. The injected domain wall had a zig-zag configuration (head-on) because the slope of the wedge was parallel to the easy axis of the film ($[110]_{\mathrm{Fe}}$). This wall was driven into the Cr covered part of the sample and the position of the domain wall was measured as a function of the applied magnetic pressure. This procedure allowed one to infer the coercive field as a function of the Cr cap layer thickness (shown in Fig. 6.10c). From this experiment one can conclude that the increase of the coercive field due to the Cr cap layer saturates at a thickness of 7 ML of Cr.

6.2.5 Field dependent magnetic properties

The measurement of the resonance frequency as a function of the bias field, shown in Fig. 6.5, directly illustrates how profoundly the magnetic parameters of the 16Fe layer are affected by the Cr cap layer. Two samples are shown: 20Au/16Fe/GaAs^n (●○) and 20Au/20Cr/16Fe/GaAs^n (★☆). Both samples were grown on the *same* substrate using a shadow mask inside the MBE chamber. One can therefore attribute the difference in magnetic properties directly to the different cap layers. In the case of the Cr cap, the g-factor that describes the data well has the unreasonable value: $g = 1.79$, and is at variance with the FMR results obtained at higher frequencies [167], as shown in Fig. 6.5. This implies that the Cr cap layer gives rise to field or frequency dependent magnetic anisotropies.

6.3 Single layer measurements in Edmonton

Using the experimental TRMOKE setup in Edmonton, the experiments were repeated with a transmission line to excite the magnetic film (see details in section 3.3.2). The magnetic field pulse was delivered using a slotline tapered down to a gap of 10 μm (see Fig. 3.17b). A GaAs based photo conductive switch generated the ps current pulses. Compared to the Schottky diode driving used in the Regensburg experiments this represents a more homogeneous excitation profile having an excitation wavelength of the order of 10 μm. This method of excitation is more versatile than the Regensburg technique since it does not require optical transparency of the magnetic film or a Schottky barrier. A disadvantage, however, is the impedance mismatch between the transmission line and the photoconductive switch which leads to a partial reflection of the pump pulse which returns to the sample many several times and effectively re-excites the sample during the free precession. As a result these pulse reflections have to be considered in the analysis of the data. Fig. 6.11 shows typical data obtained with this setup. The presence of pulse reflections is evident in the jumps occurring every 370 ps (indicated by the arrows). The data were analyzed using numerical LLG simulations which include the presence of the reflected pulses. The actual magnetic pulse shape (including the pulse reflections) was obtained from the quasi magneto-static response of the sample. The quasi magneto-static response was measured by applying the highest possible bias field (4 kOe) and filtering the resulting TRMOKE data with a running average window (see solid line in Fig. 6.11a). For the 20Au/16Fe/GaAs

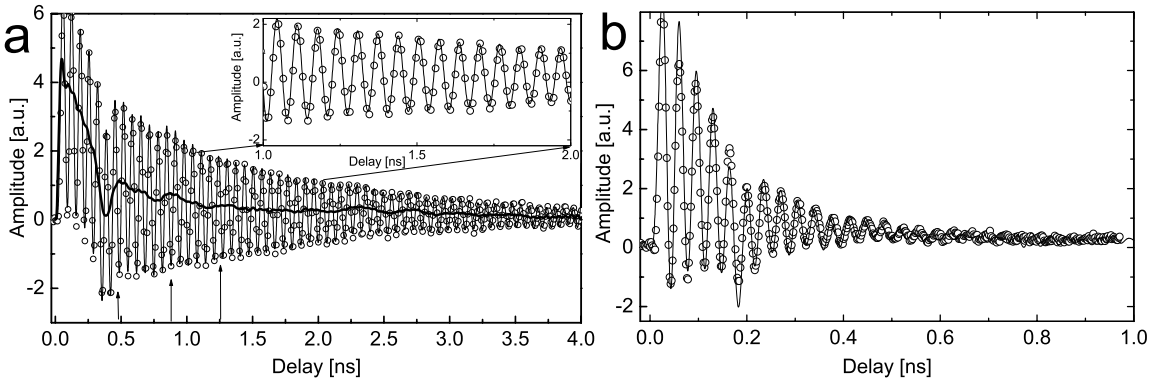

Figure 6.11: TRMOKE measurements using a stripline for **(a)** 20Au/16Fe/GaAs in the presence of a bias field $H_B = 1$ kOe ($f = 15.2$ GHz) and **(b)** 20Au/21Cr/16Fe/GaAs with $H_B = 1.2$ kOe ($f = 14.0$ GHz). In each case H_B was applied along the $[110]_{\mathrm{Fe}}$ direction. The solid line is a numeric fit using the LLG equation which takes the reflections of the pump pulse into account. The magnetic parameters used for the calculation are shown in Fig. 4.5 for **(a)** and listed in [167] for **(b)**. In **(a)** the excitation field shape used for the fits is shown in the thick solid line. This shape was obtained by filtering TRMOKE data which were measured with a higher bias field (see explanation in the text). The vertical arrows indicate the times at which the the pump pulse reflections were incident on the specimen. The inset in **(a)** has an expanded time scale to demonstrate the quality of the fit.

sample this analysis resulted in the damping constant $\alpha = 3.7 \pm 0.1 \times 10^{-3}$. This is in agreement with the damping parameter observed in FMR and 10% bigger than that measured using the TRMOKE setup in Regensburg. In the 20Au/20Cr/16Fe/GaAs sample the damping parameter was found to be $\alpha = 1.8 \pm 0.1 \times 10^{-2}$ and again 30% smaller compared to the value obtained using FMR at the same frequency, as shown in Fig. 6.8.

Since easy and hard directions of the magnetic anisotropies are known, the precessional frequency as a function of the bias field along easy $[110]_{\mathrm{Fe}}$ and hard $[1\bar{1}0]_{\mathrm{Fe}}$ directions can be used to determine not only g and $4\pi M_{\mathrm{eff}}$, but also the magnetic in-plane anisotropies $K_1^{\parallel}$ and $K_U^{\parallel}$, by comparing the data with calculations. The frequency dependence for fields applied in directions close to the $[1\bar{1}0]_{\mathrm{Fe}}$ axis was already calculated for this sample in a previous section (Fig. 4.8) where the presence of $K_1^{\parallel}$ and $K_U^{\parallel}$ leads to 3 separate FMR peaks with increasing applied field at 9.5 GHz. If H_B is applied close to the hard magnetic axis the magnetization rotates from the $[110]_{\mathrm{Fe}}$ direction to the $[1\bar{1}0]_{\mathrm{Fe}}$ direction as the field is increased from $H_B = 0$. The

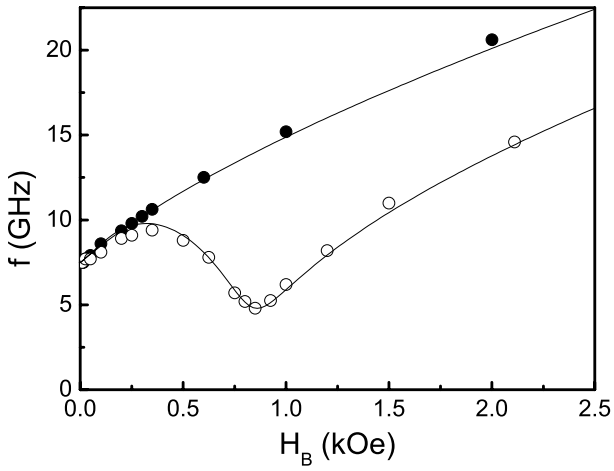

Figure 6.12: Frequency vs. bias field for the 20Au/16Fe/GaAs sample. (•) symbols were obtained with $H_B \parallel [110]_{\mathrm{Fe}}$ and (○) symbols correspond to $H_B \parallel [1\bar{1}0]_{\mathrm{Fe}}$. The solid lines were calculated using the following parameters: $4\pi M_{\mathrm{eff}} = 17.0$ kOe, $g = 2.09$, $K_1^{\parallel} = 2.5 \times 10^5$ erg/cm^3, and $K_U^{\parallel} = -5.4 \times 10^5$ erg/cm^3. A misalignment of H_B with respect to the $[1\bar{1}0]_{\mathrm{Fe}}$ direction of $\delta\varphi_H = 1.15°$ was used for the calculation of the hard axis curve.

frequency versus bias field curve has a characteristic shape with a maximum and a minimum when H_B is applied close to $[1\bar{1}0]_{\mathrm{Fe}}$ determined by the size of $K_1^{\parallel}$ and $K_U^{\parallel}$. The maximum occurs at $H_B = 2K_1^{\parallel}/M_S$ and the position of the frequency dip is given by $2(K_1^{\parallel} - K_U^{\parallel})/M_S$ ($[1\bar{1}0]_{\mathrm{Fe}}$ is the hard direction for both magnetic anisotropies and K_U is negative). The data with H_B oriented along the $[1\bar{1}0]_{\mathrm{Fe}}$ direction shown in Fig. 6.11 are consistent with an in-plane misalignment of the field of $\delta\varphi_H = 1.15°$ with respect to the $[1\bar{1}0]_{\mathrm{Fe}}$ direction. This misalignment is the reason why the precessional frequency does not drop to zero when the anisotropy fields are compensated at $H_B = 2(K_1^{\parallel} - K_U^{\parallel})/M_S$.

6.4 Summary

The dynamic properties of magnetic single layers with Gilbert damping determined from FMR measurements were well reproduced in TRMOKE experiments. In both TRMOKE configurations (Schottky diode and transmission line) the magentization was excited very inhomogeneously. Counil et al. [185] recently addressed the high frequency response of a spatially inhomogeneously excited magnetic film and found an appreciable increase in the measured frequency linewidth at low frequencies for a

50 nm Permalloy film due to dephasing of the excited spin waves. This effect was not observed in the samples discussed in this section because the magnetic films were very thin ($\sim$ 2 nm). In ultrathin films this effect is weaker because the $q_{\parallel} t_F$ term in Eq. 2.48 is small. In this case the frequency spread of the excited spin wave band is very narrow (a few MHz) compared to the intrinsic frequency linewidth ($\sim$ 100 MHz) and does not cause significant dephasing.

In the Cr/Fe/GaAs samples which exhibit a strong two-magnon relaxation, the dynamic response of these samples was clearly affected by the inhomogeneous excitation. When the wave vector of the initially excited spin wave was close to the bottom of the spin wave dispersion band the two-magnon relaxation was significantly reduced.

Chapter 7

Conclusions

High quality epitaxial single crystalline Au/Fe/GaAs(001) multilayers having sharp interfaces were grown by means of molecular beam epitaxy and characterized using refection high energy electron diffraction (RHEED), scanning tunnelling microscopy (STM) and cross-sectional transmission electron microscopy (TEM). The magnetic properties of Au/Fe/GaAs(001) single layers were investigated using ferromagnetic resonance (FMR). The homogeneity of these ultrathin magnetic films resulted in nearly ideal behavior (i.e. no extrinsic contributions to the FMR linewidth) and allowed for reproducible studies of the effect of cap layers on the ferromagnetic relaxation.

This study led to four important results:

(1) For Au/Fe/Au/Fe/GaAs(001) double layers a large increase in the Gilbert damping was observed. The additional damping scaled inversely with the Fe film thickness, i.e. the presence of a second ferromagnetic layer resulted in an additional interface Gilbert damping. This effect was explained in terms of a spin-pump/spin-sink model. A crossover of the FMR fields of the two Fe layers allowed this model to be tested in detail. Theory and experiment were found to be in excellent qualitative and quantitative agreement. For the first time a spin current was observed in absence of a charge current. This effect may lead to a new type of electronics which is independent of electric charge transport.

(2) The spin-sink effect was studied in normal metals (NM) using NM/Fe/-GaAs(001) samples, where NM=Au, Ag, Cu, and Pd. The Au, Ag, and Cu cap layers with NM thicknesses of up to 80 nm did not result in a measurable additional FMR linewidth. This is consistent with the expected large spin diffusion length in

Au, Ag, and Cu. Samples with Pd cap layers behaved differently. Pd cap layers above 10 nm acted as a perfect spin-sink with the strength of spin-pumping close to that expected from the density of free electrons in Pd. Pd is a NM that exhibits strong spin electron-electron correlations which result in paramagnons. It is argued that the spin-sink effect in Pd is due to the dissipation of the pumped spin current by the interaction with spin fluctuations inherent to Pd. The experimental result implies that the relaxation of spin momentum in Pd occurs in the ballistic limit, that is the spin mean free path is shorter than the momentum mean free path.

(3) A self organized network of misfit dislocations was identified by RHEED, plan view TEM, and STM in the lattice strained Pd/Fe/GaAs system. The magnetic relaxation in such samples increased and was strongly anisotropic; the anisotropy was observed to exhibit the rectangular symmetry of the misfit dislocation network. It was shown that this system provides a classical example of two-magnon scattering and that the angular dependence of the extrinsic relaxation can be explained by the channelling of scattered spin waves parallel to the misfit dislocations.

(4) A Cr/Fe/GaAs sample was used to test the effect of two-magnon scattering in the time domain using a time-resolved Kerr effect experiment. For this sample the effective relaxation constant was strongly dependent on the experimental conditions. The wave vector of the initial excitation of the magnetization was always constant, but the wave vector corresponding to the bottom of the spin wave dispersion band was changed by a variable magnetic bias field. When the wave vectors of the initial excitation of the magnetization and the bottom of the spin wave dispersion band coincided the two-magnon contribution to the relaxation was nearly switched off. This striking result shows that the apparent magnitude of two-magnon scattering depends on the size of the probe involved in the measurement as well as the wave vector that is used to excite the magnetization.

Appendix A

SLAC experiment

The dynamic properties of Au/Fe/GaAs(001) magnetic single layers were discussed in chapters 4 and 6. FMR and TRMOKE however only explore the dynamics in the limit of small precessional angles. For many device applications it is important to understand the magnetic relaxation at large precessional angles. The Au/Fe/GaAs magnetic single layer samples described in section 4.2 with their well defined intrinsic properties provide a model case. The generation of short magnetic field pulses strong enough to incline the magnetization in the Au/Fe/GaAs(001) samples by appreciable angle is a major challenge.

Siegmann et al. [182, 186, 183] have demonstrated the possibility of using a pulsed and focused 50 GeV electron beam in the Final Focus Test Beam (FFTB) section of the Stanford Linear Accelerator Center (SLAC) as magnetic field source. This electron beam was focussed to micrometer dimensions and provides field pulses of up to 200 kOe with 1-8 ps duration.

These are the strongest magnetic field pulses known. The principle of this experiment is illustrated in Fig. A.1. The in-plane magnetic field pulse tilts the magnetization instantaneously out of the plane and the relaxation proceeds by free precession. If the out-of-plane tilt angle exceeds 12 ° for a 10Au/15Fe/GaAs(001) sample, then the magnetization precesses at a very large cone angle ($\sim 78°$) as illustrated in Fig. A.2 in the resulting demagnetizing field. The number of large angle precessions and hence the final direction of the magnetization is determined by the size of the initial tilt angle.

The initial tilt angle depends on the size of torque $\mathbf{T} = \mathbf{M} \times \mathbf{h}$ exerted by the pulse magnetic field pulse $\mathbf{h}$. Since $\mathbf{h}$ is a circular field, and falls of as 1/r from the

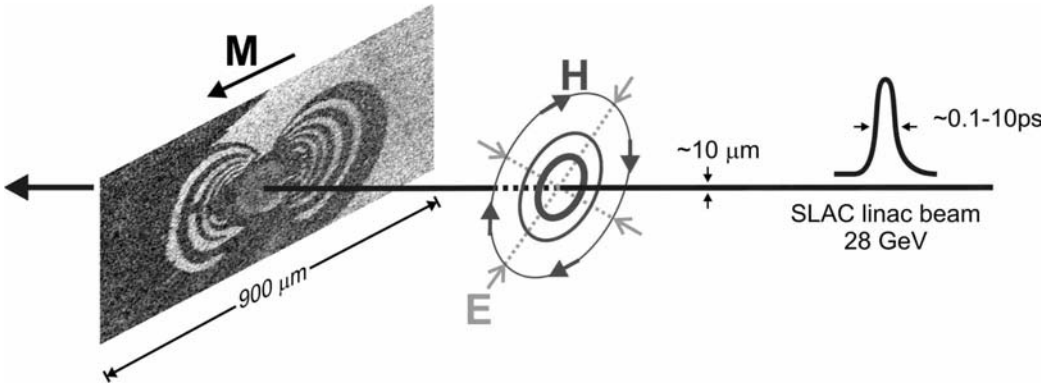

Figure A.1: Cartoon of the experimental configuration of the SLAC experiment.

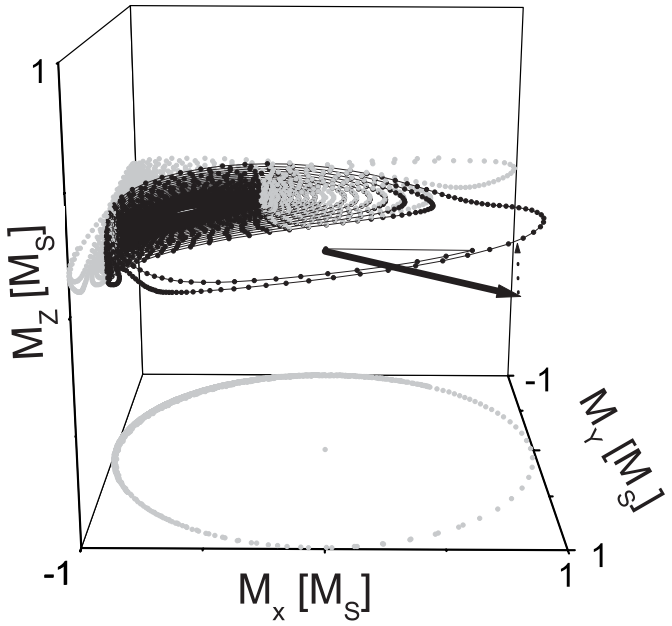

Figure A.2: 3D trajectory of the magentization in the 10Au/15Fe/GaAs(001) sample. The magnetization (big arrow) was initially oriented parallel to $[110]_{\mathrm{Fe}}$. In this example the magnetization is tilted out of the plane by 12.5 ° (dotted arrow) and precesses freely in demagnetizing and anisotropy fields (switching twice) before settling in the $[\overline{1}10]_{\mathrm{Fe}}$ direction.

center of the electron beam the resulting domain configuration consists of ∞ shaped contours each given by a nearly constant initial tilt angle.

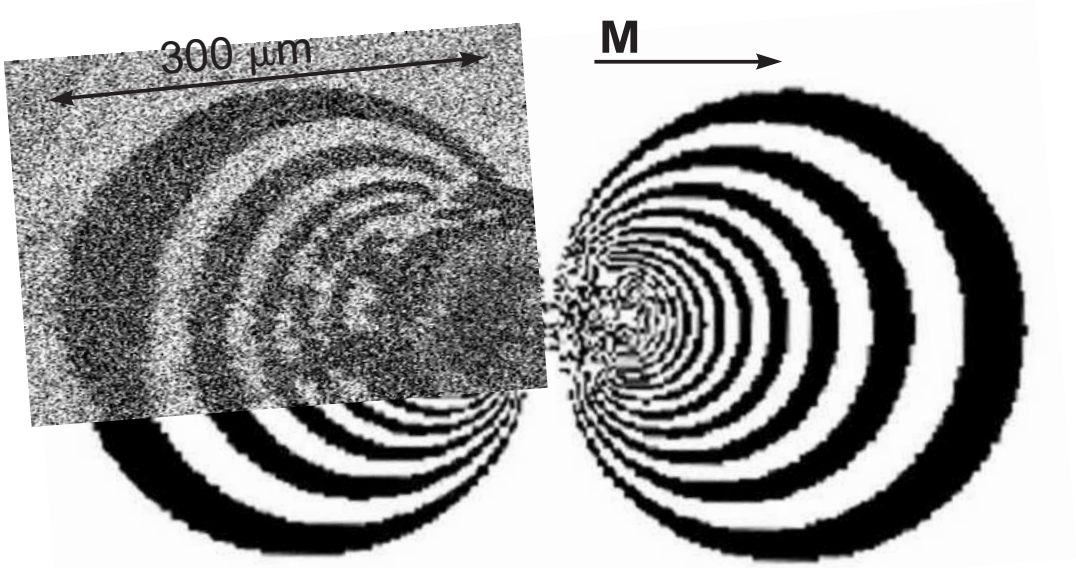

Figure A.3: Domain pattern written by a SLAC pulse into a uniaxial 10Au/15Fe/GaAs sample. The pattern was imaged by SEMPA. The background shows a calculated mangetization pattern using the LLG equation using magnetic properties consistent with FMR, see Fig. 4.5a, a damping coefficient $\alpha = 0.017$, and pulse amplitude and duration as determined during the exposure.

A.1 Results

In collaboration with Professor Hans Siegmann experiments with the SLAC electron pulses were performed with Au/Fe/GaAs(001) samples [187]. Fig. A.3 shows a switching pattern that was produced in a 10Au/15Fe/GaAs(001) sample by exposing it to a single Gaussian electron pulse of width $\tau = 2.3$ ps. Prior to the arrival of the electron bunch, the film was magnetized along its easy direction ($[110]_{\mathrm{Fe}}$), as indicated by the arrow labelled **M**. Subsequently, the Au cap layer was removed by sputtering, and the pattern was imaged with a scanning electron microscope with polarization analysis (SEMPA). The dark regions are locations where the magnetization has switched into the opposite direction while the light grey regions are the locations were the direction of **M** either remained unchanged, or switched back to the initial direction after multiple reversals. The switching pattern due to the focussed electron bunch extends to large distances (in Fig. A.3 up to 300 μm) from the center of the electron beam. A circular damaged area appears around the place where the electron bunch has passed. It is very likely caused by damage in the GaAs(001) substrate due to the electric field accompanying the electron bunch. In GaAs the **E**-field cannot be

screened on a ultrafast time scale and may produce cracks or other damage in the ionic semiconductor crystal.

The gross features of the resulting magnetization pattern shown in Fig. A.3 can be explained by uniform precession of the magnetization [188]. Specifically, the figure 8-shape of the pattern reflects the lines of constant precessional torque $\mathbf{T} = \mathbf{M} \times \mathbf{h}$. Up to 10 switches of the magnetization back and forth can be distinguished as one moves closer to the center of the electron beam. The calculated pattern in Fig. A.3 that fits the data allows one to determine anisotropies and damping constant. The magnetic anisotropies obtained from the pattern agree with the FMR results in 4.5a. On the other hand, the damping constant was found to be $\alpha = 0.017$ and hence 4 times larger than in FMR.

A.2 Discussion

Domain wall mobility measurements allow one to estimate the damping for 180° precession since the magnetic damping exerts a viscous force on a moving wall [9]. Leaver and Vojndani [189] measured the domain wall mobility in Ni at 1 MHz. Their mobility is agreement with intrinsic damping for Ni measured by FMR [131]. Nibarger et al. [190] recently measured damping constant as a function of the precessional angle from 0 up to 40° and found the damping to be independent on the precessional cone angle.

The crucial difference between these experiments and the SLAC experiment is the precessional frequency. Nibarger et al. were only able to reach a precessional angle of 40° at frequencies as low as 400 MHz. In the SLAC experiment the free precession occurs at almost 8 GHz.

A.3 Multi-magnon scattering

Recently, Dobin et al. [191] addressed large angle precession at high frequencies (fields) from a theoretical point of view. It was found that intrinsic three and four-magnon processes, which are similar to Suhl instabilities at high microwave power levels [192], can contribute to the relaxation rate of the magnetization. For a Fe film of 2 nm thickness with a bias field of 1 kOe at a precessional cone angle of 45°, they find a relaxation time of 0.3 ns corresponding to $\alpha = 0.019$ (see Fig. 3 in [191]). These con-

ditions are actually very close to the SLAC experiment since the 10Au/15Fe/GaAs and 10Au/10Fe/GaAs samples have effective bias fields of 500 and 800 Oe built-in (due to anisotropies). According to Dobin el al. [191] the magnon scattering effects are smaller for smaller applied fields, because the size of the k-space of initially degenerate magnons (shown in Fig. 5.11) decreases. This model therefore does not necessarily contradict the experiments by Nibarger et al. [190] and Leaver and Vojndani [189]. In these experiments the magnon processes were not operative since the fields (frequencies) were very small.

If multi-magnon scattering is responsible for the perceived increase in magnetic damping is remarkable that a well defined switching pattern appears. According to Dobin et al. the effective magnetization reduces by $\sim 40\%$ during the precession due to the generation of spin waves with $\mathbf{k} \neq 0$. It is remarkable that this does not lead to chaos in the resulting switching pattern.

Appendix B

Fe/Pd $L1_0$ superlattices on Au/Fe/GaAs(001)

$L1_0$ ordered alloy phases are attractive for some applications because of their large magnetic anisotropy perpendicular to the film surface can lead to perpendicularly magnetized films. A sketch of the atomic structure of this phase is shown in Fig. B.1; this ordered alloy consists of alternating layers bcc and fcc materials, e.g. Fe and Pd. It is well known, however, that high substrate temperatures during growth or high annealing temperatures around ~ 400 °C are required to reach the ordered $L1_0$ phase. On GaAs substrates these high temperatures would cause unfavorable interdiffusion of Ga and As with metallic film structures.

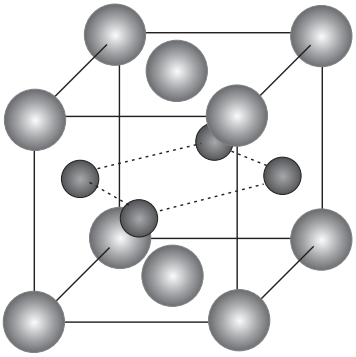

Figure B.1: $L1_0$ structure: (○):Pd, (●):Fe,

B.1 Growth

In order to avoid high temperatures alternate Pd and Fe monolayer deposition was used. Fe/Pd superlattices were grown on 40Au/10Fe/GaAs(001) templates. The template was prepared as described in section 4.1. Alternating 1 ML thick Fe and Pd layers were grown using two furnaces [193, 194]. The flux from the two sources arriving at the sample was out-of-phase and controlled by the pneumatic shutters of the furnaces. 5 and 10 multilayer repetitions were grown and capped by 20 ML Au for ambient protection.

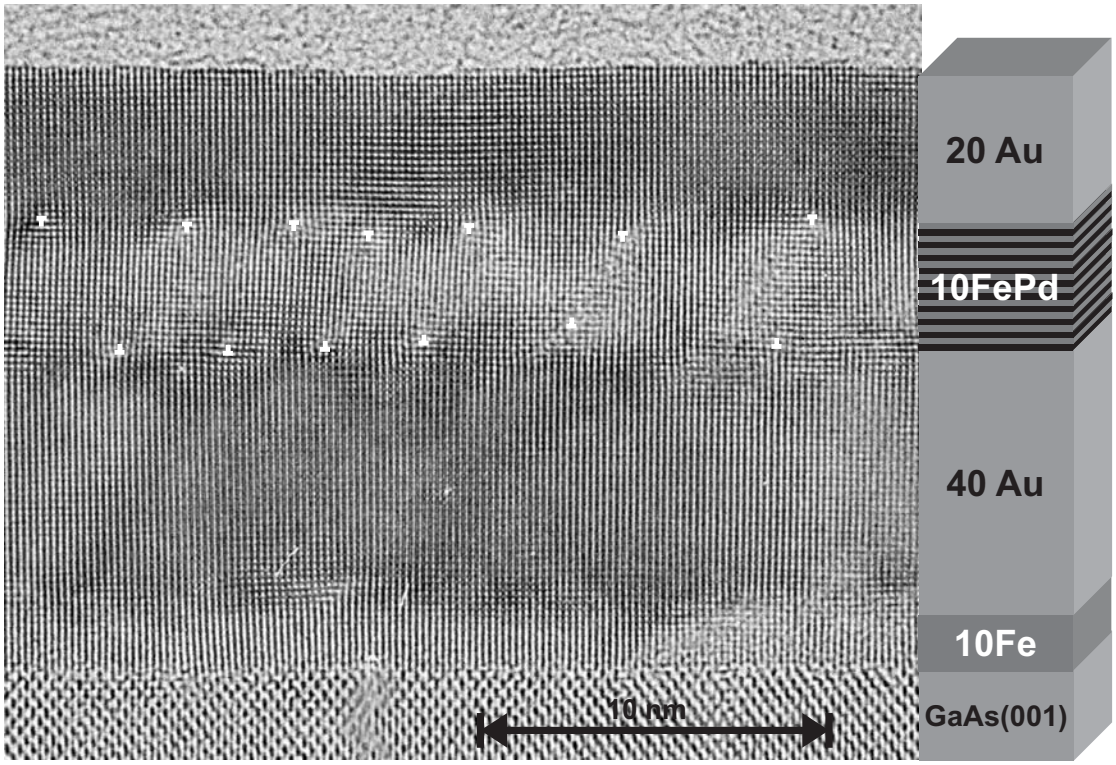

Figure B.2: Cross-sectional TEM image of the 20Au/$[FePd]_{10}$/40Au/10Fe/GaAs(001) layer system as illustrated on the right. The dislocations in the $[FePd]_{10}$ film are indicated by the white symbols.

B.2 TEM

Fig. B.2 shows a cross-sectional TEM image of the 20Au/$[FePd]_{10}$/40Au/10Fe/GaAs(001) structure. One can count the superlattice repetitions between the Au cap and buffer layers. Due to the big lattice mismatch (6.8 %) between Au ($a = 4.08$Å) and FePd ($a_{\|} = 3.83$Å) [195] lattice relaxations occur at both Au/FePd interfaces and have an average separation of ~ 3 nm. This corresponds to ~ 6.6 % relaxation in FePd and means that almost all the lattice strain is relived right at the interfaces. The inserted lattice planes on top and bottom interfaces often occur in pairs and are connected via the $\{111\}$ glide planes. $\langle 112 \rangle$ partial Shockley dislocations nucleate at the surface and glide along the $\{111\}$ plane down to the interface with the Au buffer [195] and cause stacking faults in FePd which are recognizable in Fig. B.2. Due to the 6.8% lattice mismatch the dislocation density is so high (average separation of 3 nm, see Fig. B.2) that the exchange interaction is strong enough to average out their effect. Therefore these defects do not cause two-magnon scattering.

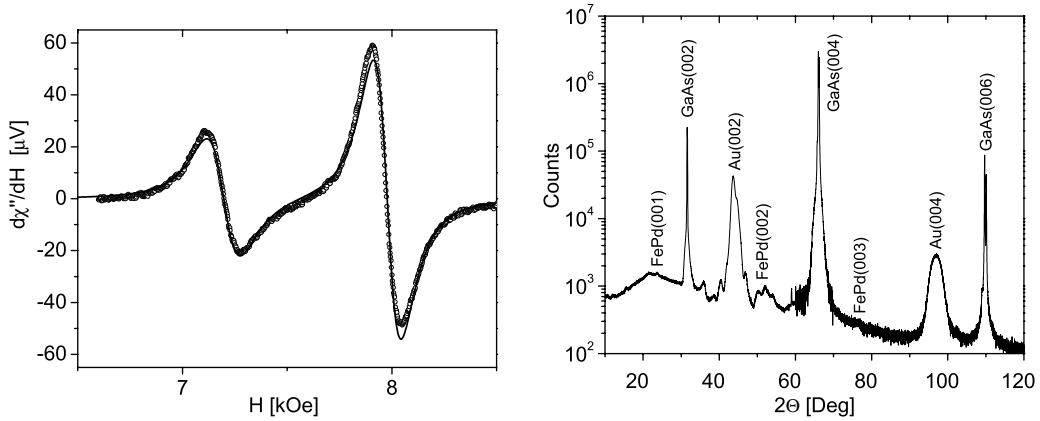

Figure B.3: **(a)** The left figure shows a FMR spectrum of the 20Au/[FePd]-$_{10}$/40Au/10Fe/GaAs(001) sample. (○) symbols correspond to the measurement and the solid line is a calculated FMR spectrum for the bilayer system including all magnetic anisotropies. Note that the slight asymmetry of the data was caused by the microwave cavity. **(b)** $\Theta - 2\Theta$ x-ray diffraction scan of the 20Au/$[\mathrm{FePd}]_{10}$/40Au/10Fe/GaAs(001) sample. The wavelength was $\lambda = 1.54$Å ($\mathrm{Cu}_{K\alpha}$). Due to the finite crystal thickness the multilayer peaks are intrinsically broadened; e.g. the intrinsic broadening of a 20 ML Au film results in $\Delta 2\Theta = 4°$ and $\Delta 2\Theta = 8°$ for the Au(002) and Au(004) peaks, respectively.

B.3 FMR

The FMR spectra of the FePd layer were given by narrow Lorentzian lines. The magnetic in-plane anisotropies observed in FMR were extremely weak. From the linear frequency dependence of the FMR linewidth with no zero frequency offset one can conclude that the damping is only intrinsic and enhanced by the spin pumping contribution due to vicinity of the 10 Fe seed layer. For the $[\mathrm{FePd}]_{10}$ layer the following magnetic parameters were found: $4\pi M_{\mathrm{eff}} = 10.1$ kG, $K_U^{\parallel} = -1 \times 10^5$ erg/cm^3, and $K_1^{\parallel} = 0$.

By direct comparison of the FMR peaks of the 10Fe layer and the $[\mathrm{FePd}]_{10}$ layer one can determine the magnetic moment of $[\mathrm{FePd}]_{10}$. The moment was estimated by superimposing calculated and measured FMR lines (see Fig. B.3). Because the 10Fe layer has a known magnetic moment, the moment of the $[\mathrm{FePd}]_{10}$ layer was adjusted to get the best fit. This procedure resulted in $M_S^{FePd} = 1180 \pm 60$ emu/cm^3, which is in very good agreement with other values reported for FePd [196, 197].

First principles calculations for the FePd structure by Stoeffler [198] indicate that

the magnetic moment per Pd atom should be 0.3 μ_B. If one correlates this with the measured saturation magnetization this results in a strongly enhanced magnetic moment for Fe 3.0 ± 0.1 μ_B. This enhancement was also predicted and is related to the atomic volume increase for Fe in the $L1_0$ structure. Similar enhancements were reported for Fe in other $L1_0$ structures [199].

Since $4\pi M_{\text{eff}}$ was nearly independent of the thickness of the superlattice the difference between $4\pi M_{\text{eff}}$ and $4\pi M_S$ is a bulk effect with $K_U^{\perp} = 3 \times 10^6$ erg/cm^3. This perpendicular uniaxial anisotropy is much weaker than it should be for the well ordered $L1_0$ phase [200]. Gehanno et al. [197] obtained a 5 times larger value for $K_U^{\perp}$ in FePd(001) films deposited at 300 °C on MgO(001).

One can get an estimate of the order in the FePd superlattice from out-of-plane x-ray diffraction (XRD) measurements. Wide angle radial scans across the reciprocal lattice normal to the growth direction provide information about the structural coherence.

The one dimensional chemical order parameter S is defined as [201]

$$S = \frac{r_{\text{Fe}} - x_{\text{Fe}}}{y_{\text{Pd}}} = \frac{r_{\text{Pd}} - x_{\text{Pd}}}{y_{\text{Fe}}}, \tag{B.1}$$

where $x_{\text{Fe(Pd)}} = \frac{1}{2}$ is the atomic fraction of Fe(Pd) in the sample, $y_{\text{Fe(Pd)}} = \frac{1}{2}$ is the fraction of Fe(Pd) atomic sites, and $r_{\text{Fe(Pd)}}$ is the fraction of Fe(Pd) sites occupied by the correct species. $S = 1$ for a perfectly ordered film of stoichiometric composition $Fe_{50}Pd_{50}$. In x-ray diffraction (XRD) this order parameter can be related to the relative ratio of the FePd fundamental (002) peak and the satellites peaks FePd(001) and FePd(003). One can write [194]

$$S^2 = \frac{[I_{\text{FePd(002)}}/I_{\text{FePd(003)}}]_{\text{observed}}}{[I_{\text{FePd(002)}}/I_{\text{FePd(003)}}]^{S=1}_{\text{calculated}}}. \tag{B.2}$$

Fig. B.3b shows a $\theta - 2\theta$ scan of the 20Au/$[\text{FePd}]_5$/40Au/10Fe/GaAs(001) sample. One can recognize peaks corresponding to GaAs, Au, and FePd. The measured ratio between FePd(002) and FePd(003) leads to $S = 0.4 \pm 0.2$ (using $I_{\text{FePd(003)}}/I_{\text{FePd(002)}}$ calculated for $S = 1$ for the FePt structure [193]).

B.4 Conclusion

Well ordered FePd superlattices with perpendicular magnetization cannot be prepared at RT even by monolayer modulated MBE. The $L1_0$ phase is preferred only at high

temperatures and the disorder from low temperature preparation results in a perpendicular anisotropy that is too small to compensate the demagnetizing field. This is a general behavior of the $L1_0$ phase and in agreement with results found for other $L1_0$ superlattices [193, 194, 201]. A feature the 20Au/$[FePd]_n$/40Au/10Fe/GaAs(001) bilayer system that may be useful for spintronics applications is that both magnetic layers are uniaxial with their easy axes parallel to each other and along the $[110]_{Fe}$ direction.

Appendix C

Theory of Spin-Pumping

At this time there is no citable reference detailing the justification of the spin-pumping theory. The following derivation of the spin-pumping theory as introduced by Tserkovnyak et al. [116] is based on lecture notes provided by Prof. Evgen Šimánek.

C.1 Diagonalization of the Hamiltonian

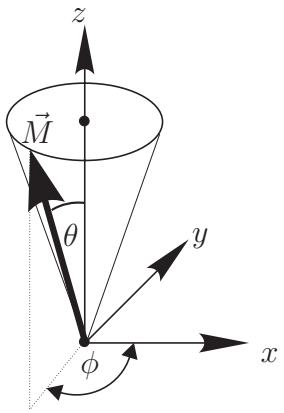

Figure C.1: Coordinate system

The Hamiltonian of conduction electrons in the laboratory system is given by

$$\hat{H} = \left[-\frac{\hbar}{2\mathrm{m}} \nabla^2 + V^n(\vec{r}) \right] \hat{1} + (\hat{\vec{\sigma}} \cdot \vec{m}) V^s(\vec{r}) \tag{C.1}$$

where $V^n(\vec{r})$ is the spin-independent and $V^s(\vec{r})$ is the spin-dependent (exchange)

potential. The unit and Pauli matrices are

$$\hat{1} = \begin{pmatrix} 1 & 0 \\ 0 & 1 \end{pmatrix}, \quad \hat{\sigma}_x = \begin{pmatrix} 0 & 1 \\ 1 & 0 \end{pmatrix}, \quad \hat{\sigma}_y = \begin{pmatrix} 0 & -1 \\ -1 & 0 \end{pmatrix}, \quad \hat{\sigma}_z = \begin{pmatrix} 1 & 0 \\ 0 & -1 \end{pmatrix}, \tag{C.2}$$

and the unit vector of the magnetization is

$$\vec{m} = \frac{\vec{M}}{M_s} = \begin{pmatrix} \sin\theta\cos\phi \\ \sin\theta\sin\phi \\ \cos\theta \end{pmatrix}, \tag{C.3}$$

where θ and ϕ are cone and phase angle of $\vec{m}$ respectively. In order to diagonalize $\hat{H}$ a unitary matrix that rotates the z-axis parallel to $\vec{m}$ is defined

$$\hat{U} = \begin{pmatrix} \cos(\frac{\theta}{2})e^{-i\frac{\phi}{2}} & -\sin(\frac{\theta}{2})e^{-i\frac{\phi}{2}} \\ \sin\frac{\theta}{2}e^{i\frac{\phi}{2}} & \cos\frac{\theta}{2}e^{i\frac{\phi}{2}} \end{pmatrix} \tag{C.4}$$

with the inverse

$$\hat{U}^{-1} = \begin{pmatrix} \cos\frac{\theta}{2}e^{i\frac{\phi}{2}} & \sin\frac{\theta}{2}e^{-i\frac{\phi}{2}} \\ -\sin\frac{\theta}{2}e^{i\frac{\phi}{2}} & \cos\frac{\theta}{2}e^{-i\frac{\phi}{2}} \end{pmatrix}. \tag{C.5}$$

The Schrödinger equation (SE) in the laboratory system is given by

$$\hat{H}\hat{\Psi} = E\hat{\Psi}, \tag{C.6}$$

where $\hat{\Psi}$ is a spinor. After a rotation about z

$$\hat{\Psi} = \hat{U}\hat{\Phi}, \quad \text{and} \quad \hat{H}_U = \hat{U}^{-1}\hat{H}\hat{U} \tag{C.7}$$

one obtains the SE in the rotated System

$$\hat{H}_U\hat{\Phi} = E\hat{\Phi}. \tag{C.8}$$

Diagonalizing the exchange part of $\hat{H}$ from C.3 one has

$$\hat{\sigma}\cdot\vec{m} = \begin{pmatrix} \cos\theta & \sin\theta e^{-i\ \phi} \\ \sin\theta e^{i\phi} & -\cos\theta \end{pmatrix} \tag{C.9}$$

Using C.4, C.5, and C.9 it follows that

$$\hat{U}^{-1}\hat{\sigma}\cdot\vec{m}\hat{U} = \begin{pmatrix} 1 & 0 \\ 0 & -1 \end{pmatrix} = \hat{\sigma}_z. \tag{C.10}$$

The resulting Hamiltonian in the rotated system is thus diagonal in the spin ($s = 1/2$) space of the conduction electrons:

$$\hat{H}_U = \left[-\frac{\hbar}{2\mathrm{m}} \nabla^2 + V^n(\vec{r}) \right] \hat{1} + \hat{\sigma}_z V^s(\vec{r}). \tag{C.11}$$

The spinor transformation in components ($s = \pm 1/2$) is:

$$\hat{\Psi}_s = \hat{U}_{s\sigma} \hat{\Phi}_\sigma, \tag{C.12}$$

where

$$\hat{\Phi}_\uparrow = \Phi(\vec{r}) \begin{pmatrix} 1 \\ 0 \end{pmatrix}, \quad \hat{\Phi}_\downarrow = \Phi(\vec{r}) \begin{pmatrix} 0 \\ 1 \end{pmatrix}. \tag{C.13}$$

C.2 Reflection matrix

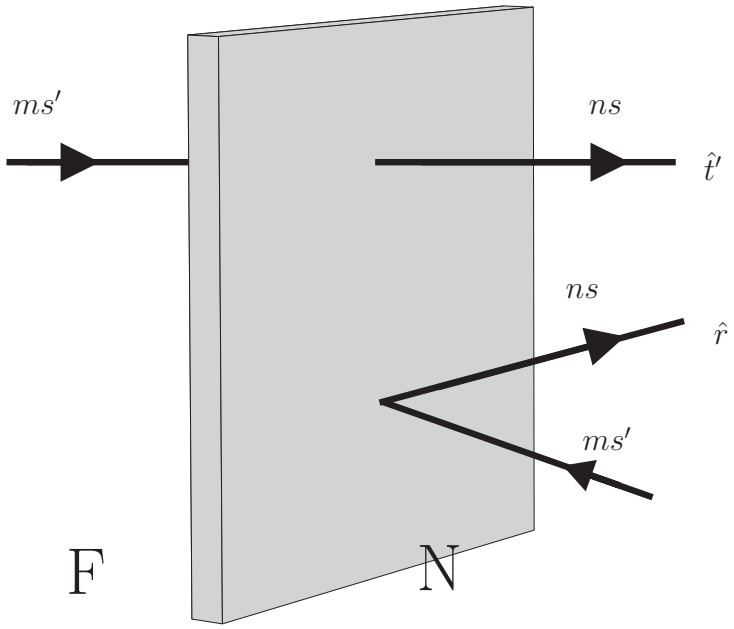

Figure C.2: Cartoon illustrating the meaning of the F/N interface scattering coefficients.

The reflection matrix is defined as

$$\hat{\Psi}_s^n = \sum_{m,s'} \frac{\chi^m(\rho)}{\sqrt{k_m}} \left[\delta_{ss'} \delta_{nm} \hat{\xi}_{s'} e^{ik_n x} + \hat{r}_{ss'}^{nm} \hat{\xi}_{s'} e^{-ik_m x} \right], \tag{C.14}$$

where the $\chi(\rho) = \chi(y, z)$ are the transverse modes. In the rotated system Eq. C.14 reads

$$\hat{\Phi}_r^n = \sum_{m,s'} \frac{\chi^m(\rho')}{\sqrt{k_m}} \left[\delta_{rs'} \delta_{nm} \hat{\xi}_{U,s'} e^{ik_n x} + \hat{r}_{U,rs'}^{nm} \hat{\xi}_{U,s'} e^{-ik_m x} \right]. \tag{C.15}$$

From C.12, C.14, and C.15 it follows

$$\hat{r}_{ss'} = (\hat{U} \hat{r}_U \hat{U}^{-1})_{ss'}. \tag{C.16}$$

Proof of C.16: Since C.15 is a solution in the rotated (diagonalized) system (see C.11), the spinor

$$\hat{\xi}_{U,\uparrow} = \begin{pmatrix} 1 \\ 0 \end{pmatrix} \quad \text{and} \quad \hat{\xi}_{U,\downarrow} = \begin{pmatrix} 0 \\ 1 \end{pmatrix} \tag{C.17}$$

According to C.12, the spinor $\hat{\xi}_{s'}$ (in C.14) in the laboratory system is

$$\hat{\xi}_{s'} = \hat{U}_{s'\sigma} \hat{\xi}_{U,\sigma}. \tag{C.18}$$

Inserting C.18 into C.14 results in

$$\hat{\Psi}_s^n = \sum_{m,s'} \frac{\chi^m(\rho)}{\sqrt{k_m}} \left[\delta_{ss'} \delta_{nm} \hat{U}_{s'\sigma} \hat{\xi}_{U,\sigma} e^{ik_n x} + \hat{r}_{ss'}^{nm} \hat{U}_{s'\sigma} \hat{\xi}_{U,\sigma} e^{-ik_m x} \right]. \tag{C.19}$$

Multiplying C.15 on the left by the matrix $\hat{U}_{sr}$ and using C.12 yields

$$\hat{\Psi}_s^n = \hat{U}_{s\gamma} \Phi_r^n = \sum_{m,s'} \frac{\chi^m(\rho)}{\sqrt{k_m}} \left[\hat{U}_{s\gamma} \delta_{rs'} \delta_{nm} \hat{\xi}_{U,s'} e^{ik_n x} + \hat{U}_{sr} \hat{r}_{U,\gamma s'}^{nm} \hat{\xi}_{U,s'} e^{-ik_m x} \right]. \tag{C.20}$$

The reflection terms of C.19 and C.20 should be equal to each other. This implies (dropping m, n indices):

$$\hat{r}_{ss'} \hat{U}_{s'\sigma} \hat{\xi}_{U,\sigma} = \hat{U}_{s\gamma} \hat{r}_{U,\gamma s'} \hat{\xi}_{U,s} =_{\text{let } s' \to \sigma} \hat{U}_{s\gamma} \hat{r}_{U,\gamma\sigma} \hat{\xi}_{U,\sigma} \tag{C.21}$$

Equation C.21 implies

$$\hat{r}_{ss'} \hat{U}_{s'\sigma} = \hat{U}_{s\gamma} \hat{r}_{U,\gamma\sigma}. \tag{C.22}$$

Multiplying C.22 on the right by $\hat{U}_{\sigma\delta}^{-1}$ and summing over σ results in

$$\hat{r}_{ss'} \hat{U}_{s'\sigma} \hat{U}_{\sigma\delta}^{-1} = \hat{U}_{s\gamma} \hat{r}_{U,\gamma\sigma} \hat{U}_{\sigma\delta}^{-1}. \tag{C.23}$$

But $\hat{U}\hat{U}^{-1} = \hat{1}$, so that

$$\hat{U}_{s'\sigma}\hat{U}^{-1}_{\sigma\delta} = \delta_{s',\delta}. \tag{C.24}$$

Using C.24 in C.23, one obtains

$$\hat{r}_{s\delta} = \left(\hat{U}\hat{r}_U\hat{U}^{-1}\right)_{s\delta}, \tag{C.25}$$

which proves relation C.16.

Since $\hat{U}$ is a function of the θ and ϕ angles of $\vec{M}$ relation C.16 allows one to calculate the effect of precession of the magnetization on $\hat{r}_{s\sigma}$(≡reflection matrix in laboratory system) from the knowledge of $\hat{r}_U$(≡reflection matrix in system where $\vec{m} \parallel z$).

C.3 Reflection without spin-flip (rotated system)

Assume

$$\hat{r}_{U,ss'} = \delta_{ss'}\hat{r}_{U,ss}, \tag{C.26}$$

this gives

$$\begin{aligned}\left(\hat{U}\hat{r}_U\hat{U}^{-1}\right)_{ss'} &= \hat{U}_{s\sigma}\hat{r}_{U,\sigma\sigma'}\hat{U}^{-1}_{\sigma's'} \\ &= \hat{U}_{s\sigma}\hat{r}_{U,\sigma\sigma}\hat{U}^{-1}_{\sigma s'} \\ &= \hat{U}_{s\uparrow}\hat{U}^{-1}_{\uparrow s'}\hat{r}_{U,\uparrow\uparrow} + \hat{U}_{s\downarrow}\hat{U}^{-1}_{\downarrow s'}\hat{r}_{U,\downarrow\downarrow}.\end{aligned} \tag{C.27}$$

Now one can evaluate the matrix element $\hat{U}_{s\uparrow}\hat{U}^{-1}_{\uparrow s'}$ from:

$$\begin{aligned}\hat{U} &= \begin{pmatrix}\hat{U}_{\uparrow\uparrow} & \hat{U}_{\uparrow\downarrow}\\ \hat{U}_{\downarrow\uparrow} & \hat{U}_{\downarrow\downarrow}\end{pmatrix} = \begin{pmatrix}\cos\frac{\theta}{2}e^{-i\frac{\phi}{2}} & -\sin\frac{\theta}{2}e^{-i\frac{\phi}{2}}\\ \sin\frac{\theta}{2}e^{i\frac{\phi}{2}} & \cos\frac{\theta}{2}e^{i\frac{\phi}{2}}\end{pmatrix} \quad \text{and} \\ \hat{U}^{-1} &= \begin{pmatrix}\hat{U}^{-1}_{\uparrow\uparrow} & \hat{U}^{-1}_{\uparrow\downarrow}\\ \hat{U}^{-1}_{\downarrow\uparrow} & \hat{U}^{-1}_{\downarrow\downarrow}\end{pmatrix} = \begin{pmatrix}\cos\frac{\theta}{2}e^{i\frac{\phi}{2}} & \sin\frac{\theta}{2}e^{-i\frac{\phi}{2}}\\ -\sin\frac{\theta}{2}e^{i\frac{\phi}{2}} & \cos\frac{\theta}{2}e^{-i\frac{\phi}{2}}\end{pmatrix},\end{aligned} \tag{C.28}$$

hence

$$\begin{aligned}\hat{U}_{\uparrow\uparrow}\hat{U}^{-1}_{\uparrow\uparrow} &= \cos^2\frac{\theta}{2} \\ \hat{U}_{\uparrow\uparrow}\hat{U}^{-1}_{\uparrow\downarrow} &= \cos\frac{\theta}{2}\sin\frac{\theta}{2}e^{-i\phi} \\ \hat{U}_{\uparrow\uparrow}\hat{U}^{-1}_{\uparrow\uparrow} &= \cos\frac{\theta}{2}\sin\frac{\theta}{2}e^{i\phi} \\ \hat{U}_{\downarrow\uparrow}\hat{U}^{-1}_{\uparrow\downarrow} &= \sin^2\frac{\theta}{2},\end{aligned} \tag{C.29}$$

this determines

$$\hat{U}_{s\uparrow}\hat{U}^{-1}_{\uparrow s'} = \begin{pmatrix} \cos^2\frac{\theta}{2} & \cos\frac{\theta}{2}\sin\frac{\theta}{2}e^{-i\phi} \\ \cos\frac{\theta}{2}\sin\frac{\theta}{2}e^{i\phi} & \sin^2\frac{\theta}{2} \end{pmatrix}_{s,s'} \quad \text{and} \tag{C.30}$$

$$\hat{U}_{s\downarrow}\hat{U}^{-1}_{\downarrow s'} = \begin{pmatrix} \sin^2\frac{\theta}{2} & -\sin\frac{\theta}{2}\cos\frac{\theta}{2}e^{-i\phi} \\ -\sin\frac{\theta}{2}\cos\frac{\theta}{2}e^{i\phi} & \cos^2\frac{\theta}{2} \end{pmatrix}_{s,s'}. \tag{C.31}$$

Eqs. C.30 and C.31 can be expressed more compactly as

$$\hat{U}_{s\uparrow}\hat{U}^{-1}_{\uparrow s'} = \frac{1}{2}\left(\hat{1} + \hat{\vec{\sigma}}\cdot\vec{m}\right)_{s,s'} \tag{C.32}$$

$$\hat{U}_{s\downarrow}\hat{U}^{-1}_{\downarrow s'} = \frac{1}{2}\left(\hat{1} - \hat{\vec{\sigma}}\cdot\vec{m}\right)_{s,s'}. \tag{C.33}$$

C.4 Spin projection operators

Define

$$\hat{u}^{(+)} = \frac{1}{2}\left(\hat{1} + \hat{\vec{\sigma}}\cdot\vec{m}\right) \tag{C.34}$$

$$\hat{u}^{(-)} = \frac{1}{2}\left(\hat{1} - \hat{\vec{\sigma}}\cdot\vec{m}\right). \tag{C.35}$$

The operator $\hat{\vec{\sigma}}\cdot\vec{m}$ has the property

$$\left(\hat{\vec{\sigma}}\cdot\vec{m}\right)^2 = \hat{1} \tag{C.36}$$

because the Pauli matrices fulfill the following theorem:

$$\left(\hat{\vec{\sigma}}\cdot\vec{A}\right)\left(\hat{\vec{\sigma}}\cdot\vec{B}\right) = \left(\vec{A}\cdot\vec{B}\right)\hat{1} + i\hat{\vec{\sigma}}\cdot\left(\vec{A}\times\vec{B}\right) \tag{C.37}$$

and by setting $\vec{A} = \vec{B} = \vec{m}$ and noting $|\vec{m}| = 1$. This implies that $\hat{u}^{(+)}$ and $\hat{u}^{(-)}$ are projection operators. In order to consider their projection properties the state vector is defined as

$$\hat{\psi} = \begin{pmatrix} \psi_\uparrow \\ \psi_\downarrow \end{pmatrix}. \tag{C.38}$$

Then define

$$\hat{\psi}^{(+)} = \hat{u}^{(+)}\hat{\psi} \tag{C.39}$$

$$\hat{\psi}^{(-)} = \hat{u}^{(-)}\hat{\psi}. \tag{C.40}$$

Using C.33 in C.39 one finds the explicit form of the vector $\hat{\psi}^{(+)}$:

$$\hat{u}^{(+)}\hat{\psi} = \begin{pmatrix} \frac{1}{2}(1+\cos\theta) & \frac{1}{2}\sin\theta e^{-i\phi} \\ \frac{1}{2}\sin\theta e^{i\phi} & \frac{1}{2}(1-\cos\theta) \end{pmatrix} \begin{pmatrix} \psi_\uparrow \\ \psi_\downarrow \end{pmatrix}. \tag{C.41}$$

Eqs. C.39 and C.41 imply

$$\hat{\psi}^{(+)} = \begin{pmatrix} \psi_\uparrow^{(+)} \\ \psi_\uparrow^{(+)} \end{pmatrix} = \begin{pmatrix} \frac{1}{2}(1+\cos\theta)\psi_\uparrow & \frac{1}{2}\sin\theta e^{-i\phi}\psi_\uparrow \\ \frac{1}{2}\sin\theta e^{i\phi}\psi_\downarrow & \frac{1}{2}(1-\cos\theta)\psi_\downarrow \end{pmatrix}. \tag{C.42}$$

Multiplication of C.39 on the left by $\hat{\vec{\sigma}}\cdot\vec{m}$ and using C.36 yields

$$\left(\hat{\vec{\sigma}}\cdot\vec{m}\right)\hat{\psi}^{(+)} = \left(\hat{\vec{\sigma}}\cdot\vec{m}\right)\frac{1}{2}\left(\hat{1}+\hat{\vec{\sigma}}\cdot\vec{m}\right)\hat{\psi} = \frac{1}{2}\left(\hat{\vec{\sigma}}\cdot\vec{m}+\hat{1}\right)\hat{\psi} = \hat{\psi}^{(+)}. \tag{C.43}$$

Hence $\hat{\psi}^{(+)}$ is an eigenvector of $\left(\hat{\vec{\sigma}}\cdot\vec{m}\right)$ with eigenvalue $+1$. Similarly

$$\left(\hat{\vec{\sigma}}\cdot\vec{m}\right)\hat{\psi}^{(-)} = -\hat{\psi}^{(-)}, \tag{C.44}$$

i.e. $\hat{\psi}^{(-)}$ is an eigenvector of $\left(\hat{\vec{\sigma}}\cdot\vec{m}\right)$ with eigenvalue -1. Note that the projection properties of $\hat{u}^{(+)}$ and $\hat{u}^{(-)}$ are a consequence of identity C.36. This result is valid for any operator. $\hat{u}^{(+)}$ and $\hat{u}^{(-)}$ are called spin projection matrices.

C.5 Transmission matrix (laboratory system)

The outgoing wave in the laboratory system $\hat{\Psi}_s^n$ is defined as

$$\hat{\Psi}_s^n = \sum_{m,s'} \frac{\chi^m(\rho)}{\sqrt{k_m}} \hat{t}_{ss'}^{nm} \hat{\xi}_{s'} e^{ik_m x}, \tag{C.45}$$

while the outgoing wave in the rotated system is $\hat{\Phi}_s^n$

$$\hat{\Phi}_s^n = \sum_{m,s'} \frac{\chi^m(\rho)}{\sqrt{k_m}} \hat{t}_{U,ss'}^{nm} \hat{\xi}_{U,s'} e^{ik_m x}. \tag{C.46}$$

The spinor $\hat{\xi}_{s'}$ satisfies C.18. Since the RHS of C.45 and C.46 has a form similar to C.14 and C.15, respectively, one can follow steps C.19-C.25, and show

$$\hat{t}_{ss'} = (\hat{U}\hat{t}_U\hat{U}^{-1})_{ss'}. \tag{C.47}$$

Hence the transformation laws for $\hat{t}$ and $\hat{r}$ are the same (see C.16). Now consider electron transmission without spin-flip (in the rotated system). Assume

$$\hat{t}_{U,ss'} = \delta_{s,s'}\hat{t}_{U,ss}. \tag{C.48}$$

Similar to C.27 one can deduce from C.48

$$\left(\hat{U}\hat{t}_U\hat{U}^{-1}\right)_{ss'} = \hat{U}_{s\uparrow}\hat{U}^{-1}_{\uparrow s'}\hat{t}_{U,\uparrow\uparrow} + \hat{U}_{s\downarrow}\hat{U}^{-1}_{\downarrow s'}\hat{t}_{U,\downarrow\downarrow}. \tag{C.49}$$

From Eqs. C.16, C.27, C.32, C.33, C.47, and C.49 one can determine the transformation for the reflection and transmission matrices:

$$\hat{r}^{mn} = \hat{r}^{mn}_{U,\uparrow\uparrow}\hat{u}^{(+)} + \hat{r}^{mn}_{U,\downarrow\downarrow}\hat{u}^{(-)} \tag{C.50}$$

$$\hat{t}^{mn} = \hat{t}^{mn}_{U,\uparrow\uparrow}\hat{u}^{(+)} + \hat{t}^{mn}_{U,\downarrow\downarrow}\hat{u}^{(-)}. \tag{C.51}$$

Although the $\hat{r}_U$ and $\hat{t}_U$ matrices are diagonal in spin space, the $\hat{r}$ and $\hat{t}$ matrices are not (due to the spin projection operators $\hat{u}^{(+)}$ and $\hat{u}^{(-)}$). This means even without spin-flip in the rotated system there is spin-flip in the laboratory system.

C.6 The scattering matrix for the N/F/N-sandwich

Now the scattering due to a ferromagnetic layer (F) inserted between two normal metal (N) layers will be treated. Left and right N layer will be called L and R respectively. The scattering matrix in (L,R) is defined by

$$\hat{S} = \begin{pmatrix} \hat{S}_{\mathrm{RR}} & \hat{S}_{\mathrm{RL}} \\ \hat{S}_{\mathrm{LR}} & \hat{S}_{\mathrm{LL}} \end{pmatrix} = \begin{pmatrix} \hat{r} & \hat{t} \\ \hat{t}' & \hat{r}' \end{pmatrix} = \begin{pmatrix} \hat{r} & \hat{t} \\ \hat{t} & \hat{r} \end{pmatrix}, \tag{C.52}$$

where the third equality is due to symmetry; L and R are assumed to be identical paramagnets meaning $\hat{t}' = \hat{t}$ and $\hat{r} = \hat{r}'$.

One needs to perform the transformation of $\hat{S}$ from the laboratory system into the rotated system. Using C.51 one has (skipping n, m labels)

$$\hat{S} = \begin{pmatrix} \hat{r}^{mn}_{U,\uparrow\uparrow}\hat{u}^{(+)} + \hat{r}^{mn}_{U,\downarrow\downarrow}\hat{u}^{(-)} & \hat{t}^{mn}_{U,\uparrow\uparrow}\hat{u}^{(+)} + \hat{t}^{mn}_{U,\downarrow\downarrow}\hat{u}^{(-)} \\ \hat{t}^{mn}_{U,\uparrow\uparrow}\hat{u}^{(+)} + \hat{t}^{mn}_{U,\downarrow\downarrow}\hat{u}^{(-)} & \hat{r}^{mn}_{U,\uparrow\uparrow}\hat{u}^{(+)} + \hat{r}^{mn}_{U,\downarrow\downarrow}\hat{u}^{(-)} \end{pmatrix} = \hat{S}_{U,\uparrow\uparrow}\hat{u}^{(+)} + \hat{S}_{U,\downarrow\downarrow}\hat{u}^{(-)}, \tag{C.53}$$

where

$$\hat{S}_{U,\uparrow\uparrow} = \begin{pmatrix} \hat{r}_{U,\uparrow\uparrow} & \hat{t}_{U,\uparrow\uparrow} \\ \hat{t}_{U,\uparrow\uparrow} & \hat{r}_{U,\uparrow\uparrow} \end{pmatrix} \quad \text{and} \quad \hat{S}_{U,\downarrow\downarrow} = \begin{pmatrix} \hat{r}_{U,\downarrow\downarrow} & \hat{t}_{U,\downarrow\downarrow} \\ \hat{t}_{U,\downarrow\downarrow} & \hat{r}_{U,\downarrow\downarrow} \end{pmatrix}. \tag{C.54}$$

C.7 Current induced by modulation of the chemical potential

The theory of Tserkovnyak et al. [116] is based on the following equation:

$$\hat{I}^{\mathrm{pump}}(t) = \mathrm{e}\frac{\partial \hat{n}(l)}{\partial X}\frac{dX(t)}{dt}, \tag{C.55}$$

where $\hat{I}^{\mathrm{pump}}$ is the matrix current (2×2 matrix in s=$\frac{1}{2}$ space), $X(t)$ is a parameter that modulates the scattering matrix $\hat{S}$, and

$$\frac{\partial \hat{n}(l)}{\partial X} = \frac{1}{4\pi i}\sum_{mn,l'}\frac{\partial \hat{S}_{nm,ll'}}{\partial X}\hat{S}_{nm,ll'} + \mathsf{h.c.} \tag{C.56}$$

is the matrix emissivity into lead l.

Eq. C.55 is a generalization of the theory of Büttiker et al. [115] which considers an ac-electric current induced by an oscillating chemical potential. This theory has been extended by Brouwer [114] to show that a dc-current can be pumped through a quantum dot by periodically varying two independent parameters X_1 and X_2. Eq. C.55 generalizes this concept to the (spin dependent) matrix current.

C.7.1 Review of the Büttiker theory

In the following a two probe conductor is considered. The Hamiltonian for the electrons is given by

$$H = H_0 + H_1. \tag{C.57}$$

H_0 is

$$H_0 = \sum_{m\alpha}\left[a^{\dagger}_{\alpha m}a_{\alpha m}(E_{m\alpha} - \mu_0) + b^{\dagger}_{\alpha m}b_{\alpha m}(E_{m\alpha} - \mu_0)\right], \tag{C.58}$$

where $a_{\alpha m}$ annihilates an incident electron in contact α (in our case $\alpha = \mathrm{L}, \mathrm{R}$) and channel m corresponds to the transverse mode $\chi_m(\rho)$. Operator $b_{\alpha m}$ refers to an outgoing electron. The perturbation H_1 is due to the modulation of the chemical potential at contact α

$$H_1 = -\sum_{m\alpha}\delta\mu_{\alpha}(t)\left[a^{\dagger}_{\alpha m}a_{\alpha m} + b^{\dagger}_{\alpha m}b_{\alpha m}\right]. \tag{C.59}$$

Time evolution of $a_{\alpha m}(t)$: From the Heisenberg equation of motion one has

$$\dot{a}_{\alpha m}(t) = \frac{1}{\hbar}\left[H_0 + H_1, a_{\alpha m}(t)\right], \tag{C.60}$$

using Eq. C.57 - C.59 and the Fermion commutation rules one has

$$a_{\alpha m}(t) = a_{\alpha m}(0)\exp\{-\frac{i}{\hbar}\int_0^t dt\left[E_{m\alpha} - \mu_0 - \delta\mu_\alpha(t)\right]\}. \tag{C.61}$$

Since only linear response is considered (assuming $\delta\mu_\alpha$ to be small), one can expand

$$a_{\alpha m}(t) \simeq a^{(0)}_{\alpha m}(t)\left(1 - i\Phi_\alpha(t)\right) \tag{C.62}$$

where

$$a^{(0)}_{\alpha m}(t) = a_{\alpha m}(0)\exp\{-\frac{i}{\hbar}\int_0^t dt\left(E_{m\alpha} - \mu_0\right)\} \tag{C.63}$$

is the unperturbed time evolution, and

$$\Phi_\alpha(t) = -\frac{1}{\hbar}\int_0^t \delta\mu_\alpha t dt \tag{C.64}$$

is the phase-shift acquired at time t.

The current incident in channel m at contact α is given by the operator

$$I^{\rm in}_{\alpha m} = \frac{e}{\hbar}a^\dagger_{\alpha m}(t)a_{\alpha m}(t). \tag{C.65}$$

The outgoing current operator is

$$I^{\rm out}_{\alpha m} = \frac{e}{\hbar}b^\dagger_{\alpha m}(t)b_{\alpha m}(t). \tag{C.66}$$

Note that Eqs. C.65 and C.66 are resembling rather charge than current densities. This can be fixed by a special normalization of the operators $a_{\alpha m}$ and $b_{\alpha m}$. The net current in contact α is

$$I_\alpha(t) = \sum_m \left[I^{\rm in}_{\alpha m}(t) - I^{\rm out}_{\alpha m}(t)\right] = \frac{e}{\hbar}\sum_m \left[a^\dagger_{\alpha m}(t)a_{\alpha m}(t) - b^\dagger_{\alpha m}(t)b_{\alpha m}(t)\right]. \tag{C.67}$$

For the sake of later introduction of the scattering matrix one defines the vectors

$$\vec{a}_\alpha = \sum_m a_{\alpha m}\vec{c}_m \quad \text{and} \quad \vec{b}_\alpha = \sum_m b_{\alpha m}\vec{c}_m, \tag{C.68}$$

where $\vec{c}_m$ is a unit vector for channel m. Using C.68, allows to write C.67 as

$$I_\alpha(t) = \frac{e}{\hbar}\left[\vec{a}^\dagger_{\alpha m}(t)\vec{a}_\alpha(t) - \vec{b}^\dagger_\alpha(t)\vec{b}_\alpha(t)\right]. \tag{C.69}$$

For an oscillating chemical potential

$$\delta\mu_\alpha(t) = \delta\mu_\alpha(0)\cos(\omega t) \tag{C.70}$$

it is useful to write C.70 in terms of Fourier transformed operators. One has

$$\vec{a}_\alpha(t) = \int_{-\infty}^{\infty}\frac{dE}{2\pi}e^{-iEt}\vec{a}_\alpha(E) \tag{C.71}$$

and

$$I_\alpha(t) = \mathrm{e}\int_{-\infty}^{\infty}\frac{dE}{2\pi}\int_{-\infty}^{\infty}\frac{dE'}{2\pi}e^{-i(E-E')t}\left[\vec{a}^\dagger_\alpha(E)\vec{a}_\alpha(E') - \vec{b}^\dagger_\alpha(E)\vec{b}_\alpha(E')\right]. \tag{C.72}$$

Inverting C.71 and using C.62, one gets

$$\vec{a}_\alpha(E) = \int_{-\infty}^{\infty}dEe^{iEt}\vec{a}_\alpha(t) = \int_{-\infty}^{\infty}dEe^{iEt}\vec{a}^{(0)}_\alpha(t)\left(1 - i\Phi_\alpha(t)\right). \tag{C.73}$$

Using C.64 and C.70 one obtains the phase shift:

$$\Phi_\alpha(t) = -\delta\mu_\alpha\int_0^t dt\cos(\omega t) = -\delta\mu\frac{\sin(\omega t)}{\hbar\omega} = -\frac{\delta\mu_\alpha}{2i\hbar\omega}\left(e^{i\omega t} - e^{-i\omega t}\right) \tag{C.74}$$

introducing C.74 in the RHS of C.73 results in:

$$\vec{a}_\alpha(E) = \vec{a}^{(0)}_\alpha(E) + \frac{\delta\mu_\alpha}{2\hbar\omega}\int_{-\infty}^{\infty}\vec{a}^{(0)}_\alpha(t)e^{iEt}\left(e^{i\omega t} - e^{-i\omega t}\right)dt. \tag{C.75}$$

after performing the time integration, Eq. C.75 yields the perturbed vector:

$$\vec{a}_\alpha(E) \cong \vec{a}^{(0)}_\alpha(E) + \frac{\delta\mu_\alpha}{2\hbar\omega}\left[\vec{a}^{(0)}_\alpha(E+\hbar\omega) - \vec{a}^{(0)}_\alpha(E-\hbar\omega)\right]. \tag{C.76}$$

Now one can Fourier transform $I_\alpha(t)$. Let

$$\begin{aligned} I_\alpha(\omega) &= \int_{-\infty}^{\infty}dte^{i\omega t}I_\alpha(t) \qquad (C.77)\\ &= \mathrm{e}\int_{-\infty}^{\infty}dte^{i\omega t}\int_{-\infty}^{\infty}\frac{dE}{2\pi}\int_{-\infty}^{\infty}\frac{dE'}{2\pi}e^{i(E-E')t}\left[\vec{a}^\dagger_\alpha(E)\vec{a}_\alpha(E) - \vec{b}^\dagger_\alpha(E)\vec{b}_\alpha(E)\right], \end{aligned}$$

the t-integration yields

$$\frac{1}{2\pi}\int_{-\infty}^{\infty}dte^{i(\hbar\omega+E-E')t} = \delta(\hbar\omega + E - E'). \tag{C.78}$$

From C.77 and C.78 and the E' integration one obtains the expectation value of $I_\alpha(\omega)$:

$$\langle I_\alpha(\omega)\rangle = \mathrm{e}\int_{-\infty}^{\infty}\frac{dE}{2\pi}\left[\left\langle \vec{a}^\dagger_\alpha(E)\vec{a}_\alpha(E+\hbar\omega)\right\rangle - \left\langle \vec{b}^\dagger_\alpha(E)\vec{b}_\alpha(E+\hbar\omega)\right\rangle\right]. \tag{C.79}$$

In linear response, using C.76 one can calculate to order $\delta\mu_\alpha$

$$\begin{aligned}\langle \vec{a}^\dagger_\alpha(E)\vec{a}_\alpha(E+\hbar\omega)\rangle &\simeq \Big\langle \left[\vec{a}^{(0)\dagger}_\alpha(E) + \frac{\delta\mu_\alpha}{2\omega}\vec{a}^{(0)\dagger}_\alpha(E+\hbar\omega) - \frac{\delta\mu_\alpha}{2\omega}\vec{a}^{(0)\dagger}_\alpha(E-\hbar\omega)\right] \\ &\times \left[\vec{a}^{(0)}_\alpha(E+\hbar\omega) + \frac{\delta\mu_\alpha}{2\omega}\vec{a}^{(0)}_\alpha(E+2\hbar\omega) - \frac{\delta\mu_\alpha}{2\omega}\vec{a}^{(0)}_\alpha(E)\right]\Big\rangle \\ &= \sum_m \frac{\delta\mu_\alpha}{2\omega}\left[f(E+\hbar\omega) - f(E)\right],\end{aligned} \tag{C.80}$$

where the result (valid for unperturbed vectors $\vec{a}^{(0)}(E)$) was used

$$\langle \vec{a}^{(0)\dagger}_\alpha(E)\vec{a}^{(0)}_\alpha(E')\rangle = \delta_{E,E'}f(E), \tag{C.81}$$

and $f(E)$ is the Fermi function. The scattering matrix transforms incoming electrons into outgoing electrons:

$$\vec{b}_\alpha(E) = \hat{S}_{\alpha\beta}\vec{a}_\alpha(E). \tag{C.82}$$

Here (α,β) refer to the contacts (R or L). In components (channels), Eq. C.82 reads

$$\vec{b}_{\alpha m}(E) = \hat{S}_{mn,\alpha\beta}\vec{a}_{\alpha n}(E) \tag{C.83}$$

this corresponds to the result obtained in C.53, which is generalization of $\hat{S}_{mn,\alpha\beta}$ to a 2×2 matrix in spin $s=\frac{1}{2}$ space. Paying attention to the transverse modes (m,n), one can now use C.82 and C.83 to evaluate the second term on the RHS of C.79:

$$\langle \vec{b}^\dagger_\alpha(E)\vec{b}_\alpha(E+\hbar\omega)\rangle = \sum_m \langle \vec{b}^\dagger_{\alpha m}(E)\vec{b}_{\alpha m}(E+\hbar\omega)\rangle. \tag{C.84}$$

Eq. C.83 implies

$$\vec{b}^\dagger_{\alpha m}(E) = \sum_{n,\beta} S^\dagger_{mn\alpha\beta}(E)\vec{a}^\dagger_{\beta n}(E) \quad \text{and} \tag{C.85}$$

$$\vec{b}_{\alpha m}(E+\hbar\omega) = \sum_{k,\eta} S_{mk\alpha\eta}(E+\hbar\omega)\vec{a}_{\eta n}(E+\hbar\omega). \tag{C.86}$$

Introducing C.86 into C.84 one has

$$\langle \vec{b}^\dagger_\alpha(E)\vec{b}_\alpha(E+\hbar\omega)\rangle = \sum_{mn,\beta}\sum_{k,\eta} S^\dagger_{mn\alpha\beta}(E)S_{mk\alpha\eta}(E+\hbar\omega)\langle \vec{a}^\dagger_{\beta n}(E)\vec{a}_{\eta k}(E+\hbar\omega)\rangle. \tag{C.87}$$

Using C.76 and C.80, yields

$$\langle \vec{a}^{\dagger}_{\beta n}(E)\vec{a}_{\eta k}(E+\hbar\omega)\rangle = \frac{\delta\mu_\beta}{2\hbar\omega}\left[f(E+\hbar\omega)f(E)\right]\delta_{\alpha,\eta}\delta_{n,k}. \tag{C.88}$$

This result substituted in C.87, and summing over η and k results in

$$\langle \vec{b}^{\dagger}_{\alpha}(E)\vec{b}_{\alpha}(E+\hbar\omega)\rangle = \sum_{mn\beta} S^{\dagger}_{mn\alpha\beta}(E)S_{mk\alpha\eta}(E+\hbar\omega)\left[f(E+\hbar\omega)f(E)\right]\frac{\delta\mu_\beta}{2\hbar\omega}. \tag{C.89}$$

With the use of C.80 and C.89, Eq. C.79 can be rewritten as

$$\langle I_\alpha(\omega)\rangle = \mathrm{e}\sum_{mn,\beta}\delta\mu_\beta\int_{-\infty}^{\infty}\frac{dE}{4\pi}\frac{f(E+\hbar\omega-f(E)}{\hbar\omega}\left[\delta_{m,n}\delta_{\alpha,\beta}-S^{\dagger}_{mn,\alpha\beta}(E)S_{mn,\alpha\beta}(E+\hbar\omega)\right]. \tag{C.90}$$

Now perform a low frequency (small ω) expansion:

$$\langle I_\alpha(\omega)\rangle \simeq \mathrm{e}\sum_{mn,\beta}\delta\mu_\beta\int_{-\infty}^{\infty}\frac{dE}{4\pi}f'(E)\left[\delta_{m,n}\delta_{\alpha,\beta}-S^{\dagger}_{mn,\alpha\beta}(E)\left(S_{mn,\alpha\beta}(E)+\omega S'_{mn,\alpha\beta}(E)\right)\right] \tag{C.91}$$

where $f'(E)$ and $S'(E)$ denote derivatives with respect to energy. With the ac-excitation ($\sim \delta\mu_\beta\cos(\omega t)$), only the term which is proportional to ω is C.91 is relevant. Denoting this term as $\delta\langle I_\alpha(\omega)\rangle$, one has

$$\delta\langle I_\alpha(\omega)\rangle = -\hbar\omega\mathrm{e}\sum_{mn,\beta}\delta\mu_\beta\int_{-\infty}^{\infty}\frac{dE}{4\pi}f'(E)S^{\dagger}_{mn,\alpha\beta}(E)S'_{mn,\alpha\beta}(E). \tag{C.92}$$

Now the T=0 K limit is considered:

$$f'(E) = -\delta(E-E_F). \tag{C.93}$$

Symmetrizing C.92 and using the unitarity of the $\hat{S}$ matrix

$$\begin{aligned} \hat{S}^{\dagger}(E)\hat{S}(E) &= \hat{1} \\ \Rightarrow \hat{S}^{\dagger}(E)\hat{S}'(E) &= -\hat{S}'^{\dagger}(E)\hat{S}(E). \end{aligned} \tag{C.94}$$

Combining C.93 and C.94 in C.92, one gets

$$\delta\langle I_\alpha(\omega)\rangle = \frac{\hbar\omega\mathrm{e}}{8\pi}\sum_{mn,\beta}\delta\mu_\beta\left[S^{\dagger}_{mn,\alpha\beta}(E_F)S'_{mn,\alpha\beta}(E_F)-S^{\dagger\prime}_{mn,\alpha\beta}(E_F)S_{mn,\alpha\beta}(E_F)\right]. \tag{C.95}$$

Noting that $S^{\dagger\prime}S = (S^{\dagger}S')^*$, C.95 can be rearranged as:

$$\delta\langle I_\alpha(\omega)\rangle = \frac{i\omega\mathrm{e}}{4\pi}\sum_{mn,\beta}\delta\mu_\beta\mathrm{Im}\left[\frac{\partial S_{mn,\alpha\beta}}{\partial E}S^{\dagger}_{mn,\alpha\beta}(E)\right]_{E=E_F}. \tag{C.96}$$

This was first derived by Büttiker et al. [115]. Now one can consider a time dependent current $\delta\langle I_\alpha(t)\rangle$. Eq. C.77 implies

$$\begin{aligned}\delta\langle I_\alpha(t)\rangle &= \frac{1}{2\pi}\int_{-\infty}^{\infty} d\omega \delta\langle I_\alpha(\omega)\rangle e^{-i\omega t} \\ &= \frac{\mathrm{e}}{4\pi}\sum_{mn,\beta}\int_{-\infty}^{\infty}\frac{d\omega}{2\pi} i\hbar\omega\delta\mu_\beta(\omega)e^{-i\omega t}\mathrm{Im}\left[\frac{\partial S_{mn,\alpha\beta}}{\partial E}S^\dagger_{mn,\alpha\beta}(E)\right]_{E=E_F} \\ &= -\frac{\mathrm{e}}{4\pi}\sum_{mn,\beta}\frac{d}{dt}(\delta\mu_\beta(t))\mathrm{Im}\left[\frac{\partial S_{mn,\alpha\beta}}{\partial E}S^\dagger_{mn,\alpha\beta}(E)\right]_{E=E_F}. \qquad \text{(C.97)}\end{aligned}$$

The RHS of C.97 is now in the form used by Brouwer [114] and Tserkovnyak [116]. In order to transform Eq. C.97 into Brouwer's notation one needs to make the following replacements:

$$\delta\mu(t) = X(t) \quad \text{and} \quad \frac{\partial S_{\alpha\beta,mn}}{\partial E}\Big|_{E=E_F} = \frac{\partial S_{\alpha\beta,mn}}{\partial X}. \qquad \text{(C.98)}$$

Making these replacements in C.97 yields Brouwer's result [114]:

$$\delta\langle I_\alpha(t)\rangle = -\frac{\mathrm{e}}{4\pi}\sum_{mn,\beta}\mathrm{Im}\left[\frac{\partial S_{mn,\alpha\beta}}{\partial X}S^\dagger_{mn,\alpha\beta}(E)\right]\frac{dX(t)}{dt}. \qquad \text{(C.99)}$$

The question which arises is whether C.98 is valid for any parameter X, that modulates $S_{mn,\alpha\beta}$. Note that as long as $X(t)$ is the deviation of the chemical potential from the equilibrium, Eqs. C.98 are consistent to each other. The point is that the $\partial S_{\alpha\beta,mn}/\partial E$ term originates from the expansion in ω

$$S_{mn,\alpha\beta}(E+\hbar\omega) \cong S_{mn,\alpha\beta}(E) + \hbar\omega\frac{\partial S_{mn,\alpha\beta}}{\partial E}, \qquad \text{(C.100)}$$

where ω is the frequency of $\delta\mu_\beta(t)$.

C.8 Generalization to "matrix current"

The important point behind the current matrix $\hat{I}$ in Eq. C.99, is that it incorporates both charge **and** spin flow. Since any 2×2 matrix may be expanded in terms of the three Pauli matrices and the identity matrix, one can write $\hat{I}$ as sum:

$$\hat{I} = \frac{I_C}{2}\hat{1} - \hat{\vec{\sigma}}\cdot\vec{I}_S(\frac{e}{\hbar}). \qquad \text{(C.101)}$$

The quantities I_C and $\vec{I}_S$ are actually expectation values. In a classical picture, these expectation values are integrals over the momentum $\vec{p}$ of the conduction. They are conveniently obtained using the Wigner distribution function (a 2×2 matrix):

$$\hat{F}(\vec{r},\vec{p}) = \frac{1}{2}\left[f_1(\vec{r},\vec{p})\hat{1} + \vec{f}(\vec{r},\vec{p})\cdot\hat{\vec{\sigma}}\right]. \tag{C.102}$$

The matrix $\hat{I}_x$ for current flow along the x-axis is

$$\hat{I}_x = \frac{\mathrm{e}}{h^3}\int d^3p v_x \hat{F}(\vec{r},\vec{p}) = e\langle v_x \hat{F}\rangle, \tag{C.103}$$

using C.102 and C.103 one obtains

$$\hat{I}_x = e\Big\langle v_x\left(f_1\hat{1} - \hat{\vec{\sigma}}\cdot\vec{f}\right)\Big\rangle. \tag{C.104}$$

From a comparison of Eqs.C.101 and C.104, one finds

$$I_C = e\langle v_x f_1\rangle \quad \text{and} \quad \vec{I}_S = -\hbar\langle v_x \vec{f}_1\rangle, \tag{C.105}$$

showing that I_C and $\vec{I}_S$ in Eq. C.101 are the charge and the spin current, respectively. From C.101, one can see that

$$\mathrm{Tr}(\hat{I}) = I_C, \tag{C.106}$$

where Tr denotes the trace in spin space. In C.106 the fact that the Pauli matrices are traceless was used. Next, consider the spin part, using C.101:

$$\mathrm{Tr}(\hat{\sigma}_i\hat{I}) = \frac{1}{2}I_C\mathrm{Tr}(\hat{\sigma}_i) - \frac{\mathrm{e}}{h}\mathrm{Tr}(\hat{\sigma}_i\sum_j \hat{\sigma}_j I_{Sj}) = -\frac{\mathrm{e}}{h}\mathrm{Tr}(\hat{\sigma}_i^2 I_{S,j}) = -\frac{2\mathrm{e}}{h}(I_{S,j}). \tag{C.107}$$

Hence the i-th ($i = x, y, z$) component of the spin current is given by

$$I_{S,i} = -\frac{h}{2\mathrm{e}}\mathrm{Tr}(\hat{\sigma}_i\hat{I}) \quad \text{or} \quad \vec{I}_S = -\frac{h}{\mathrm{e}}\mathrm{Tr}(\hat{\vec{\sigma}}\hat{I}). \tag{C.108}$$

The generalization of C.99 to a matrix current is obtained by replacing the LHS as follows:

$$\delta\langle I_\alpha(t)\rangle \Rightarrow \hat{I}(t), \tag{C.109}$$

and the scattering matrix on the RHS by

$$S_{\alpha\beta,mn} \Rightarrow \hat{S}_{\alpha\beta,mn}. \tag{C.110}$$

The quantity C.110 can be identified as the scattering matrix $\hat{s}_{mn,ll'}$ given in Eq. C.53 (for the case of "no spin-flip" at the interface).

C.9 Spin current pumped by $\vec{M}(t)$

Following Tserkovnyak et al. one can start from Eqs. C.55 and C.56 where the parameter $X(t)$ was identified with the azimuthal angle of $\vec{M}(t)$ (see C.3):

$$X(t) = \phi(t). \tag{C.111}$$

Using C.111 in C.55 and C.56, the current pumped into lead l is:

$$\hat{I}(t)^{\text{pump}} = \mathrm{e}\frac{\partial \hat{n}(l)}{\partial \phi}\frac{\partial \phi(t)}{\partial t}, \tag{C.112}$$

where

$$\frac{\partial \hat{n}(l)}{\partial \phi} = \frac{1}{4\pi i}\sum_{mnl'}\left(\frac{\partial \hat{s}_{mn,ll'}}{\partial \phi}\hat{s}^{\dagger}_{mn,ll'} + \mathsf{h.c.}\right). \tag{C.113}$$

Now consider the relation between the matrix emissivity and $\hat{I}(t)^{\text{pump}}$. Using Eq. C.54

$$\frac{\partial \hat{s}_{mn,ll'}}{\partial \phi}\frac{\partial \phi}{\partial t} = \left(s^{\uparrow}_{mn,ll'}\frac{\partial u^{\uparrow}}{\partial \phi}\frac{\partial \phi}{\partial t} + s^{\downarrow}_{mn,ll'}\frac{\partial u^{\downarrow}}{\partial \phi}\frac{\partial \phi}{\partial t}\right) = s^{\uparrow}\dot{u}^{\uparrow} + s^{\downarrow}\dot{u}^{\downarrow}, \tag{C.114}$$

where the (mn, ll') indices are dropped for a moment. Using C.34 and C.35, one has:

$$\dot{u}^{\uparrow} = \frac{1}{2}\hat{\vec{\sigma}}\cdot\frac{\partial \vec{m}}{dt} \quad \text{and} \quad \dot{u}^{\downarrow} = -\frac{1}{2}\hat{\vec{\sigma}}\cdot\frac{\partial \vec{m}}{dt}. \tag{C.115}$$

Using C.53 and C.114 in C.112 and C.113, one obtains the pumped current which is written schematically as:

$$\begin{aligned}\hat{I}(t)^{\text{pump}} &= \frac{\mathrm{e}}{8\pi i}\sum_{mn,l'}[\left(s^{\uparrow}\dot{u}^{\uparrow} + s^{\downarrow}\dot{u}^{\downarrow}\right)\left(s^{\dagger\uparrow}u^{\uparrow} + s^{\dagger\downarrow}u^{\downarrow}\right) \\ &+ \left(s^{\uparrow}u^{\uparrow} + s^{\downarrow}u^{\downarrow}\right)\left(s^{\dagger\uparrow}\dot{u}^{\uparrow} + s^{\dagger\downarrow}\dot{u}^{\downarrow}\right)].\end{aligned} \tag{C.116}$$

There are 8 products on the RHS of C.116 which can be grouped into 4 pairs:

$$\begin{aligned}\hat{I}(t)^{\text{pump}} &= \frac{\mathrm{e}}{8\pi i}\sum_{mn,l'}[s^{\uparrow}s^{\dagger\uparrow}\left(\dot{u}^{\uparrow}u^{\uparrow} - u^{\uparrow}\dot{u}^{\uparrow}\right) + s^{\downarrow}s^{\dagger\downarrow}\left(\dot{u}^{\downarrow}u^{\downarrow} - u^{\downarrow}\dot{u}^{\downarrow}\right) \\ &+ s^{\uparrow}s^{\dagger\downarrow}\left(\dot{u}^{\uparrow}u^{\downarrow} - u^{\uparrow}\dot{u}^{\downarrow}\right) + s^{\downarrow}s^{\dagger\uparrow}\left(\dot{u}^{\downarrow}u^{\uparrow} - u^{\downarrow}\dot{u}^{\uparrow}\right) +]\end{aligned} \tag{C.117}$$

The products of $\dot{u}^{\uparrow,\downarrow}$ and $u^{\uparrow,\downarrow}$ are 2×2 matrices to be evaluated with use of C.34, C.35, and C.115. Note that $\dot{u}^{\uparrow\downarrow}$ and $u^{\uparrow\downarrow}$ are non commuting matrices; this reflects the quantum nature of the pumped current. The first pair on the RHS of C.118 is:

$$\dot{u}^{\uparrow}u^{\uparrow} - u^{\uparrow}\dot{u}^{\uparrow} = \frac{1}{4}\left[(\hat{\vec{\sigma}}\cdot\dot{\vec{m}})(\hat{\vec{\sigma}}\cdot\vec{m})(\hat{\vec{\sigma}}\cdot\vec{m})(\hat{\vec{\sigma}}\cdot\dot{\vec{m}})\right] = \frac{i}{2}\hat{\vec{\sigma}}\cdot(\dot{\vec{m}}\times\vec{m}) \tag{C.118}$$

where identity C.37 was used. Consider the next pair:

$$\dot{u}^{\downarrow}u^{\downarrow} - u^{\downarrow}\dot{u}^{\downarrow} = \frac{i}{2}\hat{\vec{\sigma}}\cdot(\dot{\vec{m}}\times\vec{m}). \tag{C.119}$$

The emergence of the Gilbert term, $\vec{m}\times\dot{\vec{m}}$ on the RHS of C.118 and C.119 becomes obvious. The last two pairs in C.118 are:

$$\dot{u}^{\uparrow}u^{\downarrow} - u^{\uparrow}\dot{u}^{\downarrow} = \frac{1}{2}(\hat{\vec{\sigma}}\cdot(\dot{\vec{m}}) - \frac{i}{2}\hat{\vec{\sigma}}\cdot(\dot{\vec{m}}\times\vec{m}) \tag{C.120}$$

$$\dot{u}^{\downarrow}u^{\uparrow} - u^{\downarrow}\dot{u}^{\uparrow} = -\frac{1}{2}(\hat{\vec{\sigma}}\cdot(\dot{\vec{m}}) - \frac{i}{2}\hat{\vec{\sigma}}\cdot(\dot{\vec{m}}\times\vec{m}). \tag{C.121}$$

Using C.118-C.121, yields

$$\begin{aligned}\hat{I}^{\text{pump}}(t) &= \frac{\mathrm{e}}{8\pi i}\sum_{mn,l'}\left(s^{\uparrow}s^{\uparrow\dagger} + s^{\downarrow}s^{\downarrow\dagger} - s^{\uparrow}s^{\downarrow\dagger} - s^{\downarrow}s^{\uparrow\dagger}\right)\hat{\vec{\sigma}}\cdot(\vec{m}\times\dot{\vec{m}}) \\ &+ \frac{\mathrm{e}}{8\pi i}\sum_{mn,l'}\left(s^{\uparrow}s^{\downarrow\dagger} - s^{\downarrow}s^{\uparrow\dagger}\right)(\hat{\vec{\sigma}}\cdot\dot{\vec{m}}).\end{aligned} \tag{C.122}$$

In what follows the focus will be on the evaluation of the first sum in C.122, since it yields Gilbert damping. According to C.53 and C.54

$$s^{\uparrow} \equiv s^{\uparrow}_{mn,ll'} = S_{U,\uparrow\uparrow} = \begin{pmatrix}\hat{r}_{U,\uparrow\uparrow} & \hat{t}'_{U,\uparrow\uparrow}\\ \hat{t}'_{U,\uparrow\uparrow} & \hat{r}_{U,\uparrow\uparrow}\end{pmatrix} \quad \text{and} \tag{C.123}$$

$$s^{\uparrow} \equiv s^{\downarrow}_{mn,ll'} = S_{U,\downarrow\downarrow} = \begin{pmatrix}\hat{r}_{U,\downarrow\downarrow} & \hat{t}'_{U,\downarrow\downarrow}\\ \hat{t}'_{U,\downarrow\downarrow} & \hat{r}_{U,\downarrow\downarrow}\end{pmatrix}. \tag{C.124}$$

These relations can be schematically rewritten as:

$$s^{\uparrow} = \begin{pmatrix}r_{\uparrow} & t_{\uparrow}\\ t_{\uparrow} & r_{\uparrow}\end{pmatrix} \quad \text{and} \quad s^{\downarrow} = \begin{pmatrix}r_{\downarrow} & t_{\downarrow}\\ t_{\downarrow} & r_{\downarrow}\end{pmatrix}, \tag{C.125}$$

One can proceed to evaluate the matrix in (in (L,R)-space) of the summand in C.122.

$$\left(s^{\uparrow}s^{\uparrow} + s^{\downarrow}s^{\downarrow\dagger} - s^{\uparrow}s^{\downarrow\dagger} - s^{\downarrow}s^{\uparrow\dagger}\right) = \hat{\Gamma}, \tag{C.126}$$

where

$$\hat{\Gamma} = \begin{pmatrix}\Gamma_{\text{RR}} & \Gamma_{\text{RL}}\\ \Gamma_{\text{LR}} & \Gamma_{\text{LL}}\end{pmatrix}. \tag{C.127}$$

Using C.125, the matrix elements of $\hat{\Gamma}$ are:

$$\Gamma_{\text{RR}} = r^{\uparrow}r^{\uparrow *} + r^{\downarrow}r^{\downarrow *} - r^{\uparrow}r^{\downarrow *} - r^{\downarrow}r^{\uparrow *} + t^{\uparrow}t^{\uparrow *} + t^{\downarrow}t^{\downarrow *} - t^{\uparrow}t^{\downarrow *} - t^{\downarrow}t^{\uparrow *} \tag{C.128}$$

and

$$\Gamma_{\rm LL} = \Gamma_{\rm RR}. \tag{C.129}$$

The off-diagonal elements are not needed for the following reason: If one looks at the *net* current emitted into L and R, one has from the first term of C.122

$$\begin{aligned} \hat{I}^{\rm pump}_{\rm net} &= \sum_l \hat{I}^{\rm pump}_l = \frac{\rm e}{16\pi i}\hat{\vec{\sigma}}\cdot(\dot{\vec{m}}\times\vec{m}) \\ &\times \sum_{mn,ll'}\left(s^{\uparrow}_{mn,ll'}s^{\uparrow\dagger}_{mn,l'l} + s^{\downarrow}_{mn,ll'}s^{\downarrow\dagger}_{mn,l'l} - s^{\uparrow}_{mn,ll'}s^{\downarrow\dagger}_{mn,l'l} - s^{\downarrow}_{mn,ll'}s^{\uparrow\dagger}_{mn,l'l}\right), \end{aligned} \tag{C.130}$$

where the symmetry property

$$s^{\uparrow}_{mn,ll'} = s^{\uparrow}_{mn,l'l} \tag{C.131}$$

stemming from Eqs. C.54 was employed. The RHS of C.130 now involves traces (over L,R space) such as

$$\sum_{ll'}\left(s^{\uparrow}_{mn,ll'}s^{\uparrow\dagger}_{mn,l'l}\right) \text{ etc.} \tag{C.132}$$

Hence the pumped net current C.130 is proportional to:

$$\sum_{mn}{\rm Tr}_{\rm L,R}\left(\hat{\Gamma}_{mn}\right) = \sum_{mn}\left(\Gamma_{{\rm LL},mn} + \Gamma_{{\rm RR},mn}\right) = 2\sum_{mn}\Gamma_{{\rm RR},mn} \tag{C.133}$$

with the use of C.128 and C.133, the net current C.130 becomes

$$\hat{I}(t)^{\rm pump}_{\rm net} = \frac{\rm e}{8\pi}\hat{\vec{\sigma}}\cdot(\dot{\vec{m}}\times\vec{m})\sum_{mn}\left\{|r^{\uparrow}_{mn} - r^{\downarrow}_{mn}|^2 + |t^{\uparrow}_{mn} - t^{\downarrow}_{mn}|^2\right\}. \tag{C.134}$$

On comparing C.134 with the expansion, C.101, one obtains the spin current

$$\vec{I}^{\rm pump}_S = \frac{\hbar}{4\pi}A_r\left(\vec{m}\times\frac{d\vec{m}}{dt}\right) \tag{C.135}$$

where A_r is the interface scattering parameter

$$A_r = \frac{1}{2}\sum_{mn}\left\{|r^{\uparrow}_{mn} - r^{\downarrow}_{mn}|^2 + |t^{\uparrow}_{mn} - t^{\downarrow}_{mn}|^2\right\}. \tag{C.136}$$

Returning to Eq. C.122, the contribution to $\vec{I}^{\rm pump}_S$ of the second term is:

$$\left(\vec{I}^{\rm pump}_S\right)_{\rm 2nd\ term} = -\frac{\hbar}{4\pi}A_i\frac{d\vec{m}}{dt} \tag{C.137}$$

where

$$A_i = {\rm Im}\sum_{mn}\left\{r^{\uparrow}_{mn}r^{\downarrow *}_{mn} + t^{\uparrow}_{mn}t^{\downarrow *}_{mn}\right\}. \tag{C.138}$$

Eqs. C.135-C.138 agree with with the result first derived by Tserkovnyak et al. (Eqs. (4-6) in [116]).

C.10 Excess Gilbert damping constant

The Landau-Lifshitz-Gilbert (LLG) equation reads

$$\frac{d\vec{m}}{dt} = -\gamma\vec{m} \times \vec{H}_{\text{eff}} + \alpha\vec{m} \times \frac{d\vec{m}}{dt}, \tag{C.139}$$

where α is the Gilbert damping constant. The excess Gilbert constant α' due to the N/F/N interfaces, is obtained from the net spin current C.135 by recalling the spin conservation law:

$$\frac{d\vec{S}}{dt} = -\vec{I}_S^{\text{pump}}, \tag{C.140}$$

where $\vec{S}$ is the total spin in the ferromagnetic film. It is related to the total magnetic moment $\vec{M}_{tot}$ of the film by:

$$\vec{M}_{tot} = \vec{m}(t)M_{tot} = \gamma\vec{S}, \quad \text{where} \quad \gamma = \frac{g_L\mu_B}{\hbar} \tag{C.141}$$

Hence,

$$\frac{d\vec{m}}{dt} = -\frac{g_L\mu_B}{\hbar M_{tot}}\frac{d\vec{S}}{dt} = -\frac{g_L\mu_B}{\hbar M_{tot}}\vec{I}_S^{\text{pump}}. \tag{C.142}$$

Introducing Eq. C.135 for $\vec{I}_S^{\text{pump}}$, one has from C.142:

$$\frac{d\vec{m}}{dt} = \alpha'\vec{m} \times \frac{d\vec{m}}{dt} \tag{C.143}$$

where α' is the excess Gilbert damping constant, given by:

$$\alpha' = \frac{g_L\mu_B A_r}{4\pi M_{tot}}. \tag{C.144}$$

This is equivalent to Eq. 10 in [116] which involves the magnetic moment M in units of μ_B.

C.11 Peristaltic pumping of spins

According to Webster[202]: peristaltic≡"the rhythmic, wavelike motion of the walls of the alimentary canal and certain other hollow organs, consisting of alternate contractions and dilations of transverse and longitudinal muscles that move the contents of the tube onward".

Closest to this concept is the so-called "Thouless pump" [203]. This example considers adiabatic pumping of electrons in a one-dimensional channel, subjected to a periodic potential $U(x+a) = U(x)$. If the potential moves with a small velocity v:

$$U(x,t) = U(x - vt). \tag{C.145}$$

The potential $U(x,t)$ at each point x varies periodically with time. If the electrons follow adiabatically this variation of $U(x,t)$, a dc-current

$$I = nq_e v \tag{C.146}$$

is induced, where n is the electron density, q_e is the electron charge, and v is the velocity. The important point is that Eq. C.145 represents a travelling wave, which can be decomposed into two standing waves: Assuming a sinusoidal $U(x)$

$$U(x) = U_0 \sin \frac{2\pi x}{a}, \tag{C.147}$$

one gets:

$$\begin{aligned} U(x - vt) &= U_0 \sin \frac{2\pi}{a}(x - vt) \\ &= U_0 \sin \frac{2\pi}{a} x \cos \frac{2\pi vt}{a} - U_0 \cos \frac{2\pi}{a} x \sin \frac{2\pi vt}{a}. \end{aligned} \tag{C.148}$$

Note that the time dependence of the two standing waves differs by a phase shift $\pi/2$. Thus, two independent parameters are needed to realize pumping of electrons. A single standing wave does not generate a dc-current. This is consistent with the "singe parameter theory" by Büttiker et al. [115], which derives an ac-current in a lead as a response to an ac-variation of the chemical potential. From this point of view, it is surprising that dc-spin current results from Eq. C.55 by using a single parameter $X(t) = \phi(t)$. As pointed out by Tserkovnyak et al. [116], the explanation is that precession of $\vec{M}(t)$ involves actually two parameters

$$M_x(t) = M_x \cos \omega t \tag{C.149}$$

$$M_y(t) = M_y \sin \omega t \tag{C.150}$$

which are independent in the sense that there is a phase shift of $\pi/2$ (see Eq. C.148). Now an expression for the spin current will be derived by setting $X(t) = m_x(t)$ in C.55. Assume that the unit vector $\vec{m}$ is

$$\vec{m}(t) = (m_x(t), 0, m_z), \tag{C.151}$$

which corresponds to strictly linear polarization. One can follow Eqs. C.107-C.136 to evaluate the spin current

$$\hat{I}(t)^{\rm pump} = {\rm e}\frac{\partial \hat{n}(l)}{\partial m_x}\dot{m}_x. \tag{C.152}$$

The main difference lies in Eqs. C.109 and C.110 which now take the form:

$$\dot{u}^{\uparrow} = \frac{1}{2}\hat{\sigma}_x\dot{m}_x\dot{u}^{\downarrow} = -\frac{1}{2}\hat{\sigma}_x\dot{m}_x. \tag{C.153}$$

Using C.35,C.35 and C.55,C.56, one has (see C.113):

$$\dot{u}^{\uparrow}u^{\uparrow} - u^{\uparrow}\dot{u}^{\uparrow} = \frac{1}{4}\left[(\hat{\sigma}_x\dot{m}_x)(\hat{\vec{\sigma}}_x\cdot\dot{\vec{m}}_X) - (\hat{\vec{\sigma}}\cdot\dot{\vec{m}})(\hat{\sigma}_x\dot{m}_x)\right] = \frac{i}{2}\hat{\vec{\sigma}}\cdot(\dot{\vec{m}}\times\vec{m}) \tag{C.154}$$

The same result follows for

$$\dot{u}^{\downarrow}u^{\downarrow} - u^{\downarrow}\dot{u}^{\downarrow} = \frac{i}{2}\hat{\vec{\sigma}}\cdot(\dot{\vec{m}}\times\vec{m}). \tag{C.155}$$

Eqs. C.154 and C.155 imply that the form of Gilbert damping term is not affected by the choice: $X(t) = m_x(t)$. In other words, Eq. C.152 yields the spin current $\vec{I}_S^{\rm pump}$ given again by Eq. C.135. This is not a dc-current if $X(t) = m_x(t)$ which can be shown explicitly, by taking the time-average of C.135 under assumption C.151. Eq. C.135 in components reads:

$$I_{S,x}^{\rm pump} = \frac{\hbar}{4\pi}A_r\left(m_y\dot{m}_z - m_z\dot{m}_y\right) = 0 \tag{C.156}$$

$$I_{S,y}^{\rm pump} = \frac{\hbar}{4\pi}A_r\left(m_z\dot{m}_x - m_x\dot{m}_z\right) \neq 0 \tag{C.157}$$

$$I_{S,z}^{\rm pump} = \frac{\hbar}{4\pi}A_r\left(m_x\dot{m}_y - m_y\dot{m}_x\right) = 0. \tag{C.158}$$

The only nonzero component of $\vec{I}_S^{\rm pump}$ is $I_{S,y}^{\rm pump}$ for

$$m_x(t) = m_{x0}\cos\omega t \quad \text{and} \quad m_z = m_{z0} \tag{C.159}$$

and the time average of C.157 yields

$$I_{S,y}^{\rm pump} = -\frac{\omega\hbar}{4\pi T}A_r m_{z0}m_{x0}\int_0^T dt\sin\omega t = 0, \tag{C.160}$$

where $T = \frac{2\pi}{\omega}$ is the period. Hence there is no dc-spin current pumped by linearly polarized oscillation of $\vec{m}$. This is consistent with the general principle of peristaltic pumping. Now elliptical polarization will be assumed

$$\vec{m} = \left(m_{x0}\cos\omega t, m_{y0}\cos(\omega t - \varphi), m_{z0}\right). \tag{C.161}$$

With this ansatz, all components I_S^{pump} are nonzero, but only $I_{S,z}^{\text{pump}}$ has a nonzero time average:

$$\begin{aligned} I_{S,z}^{\text{pump}} &= -\frac{\omega\hbar}{4\pi T} A_r m_{x0} m_{y0} \int_0^T dt \left(\cos\omega t \sin\left(\omega t - \varphi\right) - \cos\left(\omega t - \varphi\right) \sin\omega t\right) \\ &= \frac{\omega\hbar}{4\pi T} A_r m_{x0} m_{y0} \sin\varphi. \end{aligned} \tag{C.162}$$

For the spin-pumping proposed by Tserkovnyak et al. [116], $\varphi = \frac{\pi}{2}$, $m_{x0} = m_{y0}$, i.e. the time-evolution of the transverse vector $(m_x(t), m_y(t))$ is described by a circle (circular polarization). For a general case, where $\varphi \neq \frac{\pi}{2}$ and $m_{x0} \neq m_{y0}$ the transverse vector evolves on an ellipse, which for $\varphi = 0$ reduces to a line. Eq. C.162 shows that $\overline{I_S^{\text{pump}}}$ is proportional to the enclosed area in the 2-parameter space. This illustrates the area theorem for dc-pumped current [114].

Bibliography

[1] G. A. Prinz. Magnetoelectronics. *Science*, 282:1660–1663, 1998.

[2] S. A. Wolf, D. D. Awschalom, R. A. Buhrman, J. M. Daughton, S. von Molar, M. L. Roukes, A. Y. Chtchelkanova, and D. M. Treger. Spintronics: A spin-based electronicsvision for the future. *Science*, 294:1488–1495, 2001.

[3] D. D. Awschalom, M. E. Flatté, and N. Samarath. Spintronics. *Scientific American*, June:67–73, 2002.

[4] B. Heinrich and J. F. Cochran. Ultrathin metallic magnetic films: magnetic anisotropies and exchange interaction. *Adv. Phys.*, 42:523–639, 1993.

[5] B. Heinrich and J. A. C. Bland. *Magnetic Ultrathin Film Structures II.* Springer Verlag, 1993.

[6] L. D. Landau and E. Lifshitz. On the theory of the dispersion of magnetic permeability in ferromagnetic bodies. *Phys. Z. Sov.*, 8:153–169, 1935.

[7] J. R. MacDonald. Ferromagnetic resonance and the internal field in ferromagnetic materials. *Proc. Phys. Soc. A*, 64:968–983, 1951.

[8] T. L. Gilbert. A Lagrangian formulation of the gyromagnetic equation of the magnetization field. *Phys. Rev.*, 100:1243–1244, 1955.

[9] W. Döring. Über die Trägheit der Wände zwischen Weißschen Bezirken. *Zeitschrift für Naturforschung*, 3a:373–379, 1948.

[10] T. L. Gilbert. *Formulation, foundations and applications of the phenomenological theory of ferromagnetism.* Phd dissertation, Illinois Institute of Technology, 1956.

[11] Z. Celinski, K. B. Urquhart, and B. Heinrich. Using ferromagnetic resonance to measure the magnetic moments of ultrathin films. *J. Mag. Mag. Mat.*, 166:6–26, 1997.

[12] R. Arias and D. L. Mills. Extrinsic contributions to the ferromagnetic resonance response of ultrathin films. *Phys. Rev. B*, 60:7395–7409, 1999.

[13] B. Heinrich, R. Urban, and G. Woltersdorf. Magnetic relaxation in metallic films. Single and multilayer structures. *J. Appl. Phys.*, 91:7523–7525, 2002.

[14] H. Suhl. Theory of the magnetic damping constant. *IEEE Trans. Magn.*, 34:1834–1838, 1998.

[15] B. Heinrich, J. F. Cochran, and K. Myrtle. The exchange splitting of phonon assisted microwave transmission at 9.5 GHz. *J. Appl. Phys.*, 53:2092–2094, 1982.

[16] B. Heinrich, D. Fraitová, and V. Kamberský. The influence of s-d exchange on relaxation of magnons in metals. *Phys. Stat. Sol.*, 23:501–507, 1967.

[17] B. Heinrich. *Temperature dependance of FMR linewidth of iron (in Czech).* Phd dissertation, Czechoslovak Academy of Sciences, 1967.

[18] S. V. Vonsovskii and J. A. Izyumov. *Fiz. Metallov i Metallovedenie*, 10:321, 1960.

[19] R. J. Elliott. Theory of the effect of spin-orbit coupling on magnetic resonance in some semiconductors. *Phys. Rev.*, 96:266–279, 1954.

[20] S. Dubois, L. Piraux, J. M. George, K. Ounadjela, J. L. Duvail, and A. Fert. Evidence for a short spin diffusion length in permalloy from the giant magnetoresistance of multilayered nanowires. *Phys. Rev. B*, 60:477–484, 1999.

[21] T. Valet and A. Fert. Theory of the perpendicular magnetoresistance in magnetic multilayers. *Phys. Rev. B*, 48:7099–7113, 1993.

[22] J. Pelzl, R. Meckenstock, D. Spodding, F. Schreiber, J. Pflaum, and Z. Frait. Spin-orbit-coupling effects on g-value and damping factor of the ferromagnetic resonance in Co and Fe films. *J. Phys. Condens. Matter*, 15:451–463, 2003.

[23] *CRC Handbook of Materials.* McGraw-Hill, 1990.

[24] B. Heinrich, K. B. Urquhart, A. S. Arrott, J. F. Cochran, K. Myrtle, and S. T. Purcell. Ferromagnetic resonance study of ultrathin bcc Fe(100) films grown epitaxially on fcc Ag(100) substrates. *Phys. Rev. Lett.*, 59:1756–1759, 1987.

[25] R. M. Bozorth. *Ferromagnetism*. D. van Nostrand Company, 1951.

[26] L. Piraux, S. Dubois, and A. Fert. Perpendicular giant magnetoresistance in magnetic multilayered nanowires. *J. Mag. Mag. Mat.*, 159:287–292, 1996.

[27] B. Heinrich, J. F. Cochran, M. Kowalewski, Z. Celinski, A. S. Arrott, and K. Myrtle. Magnetic anisotropies and exchange coupling in ultrathin fcc Co(001) structures. *Phys. Rev. B*, 44:9348–9361, 1991.

[28] G. Dewar, B. Heinrich, and J. F. Cochran. Ferromagnetic antiresonance transmission of 24 Ghz radiation through nickel (20 to 364 °C). *Can. J. Phys.*, 55:821–833, 1977.

[29] G. Gubbiotti, O. Kazakova, G. Carlotti, M. Hanson, and P. Vavassori. Spin-wave spectra in nanometric elliptical dots arrays. *IEEE Trans. Mag.*, 39:2750–2752, 2003.

[30] B. Heinrich, G. Woltersdorf, O. Mosendz, R. Urban, E. Rozenberg, G. Schmidt, L. Molenkamp, and P. Bach. Magnetic properties of NiMnSb(001) films grown on InGaAs/InP(001). *J. Appl. Phys.*, 95:7462–7464, 2004.

[31] D. N. Zubarev. Double-time Green's functions in statistical physics. *Sov. Phys. Usp.*, 3:320–345, 1960.

[32] C. J. Kriessman and H. B. Callen. The magnetic susceptibility of the transition elements. *Phys. Rev.*, 94:837–844, 1954.

[33] A. Y. Elezzabi, M. R. Freeman, and M. Johnson. Direct measurement of the conduction electron spin-lattice relaxation time T_1 in gold. *Phys. Rev. Lett.*, 77:3220–3223, 1996.

[34] S. Ingvarsson, L. Ritchie, X. Y. Liu, G. Xiao, J. C. Slonczewski, P. L. Trouilloud, and R. H. Koch. The role of electron scattering in magnetization relaxation in thin $Ni_{81}Fe_{19}$ films. *Phys. Rev. B*, 66:214416, 2002.

[35] V. Kamberský and C. E. Patton. Spin-wave relaxation and phenomenological damping in ferromagnetic resonance. *Phys. Rev. B*, 11:2668–2672, 1975.

[36] V. Kamberský. On ferromagnetic resonance damping in metals. *Czech. J. Phys. B*, 26:1366–1383, 1976.

[37] K. Baberschke. The magnetism in Ni. *Appl. Phys. A*, 62:417–427, 1996.

[38] V. Kamberský. On the Landau-Lifshitz relaxation in ferromagnetic metals. *Can. J. Phys.*, 48:2906–2911, 1970.

[39] S. N. Vonsovskii. *Ferromagnetic resonance*, chapter E. A. Turov, Chap. V. GIMFL, Moscow, 1961.

[40] S. M. Bhagat and P. Lubitz. Temperature variation of ferromagnetic relaxation in the 3d transition metals. *Phys. Rev. B*, 10:179–185, 1974.

[41] V. Korenman and R. E. Prange. Anomalous damping of spin waves in magnetic metals. *Phys. Rev. B*, 6:2769–2777, 1972.

[42] J. M. Ziman. *Principles of the theory of solids*, second edition Chapter 8. 7, page 607. Cambridge University Press, 1972.

[43] B. Heinrich, D. J. Meredith, and J. F. Cochran. Wave number and temperature dependent Landau-Lifshitz damping in nickel. *J. Appl. Phys.*, 50:7726–7728, 1979.

[44] J. Kuneš and V. Kamberský. First-principles investigation of the damping of fast magnetization precession in ferromagnetic 3d metals. *Phys. Rev. B*, 65:212411, 2002.

[45] V. Kamberský. FMR linewidth and disorder in metals. *Czech. J. Phys. B*, 34:1111–1124, 1984.

[46] V. Kamberský, J. F. Cochran, and J. M. Rudd. Anisotropic low-temperature FMR linewidth in nickel and the theory of 'anomalous' damping. *J. Magn. Magn. Mater.*, 104-107:2089–2091, 1992.

[47] Z. Celinski and B. Heinrich. Ferromagnetic resonance linewidth of Fe ultrathin films grown on a bcc Cu substrate. *J. Appl. Phys.*, 70:5935–5937, 1991.

[48] M. Sparks, R. Loudon, and C. Kittel. Ferromagnetic relaxation. I. Theory of the relaxation of the uniform precession and the degenerate spectrum in insulators at low temperatures. *Phys. Rev.*, 122:791–803, 1961.

[49] M. Sparks. *Ferromagnetic Relaxation Theory*. Mc-Graw-Hill, New York, 1966.

[50] E. Schlömann. Spin-wave analysis of ferromagnetic resonance in polycrystalline ferrites. *J. Phys. Chem. Solids*, 6:242–256, 1958.

[51] R. LeCraw, E. G. Spencer, and C. S. Porter. Ferromagnetic resonance line width in yttrium iron garnet single crystals. *Phys. Rev.*, 110:1311–1313, 1958.

[52] S. Geschwind and A. M. Clogston. Narrowing effect of dipole forces on inhomogeneously broadened lines. *Phys. Rev.*, 108:49–53, 1957.

[53] M. J. Hurben, D. R. Franklin, and C. E. Patton. Angle dependance of the ferromagnetic resonance linewidth in easy-axis and easy-plane single crystal hexagonal ferrite disks. *J. Appl. Phys.*, 81:7458–7467, 1997.

[54] C. E. Patton, C. H. Wilts, and F. B. Humphrey. Relaxation processes for ferromagnetic resonance in thin films. *J. Appl. Phys.*, 38:1358–1359, 1967.

[55] Ch. Kittel. *Introduction to solid state physics*. Wiley, New York, 1996.

[56] D. L. Mills. *Spin dynamics in confined magnetic structures II, edited by B. Hillebrands and K. Ounadjela*, chapter Spin damping in ultrathin magnetic films. Springer Verlag, 2003.

[57] J. Kerr. On the magnetisation of light and the illumination of magnetic lines of force. *Rep. Brit. Ass.*, S5:85, 1876.

[58] J. Kerr. On the rotation of the plane of polarization by reflection from the pole of a magnet. *Phil. Mag.*, 3:321–343, 1877.

[59] C. Bradley. Thermal gas cracker manual. 2002.

[60] A. J. Springthorpe, S. J. Ingrey, B. Emmerstorfer, P. Mandeville, and W. T. Moore. Measurement of GaAs surface oxide desorption temperatures. *Appl. Phys. Lett.*, 50:77–79, 1987.

[61] T. Akatsu, A. Plössl, H. Stenzel, and U. Gösele. GaAs wafer bonding by hydrogen surface cleaning. *J. Appl. Phys*, 86:7146–7150, 1999.

[62] E. J. Petit, F. Houzay, and J. M. Moison. Interaction of atomic hydrogen with native oxides on GaAs(001). *J. Vac. Sci. Technol. A*, 10:2172–2177, 1992.

[63] J. A. Venables. *Surface Physics*. Cambridge University Press, 2000.

[64] C. D. Wagner, W. M. Riggs, L. E. Davis, and J. F. Moulder. *Handbook of X-ray Photoelectron Spectroscopy*. Perkin Elmer Corporation, 1979.

[65] C. D. Wagner, W. M. Riggs, L. E. Davis, and J. F. Moulder. *Handbook of Auger Electron Spectroscopy*. Perkin Elmer Corporation, 1979.

[66] M. P. Seah and W. A. Dench. Quantitative electron spectroscopy of surfaces: a standard data base for electron inelastic mean free paths in solids. *Surf. Interface Anal.*, 1:2–11, 1979.

[67] T. L. Monchesky, B. Heinrich, R. Urban, K. Myrtle, M. Klaua, and J. Kirschner. Magnetoresistance and magnetic properties of Fe/Cu/Fe/GaAs(100). *Phys. Rev. B*, 60:10242–10251, 1999.

[68] M. Henzler. Electron diffraction and surface defect structure. *Electron Spectroscopy for Surface Analysis*, page 117, 1977.

[69] N. W. Ashcroft and N. D. Mermin. *Solid State Physics*. Saunders College, 1976.

[70] O. Thomas, Q. Shen, P. Schieffer, N. Tournerie, and B. Lépine. Interplay between anisotropic strain relaxation and uniaxial interface magnetic anisotropy in epitaxial Fe films on GaAs(001). *Phys. Rev. Lett.*, 90:017205, 2003.

[71] W. A. Harrison. *Electronic structure and properties of solids*. Freeman San Francisco, 1980.

[72] M. D. Pashley. Electron counting model and its application to island structures on molecular-beam epitaxy grown GaAs(001) and ZnSe(001). *Phys. Rev. B*, 40:10482–10487, 1989.

[73] T. L. Monchesky. *Magnetoresistance and magnetic properties of magnetic multilayers grown directly on GaAs(100)*. Phd dissertation, Simon Fraser University, 2000.

[74] Qi-Kun Xue, T. Hashizume, and T. Sakurai. Scanning tunneling microscopy of GaAs(001) surfaces. *Appl. Surf. Sci.*, 141:244–263, 1999.

[75] I. M. van Hove, P. R. Pukite, and P. I. Cohen. The dependence of RHEED oscillations on MBE growth parameters. *J. Vac. Sci. Technol.*, B3:563–567, 1985.

[76] P. R. Pukite, S. Batra, and P. I. Cohen. Anisotropic growth processes. *SPIE, Growth of Compound Semiconductors*, 796:22–26, 1987.

[77] P. R. Pukite, G. S. Petrich, G. J. Whaley, and P. I. Cohen. *Diffusion at Interfaces: Microscopic Concepts, edited by M. Grunze, H. J. Kreuzer and J. J. Weime*, chapter Reflection High Energy Electron Diffraction Studies of Diffusion and Cluster Formation During Molecular Beam Epitaxy, pages 30–54. Springer, 1988.

[78] A. S. Arrott. *Magnetic Ultrathin Film Structures I,* ed. J. A. C. Bland and B. Heinrich. Springer Verlag, 1994.

[79] W. Wulfhekel, F. Zavaliche, F. Porrati, H. P. Oepen, and J. Kirschner. Nanopatterning of magnetic anisotropy by controlled strain relief. *Europhys. Lett.*, 49:651–657, 2000.

[80] R. H. Varian and S. F. Varian. A high frequency oscillator and amplifier. *J. Appl. Phys.*, 10:321–327, 1939.

[81] Ch. P. Poole. *Electron spin resonance. A comprehensive treatise on experimental techniques.* Interscience publishers, 1967.

[82] E. L. Ginston. *Microwave Measurements.* McGraw-Hill, 1957.

[83] A. G. Gurevitch. *Ferrites at rf frequencies*, chapter 1, pages 1–103. Springer, 1960.

[84] R. Bartucci, E. Colavita, L. Sportelli, G. Balestrino, and S. Barbanera. Electron paramagnetic resonance of single-phase pellets of the high-t_c superconductor $YBa_2Cu_3O_{7-x}$. *Phys. Rev. B*, 37:2313–2316, 1988.

[85] M. R. Freeman and W. K. Hiebert. *Spin dynamics in confined magnetic structures I, edited by B. Hillebrands and K. Ounadjela*, chapter Stroboscopic Microscopy of Magnetic Dynamics, pages 92–126. Springer Verlag, 2001.

[86] Y. Acremann, M. Buess, C. H. Back, M. Dumm, G. Bayreuther, and D. Pesica. Ultrafast generation of magnetic fields in a Schottky diode. *Nature*, 414:51–54, 2001.

[87] Y. Acremann. *Magnetic Excitations on the Picosecond Timescale*. Phd dissertation, Eidgenössische Technische Hochschule, Zürich, 2000.

[88] T. C. Eschrich, R. D. Carroll, R. N. Sacks, and W. J. Tanski. MESFETs with nonalloyed ohmic contacts using a graded n^+ (InGa)As cap layer. *IEEE Trans. Elec. Dev.*, 36:1213–1215, 1989.

[89] C. Nuhoglu, M. Saglam, and A. Türüt. Cr/- and Fe/n-GaAs Schottky diodes: the stable currentvoltage characteristic produced by high-temperature annealing. *Semicond. Sci. Technol.*, 14:114–117, 1999.

[90] J. A. C. Bland, T. Taniyama, A. Hirohata, and J. S. Steinmüller. *Ultrathin Magnetic Structures III., edited by B. Heinrich and J. A. C. Bland*, chapter Optical Studies of Electron Spin Transmission. Spinger-Verlag, (to be published).

[91] A. F. Isakovic, D. M. Carr, J. Strand, B. D. Schultz, C. J. Palmstrøm, and P. A. Crowella. Optically pumped transport in ferromagnet-semiconductor Schottky diodes. *J. Appl. Phys.*, 91:7261–7266, 2002.

[92] R. People and J. C. Bean. Calculation of critical layer thickness versus lattice mismatch for Ga_xSi_{1-x}/Si strained-layer heterostructures. *Appl. Phys. Lett.*, 47:322–324, 1985.

[93] Jan H. van der Merve and W. A. Jesser. An exactly solvable model for calculating critical misfit and thickness in epitaxial superlattices: Layers of equal eleastic constants and thicknesses. *J. Appl Phys.*, 63:1509–1517, 1988.

[94] Y. B. Xu, E. T. M. Kernohan, D. J. Freeland, A. Ercole, M. Tselepi, and J. A. C. Bland. Evolution of the ferromagnetic phase of ultrathin Fe films grown on GaAs(100)-4×6. *Phys. Rev. B*, 58:890–896, 1998.

[95] M. Brockmann, M. Zölfl, S. Miethaner, and G. Bayreuther. In-plane volume and interface magnetic anisotropies in epitaxial Fe films on GaAs(001). *J. Magn. Magn. Mater.*, 198–199:384–386, 1999.

[96] R. A. Gordon, E. D. Crozier, D. T. Jiang, T. L. Monchesky, and B. Heinrich. Distorted Fe films on GaAs(100)-(4×6). *Phys. Rev. B*, 62:2151–2157, 2000.

[97] S. Chikazumi and S. H. Charap. *Physics of magnetism*, chapter Magnetostriction, pages 161–185. John Wiley & Sons, Inc, 1964.

[98] V. L. Safonov and H. N. Bertram. Linear stochastic magnetization dynamics and microscopic relaxation mechanisms. *J. Appl. Phys.*, 94:529–629, 2003.

[99] L. Berger. Emission of spin waves by a magnetic multilayer traversed by a current. *Phys. Rev. B*, 54:9353–9358, 1996.

[100] L. Berger. Multilayers as spin-wave emitting diodes. *J. Appl. Phys.*, 81:4880–4882, 1997.

[101] L. Berger. Effect of interfaces on Gilbert damping and FMR linewidth in magnetic multilayers. *J. Appl. Phys.*, 90:4632–4638, 2001.

[102] J. C. Slonczewski. Current-driven excitation of magnetic multilayers. *J. Magn. Magn. Mater.*, 159:1–7, 1996.

[103] J. C. Slonczewski. Excitation of spin waves by an electric current. *J. Magn. Magn. Mater.*, 195:261–268, 1999.

[104] M. Tsoi, A. G. M. Jansen, J. Bass, W. C. Chiang, M. Seck, V. Tsoi, and P. Wyder. Excitation of a magnetic multilayer by an electric current. *Phys. Rev. Lett.*, 80:4281–4284, 1998.

[105] M. Tsoi, A. G. M. Jansen, J. Bass, W. C. Chiang, V. Tsoi, and P. Wyder. Generation and detection of phase coherent magnons. *Nature*, 406:46–48, 2000.

[106] J. A. Katine, F. J. Albert, R. A. Buhrman, E. B. Myers, and D. C. Ralph. Current-driven magnetization reversal and spin-wave excitations in Co/Cu/Co pillars. *Phys. Rev. Lett.*, 84:3149–3152, 2000.

[107] F. J. Albert, J. A. Katine, R. A. Buhrman, and D. C. Raph. Spin-polarized current switching of a cobalt thin film nanomagnet. *Appl. Phys. Lett.*, 77:3809–3811, 2000.

[108] S. I. Kiselev, J. C. Sankey, I. N. Krivorotov, N. C. Emley, R. J. Schoelkopf, R. A. Buhrman, and D. C. Ralph. Microwave oscillations of a nanomagnet driven by a spin-polarized current. *Nature*, 425:380–383, 2003.

[109] W. H. Rippard, M. R. Pufall, S. Kaka, S. E. Russek, and T. J. Silva. Direct-current induced dynamics in $Co_{90}Fe_{10}/Ni_{80}Fe_{20}$ point contacts. *Phys. Rev. Lett.*, 92:027201, 2004.

[110] R. Urban, G. Woltersdorf, and B. Heinrich. Gilbert damping in single and multilayer uultrathin films: Role of interfaces in nonlocal spin dynamics. *Phys. Rev. Lett.*, 87:217204, 2001.

[111] A. Enders, T. Monchesky, K. Myrtle, R. Urban, B. Heinrich, J. Kirschner, X. G. Zhang, and W. H. Butler. The role of interfaces in the magnetoresistance of Au/Fe/Au/Fe/GaAs(001) ultrathin film structures. *J. Appl. Phys.*, 89:7110–7112, 2001.

[112] M. Johnson. Spin accumultation in gold films. *Phys. Rev. Lett.*, 70:2142–2145, 1993.

[113] A. Brataas, Y. V. Nazarov, and G. E. W. Bauer. Spin-transport in multi-terminal normal metal-ferromagnet systems with non-collinear magnetizations. *Euro. Phys. J. B*, 22:99–110, 2001.

[114] P. W. Brouwer. Scattering approach to parametric pumping. *Phys. Rev. B*, 58:R10135–10138, 1998.

[115] M. Büttiker, H. Thomas, and A. Pretre. Current partition in multiprobe conductors in the presence of slowly oscillating external potentials. *Z. Phys.*, B94:133–137, 1994.

[116] Y. Tserkovnyak, A. Brataas, and G. E. W. Bauer. Enhanced gilbert daming in thin ferromagnetic films. *Phys. Rev. Lett.*, 88:117601, 2002.

[117] Y. Tserkovnyak, A. Brataas, and G. E. W. Bauer. Dynamic exchange coupling and Gilbert damping in magnetic multilayers. *J. Appl. Phys.*, 93:7534–7538, 2003.

[118] K. Xia, J. P. Kelly, G. E. W. Bauer A. Brataas, and I. Turek. Spin torques in ferromagnetic/normal-metal structures. *Phys. Rev. B*, 65:220401R, 2002.

[119] M. D. Stiles and A. Zangwill. Anatomy of spin-transfer torque. *Phys. Rev. B*, 66:014407, 2002.

[120] B. Heinrich, G. Woltersdorf, R. Urban, and E. Šimánek. Role of spin currents in magnetic relaxations of metallic multilayer films. *J. Magn. Magn. Mater.*, 258:376–381, 2003.

[121] B. Heinrich, G. Woltersdorf, R. Urban, and E. Šimánek. Role of dynamic exchange coupling in magnetic relaxations of metallic multilayer films. *J. Appl. Phys.*, 93:7545–7550, 2003.

[122] R. Urban, B. Heinrich, and G. Woltersdorf. Semi-classical theory of spin transport in magnetic multilayers. *J. Appl. Phys.*, 93:8280–8282, 2003.

[123] J. C. Slonczewski. Mechanism of interlayer exchange in magnetic multilayers. *J. Mag. Mag. Mat.*, 126:374–379, 1993.

[124] E. Šimánek and B. Heinrich. Gilbert damping in magnetic multilayers. *Phys. Rev. B*, 67:144418, 2003.

[125] E. Šimánek. Gilbert damping in ferromagnetic films due to adjacent normal-metal layers. *Phys. Rev. B*, 68:224403, 2003.

[126] D. L. Mills. Ferromagnetic resonance relaxation in ultrathin metal films: The role of the conduction electrons. *Phys. Rev. B*, 68:014419, 2003.

[127] B. Heinrich, R. Urban, and G. Woltersdorf. Magnetic relaxation in metallic multilayers. *IEEE Trans. Mag.*, 38:2496–2501, 2002.

[128] R. H. Silsbee, A. Janossy, and P. Monod. Coupling between ferromagnetic and conductionn-spin-resonance modes at a ferromagnetic - normal-metal interface. *Phys. Rev. B*, 19:4382–4399, 1979.

[129] Y. Tserkovnyak, A. Brataas, and G. E. W. Bauer. Spin pumping and magnetization dynamics in metallic multilayers. *Phys. Rev. B*, 66:224403, 2002.

[130] S. Mizukami, Y. Ando, and T. Miyazaki. Ferromagnetic resonance linewidth fo NM/80NiFe/NM films (NM = Cu, Ta, Pd and Pt). *J. Magn. Magn. Mater.*, 226–230:1640–1642, 2001.

[131] B. Heinrich. *Ultrathin Magnetic Structures III., edited by B. Heinrich and J. A. C. Bland*, chapter Spin relaxation in magnetic metallic layers and multilayers. Spinger-Verlag, (to be published).

[132] G. Woltersdorf, R. Urban, and B. Heinrich. Role of spin momentum current in magnetic non-local damping od ultrathin film structures. *Mat. Res. Soc. Symp. Proc.*, 746:67, 2003.

[133] O. Krogh Andersen. Electronic structure of fcc transition metals Ir, Rh, Pt, and Pd. *Phys. Rev. B*, 2:883–906, 1970.

[134] L. J. van der Pauw. A method of measuring specific resistivity and Hall effect of disks of arbitrary shape. *Phillips Research Reports*, 13:1–9, 1958.

[135] D. H. Dye, S. A. Campbell, G. W. Crabtree, J. B. Ketterson, N. B. Sandesara, and J. J. Vuillemin. Fermi surface and many-body enhancement in Pd. *Phys. Rev. B*, 23:462–473, 1981.

[136] M. Brodsky and A. J. Freeman. Observation of a strongly enhanced magnetic susceptibility of Pd in Au-Pd-Au sandwiches. *Phys. Rev. Lett.*, 45:133–137, 1980.

[137] F. M. Mueller, A. J. Freeman, J. O. Dimmock, and A. M. Frudyma. Electronic structure of Palladium. *Phys. Rev. B*, 1:4617–4635, 1970.

[138] V. L. Moruzzi and P. M. Marcus. Magnetism in fcc rhodium and palladinum. *Phys. Rev. B*, 39:471–474, 1989.

[139] P. Larson, I. I. Mazin, and D. J. Singh. Magnetism, critical fluctuations, and susceptibility renormalization in Pd. *Phys. Rev. B*, 69:064429, 2004.

[140] J. Foros, G. Woltersdorf, B. Heinrich, and A. Brataas. Scattering of spin current injected in Pd(001). *to be published*, 2004.

[141] H. J. M. Swagten, M. M. H. Willekens, and W. J. M. de Jonge. *Frontiers in Magnetism of Reduced Dimension Systems, edited by P. Wigen and V. Baryachtiar and N. Lesnik*, chapter The Giant Magnetoresistance Effect, pages 471–499. NATO-ASI, 1996.

[142] H. Kurt, R. Loloee, K. Eid, Jr. W. P. Pratt, and J. Bass. Spin-memory loss at 4. 2 K in sputtered Pd and Pt and at Pd/Cu and Pt/Cu interfaces. *Appl. Phys. Lett.*, 81:4787–4789, 2002.

[143] F. J. Jedema, A. T. Filip, and B. J. van Wees. Electrical spin injection and accumulation at room temperature in an all-metal mesoscopic spin valve. *Nature*, 410:345–348, 2001.

[144] J. M. George, A. Fert, and G. Faini. Direct measurement of spin accumulation in a metallic mesoscopic structure. *Phys. Rev. B*, 67:012410, 2003.

[145] Z. Frait and D. Fraitová. Ferromagnetic resonance and surface anisotropy in iron single crystals. *J. Magn. Magn. Mater.*, 15-18:1081–1082, 1980.

[146] W. Platow, A. N. Anisimov, G. L. Dunifer, M. Farle, and K. Baberschke. Correlations between ferromagnetic resonance linewidth and sample quality in the study of metallic ultrathin films. *Phys. Rev. B*, 58:5611–5621, 1998.

[147] S. Mizukami, Y. Ando, and T. Miyazaki. The study on ferromagnetic resonance linewidth for NM/80NiFe/NM (NM = Cu, Ta, Pd and Pt) films. *Jpn. J. Appl. Phys.*, 40:580–585, 2001.

[148] S. Mizukami, Y. Ando, and T. Miyazaki. Magnetic relaxation of normal-metal (NM)/80NiFe/NM films. *J. Magn. Magn. Mater.*, 239:42–44, 2002.

[149] S. Mizukami, Y. Ando, and T. Miyazaki. Effect of spin diffusion on Gilbert damping for a very thin Permalloy layer in Cu/Permalloy/Cu/Pt films. *Phys. Rev. B*, 66:104413, 2002.

[150] B. Heinrich, Z. Celinski, J. F. Cochran, W. B. Muir, J. Rudd, Q. M. Zhong, A. S. Arrott, K. Myrtle, and J. Kirschner. Ferromagnetic and antiferromagnetic exchange coupling in bcc epitaxial ultrathin Fe(001)/Cu(001)/Fe(001) trilayers. *Phys. Rev. Lett.*, 64:673–676, 1990.

[151] P. Lubitz, S. F. Cheng, and F. J. Rachford. Increase of the magnetic damping in thin polycrystalline Fe films induced by Cu/Fe overlayers. *J. Appl. Phys.*, 93:8283–8285, 2003.

[152] J. Woltersdorf and E. Pippel. Substrate deformation and thin film growth. *Thin Solid Films*, 116:77–94, 1984.

[153] G. Woltersdorf, B. Heinrich, J. Woltersdorf, and R. Scholz. Spin dynamics in ultrathin film structures with a network of misfit dislocations. *J. Appl. Phys.*, 95:7007–7009, 2003.

[154] G. Woltersdorf and B. Heinrich. Two-magnon scattering in a self-assembled nanoscale network of misfit dislocations. *Phys. Rev. B*, 69:184417, 2004.

[155] J. Woltersdorf. Misfit accommodation at interfaces. *Applications of Surface Science*, 11/12:495–516, 1982.

[156] D. J. Bacon and A. G. Cocker. The elaxtic energy of symmetrical dislocation loops. *Philos. Mag.*, 12:195–198, 1965.

[157] D. Cherns and M. J. Stowell. Misfit disloctions in epitaxial films. *Thin Solid Films*, 37:249–260, 1976.

[158] J. H. van der Merwe, J. Woltersdorf, and W. A. Jesser. Low energy dislocation structures in epitaxy. *Mat. Sci. Eng.*, 81:1–33, 1986.

[159] B. Heinrich, Y. Tserkovnyak, G. Woltersdorf, R. Urban, A. Brataas, and G. E. W. Bauer. Dynamic exchange coupling in magnetic bilayers. *Phys. Rev. Lett.*, 90:187601, 2003.

[160] D. J. Twisselmann and R. D. McMichael. Intrinsic damping and intentional ferromagnetic resonance broadening in thin permalloy films. *J. Appl. Phys.*, 93:6903–6905, 2003.

[161] J. Lindner, L. Lenz, K. Kosubek, K. Baberschke, D. Spoddig, R. Meckenstock, J. Pelzl, Z. Frait, and D. L. Mills. Non-gilbert-type damping of the magnetic relaxation in ultrathin ferromagnets: Importance of magnon-magnon scattering. *Phys. Rev. B*, 68:060102(R), 2003.

[162] R. Arias and D. L. Mills. Extrinsic contributions to the ferromagnetic resonance response of ultrathin films. *J. Appl. Phys.*, 87:5455–5456, 2000.

[163] R. D. McMichael. *private communication.*

[164] R. D. McMichael, D. J. Twisselmann, and A. Kunz. Localized ferromagnetic resonance in inhomogeneous thin films. *Phys. Rev. Lett.*, 90:227601, 2003.

[165] P. Bach, A. S. Bader, C. Rüster, C. Gould, C. R. Becker G. Schmidt, L. W. Molenkamp, W. Weigand, C. Kumpf, E. Umbach., R. Urban., G. Woltersdorf, and B. Heinrich. Molecular-beam epitaxy of the half-Heusler alloy NiMnSb on (In,Ga)As/InP (001). *Appl. Phys. Lett.*, 83:531–523, 2003.

[166] A. Koveshnikov, G. Woltersdorf, O. Mosendz, K. L. Kavanagh, B. Heinrich, G. Schmidt, L. Molenkamp, and P. Bach. Structural and magnetic properties of NiMnSb/InGaAs/InP(100). *J. Appl. Phys.*, page submitted, 2004.

[167] R. Urban, B. Heinrich, G. Woltersdorf, K. Ajdari, K. Myrtle, J. F. Cochran, and E. Rozenberg. Nanosecond magnetic relaxation processes in ultrathin metallic films prepared by MBE. *Phys. Rev. B*, 65:020402, 2002.

[168] H. Hopster. Magnetic domain formation in Fe films on Cr(001). *Phys. Rev. Lett.*, 83:1227–1230, 1999.

[169] H. Hopster. Temperature dependent magnetic domain structure in ultrathin Fe films on Cr(001). *J. Appl. Phys.*, 87:5475–5477, 2000.

[170] R. D. McMichael, M. D. Stiles, P. J. Chen, and Jr. W. F. Egelhoff. Ferromagnetic resonace studies of NiO-coupled thin films of $Ni_{80}Fe_{20}$. *Phys. Rev. B*, 58:8605–8612, 1998.

[171] R. D. McMichael, M. D. Stiles, P. J. Chen, and W. F. Egelhoff, Jr. . Ferromagnetic resonance linewidth in thin films coupled to NiO. *J. Appl. Phys.*, 83:7037–7039, 1998.

[172] P. Lubitz, M. Rubenstein, J. J. Krebs, and S. F. Cheng. Frequency and temperature dependence of ferromagnetic linewidth in exchange biased permalloy. *J. Appl. Phys.*, 89:6901–6903, 2001.

[173] S. M. Rezende, M. A. Lucena, A. Azevedo amd F. M. de Aguiar, J. R. Fermin, and S. S. P. Parkin. Exchange anisotropy and spin-wave damping in CoF/IrMn bilayers. *J. Appl. Phys.*, 93:7717–7720, 2003.

[174] B. K. Kuanr, R. E. Camley, and Z. Celinski. Exchange bias of Nio/NiFe: Linewidth broadening and anomalous spin wave damping. *J. Appl. Phys.*, 93:7723–7726, 2003.

[175] P. Böedeker, A. Hucht, A. Schreyer, J. Borchers, F. Güthoff, and H. Zabel. Reorientation of spin density waves in Cr(001) films induced by Fe(001) cap layers. *Phys. Rev. Lett*, 81:914–917, 1998.

[176] A. Schreyer, C. F. Majkrzak, Th. Zeidler, T. Schmitte, P. Böedeker, K. Theis-Bröhl, A. Abromeit, J. A. Dura, and T. Wantanabe. Magnetic structure of Cr in exchange coupled Fe/Cr(001) superlattices. *Phys. Rev. Lett*, 79:4914–4917, 1997.

[177] F. Y. Yang and C. L. Chien. Oscillatory exchange bias due to an antiferromagnet with incommensurate spin-density waves. *Phys. Rev. Lett*, 90:147201, 2003.

[178] U. Schlickum, N. Janke-Gilman, W. Wulfhekel, and J. Kirschner. Step-induced frustration of antiferromagntic order in Mn on Fe(001). *Phys. Rev. Lett.*, 92:107203, 2004.

[179] B. Heinrich, S. T. Purcell, J. R. Dutcher, J. F. Cochran, and A. S. Arrott. Structural and magnetic properties of ultrathin Ni/Fe bilayers grown epitaxially on Ag(001). *Phys. Rev. B*, 38:12879–12896, 1988.

[180] B. Heinrich, Z. Celinski, H. Konno, A. S. Arrott, R. Ruhrig, and A. Hubert. Magnetization loops in Fe/Ag/Fe/Ni(001) structures. *Mat. Res. Soc. Symposium Proceedings*, 313:485–490, 1993.

[181] M. Buess, P. J. Knowles, U. Ramsperger, D. Pescia, and C. H. Back. Phase-resolved pulsed precessional motion at a Schottky barrier. *Phys. Rev. B*, 69:174422, 2004.

[182] H. C. Siegmann, E. L. Garwin C. Y. Prescott, J. Heidmann, D. Mauri, D. Weller, R. Allenspach, and W. Weber. Magnetism with picosecond field pulses. *J. Mag. Mag. Mat.*, 151:L8–12, 1995.

[183] C. H. Back, , R. Allenspach, W. Weber, S. S. P. Parkin, D. Weller, E. L. Garwin, and H. C. Siegmann. Minimum field strength in precessional magnetization reversal. *Science*, 285:864–867, 1999.

[184] G. Woltersdorf, M. Buess, B. Heinrich, and C. Back. Time resolved magnetization dynamics of ultrathin Fe(001) film having Au(001), Pd(001), and Cr(001) cap layers. *to be published*, 2004.

[185] G. Counil, Joo-Von Jim, T. Devolder, C. Chappert, K. Shigeto, and Y. Otani. Spin wave contributions to the high frequency magnetic response of thin films obtained with inductive methods. *J. Appl. Phys.*, 95:5646–5652, 2004.

[186] C. H. Back, D. Weller, J. Heidmann, D. Mauri, D. Guarisco, E. L. Garwin, and H. C. Siegmann. Magnetization reversal in ultrashort magnetic field pulses. *Phys. Rev. Lett.*, 81:3251–3254, 1998.

[187] C. Stamm, I. Tudosa, J. Stöhr, H. C. Siegmann, A. Yu. Dobin, G. Woltersdorf, B. Heinrich, and A. Vaterlaus. Spin relaxation in magnetic switching. *to be published*, 2004.

[188] L. He and W. D. Doyle. A theoretical description of magnetic switching experiments in picosecond field pulses. *J. Appl. Phys.*, 79:6489–6491, 1996.

[189] K. D. Leaver and S. Vojdani. Domain wall motion in single-crystal nickel platelets. *Appl. Phys. D*, 3:729–735, 1970.

[190] J. P. Nibarger, R. Lopusnik, and T. J. Silva. Damping as function of pulsed field amplitude and bias field in thin film permalloy. *Appl. Phys. Lett.*, 82:2112–2114, 2003.

[191] A. Yu. Dobin and R. H. Victora. Intrinsic nonlinear ferromagnetic relaxation in thin metallic films. *Phys. Rev. Lett.*, 90:167203, 2003.

[192] H. Suhl. The theory of ferromagnetic resonance at high signal powers. *J. Phys. Chem. Solids*, 1:209–227, 1957.

[193] T. Shima, T. Moriguchi, S. Mitani, and K. Takanashi. Low-temperature fabrication of $L1_0$ ordered FePt alloy by alternate monatomic layer deposition. *Appl. Phys. Lett.*, 80:288–290, 2002.

[194] T. Shima, K. Takanashi, Y. K. Takahashi, and K. Hono. Preparation and magnetic properties of highly coercive FePt films. *Appl. Phys. Lett.*, 81:1050–1052, 2002.

[195] D. Halley, Y. Samson, A. Marty, P. Bayle-Guillemaud, C. Beigne, B. Gilles, and J. E. Mazille. Anormaly of strain relaxation in thin ordered FePd layers. *Phys. Rev. B*, 65:205408, 2002.

[196] N. Miyata, H. Asami, T. Misushima, and K. Sato. Ferromagnetic crystalline anisotropy of $Pd_{1-x}Fe_x$ alloys. *J. Phys. Soc. Jpn.*, 59:1817–1824, 1990.

[197] V. Gehanno, A. Marty, and B. Gilles Y. Samson. Magnetic domains in epitaxial ordered FePd thin films with perpendicular magnetic anisotropy. *Phys. Rev. B*, 55:12552–12555, 1997.

[198] D. Stoeffler, K. Ounadjela J. Sticht, and F. Gautier. Ab initio study of the induced magnetic polarization in Fe/Pd(001) superlattices. *J. Mag. Mag. Mat.*, 140-144:557, 1995.

[199] K. Sato, E. Takeda, M. Akita, M. Yamaguchi, K. Takanashi, S. Mitani, H. Fujimori, and Y. Suzuki. Magneto-optical spectra of Au/Fe artificial superlattices modulated by integer and noninteger atomic layers. *J. Appl. Phys.*, 86:4985–4996, 1999.

[200] L. Szunyogh, J. Zabloudil, A. Vernes, P. Weinberger, B. Ujfalussy, and C. Sommers. Magnetic anisotropy of ordered and disordered FePd thin films. *Phys. Rev. B*, 63:184408, 2001.

[201] A. Nefedov, T. Schmitte, K. Theis-Bröhl, H. Zabel, M. Doi, E. Schuster, and W. Keune. Growth and structure of $L1_0$ ordered Fe/Pt(001) films on GaAs(001). *J. Phys. Cond. Mat.*, 14:12273–12286, 2002.

[202] *Webster's New World Dictionary.* Macmillan Pubishers, 2002.

[203] D. J. Thouless. Quantization of particle transport. *Phys. Rev. B*, 27:6083–6087, 1983.